Effects of the Helical Tip Mach Number on the Aeroacoustic Performance of a Propeller in Non-Uniform Flow

Master's Thesis

Andrea Improta

Technische Universiteit Delft

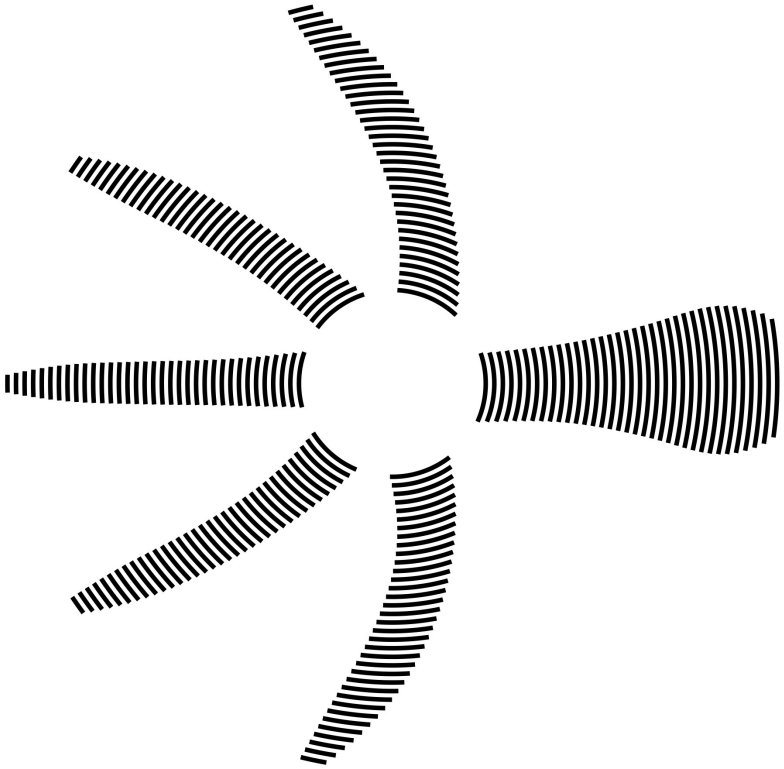

TU Delft Delft University of Technology

Challenge the future

Effects of the Helical Tip Mach Number on the Aeroacoustic Performance of a Propeller in Non-Uniform Flow

Master's Thesis

by

Andrea Improta

in partial fulfillment of the requirements for the degree of

Master of Science
in Aerospace Engineering

at the Delft University of Technology,
to be defended publicly on Thursday March 27, 2025 at 13:00.

Thesis committee:	Prof. dr. ing. G. Eitelberg,	TU Delft, chair
	Dr. ir. T. Sinnige,	TU Delft, supervisor
	Ir. F. do Nascimento Monteiro,	TU Delft, supervisor
	Dr. ir. F. de Prenter,	TU Delft, external examiner

TU Delft Delft University of Technology

PREFACE

This thesis represents the culmination of the journey I embarked upon throughout the course of this research at TU Delft. What began as an initial curiosity has grown into a focused and dedicated exploration of propeller aeroacoustics. It is the product of rigorous research and the application of advanced concepts, aiming to contribute to a deeper understanding of propeller noise emissions within the aeroacoustic community.

I would like to express my deepest gratitude to my supervisors, Tomas Sinnige and Fernanda do Nascimento Monteiro, whose invaluable expertise and unwavering support have guided me throughout this journey.

I would also like to thank all the staff at TU Delft for providing the tools and resources that enabled me to complete this research.

I would like to extend my heartfelt thanks to my friends, whose positive energy has truly been a source of motivation, and I'm deeply grateful for their presence in my life.

Finally, a special mention goes to my parents, to whom I am deeply grateful for allowing me to pursue my passions, and to my entire family, who, even when far away, I have never felt distant from.

Andrea Improta
Delft, March 2025

ABSTRACT

The demand for more efficient propulsion systems originating from growing environmental concerns has brought attention to propeller-based solutions. However, the absence of a nacelle poses a significant challenge on noise emissions. Another challenge arises when attempting to scale propeller noise measurements from wind tunnel tests to full-scale propellers. While experimental studies typically ensure the proper scaling of the advance ratio, testing under ambient conditions often leads to a reduced free-stream Mach number and, if the advance ratio is maintained, to a reduced tip Mach number. This decrease significantly influences the propeller's loading characteristics, which in turn affects its response to the unsteady inflow it experiences due to installation effects.

To date, there is a lack of systematic research in the current literature regarding the sensitivity of propeller noise to Mach number variations under non-uniform inflow conditions, and the physical mechanisms responsible for such noise are not well understood. At this stage, the research can be focused on using low-fidelity solvers and investigating tonal noise emissions alone. The main aim of this thesis is to examine how a propeller's far-field tonal noise emissions are affected by changes in the helical tip Mach number when operating under typical non-uniform inflow conditions, namely at a non-zero angle of attack and undergoing wake encounter, using low-fidelity methods. Additionally, this study aims to provide a physical understanding of the propeller's aeroacoustic characteristics.

To meet this objective, several low-fidelity numerical tools were employed. Specifically, the propeller's aerodynamic performance under uniform flow conditions was estimated using Blade Element Momentum Theory (BEMT). The resulting performance maps, which show the radial distributions of blade loading across different advance ratios, were used as input to Van Arnhem's engineering method for aerodynamic performance prediction in non-uniform flow. The inflow profiles, which were previously computed using Computational Fluid Dynamics (CFD) to validate this method, were made available for this thesis. The resulting unsteady blade pressure distribution served as input to an in-house time-domain aeroacoustic solver based on Hanson's near-field theory, suitably adapted to handle unsteady blade loading cases. Although the time-domain method used in this study is computationally more expensive than frequency-domain methods, it has the advantage of preserving pressure time histories, thus allowing the analysis of interactions between acoustic pressure waveforms. A thorough validation of both the aerodynamic and aeroacoustic solvers was conducted under uniform and non-uniform flow conditions, showing reasonable agreement with high-fidelity data.

The analyses were conducted using the six-bladed TUD-XPROP-S propeller with a pitch setting of $\beta_{0.7R_p} = 30°$. During the analyses, the advance ratio was kept at $J = 0.8$, representing nominal operating conditions, while the helical tip Mach number was varied from a baseline value of $M_{ht} = 0.357$ to a value representative of full-scale propellers in cruise conditions, i.e. $M_{ht} = 0.8$. The blade pressure was scaled accordingly from its value at the baseline Mach number, ensuring that the propeller's non-dimensional performance remained unchanged. This approach enabled the isolation of acoustic effects due to Mach number variations while not entirely capturing the correct scaling of forces resulting from compressibility effects.

Due to limitations in the current implementation of the aeroacoustic solver, variations in source speed were not considered in the wake encounter case. However, they were taken into account in the angle of attack case, although not entirely correctly, since the nacelle upwash effect cannot be properly accounted for in the aeroacoustic code. Overall, it is expected that the modulation effect of a varying source speed on noise sources is more significant in the angle of attack case, while this effect

is diminished in the wake encounter case due to the velocity deficit being confined to a relatively small disk region.

An aeroacoustic analysis of the uninstalled propeller was initially performed to focus on the key aspects of Hanson's time-domain formulation. While the presence of a directivity factor modulating source strength in the acoustic pressure equations is not exclusive to Hanson's formulation, the unique use of the acoustic chord as an integration variable distinguishes it. As the Mach number increases, the acoustic chord undergoes greater deformation over time. Additionally, visualizations of the acoustic planform, defined by the locations of the blade elements at the retarded time, provided an intuitive understanding of the increasingly peaky blade pressure waveforms that characterize higher Mach numbers, leading to less effective destructive acoustic interference. By analyzing radial pressure contours and accounting for the directivity factor and the variation of the acoustic chord, it was possible to explain why destructive interference between loading waveforms from different radial sections at the same time is observed at high Mach numbers, resulting in reduced loading noise levels at specific observer angles.

Next, the wake encounter case was studied. To provide context for the aeroacoustic analysis in comparison to the angle of attack case, it is noted that the magnitudes of the side force and normal force are 0.15% and 0.05% of the propeller thrust in uniform flow. An examination of the Thrust-Specific Sound Pressure Level (TSSP) at the propeller plane revealed that, while the isolated propeller exhibits a variation in TSSP of 39 dB between the lowest and highest helical tip Mach numbers considered, this variation expands to a range of 33-46 dB under wake impingement. Overall, wake encounter amplifies the noise sensitivity to operating conditions at observer locations where noise levels are lower compared to uniform flow, while at other positions, this sensitivity is reduced. This phenomenon occurs because, as the Mach number increases, the variation in noise emissions relative to uniform flow decreases. This result is attributed to the increasing importance of steady loading noise sources as the Mach number rises. The reason for this shift is that the impact of temporal variations in the acoustic chord, which alters the degree of interference between the waveforms of individual blades, is less significant for unsteady loading compared to steady loading at higher Mach numbers. The different interference between steady and unsteady loading noise waveforms at varying Mach numbers leads to a phase shift in loading noise relative to the uniform flow case, causing changes in interference with thickness noise. Consequently, the total noise directivity pattern is affected, as seen particularly at lower Mach numbers.

Spectral analyses of the Power Spectral Density (PSD) showed that at $M_{ht} = 0.357$, higher harmonics contribute significantly more to the noise due to wake encounter. However, at $M_{ht} = 0.8$, the difference in noise levels between uniform and non-uniform flow conditions across the spectrum is considerably reduced due to the dominance of steady loading noise.

Finally, the angle of attack case was considered. The side force and normal force magnitudes are 1.2% and 4.8% of the propeller thrust at $\alpha = 0°$, suggesting a substantially higher load unsteadiness than in the wake encounter case. An analysis of the TSSP in the rotation plane showed that, while the propeller at $\alpha = 0°$ exhibits a TSSP variation of 39 dB between the lowest and highest helical tip Mach numbers considered, this range extends to 36-43 dB at $\alpha = 10°$. Similar to the wake encounter case, a non-zero angle of attack amplifies the sensitivity of noise to operating conditions at observer locations where noise levels are lower than those in uniform flow, while the sensitivity diminishes in regions where the noise levels are higher. This behavior is once again attributed to the fact that as the Mach number increases, the change in noise relative to uniform flow decreases due to the dominance of steady noise components. As observed for the wake encounter case, variations in the total noise directivity pattern as the Mach number rises emerge due to differences in the interference between loading and thickness noise.

The influence of the cross-flow velocity component at an angle of attack, which causes a circumferential variation in source speed and is known to asymmetrically modulate steady noise sources,

was examined for thickness noise. It was found that this effect is less pronounced at $M_{ht} = 0.8$ compared to $M_{ht} = 0.357$. This can be attributed to the use of a moderate number of blades, whereas this effect would be more significant with a higher blade count. In the case analyzed, however, it appears to be overshadowed by the greater impact of steady noise sources at higher Mach numbers.

Waveform analyses suggest that the reduction in loading noise on the side of the propeller tilt results from destructive interference between steady and unsteady loading noise waveforms, caused by the opposing signs of blade aerodynamic pressure fluctuations on the retreating side compared to the steady aerodynamic pressure. On the other hand, constructive interference occurs in the opposite region.

When comparing the results for $\alpha = 10°$ and the wake encounter case at $M_{ht} = 0.357$ in the propeller plane, specifically at the respective locations of maximum loading noise increase relative to uniform flow, it is observed that, despite lower aerodynamic blade loading unsteadiness in the wake encounter case, unsteady loading noise is higher at the respective observer angles in the wake impingement scenario, owing to the large time gradient of aerodynamic forces. The impulsive nature of the unsteady loading caused by wake impingement leads to more pronounced noise emissions than the gradually varying loading associated with an angle of attack. However, at $M_{ht} = 0.8$, unsteady loading noise for $\alpha = 10°$ exceeds that of the wake encounter case, due to the larger effect of the strong periodic variations in the acoustic chord. In contrast, the waveform shape in the wake encounter case is primarily governed by the time gradient of aerodynamic loading. Consequently, despite the lower time gradient of aerodynamic loading, the angle of attack case results in a higher root mean square of the unsteady loading waveform.

The PSD spectra for $\alpha = 10°$ reveal an increased contribution from higher harmonics at $M_{ht} = 0.357$, with the difference in spectral content relative to $\alpha = 0°$ diminishing at $M_{ht} = 0.8$ due to the greater influence of steady noise sources.

In conclusion, the analyses demonstrate that variations in far-field tonal noise amplitude, directivity, and spectral content due to non-uniform flow depend on the propeller helical tip Mach number. The results suggest that, in principle, the aeroacoustic signature of a propeller obtained from experimental studies using low helical tip Mach numbers cannot be directly scaled to full-scale propellers operating at higher Mach numbers.

Due to the limitations of the current implementation of the aeroacoustic solver, a proper change in source speed could not be included in the analysis. Therefore, it is suggested that future research fully incorporate this effect into the noise model. Follow-up studies should also systematically investigate how the impact of asymmetric modulation of steady noise sources due to the cross-flow component varies with the number of blades. Additionally, the inclusion of aero-elastic models to account for blade deformation is recommended. Finally, future studies could explore the impact of propeller design variables in arbitrary non-uniform flows, employing waveform analysis similar to that used in the present thesis to gain physics-based insights and support the design of quieter propellers.

CONTENTS

List of Figures

List of Tables

NOMENCLATURE

List of Abbreviations

BEMT	Blade Element Momentum Theory
BPF	Blade Passage Frequency
CAA	Computational Aeroacoustics
CFD	Computational Fluid Dynamics
DEP	Distributed Electric Propulsion
LLT	Lifting Line Theory
OSPL	Overall Sound Pressure Level
PSD	Power Spectral Density
RMS	Root Mean Square
SPL	Sound Pressure Level
TSSP	Thrust-Specific Sound Pressure Level
VLM	Vortex Lattice Method

List of Greek Symbols

α	Angle of attack [deg]
α_i	Induced angle of attack [deg]
β	Local blade pitch angle [deg]
Δp	Difference between blade upper and lower surface pressure [Pa]
η	Propeller efficiency [-]
γ	Distance backward in the helical surface [m]
Γ_θ	Tangential component of helical circulation [$m^2\ s^{-1}$]
Γ_{bound}	Radial circulation [$m^2\ s^{-1}$]
Γ_{root}	Axial circulation [$m^2\ s^{-1}$]
Γ_{Tip_vortex}	Helical circulation [$m^2\ s^{-1}$]
Γ_x	Axial component of helical circulation [$m^2\ s^{-1}$]
Ω	Propeller angular velocity [rad s^{-1}]
ϕ	Observer azimuthal angle; local helix angle [deg]
ρ_∞	Free-stream air density [kg m^{-3}]
θ	Observer axial angle [deg]
ξ	Normal coordinate to the helical surface [Pa]

List of Roman Symbols

c	Section chord of the rotor blade [m]
c_0	Ambient speed of sound [m s^{-1}]
C_d	Sectional drag coefficient of rotor blade [-]
C_l	Sectional lift coefficient of rotor blade [-]
C_P	Propeller power coefficient ($=P/\rho_\infty n^3 D_p^5$) [-]
C_p	Sectional power coefficient ($=P'/\rho_\infty n^3 D_p^4$) [-]
C_Q	Propeller torque coefficient ($=Q/\rho_\infty n^2 D_p^5$) [-]
C_q	Sectional torque coefficient ($=Q'/\rho_\infty n^2 D_p^4$) [-]
C'_Q	Sectional torque coefficient per unit span ($=Q'/\rho_\infty n^2 D_p^5$) [$m^{-1}$]
C_T	Propeller thrust coefficient ($=T/\rho_\infty n^2 D_p^4$) [-]
C_t	Sectional thrust coefficient ($=T'/\rho_\infty n^2 D_p^3$) [-]

C'_T Sectional thrust coefficient per unit span ($=T'/\rho_\infty n^2 D_p^4$) [$m^{-1}$]

C_Y Propeller in-plane side force coefficient ($=F_Y/\rho_\infty n^2 D_p^4$) [-]

C_Z Propeller in-plane normal force coefficient ($=F_Z/\rho_\infty n^2 D_p^4$) [-]

D_p Propeller diameter [m]

dD Sectional drag of rotor blade [N]

dF_p Sectional pressure force of rotor blade [N]

dL Sectional lift of rotor blade [N]

dQ Sectional torque of rotor blade [Nm]

dr Blade element span [m]

dT Sectional thrust of rotor blade [N]

F Force [N]

h Blade thickness distribution [m]

J Propeller advance ratio [-]

J_{eff_a} Effective advance ratio due to axial inflow [-]

J_{eff_t} Effective advance ratio due to tangential inflow [-]

M_∞ Free-stream Mach number [-]

M_{ht} Helical tip Mach number $\left(=\sqrt{M_\infty^2 + M_{rot}^2}\right)$ [-]

M_{rot} Tip rotational Mach number ($=\Omega R_p/c_0$) [-]

n Propeller rotational speed [s^{-1}]

N_B Number of blades [-]

P Propeller power [W]

P' Sectional power per unit span [N s^{-1}]

p' Fluctuating sound pressure [Pa]

p_L Loading acoustic pressure [Pa]

p_{LF} Loading far-field acoustic pressure [Pa]

p_{LN} Loading near-field acoustic pressure [Pa]

p_{ref} Reference sound pressure [Pa]

p_{rms} Root mean square sound pressure [Pa]

p_{TH} Thickness acoustic pressure [Pa]

Q Propeller torque [Nm]

Q' Sectional torque per unit span [N]

Q_C Propeller torque coefficient ($=Q/\rho_\infty V^2 D_p^3$) [-]

R Source-to-observer distance [m]

r Blade radial coordinate [m]

R_p Propeller radius [m]

T Propeller thrust [N]; and Propeller period [s]

t Observer reception time [s]

T' Sectional thrust per unit span [N m^{-1}]

T_C Propeller thrust coefficient ($=T/\rho_\infty V^2 D_p^2$) [-]

U Local helical source speed [m s^{-1}]

u, v, w Inflow velocity components [m s^{-1}]

V_∞ Free-stream velocity [m s^{-1}]

V_E Effective sectional velocity [m s^{-1}]

w Resultant induced velocity [m s^{-1}]

w_a Induced axial velocity [m s^{-1}]

w_t Induced tangential velocity [m s^{-1}]

x, y, z Cartesian coordinates [m]

I

BACKGROUND

1

INTRODUCTION

This chapter introduces the thesis work by presenting the motivation behind the research, defining the research objective, and outlining the structure of the thesis.

1.1. RESEARCH MOTIVATION

Propeller propulsion has been a cornerstone of aviation since the earliest days of powered flight. The first successful airplane propeller was designed by the Wright brothers in 1903.

Despite advancements in propeller technology lead to more efficient designs [1], transition from propeller-driven aircraft to turbojet and turbofan engines began in the mid-20th century, primarily due to the pursuit of higher speeds and improved performance. During World War II, advancements in jet engine technology demonstrated the potential for significantly faster aircraft, leading to a shift in research focus. By the 1950s, the success of turbojet and turbofan propulsion resulted in a decline in propeller research, as these new engines offered superior efficiency at high speeds and altitude.

This trend continued until the mid-1970s, when the aviation industry faced significant challenges due to the oil crisis of 1973, which led to sharp increases in fuel prices. This event prompted a renewed focus on fuel efficiency in aircraft propulsion systems. In response to the escalating fuel costs, NASA initiated the Aircraft Energy Efficiency program in the 1970s, aiming to reduce fuel consumption by 50%. This program explored various technologies, including the development of advanced engine designs. One notable outcome was the concept of the propfan, also known as the unducted fan, whose concept was developed by Rohrbach and Metzger [2]. It combined elements of turbofan and turboprop engines to achieve high efficiency at jet-like speeds. The propfan featured exposed, highly swept blades designed to operate efficiently at high subsonic speeds. General Electric's GE36 engine was a prominent example of this technology.

Figure 1.1 illustrates the installed propulsive efficiency of turboprops, advanced turboprops (i.e., propfan engines), and turbofan engines across varying cruise Mach numbers. The figure highlights that the efficiency of turboprops declines sharply with increasing flight speed, whereas turbofan engines maintain operational capability over a broader speed range, albeit with a lower propulsive efficiency. This trend arises from the fundamental differences in propulsion mechanisms. Propellers achieve thrust by accelerating a large mass of air at a low velocity, resulting in high efficiency at low to moderate speeds. However, as velocity increases, compressibility effects and shock-induced losses on the blades degrade performance, reducing their efficiency at high-subsonic cruise Mach numbers. In contrast, turbofan engines produce thrust by imparting a higher velocity to a smaller mass of air. The ducted fan system enables a compromise between efficiency and operational speed. Meanwhile, propfan engines offer superior efficiency compared to turbofans, even at high-subsonic flight speeds.

However, by the late 1980s, declining fuel prices and concerns over noise levels due to the

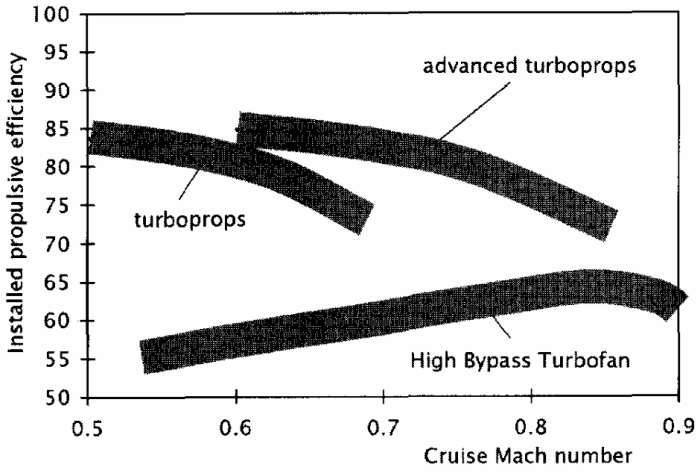

Figure 1.1: Installed propulsive efficiency of turboprops, advanced turboprops (or propfan engines) and turbofan engines with varying Mach number [3].

absence of a surrounding nacelle led to a reduced interest in propfan technology, and it was not widely adopted in commercial aircraft.

In the 21st century, rising fuel costs and environmental concerns have once again placed emphasis on the need for more efficient propulsion systems, bringing renewed attention to propeller propulsion. In order to cut the aviation carbon footprint, the Advisory Council for Aviation Research and Innovation in Europe (ACARE) developed the Flightpath 2050 report [4] setting ambitious goals for aircraft by 2050. These goals include reducing CO2 emissions by 75%, NOx emissions by 90%, and perceived noise emissions by 65% compared to 2000 levels. In response to to these escalating constraints the imperative for aviation manufacturers has shifted toward developing innovative solutions for designing vehicles with heightened environmental sustainability in terms of chemical and noise pollution. A propulsion concept that was developed to tackle these challenges is Distributed Electric Propulsion (DEP). In essence, multiple electrically-driven propulsors are strategically positioned along the airframe with the purpose of improving aircraft's aerodynamic and propulsive performance [5, 6]. When propellers operate in close proximity to each other, complex aerodynamic and aeroacoustic interactions occur. Moreover, when installed on an aircraft's wing, they are subject to azimuthal inflow distortions due to the wing's upwash effect. These interactions lead to load unsteadiness on the propeller blades, causing unsteady loading noise which is most often of primary importance compared to the steady loading one [7].

Before investigating complex configurations, it is essential to first develop an understanding of the aerodynamic and aeroacoustic performance of a propeller operating in relatively common non-uniform flow conditions. To this end, studies have been performed on a propeller at a non-zero angle of attack [8, 9], which is a condition similar to a wing-mounted tractor propeller arrangement [3], as well as on a propeller immersed in the wake of an upstream pylon [10], representative of a wing-mounted pusher propeller configuration. The findings of these studies are presented in Chapter 2. These investigations demonstrated that unsteady blade loading leads to modifications in noise emissions in terms of amplitude, directivity, and spectral characteristics. However, the current literature lacks comprehensive aeroacoustic studies that systematically examine the impact of non-uniform inflow conditions on noise emissions across different Mach numbers. The outcomes of the few studies addressing this topic are discussed in Chapter 3. Such analyses are particularly relevant when scaling results from experimental studies to full-scale configurations. In fact, while experimental campaigns typically ensure proper scaling of the advance ratio, conducting tests at ambient conditions often leads to a reduced free-stream Mach number, and, if the advance ratio

is maintained, to a reduced tip Mach number. This decrease significantly affects propeller loading, thereby influencing its response to unsteady inflow. Although unsteady loading noise is known to be particularly significant at low flight speeds [11], a systematic investigation into the sensitivity of propeller noise to Mach number under non-uniform inflow conditions, along with a physical interpretation of the underlying noise mechanisms, remains absent in the literature.

1.2. RESEARCH OBJECTIVE AND QUESTIONS

As discussed in the previous section, current research on the effects of Mach number on aeroacoustic emissions in non-uniform flow is limited, and is then the focus of this thesis. In particular, attention is given to two commonly encountered non-uniform flow scenarios: a propeller at non-zero angle of attack and a propeller subject to the impingement of an upstream wake. These cases were selected because, despite their conceptual simplicity from an aerodynamic perspective, they allow for a focused analysis that provides physics-based insights on the aeroacoustic signature, which can potentially be extended to more complex non-uniform flow scenarios. At this stage of the investigation, it is appropriate to analyze the Mach number effects using low-fidelity tools, as this approach aligns with the objective of developing a fundamental physical understanding of the underlying phenomena. To narrow down the scope of the analysis, focus is put on far-field tonal noise emissions, which, in the propeller plane, are dominant over broadband noise emissions. For this reason, the objective of this thesis is formulated as follows:

To analyze the sensitivity of a propeller's far-field tonal noise emissions to variations in helical tip Mach number when operating at a non-zero angle of attack and experiencing wake encounter, using low-fidelity methods.

To enable a physical interpretation of the noise mechanisms, a time-domain aeroacoustic theory is employed, specifically Hanson's near-field theory [12]. Utilizing a time-domain solver ensures the preservation of the acoustic pressure time history, allowing to analyze the interactions between acoustic pressure waveforms. Accordingly, the sub-objective of this thesis is defined as follows:

To give a physical interpretation to the propeller's aeroacoustic signature by employing Hanson's time-domain theory.

To address the research objective, several research questions have been developed. Initially, since Hanson's near-field theory exhibits unique characteristics compared to other time-domain theories, it is crucial to understand how it can be applied to analyze the underlying physics of noise emissions. Hence, the first research question is stated as follows:

RQ1. How can the physics of noise emissions be analyzed by employing Hanson's time-domain aeroacoustic theory for propeller noise?

Upon acquiring this understanding, the focus shifts to investigating the sensitivity of the aeroacoustic performance of a propeller to the helical tip Mach number in the scenario where an upstream wake impinges on the propeller:

RQ2. How does the aeroacoustic performance of a propeller scale with the helical tip Mach number under the influence of a wake impingment relative to a propeller operating in uniform flow?

In the case of wake encounter, the inflow disturbance to the propeller is purely axial. Therefore, once the analysis for this case is completed, attention can be directed towards a conceptually more

intricate scenario, namely, a propeller operating at a non-zero angle of attack, where the inflow disturbance includes both axial and tangential components:

RQ3. How does the aeroacoustic performance of a propeller scale with the helical tip Mach number under the influence of a non-zero angle of attack relative to a propeller aligned with the free-stream?

Analyzing two different non-uniform flow scenarios also allows to put the two in perspective.

1.3. THESIS OUTLINE

The thesis is structured into four parts. Part I provides the background information related to the research topic. It consists of two chapters: Chapter 2, which gives an overview of propeller aerodynamic and aeroacoustic theory, and Chapter 3, which discusses various considerations regarding propeller operating conditions. Part II then outlines the methodology adopted in this work. The models used for predicting aerodynamic and aeroacoustic performance are detailed in Chapter 4 and Chapter 5, respectively, with the rationale behind their selection explained. Part III presents the validation of the models and the results of the analysis. Specifically, Chapter 6 covers the verification and validation of the aerodynamic and aeroacoustic models, while Chapter 7 elaborates on the analytical setup. Chapter 8 presents the aeroacoustic characterization of the isolated propeller in uniform flow, addressing *RQ1*, and Chapter 9 and Chapter 10 examine the effects of wake encounter and non-zero angle of attack, answering *RQ2* and *RQ3*, respectively. Finally, in Part IV, conclusions drawn from the analysis are provided. In particular, Chapter 11 offers answers to the research questions and conclusions, while Chapter 12 proposes several recommendations for future research.

2

PROPELLER THEORY

This chapter provides a summary of propeller theory, covering both aerodynamic and aeroacoustic performance in Section 2.1 and Section 2.2, respectively. The influence of non-uniform inflow, with particular emphasis on angle of attack and wake encounter, is addressed in Section 2.3.

2.1. AERODYNAMIC PERFORMANCE

A propeller functions akin to a rotating wing due to its airfoil-shaped design. While a wing primarily generates lift for upward motion, a propeller's main purpose is to produce thrust by imparting momentum to the air in the direction opposite to the desired aircraft motion. A propeller blade element of width dr, positioned at a radial distance r from the hub of a propeller with a total radius R_p and rotating at an angular velocity Ω, is illustrated in Figure 2.1a. Additionally, Figure 2.1b presents a cross-sectional view of the blade element, depicting the associated angles, velocities, and forces.

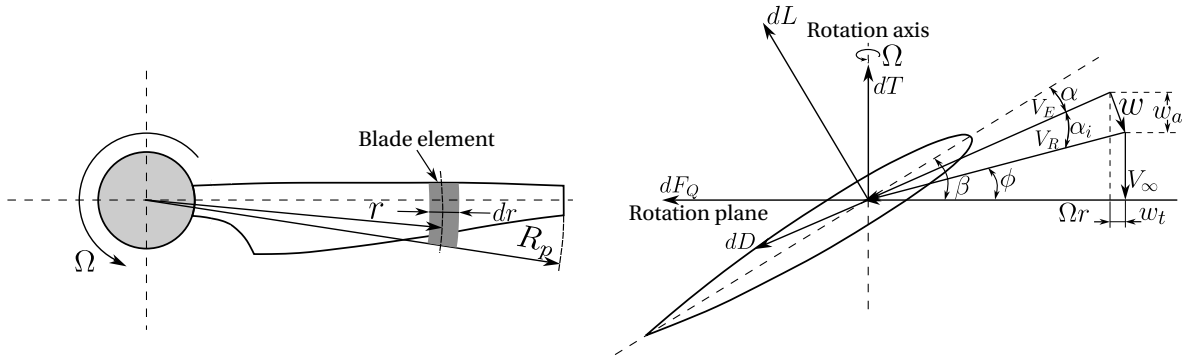

(a) Propeller blade element.

(b) Blade element cross-section.

Figure 2.1: Illustration of a propeller blade element (a) and blade element cross-section (b).

Besides the translational (free-stream) and tangential velocities (V_∞ and Ωr, respectively), a self-induced velocity field characterizes the rotating blade section. Specifically, an axial induced velocity vector (w_a) and a tangential (or swirl) one (w_t) are present, the resultant of which is the induced velocity w. Due to the induced angle of attack α_i, the blade section experiences an effective angle of attack α and the resultant local flow velocity vector is given by V_E. A lift force perpendicular to V_E and a drag force parallel to it are generated. Lift and drag forces can be decomposed into the local thrust force dT and the local torque dQ ($= r\,dF_Q$).

2.1.1. AERODYNAMIC PERFORMANCE METRICS

A useful metric in propeller analysis is the advance ratio J. It relates the free-stream velocity V_∞ to the propeller diameter D_p and rotational speed n:

$$J = \frac{V_\infty}{nD_p} \tag{2.1}$$

Another metric that facilitates comparisons among propellers with different geometries and operating conditions is the helical tip Mach number:

$$M_{ht} = \sqrt{M_\infty^2 + M_{rot}^2} \tag{2.2}$$

where $M_\infty = V_\infty / c_0$ is the free-stream Mach number and $M_{rot} = \Omega R_p / c_0$ is the tip rotational Mach number.

Additionally, the Reynolds number based on the propeller diameter is given by:

$$Re_D = \frac{\rho_\infty V_\infty D_p}{\mu_\infty} \tag{2.3}$$

The thrust force T and shaft power P can be non-dimensionalized with an effective dynamic pressure defined using the propeller rotational speed n. The thrust coefficient C_T and the power coefficient C_P are defined in Equation 2.4 and Equation 2.5 [13].

$$C_T = \frac{T}{\rho_\infty n^2 D_p^4} \tag{2.4}$$

$$C_P = \frac{P}{\rho_\infty n^3 D_p^5} (= 2\pi C_Q) \tag{2.5}$$

This type of non-dimensionalization is more suitable for the analysis of the propeller performance at blade level, whereas the coefficients $T_C = T/(\rho_\infty V_\infty^2 D_p^2)$ and $P_C = P/(\rho_\infty V_\infty^3 D_p^2)$, normalizing the thrust and the power with respect to the free-stream velocity and disk area, are more indicated for analyzing the propeller performance at aircraft design level [14]. It should be noted that the power coefficient was expressed in function of the torque coefficient by knowing that $P = \Omega Q$ and $C_Q = Q/(\rho_\infty n^2 D_p^5)$.

The propeller efficiency is defined in Equation 2.6.

$$\eta = \frac{T V_\infty}{P} = J \frac{C_T}{C_P} \tag{2.6}$$

2.1.2. PROPELLER SLIPSTREAM

Each blade section sees a different angle of attack due to the different local blade pitch angle β, helix angle ϕ and induced angle of attack α_i. In particular:

$$\alpha = \beta - \phi - \alpha_i \tag{2.7}$$

Moreover, the pressure forces are zeroed at the tip. Due to the radial variation of the circulation distribution, vorticity is shed into the slipstream. The vortex sheets travel in helicoidal motion and induce velocities which alter the propeller's blade loading.

A useful model to characterize the induced effects of the trailing vortex system behind a propeller is the vorticity tube model [15]. In this conceptual framework, the helical vortex sheets are substituted with two overlaid continuous vorticity distributions. The first distribution comprises axial vorticity, oriented parallel to the rotation axis and spread across concentric cylinders. The second vorticity distribution comprises vortex rings positioned on identical cylindrical surfaces but situated on planes

perpendicular to the rotation axis. Figure 2.2 sketches the three relevant vorticity distributions: Γ_{root} in the axial direction, Γ_{bound} in the radial direction and Γ_{Tip_vortex} representing the helical vorticity. This last is decomposed into Γ_x and Γ_θ, respectively along the axial and tangential direction.

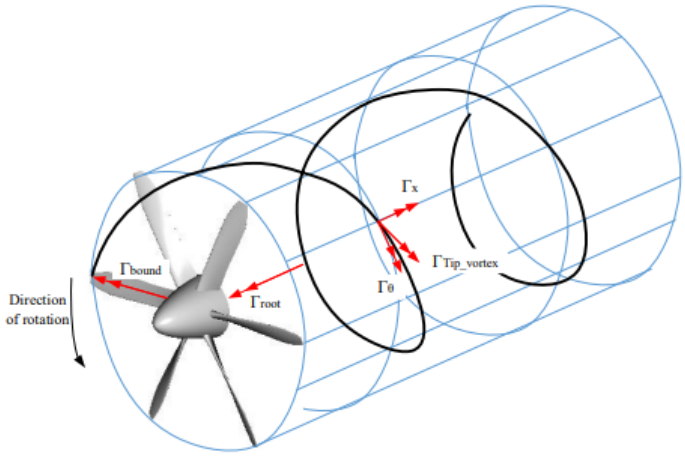

Figure 2.2: Representation of the vorticity tube model [16].

Γ_θ is responsible for inducing axial and radial velocities, while the bound and axial vorticity distributions only affect the swirl velocity in the slipstream [3].

The axial and tangential induced velocities vary along the blade radius. The characteristic variation of the axial velocity suggests that the blade loading is particularly low in the hub region and increases while going outward towards the tip, with a maximum at approximately 3/4 R_p.

Figure 2.3 shows the radial distribution of axial and tangential velocity (left) and static and total pressure (right) of a 6-bladed lightly-loaded propeller. At the hub, the local chord and twist are such that the sectional lift vector shown in Figure 2.1b is almost aligned with the torque axis. As a result, the axial velocity (responsible for the thrust production) is practically zero, unlike the tangential velocity. Moving radially towards the tip, the sectional lift vector starts to align more with the thrust axis. Thus, v_a overtakes v_t at approximately 1/4 R_p.

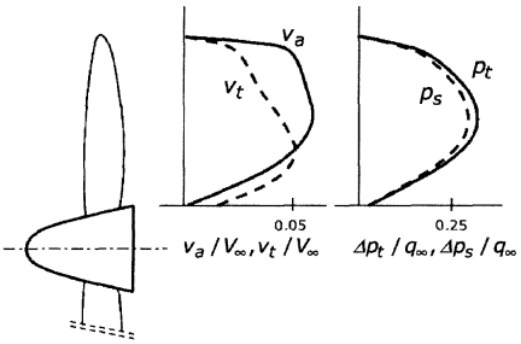

Figure 2.3: Typical distribution of axial and tangential velocities (left) and static and total pressure (right) over the radius of a 6-bladed lightly-loaded propeller [3].

2.2. AEROACOUSTIC PERFORMANCE

A propeller noise spectrum is characterized by two noise categories: harmonic (or tonal) noise and broadband noise. Figure 2.4 shows the main contributors to them. Three main noise mechanisms can be identified. They can be grouped by steady sources, unsteady sources and random sources.

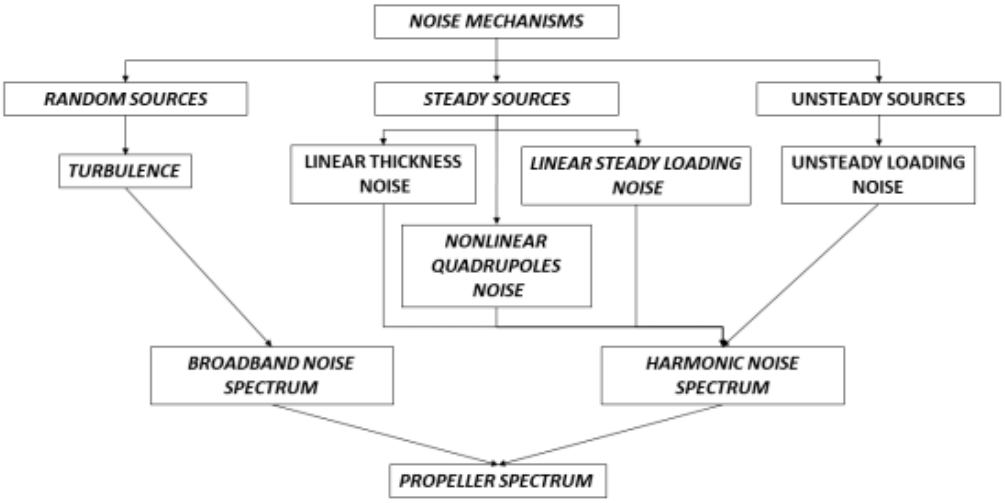

Figure 2.4: Propeller noise contributions [17].

For an observer in a non-rotating frame, steady sources are periodic, meaning that they repeat themselves at a period which is given by the inverse of the Blade Passage Frequency (BPF), defined as:

$$BPF = N_B n \tag{2.8}$$

where N_B is the number of blades of the propeller.

Figure 2.5 illustrates the propeller harmonic noise spectrum in time and frequency domain. As can be seen, noise is emitted at the BPF and its harmonics.

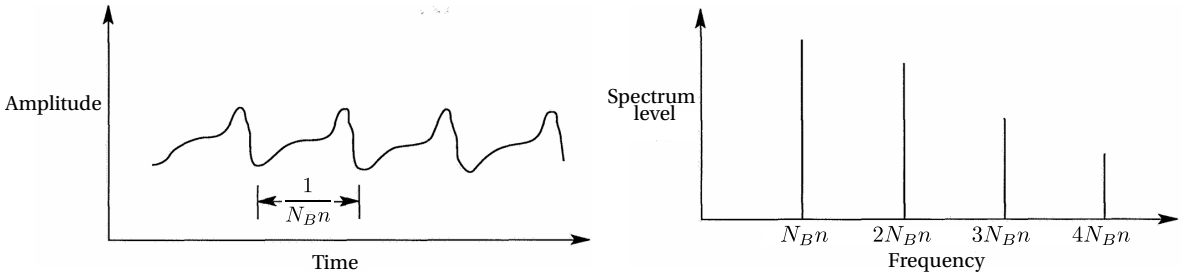

Figure 2.5: Harmonic spectrum in time domain (left) and frequency domain (right) (adapted from [11]).

Steady sources include linear thickness noise, linear steady loading noise and non-linear quadrupoles noise [11]. Thickness noise is generated as a result of the periodic displacement of air as a blade move through the air and is proportional to the blade volume, while its frequency depends on the shape of the airfoil and rotational speed. This type of noise can be modeled as a monopole source distribution over the blade surface and is particularly relevant at high speeds. On the other hand, linear steady loading noise is emitted due to the blade forces produced as a result of the pressure field generated on the rotating blade. This noise can be modeled by dipoles source distribution and is relevant at low to moderate flight speeds. However, in transonic conditions non-linear effects arise (such as shock waves) and non-linear quadrupoles noise enhances the linear thickness and loading noise [11].

Unsteady sources characterize propellers subject to periodic inflow distortions, such as a propeller at a non-zero angle of attack or subject to the impingement of an upstream wake. It is

highlighted that the unsteady sources classified here are periodic in nature. The periodic lift fluctuations on the blade repeat equally for every propeller revolution, provided that the inflow distortion is invariant with time. As a result, unsteady loading noise is generated at harmonics of the blade passage frequency [11, 7]. This type of noise is especially relevant at low flight speeds [11].

Broadband noise results from two main mechanisms, i.e. the interaction of the turbulent flow with the blade leading edge and the interaction of the turbulent flow developing over the blade surface with the blade trailing edge [11]. It is highlighted that broadband noise sources are random in nature. The broadband noise spectrum differs from the harmonic one since the acoustic energy is emitted at a broad range of frequencies. An illustration of the broadband spectrum in time and frequency domain is provided in Figure 2.6.

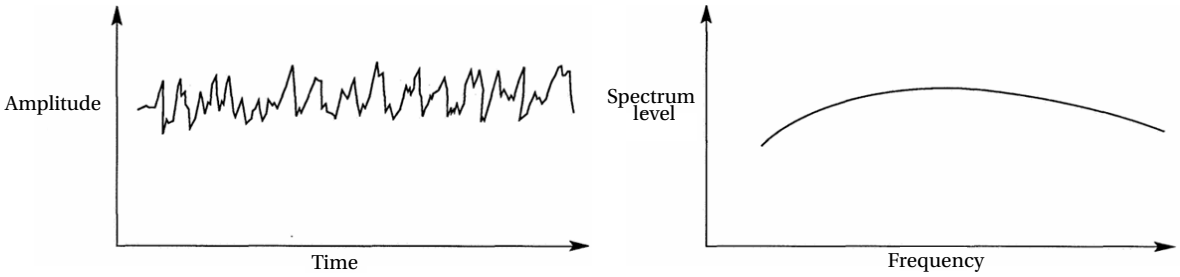

Figure 2.6: Broadband spectrum in time domain (left) and frequency domain (right) (adapted from [11]).

An example of the propeller noise spectrum, including both tonal and broadband components, is provided in the frequency domain in Figure 2.7. It can be seen that tonal peaks develop over a broadband hump and are particularly relevant at low frequencies.

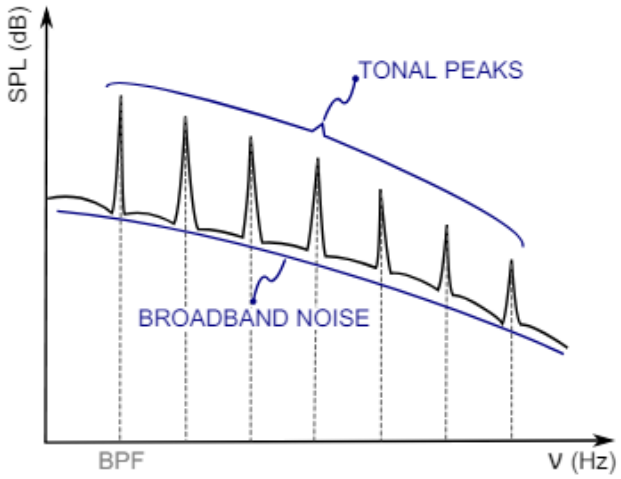

Figure 2.7: Typical propeller noise spectrum in the frequency domain [18].

As can be seen, tonal noise is typically the major noise component for a propeller in forward flight. However, it should be observed that, at directivity angles near the propeller axis, broadband noise may dominate. In general, at low to moderate speeds thickness and, especially, loading noise dominate over the contributions given by non-linear quadrupoles and random sources.

2.2.1. AEROACOUSTIC PERFORMANCE METRICS

The most common indicator for a propeller aeroacoustic performance is the Sound Pressure Level (SPL). SPL is a logarithmic measure of the sound pressure of a sound wave in relation to a reference level. For the purpose of this study, the focus is placed on this quantity rather than the Sound Power Level (PWL). The latter represents the acoustic energy produced by the propeller, irrespective of distance and observation angle. However, this thesis aims to evaluate far-field noise emissions and characterize directivity patterns. The reference level is typically set at the threshold of human hearing, which is $20\,\mu Pa$ at a frequency of $1,000\,Hz$. SPL is expressed in dB and defined in Equation 2.9 [19].

$$SPL = 20\ log_{10}\left(\frac{p'_{RMS}}{p_{ref}}\right) \tag{2.9}$$

where p'_{RMS} is the Root Mean Square (RMS) of the acoustic pressure fluctuations and p_{ref} is the reference acoustic pressure. The use of a logarithmic scale is important because human perception of loudness is roughly logarithmic. This means that a doubling of sound pressure does not result in a perceived doubling of loudness. p'_{RMS} is defined as:

$$p'_{RMS} = \sqrt{\frac{1}{2T_s}\int_{-T_s}^{T_s} p'(t)^2\,dt} \tag{2.10}$$

where T_s is the duration of the signal and $p'(t) = p(t) - p_0$ is the fluctuating pressure. $p(t)$ is the acoustic pressure at the time t and p_0 is the time-averaged pressure value.

An additional metric for propeller noise can be formulated by relating the SPL with the phenomenon of interest. Thus, the Thrust-Specific Sound Pressure Level (TSSP) can be defined as:

$$TSSP = 20\ log_{10}\left(p'_{RMS}\frac{D_p^2}{T}\right) \tag{2.11}$$

As can be seen, p'_{RMS} has been non-dimensionalized with the pressure jump over the propeller disk. For this reason, it is especially valuable for evaluating noise emissions under varying operating conditions, making it well-suited for assessing the propeller's aeroacoustic signature across different Mach numbers, as examined in this thesis.

By means of the Fourier transform technique it is possible to shift from the time domain to the frequency domain to see how noise distributes over frequency. For this purpose, the concept of Power Spectral Density (PSD) is hereby introduced. The PSD is a measure of how the power of a signal is distributed across different frequency components. The PSD, denoted as $S_{pp}(f)$ is defined as the Fourier transform of the autocorrelation function of the sound pressure signal [20]. Mathematically, it is expressed as:

$$S_{pp}(f) = \lim_{T_s\to\infty}\frac{1}{T_s}\left|\int_0^{T_s} p(t)e^{-i2\pi f t}\,dt\right|^2 \tag{2.12}$$

In practice, the PSD is often estimated using techniques like the fast Fourier transform (FFT) for discrete signals. The units of PSD are Pa^2/Hz, or dB/Hz when converting to the decibel scale. By ensuring that the PSD represents power per unit frequency rather than per frequency bin, normalization enables consistent analysis of how noise scales with Mach number.

2.3. NON-UNIFORM INFLOW EFFECTS

In flight conditions, a propeller can be subject to non-uniform inflow due to several sources. Figure 2.8 shows some examples of non-uniform inflow experienced by a propeller. Case a) and b) are comparable, as it is known that a trailing wing induces an upwash on the tractor propeller

which causes asymmetric inflow conditions similar to those experienced by an isolated propeller operating at a non-zero angle of attack [3]. The case of a propeller at a non-zero angle of attack is hereby discussed. Subsequently, case i) will be discussed, as it is also relevant for this report.

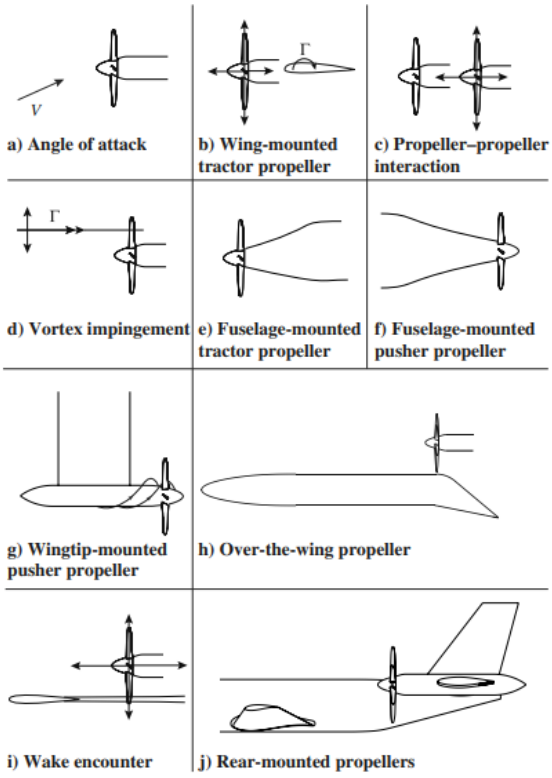

Figure 2.8: Typical cases of non-uniform inflow for a propeller [21].

2.3.1. NON-ZERO ANGLE OF ATTACK EFFECTS ON PROPELLER AERODYNAMIC PERFORMANCE

A propeller operating at a non-zero angle of attack experiences azimuthal inflow distortions as the incoming flow is not aligned with the propeller axis [3, 7]. Due to the in-plane velocity component in-plane velocity component $V_\infty \sin(\alpha)$, the downgoing blade experiences a higher effective velocity and angle of attack compared to the upgoing blade, as illustrated in Figure 2.9.

Due to the higher in-plane velocity on the downgoing side and lower on the opposite side, the effective advance ratio gets lower on the advancing blade side and higher on the retreating one. As a result, the local angle of attack increases on the advancing side and reduces on the opposite side, leading to an increase in the thrust coefficient on the downgoing side of the blade and a decrease on the upgoing side, in a sinusoidal fashion. This is illustrated in Figure 2.10 for a propeller at $J_\infty = 1.8$ and $\alpha = 5\,\text{deg}$.

Notably, the most substantial changes in advance ratio occur at $\phi = 90°$ and $\phi = 270°$ at the hub region, due to the lower local Ωr. The maximum change in the effective advance ratio reaches 35% of the free-stream value. However, the region of highest loading in uniform flow conditions, i.e. $r/R_p = 0.8$ to 0.9, is subject to the greatest variation in the thrust coefficient. The thrust coefficient variation presents a phase delay with respect to the advance ratio variation of approximately 15° due to the delayed aerodynamic response of an airfoil section to a flow disturbance. As mentioned by Van Arnhem [22], the phase delay is primarily determined by the slenderness of the blades. This is because the unsteady response depends on the reduced frequency ($k = \frac{\Omega c}{2V}$) of the inflow to the elemental section of chord c. As the inflow is sinusoidal, the factor that affects the response delay is the blade slenderness. Since modern propellers exhibit relatively similar slenderness ratios, a similar

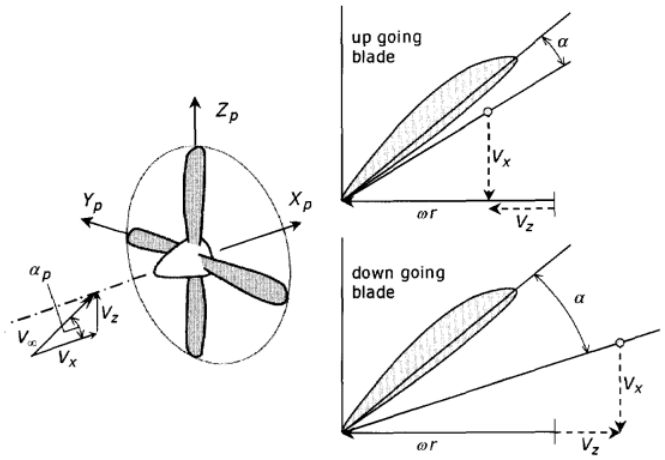

Figure 2.9: Different effective angle of attack for the upgoing and downgoing blade due to propeller at a non-zero angle of attack [3].

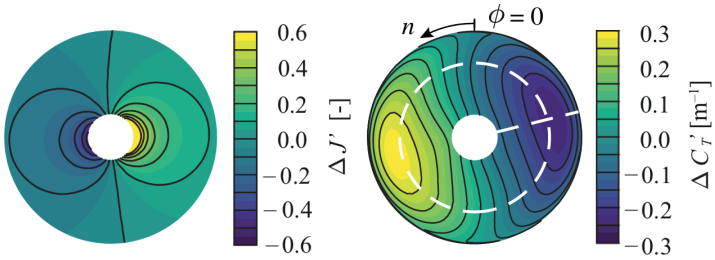

Figure 2.10: Change in effective advance ratio (left) and local thrust coefficient (right) for $J_\infty = 1.8$ and $\alpha = 5\,\text{deg}$ [22].

phase delay is generally observed across different designs.

The response of a propeller to a flow non-uniformity depends on the operating conditions. As shown by Sinnige et al. [23], at higher advance ratios the thrust coefficient is more sensitive to a change in the angle of attack with respect to lower advance ratios. This is illustrated in Figure 2.11. The reason for this is that, at higher rotational velocities (lower advance ratios), the blade sees a lower effective angle of attack.

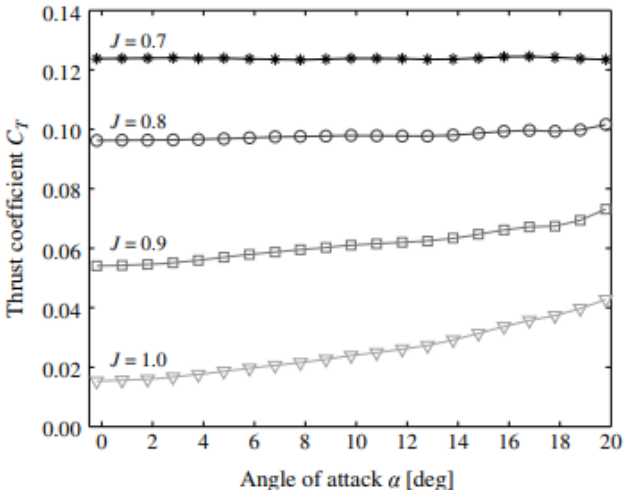

Figure 2.11: Propeller thrust coefficient with varying propeller angle of attack at various advance ratios [23].

In terms of integral propeller performance, the angle of attack has a minor influence on integral shaft forces, with only slight increases in the propeller thrust and torque coefficients. This minor rise is attributed to a slightly higher loading increase on the advancing side compared to the decrease on the retreating side [22].

2.3.2. NON-ZERO ANGLE OF ATTACK EFFECTS ON PROPELLER AEROACOUSTIC PERFORMANCE

As discussed by Mani [24], in addition to the circumferential variation in aerodynamic loading, a key factor contributing to the asymmetry of noise around the propeller axis at a non-zero angle of attack is the modulation effect caused by the periodic variation in source speed due to the presence of a cross-flow velocity component normal to the propeller axis. The circumferential variation in source speed effectively modulates the steady loading and thickness noise. This modulation becomes particularly significant for high-blade-count propellers operating at high tip speeds, where it surpasses the contribution of the once-per-revolution unsteady blade loading variation as the main driver of the azimuthal asymmetry in noise.

Figure 2.12 emphasizes the importance of accounting for the modulation effect caused by the circumferential variation in source speed, as identified by Mani [24]. This analysis focuses on a counter-rotation propeller with 11 forward blades and 9 aft blades, tested in the NASA Lewis Anechoic Wind Tunnel by Woodward [25] at $M_\infty = 0.2$. The propeller operates at an angle of attack $\alpha = 16°$, with a high helical tip Mach number, i.e. $M_{ht} = 0.74$, and an advance ratio $J = 0.88$. When comparing the experimental data (circular markers) with the analytical far-field BPF noise predictions for the front rotor obtained using a frequency-domain method that assumes acoustically compact source distributions in the chordwise direction (line source model), it is evident that the analytical predictions significantly underestimate the noise variation in the propeller plane. However, when the source speed modulation effect is incorporated (solid line), a substantial improvement is achieved.

According to Mani [24], the modulation effect on steady loading and thickness noise sources

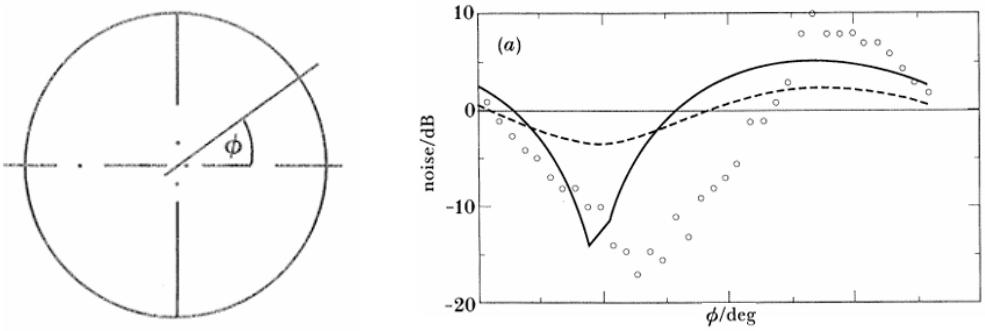

Figure 2.12: Azimuthal variation in BPF noise emissions of front rotor due to an angle of attack $\alpha = 16°$ for a 11x9 bladed counter-rotation propeller at $M_{ht} = 0.74$ and $J = 0.88$ [24]. Experimental data source (circular markers) is Woodward [25]. The dashed line does not account for source speed modulation, while the solid line does.

scales with the harmonic number (an integer multiple of the BPF), the number of blades, and the tip rotational Mach number.

Figure 2.13 presents the same analysis as Figure 2.12, but for the rear rotor. Notably, even when accounting for the cross-flow effect, the underpredictions remain considerable. Clearly, due to the reduced number of blades (9, compared to the 11 blades of the front rotor), the modulation effect is smaller. However, the exact reasons for the underprediction were not identified.

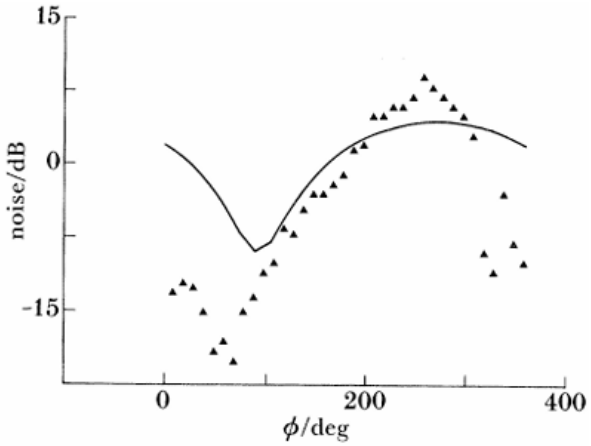

Figure 2.13: As Figure 2.12 but rear rotor BPF.

Figure 2.14 illustrates the impact of an angle of attack $\alpha = 10°$ on the directivity of the far-field overall sound pressure level (OSPL) in the propeller plane for a 3-bladed propeller at $J = 0.60$ and $M_{ht} = 0.47$, computed within the BPF range $0.9 \leq \text{BPF} \leq 10$ using high-fidelity simulations by Goyal et al. [8]. This study considered both tonal and broadband noise. Notably, while the directivity pattern at $\alpha = 0°$ is axisymmetric around the propeller axis, at $\alpha = 10°$, the OSPL increases in the direction opposite to the tilt of the propeller and decreases on the other side, consistent with previous findings [24, 26]. For the analyzed propeller at the given operating conditions, the proximity of the blue-cross markers (representing total noise without the modulation effect induced by the cross-flow component) to the solid black line (representing total noise including this modulation effect) indicates that the influence of the source speed modulation effect on noise remains marginal.

Figure 2.15 illustrates the impact of an angle of attack $\alpha = 10°$ on the directivity of the far-field OSPL in the plane along the propeller axis. Consistent with the trend observerd in the propeller plane, the OSPL increases in the region from which the propeller is tilted away and decreases on

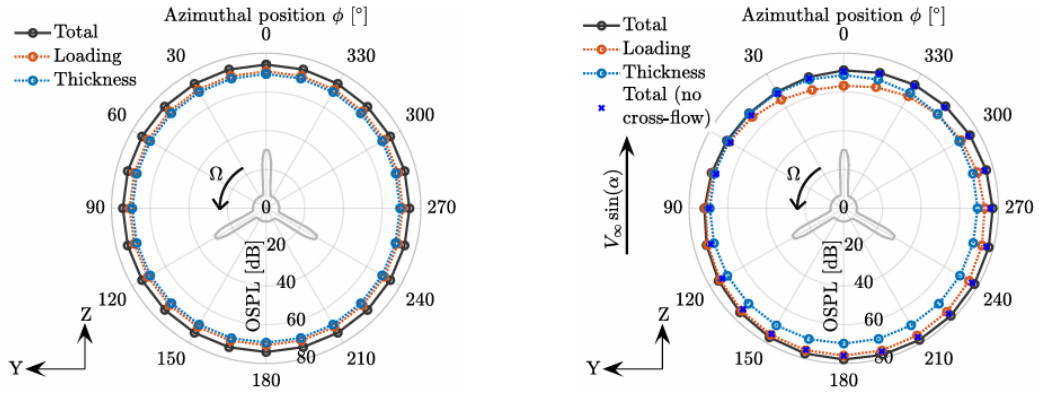

(a) $0.9 \leq \text{BPF} \leq 10$, $\alpha_\infty = 0°$ (b) $0.9 \leq \text{BPF} \leq 10$, $\alpha_\infty = 10°$

Figure 2.14: Effect of angle of attack on the azimuthal directivity of the overall sound pressure level; $J = 0.60$ [8].

the opposite side. Non-zero noise levels along the propeller axis are due to broadband noise, which mainly radiates in this direction, and unsteady loading noise at $\alpha = 10°$.

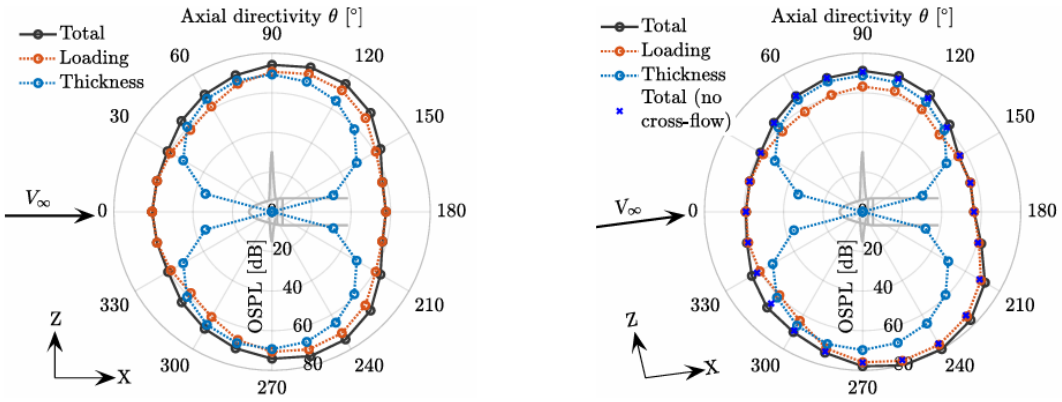

(a) $0.9 \leq \text{BPF} \leq 10$, $\alpha_\infty = 0°$ (b) $0.9 \leq \text{BPF} \leq 10$, $\alpha_\infty = 10°$

Figure 2.15: Effect of angle of attack on the axial directivity of the overall sound pressure level; $J = 0.60$ [8].

2.3.3. WAKE ENCOUNTER EFFECTS ON PROPELLER AERODYNAMIC PERFORMANCE

While a non-zero angle of attack introduces an axial and, predominantly, tangential inflow disturbance that influences the entire propeller disk, a wake originating from an upstream wing or pylon results in an axial inflow disturbance whose effect is localized to a specific region of the disk. Figure 2.16 depicts various wing positions analyzed by Van Arnhem [22] for aerodynamic performance calculations under wake encounter conditions, as well as the extent to which wake impingement affects propeller performance depending on the affected disk region. In particular, the figure highlights that a disturbance impacting the outer disk region can have a more significant effect than one affecting the central part of the disk. This is because the outer blade sections exhibit greater sensitivity to variations in loading due to flow non-uniformity, thereby increasing the product between swept area and sensitivity.

Figure 2.16 shows the change in effective advance ratio due to a wake trailing from a straight, untapered, and untwisted wing whose trailing edge is located at an axial location $3.2R_p$ upstream

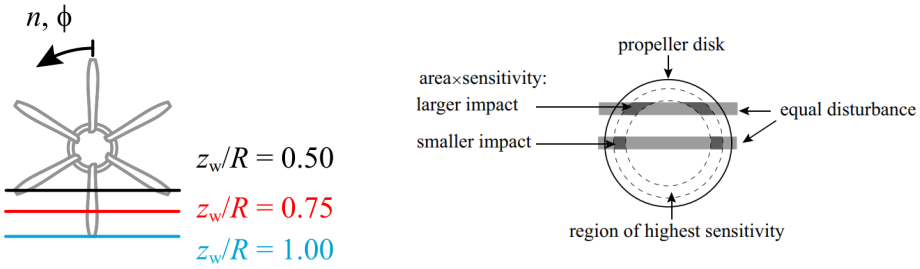

Figure 2.16: Illustration of several wing locations (left) and impact of wake encounter disturbance depending on affected disk region (right) [22].

of the propeller and a vertical location $z_w/R_p = 0.5$ for a propeller operating at $J_\infty = 1.8$, as well as the corresponding change in local thrust coefficient. It can be observed that the axial velocity deficit induced by the wake leads to a 10% reduction in the effective advance ratio over a distinct disk region. A study conducted by Sinnige et al. [10] on the aerodynamic and aeroacoustic interaction effects for a propeller in the wake of an upstream pylon (resembling a pusher configuration) highlighted that the wake width and velocity deficit decrease with an increase in thrust setting due to a favorable pressure gradient produced by the larger suction of the propeller. As a result of the increase in sectional angle of attack, the sectional thrust is increased locally. The highest rise is found at the highly-loaded outboard regions, as expected.

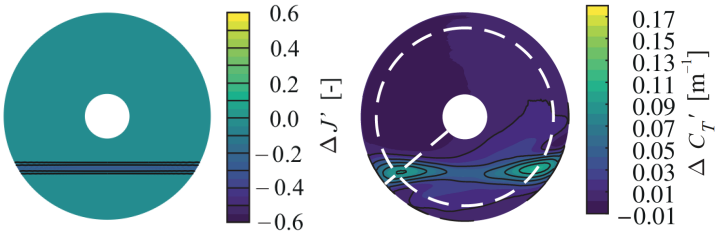

Figure 2.17: Change in effective advance ratio (left) and local thrust coefficient (right) for $J_\infty = 1.8$ and upstream wing vertical location $z_w/R_p = 0.5$ [22].

Figure 2.18 illustrates the azimuthal variation of the ratio between the blade thrust coefficient under wake encounter conditions and that of the isolated blade for different vertical positions of the upstream wing. Notably, for $z_w/R_p = 0.50$, thrust exhibits a distinct increase in two regions, with peaks occurring where the highly loaded outboard sections sweep through the wake. In contrast, for $z_w/R_p = 0.75$, the thrust increase is more gradual, while for $z_w/R_p = 1.00$, where the wake is encountered at the propeller tip, a smaller increase in thrust is observed, occurring once per revolution. This implies that the dominant noise frequencies are influenced by the location of wake encounter. As noted by Van Arnhem [22], the frequency of the blade forcing is either n if $z_w > 0.8$ or $2n$ if $z_w < 0.8$.

The influence on propeller integral forces is minor as the disk region affected by the wake impingement is relatively small [10, 22, 27].

2.3.4. WAKE ENCOUNTER EFFECTS ON PROPELLER AEROACOUSTIC PERFORMANCE

Although the time-averaged propeller performance is largely unaffected by the wake encounter, the abrupt change in blade loading leads to a significant increase in noise emissions [10, 28]. The afore mentioned study conducted by Sinnige et al. on pylon-propeller aerodynamics and aeroacoustics revealed that the magnitude of noise penalty caused by the wake trailing from an upstream pylon depends on the thrust setting of the propeller. Figure 2.19 shows the pylon installation effect on

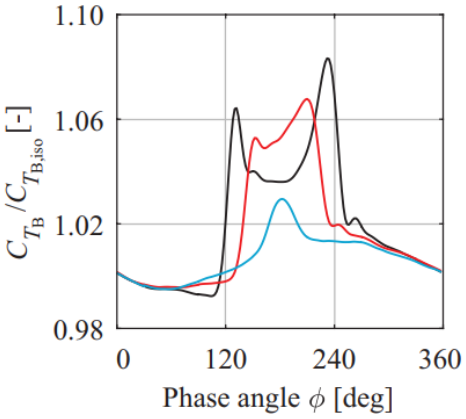

Figure 2.18: Azimuthal variation of the ratio of blade thrust coefficient due to wake encounter to isolated thrust coefficient for $J_\infty = 1.8$ and several upstream wing vertical locations [22].

noise spectra for three different thrust settings. It can be observed that, at high thrust levels (low advance ratios), the installation noise penalty is reduced. Furthermore, it can be noted that the pylon installation leads to a redistribution of the spectral content of noise, with higher harmonics having a more prominent contribution.

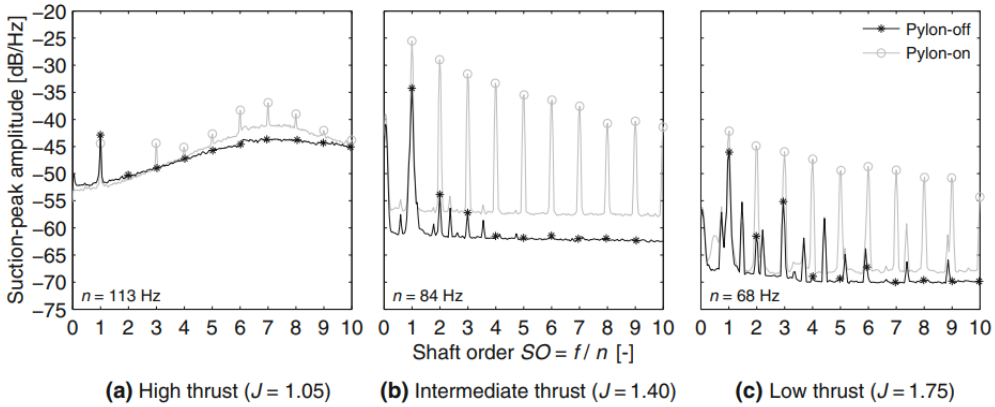

Figure 2.19: Pylon installation effect on noise spectra for three different thrust settings [10].

3

Operating Conditions Considerations

If subscale propellers are analyzed at ambient conditions while maintaining the advance ratio, the free-stream Mach number will be lower. Consequently, the helical tip Mach number will also be lower. Additionally, due to the smaller blade chord in a scaled-down design, the Reynolds number will be reduced as well. This chapter examines the sensitivity of the propeller aerodynamic performance to operating conditions in Section 3.1 and discusses findings from previous studies on the propeller aeroacoustic performance propeller under varying operating conditions in Section 3.2.

3.1. Aerodynamic Performance

Figure 3.1 shows the Reynolds number's effect on propeller performance. Looking at Figure 3.1a, it can be observed that the $C_T - J$ curve shifts up with increasing Reynolds number. The reason for this is that, as Reynolds number rises, the boundary layer thickness reduces. A thinner boundary causes the airfoil curvature to increase, and with that the suction. This increases the blade lift, making the thrust increase. Furthermore, the faster increase in thrust with respect to the torque causes the efficiency to rise as the Reynolds number gets higher, as evident in Figure 3.1b.

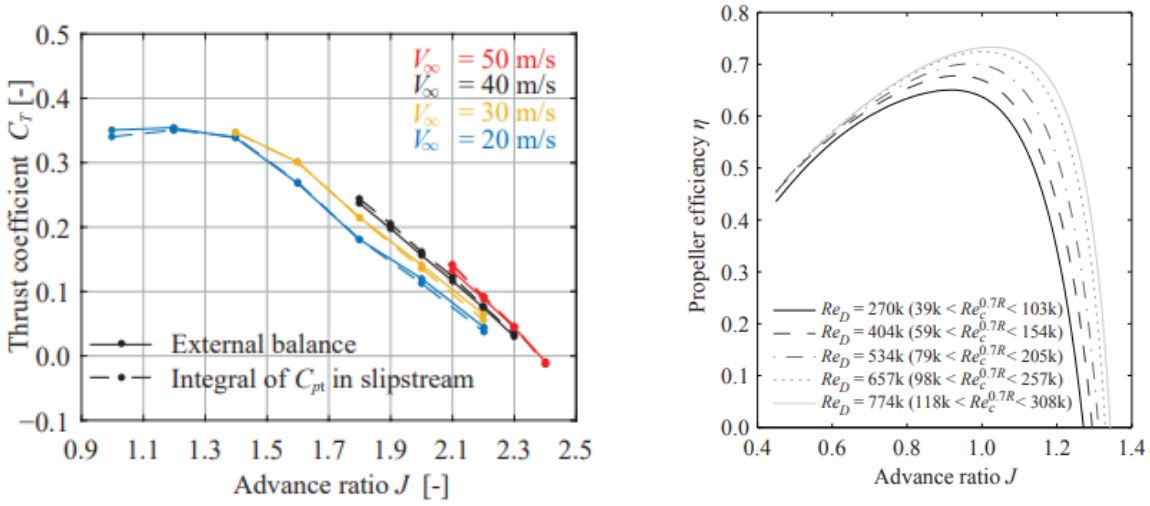

(a) Propeller thrust coefficient [22].

(b) Propeller efficiency [13].

Figure 3.1: Reynolds number effect on propeller performance.

The effect of the helical tip Mach number on the radial distribution of the sectional thrust is shown in Figure 3.2. It can be seen that, due to compressibility effects, the sectional loading

increases. Essentially, at higher speeds, some of the energy is used to compress the air, leading to local variations in air density. The change in air density is proportional to the square of the Mach number [29]. Compressibility effects influence the aerodynamic forces, as these forces are dependent on air density.

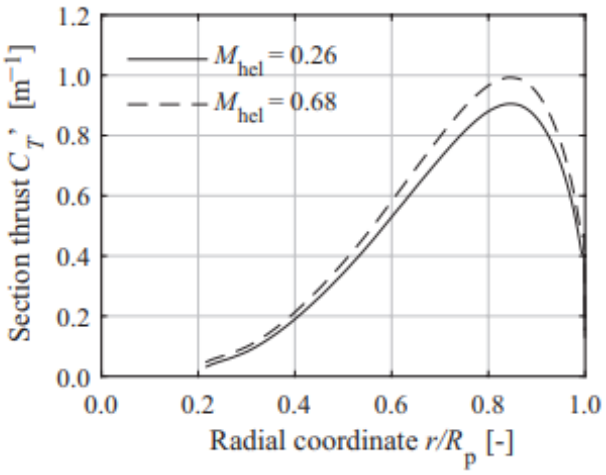

Figure 3.2: Helical tip Mach number effect on blade sectional thrust coefficient [22].

Evidently, different Reynolds and Mach number with respect to the ones characteristic of full-scale designs make the performance curves shift. As pointed out by Van Arnhem [22], this can be prevented by selecting a higher blade pitch. However, this causes the advance ratio not to be the same as the one of maximum efficiency of the full-scale design. Furthermore, a variable pitch propeller might not be available due to manufacturing limitations.

3.2. AEROACOUSTIC PERFORMANCE

An increase in aerodynamic performance due to a higher Mach number can lead to a nonlinear scaling of aeroacoustic performance, owing to the higher sensitivity to an increase in load of outboard radial sections. Moreover, as the thrust-to-torque ratio is also affected, some degree of modification in the directivity pattern is expected.

A computational study by Zhou et al. [30] analyzed the far-field noise footprint of a wingtip-mounted propeller configuration at a variety of Mach numbers and angles of attack. Specifically, two different Mach numbers ($M_\infty = 0.08$ and 0.11) and three angles of attack ($\alpha = 0°$, 5° and 15°) were tested. Since the Mach numbers considered are subsonic, broadband noise was neglected. The OSPL on the propeller plane is shown in Figure 3.3. The noise directivity due to the propeller-spinner contribution resembles a distorted monopole which at both the Mach numbers ($M_\infty = 0.08$ on the left and $M_\infty = 0.11$ on the right), as the angle of attack increases, becomes even more distorted. It can be observed that, as previously discussed, as the angle of attack increases, the noise gets higher in the region from which the propeller is tilted away, and gets lower on the opposite side. It can also be noted that, at $M_\infty = 0.08$, at a given angle of attack the propeller noise is 1-2 dB higher than the one at $M_\infty = 0.11$. This is because of the fact that the blade pitch is not changed as the Mach number is reduced, resulting in a higher effective angle of attack seen by the blade and in a larger extent of leading edge flow separation at the lower Mach number. As noted by the authors, this is common for propellers featuring sharp leading edges and operating at low speeds.

Although distributed electric propulsion (DEP) configurations are not the focus of this thesis, it is still worth it to mention the findings of the computational study by Poggi et al. [31], which focused on the effects of the tip Mach number on the noise emitted by two co-rotating and counter-rotating side-by-side propellers. The lower tip Mach number analyzed is representative of scaled models for

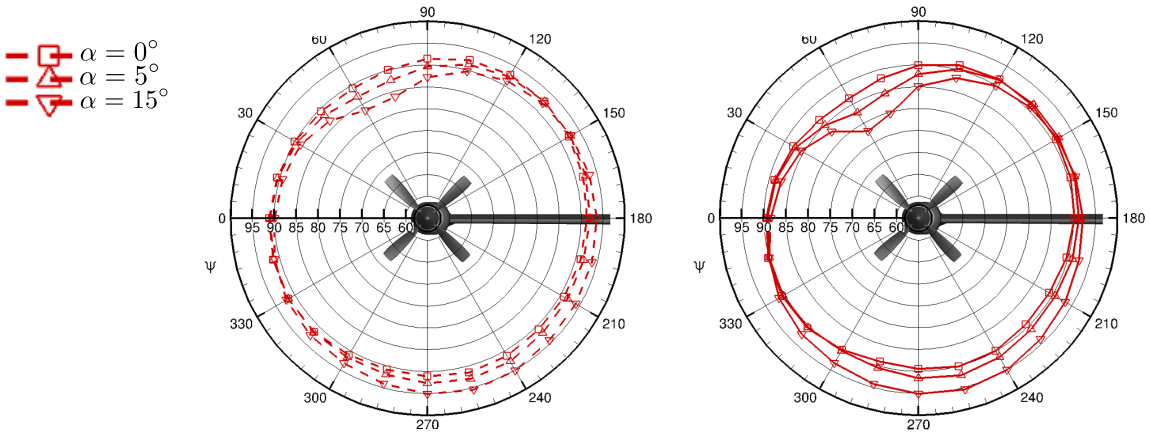

Figure 3.3: Angle of attack effect on the azimuthal directivity of the overall sound pressure level, propeller-spinner contribution; $M_\infty = 0.08$ (left) and $M_\infty = 0.11$ (right) [30].

wind tunnel experiments, while the higher one is associated to real-life DEP setups. The propeller thrust and advance ratio are maintained. When comparing the far-field noise emissions for different tip clearances they observed that, although the higher Mach number leads to a noise increase of about 10 dB, the directivity patterns remain similar. This finding is particularly insightful when it comes to assess the validity of scaling the aeroacoustic results obtained in low-Mach number wind tunnel experiments to high-Mach number full-scale setups.

II

Methodology

4

AERODYNAMIC PERFORMANCE PREDICTION

This chapter focuses on the aerodynamic performance models used in this work. First, the rationale behind the choice of the models used to simulate the propeller's aerodynamic performance in uniform and non-uniform flow conditions is provided in Section 4.1. Next, a detailed description of the uniform-flow aerodynamic performance model is given in Section 4.2. Finally, an explanation of the method for blade loading estimation in non-uniform flow is detailed in Section 4.3.

4.1. MODELS SELECTION

Since the aeroacoustic code requires propeller blade loading as input, it is necessary to select a prediction model to obtain the propeller's aerodynamic performance under non-uniform flow conditions. As this thesis aims to provide a physical understanding of unsteady loading noise phenomena rather than performing a configuration-specific study, it was decided to rely on low-fidelity tools. Although the one required must be a low-fidelity model, it needs to be accurate enough for the aeroacoustic code to return reliable results. In fact, excessive deviations of aerodynamic performance from high-fidelity data can invalidate noise predictions. The model must also be suitable for a plurality of non-uniform flow conditions. Given these requirements, the choice immediately fell on the engineering method for blade loading estimation in non-uniform flow of Van Arnhem et al. [21]. The method proved to be able to rapidly and accurately predict the propeller aerodynamic performance in arbitrary non-uniform flow. Specifically, the method was validated against CFD simulations and experimental data for four cases, namely isolated propeller at a non-zero angle of attack, wake encounter, over-the-wing propeller and wingtip-mounted pusher propeller. The errors in integral propeller loads with respect to validation data were between 0.5 and 12% with a computational cost of just several CPU seconds, seven orders of magnitude lower than a full-blade Reynolds averaged Navier–Stokes (RANS) CFD simulation. The inputs to this method are an inflow field and the radial distribution of thrust and torque to a change in advance ratio for the isolated propeller in uniform flow. The former can be obtained with computationally inexpensive CFD simulations as will be explained in Section 4.3, while the latter can either be obtained with CFD simulations or with a low-fidelity code. As this work relies on simplified models, a survey was conducted to choose an appropriate low-fidelity approach.

Among the most basic models is the actuator disk model. Such method simplifies the prediction of propeller performance but overlooks important factors. It neglects viscous effects, the rotation of vortex sheets in the slipstream, and does not account for the characteristic geometry of the propeller, aspect that is essential for the purpose of computing the aeroacoustic signature in a later stage of the work. On the other hand, low-order aerodynamic performance models that take the specific geometry of the propeller into account are the Blade Element Momentum Theory (BEMT) and vortex

methods such as the Lifting Line Theory (LLT) and the Vortex Lattice Method (VLM). Specifically, BEMT divides the propeller blade into small sections and analyses each as an independent airfoil. This allows for the consideration of the varying geometry, pitch and chord distribution along the blade. LLT replaces the blade lifting surface as a line of discrete vortices, while VLM represents it as a lattice of bound vortices. This allows for an accurate representation of the blade geometry. Moreover, in the case of VLM, since the blade is discretised into both the chordwise and the spanwise directions, its complex three-dimensional shape can be captured, thus allowing to account for the sweep angle. Since analysing the effects of blade sweep angle on noise is not considered of paramount importance at this stage of research, it is not necessary to use VLM. Although the LLT is able to consider wake effects unlike the BEMT, as shown by Branlard et al. [32] the BEMT is able to provide reasonably accurate results within seconds instead of minutes like the vortex methods mentioned. This advantage in terms of computational speed, besides being beneficial for this thesis work in which different configurations are analyzed, may come in handy in future applications of the developed program, e.g., design optimization studies. For this reason, it was decided to use BEMT to simulate the aerodynamic performance of a propeller in uniform flow.

4.2. THE BLADE ELEMENT MOMENTUM THEORY

The Blade Element Momentum Theory (BEMT) is a fundamental approach used in the analysis and design of propellers. It combines two key theories: the Blade Element Theory (BET), which considers the forces on each small section of the blade (or blade element) independently, and the Momentum Theory, which provides a global analysis of the propeller's impact on the airflow. BEMT is particularly useful as it allows for the calculation of the propeller's performance at different operating conditions. It does this by breaking down the propeller blade into small sections, or elements, and analysing each one individually. This approach takes into account the local variations in aerodynamic conditions along the blade's length, such as changes in relative wind speed and angle of attack. The following key assumptions are done:

- Independence of Blade Elements: This is a core assumption of BEMT. The theory considers each blade element independently. This means that the aerodynamic forces on a particular section of the blade do not directly affect the forces on other sections. While this simplifies calculations, it's worth noting that in reality there can be interactions between different sections of the blade, especially near the blade tips where tip vortices form.

- Flow Characteristics: BEMT assumes that the flow over each blade element can be treated as a two-dimensional problem. This means that the flow properties at a given radial position are assumed to be constant along the span of the blade element. In reality, three-dimensional effects can become significant, especially near the root and tip of the blade. Furthermore, the theory assumes that the inflow to the propeller is steady. This means that the velocity and direction of the airflow are constant over time. Finally, it should be said that, although BEMT does not inherently account for viscous and compressibility effects, the airfoil aerodynamic performance will be interpolated from an XFOIL database that accounts for viscous effects. A compressibility correction will also be applied. This will be further explained later.

- No Blade Flexibility: The theory typically assumes that the blades are rigid, i.e., they do not bend or twist under the action of aerodynamic forces or due to the centrifugal force from the rotation. In reality, propeller blades can have significant flexibility, and their deformation can affect the aerodynamic performance.

A rigorous discussion about the BEMT was done by Gudmundsson [33] and is hereby presented.

As said, using BET the aerodynamic performance of a propeller can be calculated by dividing the blade into a series of segments called blade elements. The region of width dr swept by the blade

elements at a radial distance r defines an annulus, of which an illustration is given in Figure 4.1a. Essentially, the aerodynamic properties of each blade element (treated as a two-dimensional airfoil) are determined to then, by integration, obtain the performance of the entire propeller. A representation of a propeller blade element of width dr located at a distance r from the hub of a propeller of radius R_p rotating at an angular velocity Ω is provided in Figure 4.1b, while a cross-sectional view of the blade element alongside its associated angles, velocities and forces is provided in Figure 4.1c.

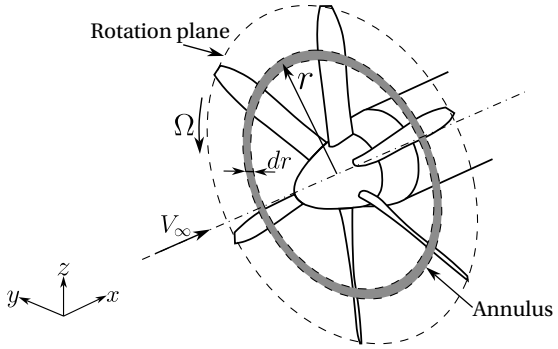

(a) Propeller annulus.

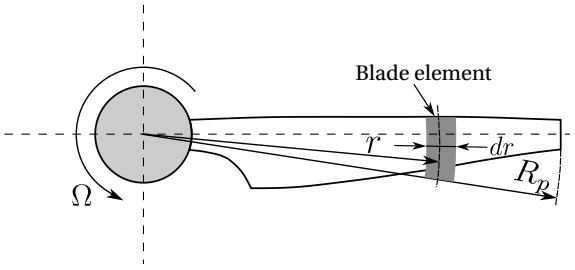

(b) Propeller blade element.

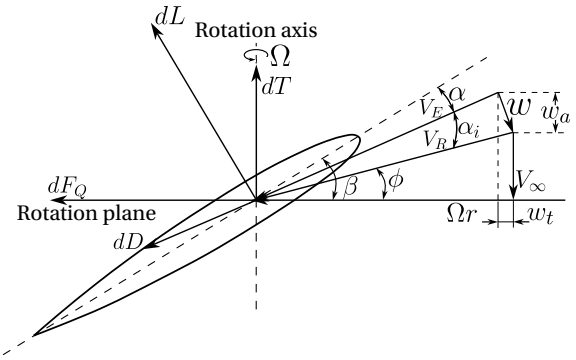

(c) Blade element cross-section.

Figure 4.1: Illustration of a propeller annulus (a), propeller blade element (b) and blade element cross-section (c).

In Figure 4.1c, α is the local angle of attack, β is the pitch angle, ϕ is the local helix angle, α_i is the induced angle of attack, V_∞ is the translational (free-stream) velocity, Ωr is the rotational velocity, V_R is the resultant velocity that stems from V_∞ and Ωr. V_E is the velocity effectively perceived by the elemental airfoil and it results from the fact that a local induced velocity w, which has an axial (w_a) and a tangential (w_t) component, is present. w is due to the airspeed inside the streamtube being faster than the far-field airspeed, as a result of which V_R rotates by an induced angle of attack α_i. This makes the blade element experience an effective resultant velocity V_E, thus a lower angle of attack. About the forces, dL is the differential lift of the blade element, dD is the differential drag, dT is the differential thrust and dF_Q is the differential torque force from which the differential torque can be calculated as $dQ = r\,dF_Q$.

The presence of the above mentioned induced flow in the streamtube is neglected by the BET. Hence, employing the Momentum Theory is necessary to account for that. Specifically, the BEMT attempts to determine the induced angle of attack α_i, which, as can be seen from Figure 4.1c, depends on the induced velocity w, which in turn depends on the blade loading. Thus, an iterative procedure must be employed. In short, an initial guess for w is made, after which α_i is determined and subsequently the local lift and drag coefficients C_l and C_d. The propeller loading is then changed,

hence a new iteration is performed until the loading remains unchanged. The flowchart of the implemented BEMT is shown in Figure 4.2.

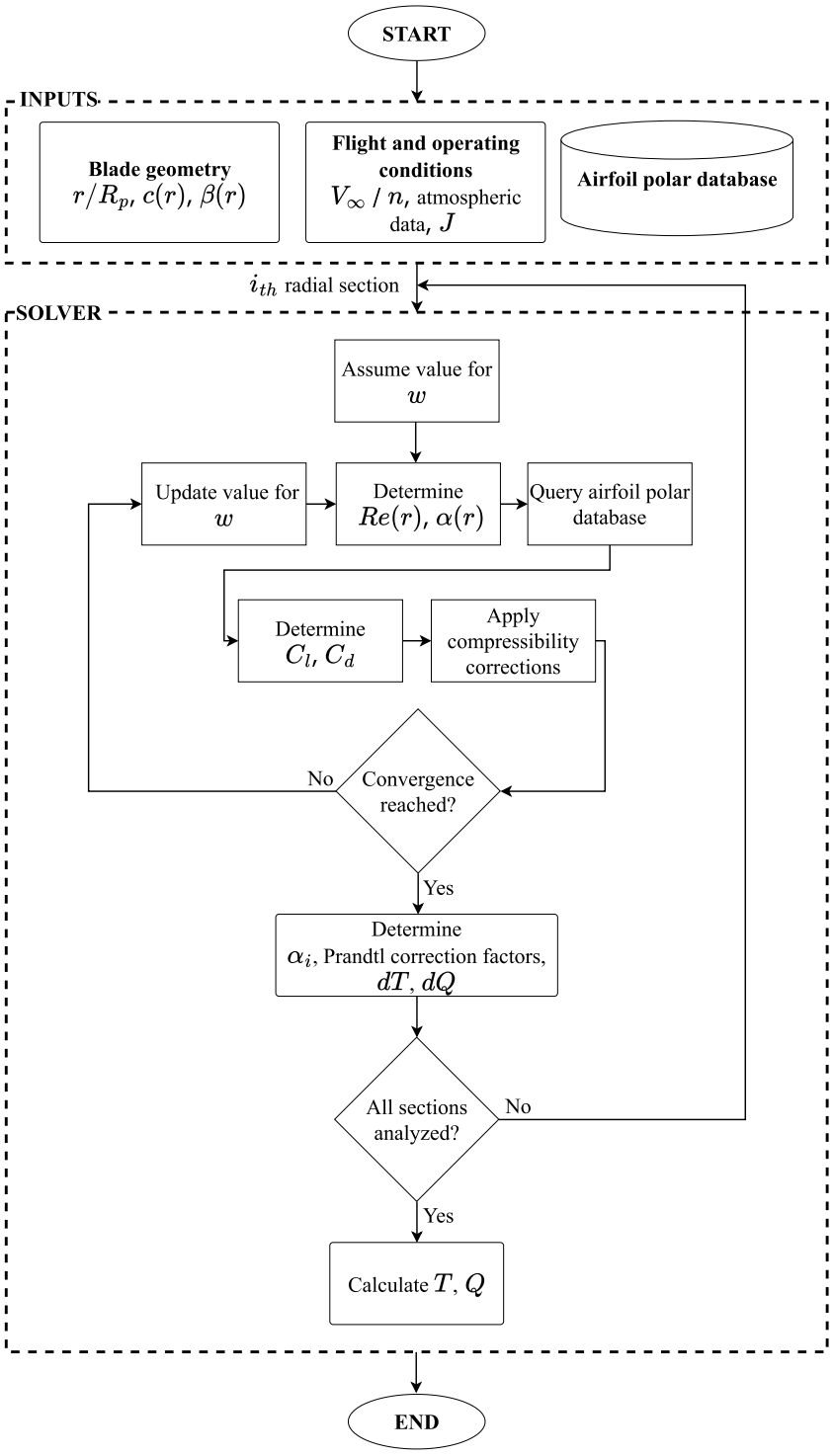

Figure 4.2: Flowchart of the implemented BEMT.

Step 1: Inputs The BEMT procedure requires a number of inputs. These include blade geometry (radial chord and pitch distribution), some flight and operating conditions (wind speed or propeller rotational speed, altitude and advance ratio) and an airfoil polar database. This last was computed

by Willemsen [34] using XFOIL. It contains the lift, drag and pitching moment coefficients for the TUD-XPROP airfoil at Reynolds number raging from $Re_c = 50,000$ to $Re_c = 700,000$ with a step size of 25000. The angle of attack ranges from $\alpha = -90°$ to $\alpha = +90°$. XFOIL makes use of the e^N transition method, where N is the amplification factor [35]. To obtain the polars contained in this database, the amplification factor was set to $N_{crit} = 1$. Furthermore, the transition for both the upper and the lower surface was forced at the leading edge, specifically at $x/c = 0.05$. This made sure that the whole airfoil was subject to turbulent flow. Although the transition point could be different in the 3D case, more sophisticated 3D flow transition methods for propellers are currently not substantiated [36]. Moreover, employing a more advanced transition method is outside the scope of the present research. Such polar database, as mentioned, was obtained for the TUD-XPROP propeller. However, in order to perform an unbiased validation with experimental data, the propeller used for this research is a 50% scaled version of it known as XPROP-S, having an aerodynamic performance similar to the XPROP [22].

Step 2: Solver The procedure used in the BEMT is now explained. First, the propeller angular velocity is computed as:

$$\Omega = \frac{V_\infty \pi}{JR} \tag{4.1}$$

The local helix angle can then be determined as:

$$\phi = tan^{-1}\left(\frac{V_\infty}{\Omega r}\right) \tag{4.2}$$

The effective resultant velocity and the blade element Reynolds number can then be calculated:

$$V_E \approx \sqrt{(V_\infty + w)^2 + (\Omega r)^2} \tag{4.3}$$

$$Re = \frac{V_E c}{\nu} \tag{4.4}$$

Afterwards, the induced angle of attack can be evaluated:

$$\alpha_i \approx tan^{-1}\left(\frac{w}{V_E}\right) \tag{4.5}$$

For the first loop iteration, a guess is used for the induced velocity w. Following that, the local angle of attack can be computed:

$$\alpha = \beta - \phi - \alpha_i \tag{4.6}$$

The airfoil polar database is then queried to compute the elemental lift and drag coefficients for the given section at a certain angle of attack and Reynolds number. As sweep is not taken into account in this work, correcting for it is not needed. However, to account for compressibility effects, a Karman-Tsien compressibility correction is applied to the lift and drag coefficients as follows:

$$C_l = \frac{C_l}{\sqrt{1-M^2} + \frac{M^2}{2(1+\sqrt{1-M^2})} \cdot C_l} \tag{4.7}$$

The differential lift and drag can then be determined:

$$dL = \frac{1}{2}\rho V_E^2 C_l c dr \tag{4.8}$$

$$dD = \frac{1}{2}\rho V_E^2 C_d c dr \tag{4.9}$$

Next, the tangential and the normal force can be evaluated as:

$$f_{\text{tan}} = dL\sin(\phi+\alpha_i) + dD\cos(\phi+\alpha_i) \tag{4.10}$$

$$f_{\text{nor}} = dL\cos(\phi+\alpha_i) - dD\sin(\phi+\alpha_i) \tag{4.11}$$

The BET presented so far ignores the reduction of the local lift coefficient at the tip and at the hub of the blade due to three-dimensional flow effects. For the purpose of factoring this in, Prandtl loss factors are introduced. These factors improve prediction accuracy, as without them, performance would be overestimated in these regions. First, the tip and hub correction parameters are defined:

$$P_{\text{tip}} = \frac{N_B}{2}\frac{R-r}{r\sin\phi} \tag{4.12}$$

$$P_{\text{hub}} = \frac{N_B}{2}\frac{r-R_{hub}}{r\sin\phi} \tag{4.13}$$

Thereafter, the tip and hub correction factors are determined:

$$F_{\text{tip}} = \frac{2}{\pi}\cos^{-1}(e^{-P_{\text{tip}}}) \tag{4.14}$$

$$F_{\text{hub}} = \frac{2}{\pi}\cos^{-1}(e^{-P_{\text{hub}}}) \tag{4.15}$$

Finally, an overall Prandtl loss correction factor is computed:

$$F_{\text{Pr}} = F_{\text{hub}}F_{\text{tip}} \tag{4.16}$$

According to the BET, the differential thrust and torque of the propeller annulus swept by the blade elements at a given radial location r can be evaluated as:

$$dT = N_B f_{\text{nor}} F_{\text{Pr}} = \frac{N_B}{2}\rho V_E^2 c\left[C_l(\cos(\phi+\alpha_i) - C_d\sin(\phi+\alpha_i))\right]dr\,F_{\text{Pr}} \tag{4.17}$$

$$dQ = N_B f_{\text{tan}} r F_{\text{Pr}} = \frac{N_B}{2}\rho V_E^2 c\left[C_l(\sin(\phi+\alpha_i) + C_d\cos(\phi+\alpha_i))\right]r\,dr\,F_{\text{Pr}} \tag{4.18}$$

As mentioned earlier, the BET introduced so far neglects the presence of the induced flow in the propeller streamtube. However, since the induced angle of attack α_i depends on the induced velocity w, accounting for it is crucial. For this reason, the BET was improved by making use of the Momentum Theory. According to the momentum theory, the differential thrust can be defined as:

$$dT = 2\rho dA(V_\infty + w)w = 2\rho(2\pi r\,dr)(V_\infty + w)w \tag{4.19}$$

where dA is the annulus area. Looking at Figure 4.1c, the following relations can be introduced:

$$\cos(\phi+\alpha_i) \approx \frac{\Omega r}{V_E} = \frac{\Omega r}{\sqrt{(V_\infty+w)^2+(\Omega r)^2}} \tag{4.20}$$

$$\sin(\phi+\alpha_i) \approx \frac{V_\infty + w}{V_E} = \frac{V_\infty + w}{\sqrt{(V_\infty+w)^2+(\Omega r)^2}} \tag{4.21}$$

Inserting Equation 4.20 and Equation 4.21 into Equation 4.17 and simplifying appropriately, the following can be derived:

$$dT = \frac{N_B}{2}\rho c\sqrt{(V_\infty+w)^2+(\Omega r)^2}\left[C_l(\Omega r) - C_d(V_\infty+w)\right]dr \tag{4.22}$$

Equating Equation 4.19 and Equation 4.22 and applying suitable simplifications leads to:

$$\frac{8\pi r}{N_B c} w = \frac{\sqrt{(w+V_\infty)^2+(\Omega r)^2}}{V_\infty + w} \left[C_l(\Omega r) - C_d(V_\infty + w)\right] \tag{4.23}$$

The non-linear Equation 4.23 can be solved iteratively to find the value of w. Several approaches can be pursued for this purpose. For this work it was decided to use the Newton-Raphson method, an iterative numerical technique used to find approximations to the roots (or zeros) of a real-valued function. It's particularly useful for solving equations where analytical solutions are difficult to obtain, hence it suits this case. The function of which the root has to be found is given by:

$$f(w) = \frac{8\pi r}{N_B c} w - \frac{\sqrt{(w+V_\infty)^2+(\Omega r)^2}}{V_\infty + w} \left[C_l(\Omega r) - C_d(V_\infty + w)\right] \tag{4.24}$$

An initial guess w_0 for the root is chosen, given which the function and its derivative $f'(w)$ are computed. The estimate is then updated by means of the Newton-Raphson formula:

$$w_{n+1} = w_n - \frac{f(w_n)}{f'(w_n)} \tag{4.25}$$

If the difference $|w_{n+1} - w_n|$ is less than a pre-specified tolerance (set to 10^{-8}), the iteration stops. Otherwise, w_n is set to w_{n+1} and the iteration continues with this updated estimate. Since w depends on the blade loading, the iteration loop runs until the loading doesn't change anymore. Once convergence is reached, the blade element loading is finally known. The BEMT procedure is then applied to compute the aerodynamic performance of the next section. Once all the sections have been analyzed, the propeller thrust and torque can be calculated:

$$T = N_B F_{\text{Pr}} \int_{R_{hub}}^{R_p} f_{nor}\, dr \tag{4.26}$$

$$Q = N_B F_{\text{Pr}} \int_{R_{hub}}^{R_p} r f_{tan}\, dr \tag{4.27}$$

The propeller thrust and torque coefficients can then be computed:

$$C_T = \frac{T}{\rho_\infty n^2 D^4} \tag{4.28}$$

$$C_Q = \frac{Q}{\rho_\infty n^2 D^5} \tag{4.29}$$

4.3. ENGINEERING METHOD FOR AERODYNAMIC PERFORMANCE IN NON-UNIFORM FLOW

Van Arnhem et al. [21] developed a computationally efficient engineering method capable of accurately estimating the aerodynamic performance of a propeller operating in an arbitrary non-uniform flow. This method requires two inputs, namely the blade loading distributions of a propeller operating in uniform flow for a range of advance ratios (performance maps) and an inflow field, i.e. the in- and out-of-plane velocity perturbations at the location of the propeller disk which exist in absence of the propeller. The method treats the response of a propeller to a non-uniform flow field as a quasi-steady problem. Subsequently, corrections are applied to account for unsteady effects.

An inflow disturbance to a propeller operating at an advance ratio J_∞ leads to a change in local advance ratio $\Delta J'$ (where the prime indicates that this change is localized at a certain radial position r/R_p and azimuthal angle ϕ). The method assumes that this $\Delta J'$ results in a variation in the sectional

loads C'_T and C'_Q and in the induced velocity field as if $\Delta J'$ was applied to the full propeller disk. This is schematically shown in Figure 4.3.

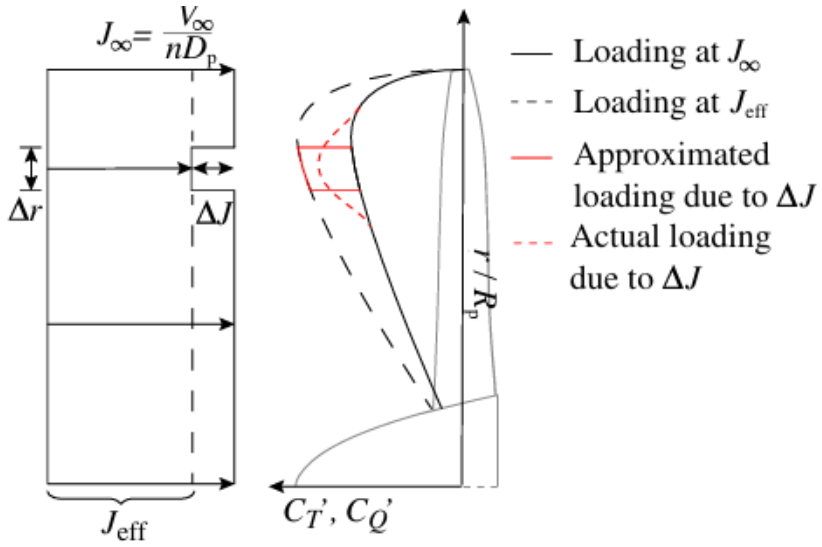

Figure 4.3: Schematic of the assumption underlying the engineering method to analyse propeller performance in non-uniform flow [21].

This assumption rests on a series of principles:

- The local sensitivity of a blade section to a change in advance ratio, caused by a flow non-uniformity, is proportional to the nominal load distribution that exists in uniform flow conditions. As the normalized thrust distribution of a propeller blade is nearly independent of advance ratio [21] (as will be shown in Section 6.1), the sensitivity to variations in advance ratio is also proportional to the nominal load distribution.

- Although a radial loading redistribution occurs due to the upwash and downwash induced to adjacent sections by the vorticity shed resulting from a flow disturbance, this is assumed to be a second-order effect and is thus neglected.

- The load perturbation causes interference between adjacent blades. However, that is considered to be a second-order effect with respect to the load perturbation itself.

The propeller inflow field is characterized by two in-plane velocity components, v and w, and an out-of-plane one, u. Assuming the inflow field disturbance is small, the propeller load distribution can be treated as a linear superposition of the response to the in-plane disturbances Δv and Δw and the out-of-plane disturbance Δu, which exist in absence of the propeller disk. Owing to this, a computationally demanding analysis of the whole propeller annulus can be avoided. In fact, the inflow field in absence of the propeller can be obtained with computationally inexpensive CFD simulations.

As previously stated, an input to the method is the radial blade loading distribution for a range of advance ratios for the isolated propeller in uniform flow. The BEMT code allows to obtain these required $C'_T(r, J_\infty)$ and $C'_Q(r, J_\infty)$, which now need to be evaluated in case of non-uniform inflow at the local effective advance ratio $J_{eff} = J_\infty + \Delta J$ which, as said, is assumed to be applied to the whole propeller.

Considering the axial and tangential velocity components, a distinction can be made between the effective advance ratio due to axial inflow J_{eff_a} and the effective advance ratio due to tangential

inflow J_{eff_t}. It should be noted that in uniform flow $J_{\text{eff}_a} = J_\infty$ and $J_{\text{eff}_t} = 0$. J_{eff_a} at a radial location r and azimuthal angle ϕ is defined as:

$$J_{\text{eff}_a}(r,\phi) = \frac{\Delta u(r,\phi)}{nD_p} + \frac{V_\infty}{nD_p} \tag{4.30}$$

The in-plane velocities Δv and Δw are decomposed into a tangential velocity ΔV_t:

$$\Delta V_t = -\Delta v\ cos\phi - \Delta w\ sin\phi \tag{4.31}$$

This leads to the tangential effective advance ratio $J_{\text{eff}_t}(r,\phi)$:

$$J_{\text{eff}_t}(r,\phi) = \frac{V_\infty}{\left(n + \frac{\Delta V_t}{2\pi r}\right) D_p} - \frac{V_\infty}{nD_p} \tag{4.32}$$

These effective advance ratios are used to compute the corresponding changes in sectional thrust ($\Delta T'_a$ and $\Delta T'_t$) and torque ($\Delta Q'_a$ and $\Delta Q'_t$). A detailed discussion and derivation of the equations is shown in [21]. The total local change in normalized blade loading are:

$$\Delta C'_T(r,\phi) = \frac{\Delta T'_a + \Delta T'_t}{\rho_\infty n^2 D_p^4} \tag{4.33}$$

$$\Delta C'_Q(r,\phi) = \frac{\Delta Q'_a + \Delta Q'_t}{\rho_\infty n^2 D_p^5} \tag{4.34}$$

With the load distribution computed at each radial and azimuthal location, an integration is performed to obtain the integral propeller forces.

The method also includes a correction to account for unsteady effects. As shown by Sears [37], due to the leading edge downwash induced by the bound and wake vorticities, an airfoil does not respond immediately to a change in inflow. Thus, the present method corrects the radial distribution of thrust and torque by transforming the calculated quasi-steady forces to the frequency domain and multiplying them with the Sears' function.

It should be said that this method is particularly suitable for unswept propeller blades, as blade sweeping introduces coupling between adjacent blade sections, which is assumed not be present. Furthermore, as the inflow is evaluated for blades represented by lines (i.e., zero chord-length), an offset in the predicted forces is expected. Although a suitable weighting function could be employed to determine the velocity field along the projected chord in the plane of rotation, the impact of it on propeller forces was found to be marginal [22] and is therefore not used in this work. Another limitation concerns the limited advance ratio range for which the isolated propeller performance in uniform inflow is computed. This loading serves as an input to the non-uniform method, which then computes ΔJ, thereafter the performance in non-uniform inflow is estimated. Under certain non-uniform inflows (for instance at high angles of attack) ΔJ might exceed the range of available advance ratios. In such case, the method uses either the results for the minimum or for the maximum advance ratio. Finally, it should be observed that, since the employed inflow field is the one that exists in absence of the propeller, the propeller's influence on the inflow field is not considered.

The method was validated against CFD simulations and experimental data for four cases, namely isolated propeller at a non-zero angle of attack, wake encounter, over-the-wing propeller and wingtip-mounted pusher propeller. The errors in integral propeller loads with respect to validation data were between 0.5 and 12%.

5

AEROACOUSTIC PERFORMANCE PREDICTION

This chapter centers on the aeroacoustic performance model employed in this work. Section 5.1 elucidates the rationale behind the selection of the model, while Section 5.2 provides a description of it.

5.1. MODEL SELECTION

The Ffowcs Williams and Hawkings equation can be solved by means of time-domain or a frequency-domain method. Time-domain methods preserve the pressure time-history at the expense of higher computational cost, as the computation of the retarted locations of the blades is required [38]. As this thesis focuses on the physics of noise emissions, preserving the pressure time-history is crucial to visualize acoustic waveforms and analyze their interference. The chosen time-domain method was proposed by Hanson [12] for steady blade loading cases and adapted to unsteady (but periodic) conditions by Monteiro et al. [39] to predict the tonal noise emissions of a distributed propeller configuration. This method neglects the quadrupole source term of the FWH equation, which is an acceptable approximation for subsonic tip Mach numbers. However, predictions in areas where broadband noise is dominant (such as near the propeller axis) are not reliable. This method was also validated by showing that the noise prediction of an isolated propeller shows a 1.53 dB difference compared to high-fidelity values up to the fifth BPF for an observer in the far-field 10 diameters away from the propeller center and at the propeller plane. When analyzing the source directivity at the first BPF, a difference of about 0.5 dB is observed at the propeller plane. However, this difference grows to 6 dB for directivity angles near the inflow direction [39]. As this thesis focuses on tonal noise, this is deemed to be a suitable low-fidelity tool to predict propeller tonal noise emissions.

5.2. HANSON'S NEAR-FIELD THEORY

Hanson's near-field theory aims at estimating the tonal noise emitted by propellers operating at supersonic or high-subsonic tip speeds [12]. However, the theory can also be employed in case of propellers operating at subsonic tip Mach numbers. The theory is based on the FWH equation:

$$\nabla^2 p - \frac{1}{c^2}\frac{\partial^2 p}{\partial t^2} = -\frac{\partial}{\partial t}\rho s + \nabla \cdot \vec{F} - \frac{\partial^2 T_{ij}}{\partial x_i \partial x_j} = f(\vec{r}, t) \tag{5.1}$$

The left-hand side of the equation contains the wave operator applied to the acoustic pressure $p(\vec{r}, t)$, while the right-hand side features three source terms. The first one is the monopole source term, where ρ is the fluid density and s is the fluid specific entropy. Considering a fluid with uniform properties and adiabatic conditions, $\frac{\partial}{\partial t}\rho s = \rho\frac{\partial q}{\partial t}$. Being q the volume displacement per unit time and unit volume dependent upon the blade thickness distribution, the monopole term is associated

to thickness noise. The second term is the loading source term, where $\vec{F}$ is the force per unit volume exerted on the fluid by the blade pressure distribution and is thus associated to loading noise. In the context of the third source term, T_{ij} is the Lighthill stress tensor, which contains the Reynolds stress $\rho u_i u_j$ arising from the turbulent fluctuations of the velocity field. This last term accounts for non-linear effects and is referred to as quadrupole source term.

Hanson's theory is based on the following assumptions:

- The quadrupole source term can be neglected as the non-linear effects it accounts for are of second order compared to the volume displacement in the thickness term. In fact, while the Lighthill stress tensor includes a multiplication between two velocity components, the volume displacement depends directly on the perturbation velocity.
- The blade is assumed to be thin, hence the volume displacement and force imposed by the blade on the surrounding fluid are considered to act on the chord of each radial section. This assumption is supported by the fact that the distance between the upper and lower airfoil surfaces is small compared to the source-to-observer distance, particularly in case of a far-field observer.

The solution to Equation 5.1 presented by FWH is:

$$p(\vec{r},t) = \int\int\int\int f(\vec{r}_o,\tau)\; g(\vec{r},t;\vec{r}_o,\tau)\; d\vec{r}_o d\tau \tag{5.2}$$

where $\vec{r}$ is the observer location, $\vec{r}_o$ is the source location, t is the observer reception time, τ is the source emission time and g is the Green function, defined as:

$$g(\vec{r},t;\vec{r}_o,\tau) = \frac{\delta(t-\tau-R/c)}{4\pi R} \tag{5.3}$$

where $R = |\vec{r}-\vec{r}_o|$ is the distance between the source and the observer locations and δ is the Dirac delta function. It should be observed that the reception time t is the sum of the emission time τ and the time it takes for the signal to travel from the source to the observer, which is R/c. Hence, $t = \tau + R/c$.

The source function is:

$$f(\vec{r}_o,\tau) = \rho\frac{\partial q(\vec{r}_o,\tau)}{\partial\tau} - \vec{\nabla}\cdot\vec{F}(\vec{r}_o,\tau) \tag{5.4}$$

A fluid-fixed coordinate system is used. During forward flight, the blade traces a helical path determined by its angular velocity Ω and the flight speed V_f. A helical coordinate system can then be defined, which is illustrated in Figure 5.1 along with a Cartesian coordinate system.

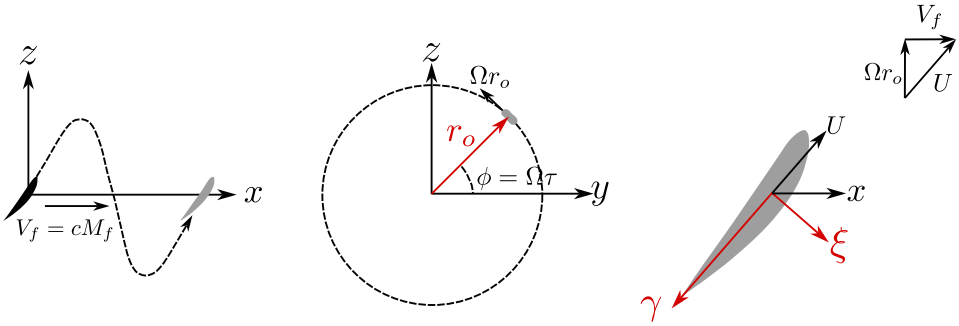

Figure 5.1: Helical (in red) and Cartesian coordinates (adapted from [39]).

It can be noted that the blade travels along the positive x-axis direction and the y-axis coincides with the blade pitch change axis at time $t = 0$. The helical coordinates that define the position of a

blade element are r_o, γ and ξ, where r_o is the radial distance from the propeller shaft, γ is the distance backward in the helical surface and ξ is normal to the helical surface. U is the blade element velocity. The helical surface (source surface) is assumed to be fixed with respect to the fluid. By defining the source in the fluid-fixed reference frame, the mathematical singularity that occurs when the source moves towards the observer at sonic speed is avoided.

The acoustic pressure in Equation 5.2 can be decomposed into its thickness and loading noise components:

$$p(\vec{r}, t) = p_{TH}(\vec{r}, t) + p_L(\vec{r}, t) \tag{5.5}$$

The procedure to compute the thickness and loading noise components is hereby outlined.

As for thickness noise, the monopole source term $\frac{\partial q}{\partial \tau} d\vec{r}_o$ in Equation 5.4 must be rewritten to relate it to the blade element thickness distribution. Calling $h(\gamma, r_o)$ the sectional thickness distribution and $\xi = h_1(\gamma, r_o)$ the camber surface of the airfoil, the volume displacement per unit time is:

$$U \frac{\partial h_1(\gamma, r_o)}{\partial \gamma} d\gamma \, dr_o \tag{5.6}$$

Here, $d\gamma \, dr_o$ is the differential area element of the airfoil surface and $\frac{\partial h_1(\gamma, r_o)}{\partial \gamma}$ represents the rate of change of the camber surface height with respect to γ. Multiplying by U allows to reflect the amount of fluid displaced per unit time by accounting for the speed of the blade. A similar form can be given for the other face side of the airfoil, i.e. h_2. The assumption (also used by Hawkings and Lowson [40]) that the volume displacements of both the sectional surfaces act on the chord line $\xi = \xi_o$ effectively yields:

$$q \, d\vec{r}_o = U \frac{\partial h(\gamma, r_o)}{\partial \gamma} \delta(\xi - \xi_o) \, d\xi \, d\gamma \, dr_o \tag{5.7}$$

at $t = 0$, where $d\xi \, d\gamma \, dr_o$ is the differential volume and $\delta(\xi - \xi_o)$ is a delta function necessary to localize the volume displacement to the specific chord line. As will be shown later, when integrating over the entire chord line, the delta function ensures that only the displacement at $\xi = \xi_o$ is considered. It should also be noted that $\gamma = \gamma_o + U\tau$, i.e. the γ coordinate is given by the sum of the initial position γ_o and the space covered by the blade along the helical surface until the emission time τ. The source term for times $\tau \neq 0$ becomes:

$$\frac{dq}{d\tau} d\vec{r}_o = U^2 h''(\gamma_o + U\tau, r_o) \delta(\xi - \xi_o) \, d\xi \, d\gamma \, dr_o \tag{5.8}$$

where h'' is the second derivative of h with respect to γ.

Similarly, for loading noise, the force per unit volume exerted on the fluid $\vec{F}$ in Equation 5.4 must be related to the blade pressure distribution. For this purpose, $\vec{F}$ is assumed to act in the direction of the unit vector normal to the helical surface, effectively becoming a force per unit area (or pressure) at $t = 0$:

$$\vec{F}(\vec{r}_o, \tau) = \Delta p \, (\gamma_o + U\tau, r_o) \delta(\xi - \xi_o) \, \hat{n} \tag{5.9}$$

where $\Delta p(\gamma, r_o)$ is the difference between the pressures of the upper and lower surfaces of the airfoil, where the sign convention is such that $\Delta P > 0$ generates positive lift. Again, the delta function ensures that the force exerted by the blade on the surrounding fluid is localized at the chord line ξ_o.

With the source terms established, integration can be carried out to obtain the pressure given by Equation 5.2. The loading pressure reads:

$$p_L(\vec{r}, t) = -\int\int\int\int \frac{\vec{\nabla}_o \cdot \vec{F}(\vec{r}_o, \tau) \delta(t - \tau - R/c) \, d\vec{r}_o \, d\tau}{4\pi R} \tag{5.10}$$

Using vector calculus properties detailed in [12], Equation 5.10 becomes:

$$p_L(\vec{r},t) = \frac{1}{4\pi}\int\int\int\int \vec{R}\cdot\left[\frac{1}{R^3}\vec{F}(\vec{r_o},\tau)+\frac{1}{cR^2}\frac{\partial}{\partial\tau}\vec{F}(\vec{r_o},\tau)\right]\delta(t-\tau-R/c)\,d\vec{r_o}\,d\tau \tag{5.11}$$

Equation 5.9 can be used to obtain:

$$p_L(\vec{r},t) = \frac{1}{4\pi}\int\int\int\int \vec{R}\cdot\hat{n}\left[\frac{1}{R^3}\Delta p(\gamma_o+U\tau,r_o)+\frac{M_r}{R^2}\Delta p'(\gamma_o+U\tau,r_o)\right]\delta(\xi-\xi_o)\delta(t-\tau-R/c)\,d\vec{r_o}\,d\tau \tag{5.12}$$

where $\Delta p'$ is the first derivative of Δp with respect to γ and $M_r = U/c$ is the sectional Mach number. Equation 5.12 presents four integrals whose variables of integration are $\vec{r_o} = \langle\xi,\gamma,r\rangle$ and τ, and two delta functions. By exploiting the Dirac delta function property:

$$\int_{-\infty}^{\infty} f(x)\delta(x-a)\,dx = f(a) \tag{5.13}$$

the ξ_o and τ integrals can readily be solved. The acoustic pressure p_L can be separated into a near-field component and a far-field component. The near-field component (p_{LN}) scales with R^{-3}, while the far-field component (p_{LF}) scales with R^{-2}:

$$p_{LN}(\vec{r},t) = \int_0^{R_p}\int_{-\infty}^{\infty}\Delta p(\gamma_o+Ut-M_rR,r_o)\frac{\vec{R}\cdot\hat{n}}{4\pi R^3}\,d\gamma\,dr_o \tag{5.14}$$

and:

$$p_{LF}(\vec{r},t) = \int_0^{R_p}\int_{-\infty}^{\infty}\Delta p'(\gamma_o+Ut-M_rR,r_o)\frac{M_r\vec{R}\cdot\hat{n}}{4\pi R^2}\,d\gamma\,dr_o \tag{5.15}$$

which is equivalent to:

$$p_{LF}(\vec{r},t) = \frac{\partial}{\partial t}\int_0^{R_p}\int_{-\infty}^{\infty}\Delta p(\gamma_o+Ut-M_rR,r_o)\frac{\vec{R}\cdot\hat{n}}{4\pi cR^2}\,d\gamma\,dr_o \tag{5.16}$$

It can be noted that, if the time derivative of Equation 5.16 is brought inside the integral of Equation 5.15, $\vec{R}\cdot\hat{n}$ is not affected by it. This is achieved through the use of the Green function, essentially a delta function that ensures that $\vec{R}\cdot\hat{n}$ is only considered at a specific point in time, namely when the noise emitted by a blade element at a given time τ reaches the observer at a given time t.

Regarding the thickness pressure, it is given by:

$$p_{TH}(\vec{r},t) = \int\int\int\int \frac{\rho}{4\pi R}\frac{\partial q(\vec{r_o},\tau)}{\partial\tau}\delta(t-\tau-R/c)\,d\vec{r_o}\,d\tau \tag{5.17}$$

By employing Equation 5.8 and the delta function property in Equation 5.13, the ξ_o and τ integrals can readily be solved. The four integrals then reduce to:

$$p_{TH}(\vec{r},t) = \int_0^{R_p}\int_{-\infty}^{\infty}\frac{\rho U^2}{4\pi R}h''(\gamma_o+Ut-M_rR,r_o)\,d\gamma\,dr_o \tag{5.18}$$

or, alternatively:

$$p_{TH}(\vec{r},t) = \frac{\partial^2}{\partial t^2}\int_0^{R_p}\int_{-\infty}^{\infty}\frac{\rho}{4\pi R}h(\gamma_o+Ut-M_rR,r_o)\,d\gamma\,dr_o \tag{5.19}$$

The area of integration in the loading and thickness pressure expressions is the helical surface swept out by the blade as it travels along the x-axis. Radially, this surface extends up to the propeller tip radius R_p. On the other hand, in the chordwise direction the range is infinite, i.e. $-\infty \le \gamma \le \infty$. However, as the source function has been multiplied by the Green function in Equation 5.2, the property of the latter expressed in Equation 5.13 can be exploited. For this reason, only the integration in the range $\gamma_L \le \gamma_o + Ut - M_rR \le \gamma_T$ (where γ_L and γ_T are the leading and trailing edge coordinates, respectively) is performed. It is worth nothing that $U\tau = Ut - M_rR$, thus the retarded time is $\tau = t - R/c$. Outside of the aforementioned integration range, the source strength is zero because the blade was not there at the retarded time τ.

5.2.1. COMPUTATIONAL FRAMEWORK

As mentioned in Section 5.1, Hanson's near-field theory was implemented and validated by Monteiro et al. [39]. The code architecture is illustrated in Figure 5.2.

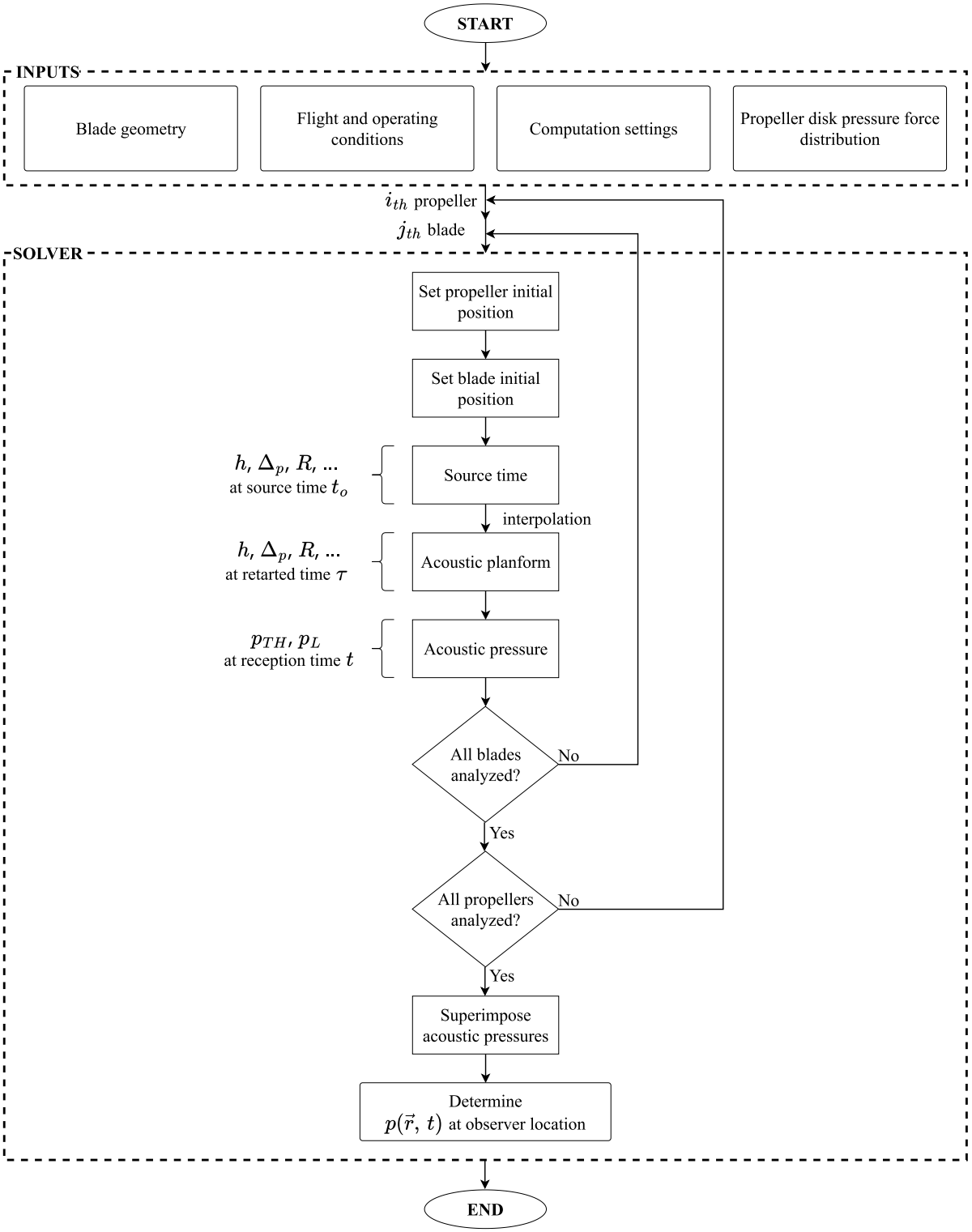

Figure 5.2: Flowchart of the code architecture (adapted from [39]).

The inputs required by the code are the blade geometry, flight and operating conditions, some computation settings (such as the number of radial and chordwise stations to discretize the blade and the number of time steps per period) and the propeller disk pressure force distribution. This last can readily be determined knowing the radial distributions of thrust and torque computed by means of the aerodynamic solvers and the blade geometry. In fact, the pressure force is just the normal force to the chordal surface. In case of non-uniform flow, the pressure force distribution must be known at each time step of the rotation period.

Once the propeller and the blade initial positions are set, the relevant parameters at the source time are computed. Among them are the thickness distribution h, the pressure Δ_p and the source-to-observer distance magnitude R. A constant time step sequence for the observer is then defined. At each of the observer time steps, the acoustic planform (i.e., the surface defined by the locations of the blade elements at the retarded time) is determined by interpolating the positions of the blade elements at the previous time step. Likewise, the values needed to compute Equations 5.14, 5.16, and 5.19 are obtained by means of interpolation. Afterwards, the loading and thickness pressure at the reception time can be evaluated. Once all the blades and propellers of the studied setup have been analyzed, the acoustic pressure of each blade (and each propeller) is superimposed (namely, added up) to retrieve the overall noise at the observer location.

A limitation of the current code implementation is its inability to account for the deformation of the helical surface caused by an inflow velocity asymmetry that affects the blade elements differently over the azimuth. This will be further explained in Section 7.2, along with a discussion of its implications for the analysis.

Another limitation is that the code is not suited for handling cases in which $M_r > 1$. As pointed out by Hanson, as M_r approaches 1 the acoustic planform becomes increasingly distorted and even splits for $M_r > 1$. This occurs because the signals emitted by some blade elements at different instants reach the observer simultaneously. This behavior of the acoustic planform highlights the non-compactness of the noise source. Currently, the interpolation used in the code is not designed for obtaining these two values. For this reason, caution is necessary when analysing higher tip Mach number configurations so as to ensure that M_r remains subsonic.

III

Validation & Results

6

VERIFICATION & VALIDATION

This chapter discusses the verification and validation of the numerical tools used for this work in order to find their fidelity to the experimental data within a certain degree of accuracy. Starting with the BEM model, covered in Section 6.1, the focus is then shift to the non-uniform inflow aerodynamic model in section Section 6.2 and finally to the aeroacoustic model in section Section 6.3.

6.1. BEM MODEL

The datasets utilized for validation are for the XPROP-S propeller, a scaled-down version of the TUD-XPROP propeller. The XPROP-S has 6 blades and a diameter of 0.2032 m. The blade-pitch angle is set at 45° at 70% of the radius, which ensures that high thrust and torque coefficients are achieved at relatively high advance ratios, as would be expected in the case of a full-scale aircraft during cruise conditions [41]. The blade sweep is negligible [21]. The pitch and chord distributions are given in Figure 6.1a while a picture of the wind-tunnel propeller model is shown in Figure 6.1b.

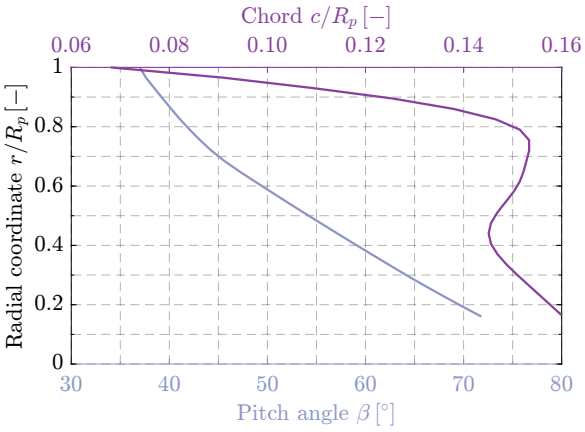

(a) Propeller pitch and chord distributions.

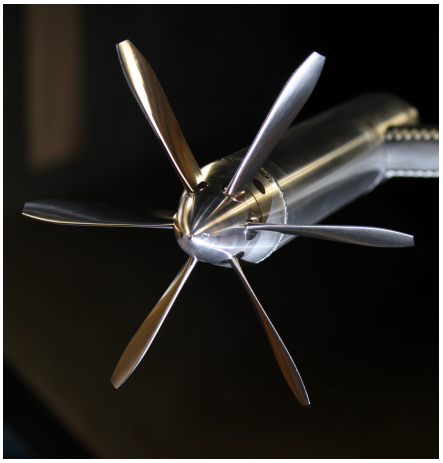

(b) Wind-tunnel propeller model.

Figure 6.1: XPROP-S propeller geometry (a) and wind-tunnel model (b).

The key geometrical and operational parameters of the propeller used for validating the aerodynamic models are presented in Table 6.1. The rotation direction of the propeller is anti-clockwise if seen from the front and the reference frame employed coincides with the one shown in Figure 4.1a. Notably, to compute the propeller's performance, the advance ratio is varied between $J = 1$ and 3,

enabling the generation of performance maps required for the non-uniform inflow aerodynamic performance method.

Parameter	Value	Unit
Propeller diameter - D	0.2032	m
Hub-to-tip ratio - R_{hub}/R_p	0.23	–
Blade pitch at $r/R_p = 0.7$	45	°
Number of blades - N_B	6	–
Free-stream static pressure - p_∞	101325	Pa
Free-stream static temperature - T_∞	288.15	K
Free-stream Mach number - M_∞	0.118	–
Helical tip Mach number - M_{ht}	0.388 - 0.170	–
Advance ratio - J	1.0 - 3.0	–
Maximum chord-based Reynolds number - max Re_c	1.19×10^5 - 5.41×10^4	–

Table 6.1: Key parameters for validating the aerodynamic models.

Before validating the BEMT, a grid dependency assessment must be performed by gradually increasing the number of elements in the radial direction chosen to discretise the propeller blade. As explained in Section 4.2, blade element theory is based on dividing the blade into small sections, i.e., blade elements, and analysing the aerodynamic performance of each of them. The choice of the number of elements should be made by trying to strike a balance between good blade discretisation and computational time. Consequently, the relative difference between the C_T computed with a certain number of elements and the C_T computed with an arbitrary maximum number of elements is:

$$\epsilon_{BEMT} = \frac{C_T - C_{T,maxN_{el}}}{C_{T,maxN_{el}}} \tag{6.1}$$

In Figure 6.2, the propeller thrust coefficient C_T is plotted as a function of the number of radial elements N_{el} at an advance ratio of $J = 1.8$ (corresponding to the nominal condition of the isolated propeller). The execution time of the BEM procedure is also shown. This analysis was conducted on a system with an Intel® Core™ i7-10750H CPU @ 2.60 GHz and 16 GB of RAM. Both a linear spacing between elements and cosine spacing were considered. Unlike the former, in which the blade elements are equally spaced along the blade length, the latter is characterized by a higher density of elements close to the hub and the tip. Cosine spacing can thus enhance the accuracy of BEMT, being it particularly suitable for the Prandtl hub and tip loss models used in this work. The number of elements required to obtain a relative difference of 0.1% is shown with black vertical lines. The margin of difference is considered to be low enough to ensure adequate verification of the model. What emerges from the figure is that cosine spacing ensures quicker convergence, necessitating of 40 elements to achieve the desired relative difference compared to the 54 elements required by linear spacing. However, the difference between the BEMT execution time of the two types of spacing is only marginal (less than 0.015 s), as shown in the zoomed-in portion of the plot. For the same number of radial elements, the execution time is comparable.

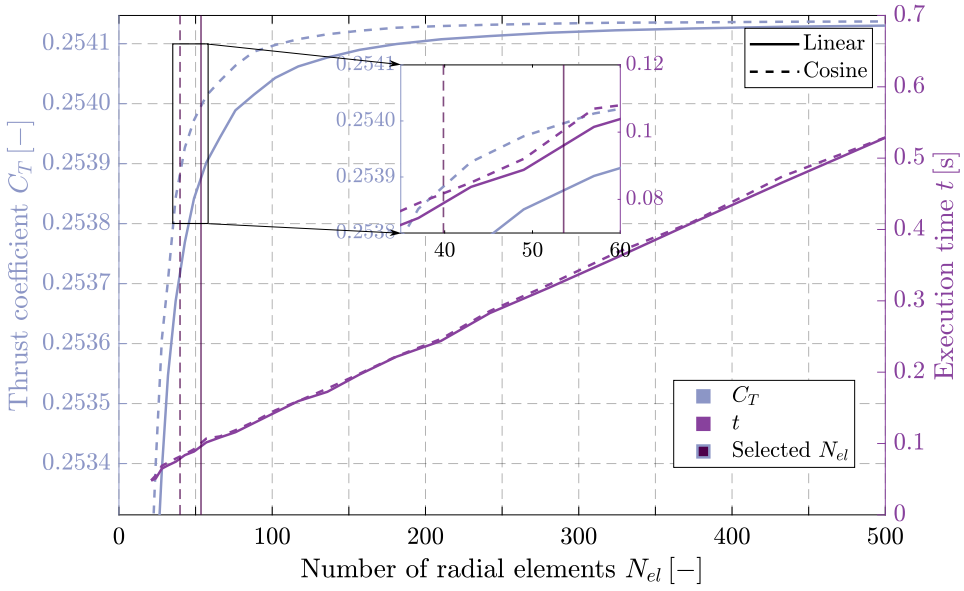

Figure 6.2: Propeller thrust coefficient with increasing number of radial elements; $J = 1.8$.

Figure 6.3 clearly shows that the cosine spacing ensures quicker convergence, as it reaches the difference threshold of 0.1% with a smaller amount of elements. It can be observed that, for the same number of radial elements, the relative difference is smaller.

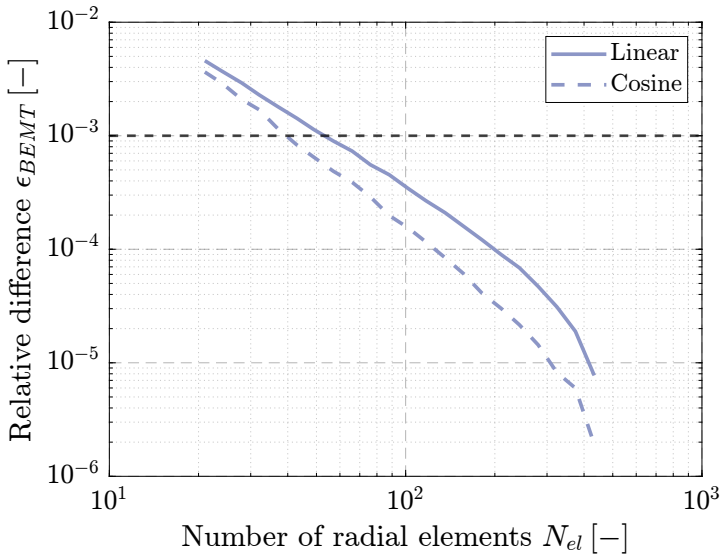

Figure 6.3: Relative difference as a function of the number of elements; $J = 1.8$.

Since cosine spacing provides quicker convergence and lower relative difference for the same number of radial elements without affecting computational time, it would seem convenient to opt for it for this work. However, before making a decision, it must be verified that cosine spacing ensures an adequate discretisation of the propeller blade in the region of maximum loading, which, as reported by Van Arnhem et al. [21], for the XPROP-S at the analyzed operating conditions is between $r/R_p =$ 0.8 and 0.9. Being this region critical for propeller aerodynamic and aeroacoustic performance, it is of paramount importance to discretise it appropriately. Figure 6.4 shows a comparison of linear and cosine spacing for $N_{el} = 65$. This number of blade elements was chosen based on the analysis performed in Figure 6.2. That analysis revealed that 54 blade elements are needed to obtain

sufficiently accurate results in case of linear spacing and 40 in case of cosine spacing. To make the two comparable, in Figure 6.4 it was chosen to use 65 blade elements to ensure that both discretisations return accurate results with some more elements than what would be needed so as to make sure that, if linear spacing was chosen for the rest of this work, there would be a margin of safety for further analyses under different inflow and operational conditions. The average spacing between blade elements in the range $r/R_p = 0.8$ to 0.9 is slightly below 0.012 for linear spacing and just above 0.014 for cosine spacing, making the linear spacing discretization approximately 14% finer than the cosine spacing one locally. Given that a good discretisation in the radial range of interest is essential and being the impact on computational time of using linear over cosine spacing spacing negligible, it was decided to opt for linear spacing with $N_{el} = 65$ for this work.

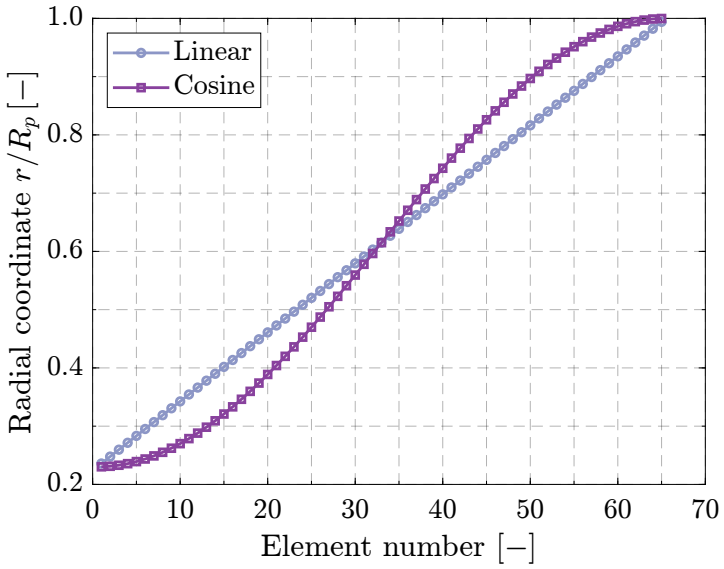

Figure 6.4: Linear and cosine spacing between the radial blade elements.

A comparison of BEMT predictions with CFD and experimental data is provided in Figure 6.5. Table 6.2 shows the percentage difference of the BEMT-predicted performance metrics with respect to CFD and experimental data at the nominal advance ratio $J = 1.8$. The propeller thrust coefficient is plotted as a function of the advance ratio in Figure 6.5a. The CFD and experimental data were obtained by Van Arnhem et al. [21]. The CFD data refer to a numerical simulation performed by solving the RANS equations for compressible flow using ANSYS Fluent software, while the experimental data refer to measurements made in the Low-turbulance tunnel at Delft University of Technology by attaching the propeller model attached to a support strut to a six-component external balance. The BEMT analysis was conducted with a fixed inflow velocity of $V = 40\,\mathrm{m/s}$ while varying the propeller rotational speed across a range of advance ratios between $J = 1$ and $J = 2.4$. Within the nominal operating range of the propeller ($J = 1.4$ to $J = 2$), the BEMT and CFD results show reasonably good agreement, with C_T overpredicted by 4.7% compared to CFD data at $J = 1.8$. At advance ratios higher than the nominal operating range, the contribution of viscous forces relative to pressure forces is dominant. Viscous effects are not inherently accounted for by the BEM model, except for those captured in obtaining the two-dimensional airfoil polars. Generally, the slope and values predicted by BEMT are close to those from CFD even for advance ratios greater than $J = 2$, with just a slight overprediction due to underprediction of viscous effects. Moreover, it must be noted that the BEMT does not account for the nacelle blockage effect. This effect causes variations in the aerodynamic performance of the propeller near the hub. However, this factor is of lesser importance as the forces in that blade region are relatively low, thus having a minimal impact on propeller performance.

More significant deviations are observable at advance ratios between $J = 1$ and 1.2. At these lower advance ratios, three-dimensional flow effects become significant due to the blade experiencing higher angles of attack. These effects include tip vortices, spanwise flow effects, and flow separation. BEMT is not designed to capture the complex vortex dynamics at those operating conditions, leading to deviations in propeller performance predictions at low advance ratios compared to CFD. It is also evident that the thrust coefficient decreases at a lower advance ratio for BEMT compared to CFD. This earlier onset of reduced propulsive performance arises because BEMT does not account for rotational effects. A key rotational effect not captured by BEMT is the Himmelskamp effect [42]. As the propeller blade rotates, centrifugal force pushes air outward from the blade root to the tip. This outward movement is accompanied by the Coriolis force, which acts perpendicular to the flow direction due to the blade's rotation. The Coriolis force causes the air to deflect, creating a spanwise flow along the blade. This combination of centrifugal and Coriolis forces helps to maintain a favorable pressure gradient, delaying the separation of airflow from the blade surface. By preventing premature stall, the Himmelskamp effect enhances lift and improves aerodynamic performance, especially at higher angles of attack. It has been shown by Goyal et al. [43] that rotational effects are particularly relevant at high angles of attack (associated to stall or near stall conditions), such as the ones experienced by the blade sections (especially the outboard ones) at the lowest advance ratios of Figure 6.5a. Experimental data are available for a limited range of advance ratios, specifically between $J = 1.6$ and $J = 2.3$. Some deviations are observed in both slope and values compared to BEMT and CFD results. At $J = 1.8$, the percentage difference in C_T between BEMT and experimental data is 5.35%. A significant factor explaining this discrepancy is the flow over the blade. During the experiment, the flow was predominantly laminar, whereas, for obtaining the two-dimensional airfoil polars, the transition was fixed at $x/c = 0.05$. The reduction in the effective camber of the boundary layer due to turbulent flow causes a decrease in the lift-curve slope. This results in a lower slope, as observed in the figure. Conversely, the offset in values relative to the wind tunnel data can be attributed to the influence of interference drag, arising from the interaction between the propeller slipstream and the support strut. Experimental data are subject to interference drag because they are derived by subtracting propeller-off forces (balance measurements of the model forces with uninstalled blades) from propeller-on forces to isolate the propeller-generated forces. The propeller-off measurements account for the base drag of the model. However, when blades are installed, the model experiences both base drag and interference drag. This additional interference drag affects the calculated propeller forces, leading to discrepancies between the numerical and experimental results. Notably, at lower advance ratios, this discrepancy diminishes, likely due to the contraction of the propeller slipstream at higher thrust settings. The resulting reduction in slipstream cross-sectional area minimizes its interaction with the support strut, thereby reducing the extent of interference drag.

The plot of the propeller power coefficient versus advance ratio, shown in Figure 6.5b, reveals excellent agreement between BEMT and CFD predictions within the range of advance ratios from $J = 1.3$ to 2.3. At $J = 1.8$, the match is flawless up to the third decimal digit. This is due to the fact that the lift and drag components are summed in the definition of the torque force (see Equation 4.18), which in turn determines the power coefficient. As known, viscous effects increase drag and decrease lift. However, when lift and drag are summed, the impact of underpredicted viscous effects is effectively balanced out. However, at advance ratios lower than $J = 1.3$, BEMT underestimates the power coefficient. This significant deviation can be attributed to the BEMT neglecting rotational effects. At lower advance ratios, some outboard blade sections experience high angles of attack, leading to stall. This stall reduces lift and increases drag. While both lift and drag changes influence the power coefficient, the larger drop in lift compared to the increase in drag has a more significant effect, given that lift coefficients are much higher than drag coefficients. Thus, BEMT's underestimation of power requirements at lower advance ratios is due to this limitation in accounting for rotational effects.

The propeller efficiency versus advance ratio is plotted in Figure 6.5c. The figure shows that the efficiency is overpredicted by BEMT across the entire range of advance ratios. At $J = 1.8$, the overprediction amounts to 4.97%. This observation is consistent with what is seen in Figure 6.5a and Figure 6.5b, namely an overprediction in thrust coefficient over a large part of the advance ratio range and a generally good agreement of the power coefficient with CFD data, except at the lowest advance ratios. Nonetheless, the trend is well predicted, with a maximum efficiency at $J = 2$.

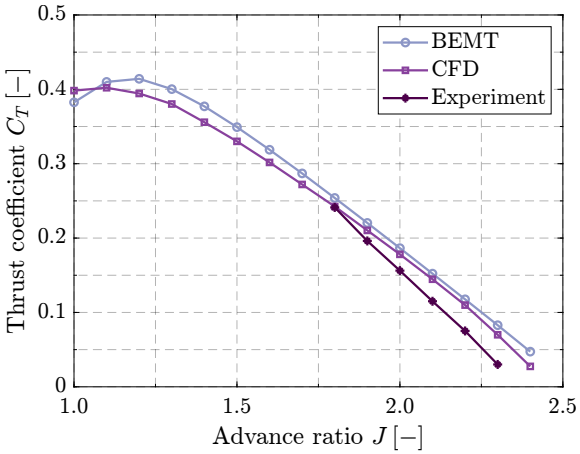

(a) Propeller thrust coefficient versus advance ratio.

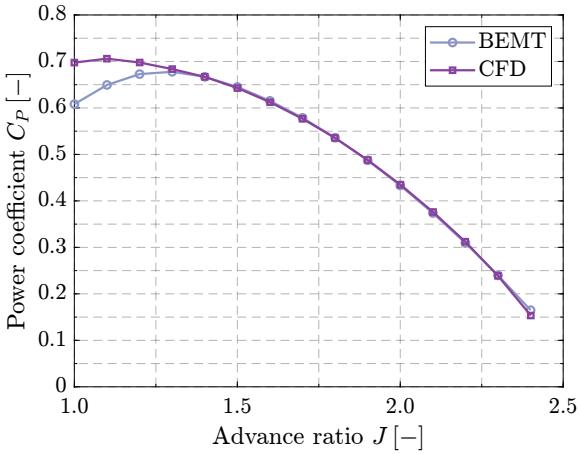

(b) Propeller power coefficient versus advance ratio.

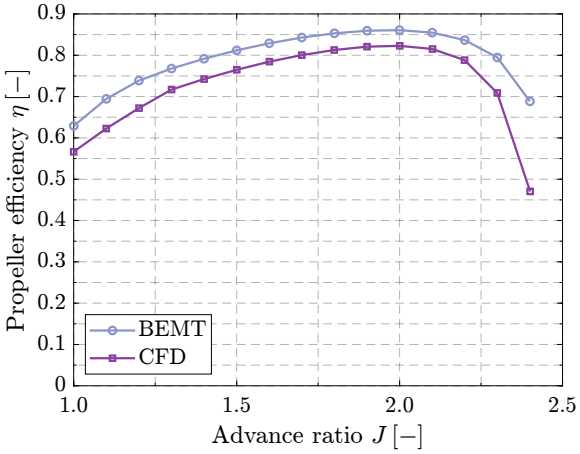

(c) Propeller efficiency versus advance ratio.

Figure 6.5: Comparison of BEMT predictions with CFD and experimental data.

	BEMT	CFD	Experiment	$\Delta\%_{\text{CFD}}$	$\Delta\%_{\text{Experiment}}$
C_T	0.2539	0.2425	0.2412	4.70%	5.35%
C_P	0.5358	0.5355	–	0.06%	–
η	0.8531	0.8127	–	4.97%	–

Table 6.2: Percentage difference of propeller performance metrics between BEMT, CFD simulation and experiment at $J = 1.8$.

Figure 6.6 illustrates the effect of the Reynols number on the propeller thrust coefficient. BEMT

and experimental data are compared. The wind-tunnel test shows that thrust values increase with rising Reynolds number. This is also predicted by the BEMT and is caused by the fact that, since at a higher Reynolds number the boundary layer is thinner, there is more concentrated momentum near the airfoil surface. This causes lift enhancement and therefore results in increased thrust. Notably, at a higher Reynolds number the C_T-J curve slope is higher. Furthemore, as the results at higher Reynolds number are also at higher Mach number, compressibility effects also play a role in loading enhancement.

The lower slope of the BEMT predictions compared to the experimental data is due, as explained earlier, to the different boundary layer conditions, predominantly laminar in the wind-tunnel test and turbulent in the two-dimensional airfoil analysis whose polars are provided to the BEMT. On the other hand, as previously mentioned, the offset in values can be atttributed to the presence of interference drag in the wind tunnel results. The turbulent flow causes a shift in the airfoil lift-curve and a reduction in the slope of the same due to the reduced effective camber of the airfoil, thus causing an offset and a reduction in the slope of the C_T-J curve.

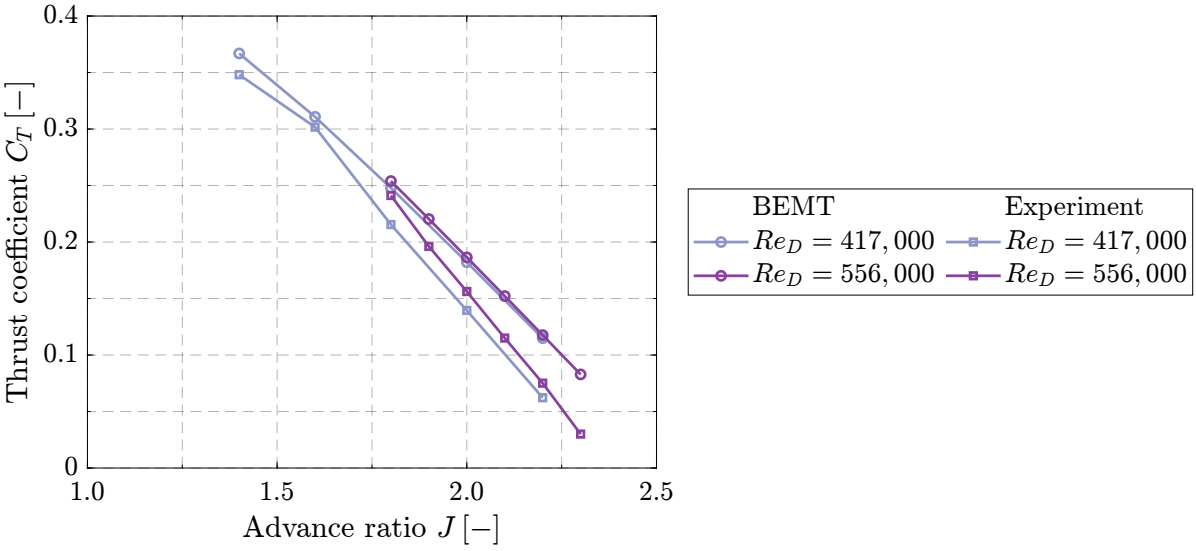

Figure 6.6: Reynolds number effect on propeller thrust coefficient.

While validating integral performance is fundamental, it does not provide a comprehensive assessment of propeller performance. To thoroughly evaluate the propeller, it is essential to analyze the radial distribution of aerodynamic performance metrics along the blade. This is particularly important because the propeller's tonal noise characteristics are highly sensitive to local blade loading. Even if the overall thrust predicted by BEMT aligns with validation data, discrepancies in sectional performance can lead to significant issues. For instance, if the inboard sections of the blade are underpredicted while the outboard sections are overpredicted, these errors might balance out in the integral thrust calculation, providing a misleading sense of accuracy. However, this uneven distribution of aerodynamic forces does not lead to a cancellation of tonal noise; instead, it significantly alters the noise characteristics since the outboard sections, which are the most loaded and rotate at higher Ωr, are the primary contributors to noise emissions.

A comparison of the sectional thrust and power coefficients radial distributions between BEMT and CFD is provided in Figure 6.7 and Figure 6.8. The comparison is made at different advance ratios: two within the design operating range of the propeller ($J = 1.6$ and 1.8), and two representing outlying conditions ($J = 1.1$ for very low and $J = 2.3$ for very high advance ratios). Including these peripheral values in the comparison is beneficial for a comprehensive assessment of BEMT performance, since the performance maps needed for the non-uniform inflow method cover a wide range of advance

ratios. For ease of interpretation, the x-axis range is kept consistent across all operating conditions.

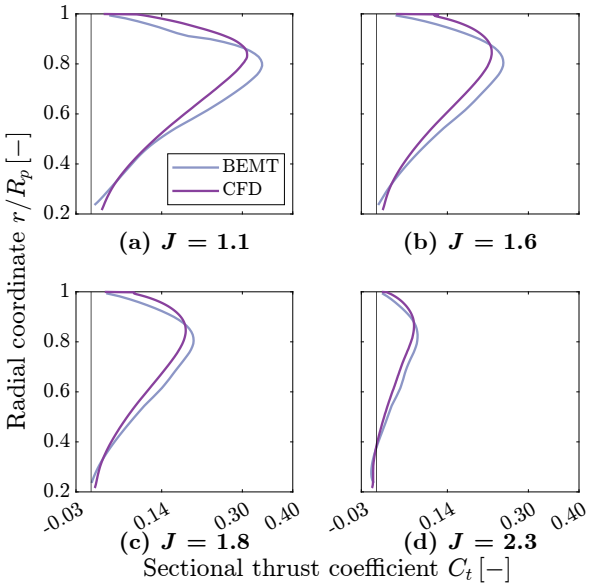

Figure 6.7: Sectional thrust coefficient distribution at various advance ratios.

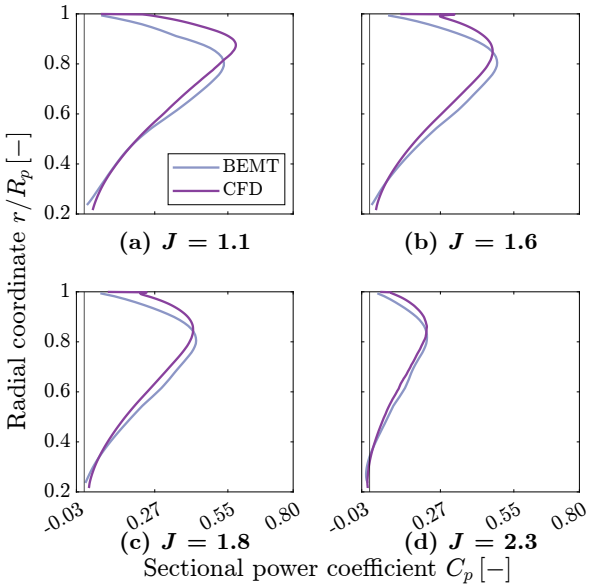

Figure 6.8: Sectional power coefficient distribution at various advance ratios.

Overall, it can be observed that the BEMT effectively captures the radial trends predicted by CFD, with the maximum loading occurring in the outboard portion of the blade. The reduced performance in the root and tip regions is attributed to, respectively, the lower local effective velocity and root vortex effects and the tip vortex. Vortices are complex three-dimensional flow features that CFD can capture unlike BEMT, and they lead to a lift deficit. In the case of BEMT, the Prandtl loss corrections simulate the gradual lift reduction near the hub and tip. Despite their simplicity, Prandtl corrections, when applied with adequate resolution, provide a reasonable approximation of the lift loss resulting from the aforementioned vortices.

For the two operating conditions in the nominal range, the BEMT provides a good representation of both thrust and power distributions. As for the offsets, there is a slight overprediction in the range $r/R_p = 0.45$ to approximately 0.85, attributed to the drag underestimation arising from underestimated viscous effects, and an underprediction beyond $r/R_p = 0.85$, likely resulting from inaccuracies of the Prandtl tip loss correction. A slightly worse performance compared to CFD is observed close to the hub. This highlights the limitations of Prandtl hub and tip loss models. Additionally, BEMT predicts the highest-loaded radial station to be around $r/R_p = 0.8$, whereas CFD estimates it to be approximately $r/R_p = 0.84$. Overall, the trends are predicted with a satisfactory level of accuracy.

More significant deviations occur at $J = 1.1$, where three-dimensional flow effects become more dominant. As mentioned, vortex phenomena are not captured by the BEMT. At this lower advance ratio, the blade experiences higher angles of attack, which significantly impacts the flow characteristics over the blade surface. Notably, the BEMT tends to overpredict the thrust coefficient more significantly in the mid-span region compared to the power coefficient. Conversely, larger underestimations are observed in the outboard sections for the power coefficient than for the thrust coefficient. These discrepancies are attributed to the influence of three-dimensional flow effects and the limitations of the BEMT aerodynamic predictions at elevated angles of attack. Although the mid-span overprediction and the outboard-span underprediction of sectional thrust by the BEMT offset each other resulting in a comparable integral thrust coefficient (see Figures 6.5a and 6.7a), the underestimation of the outboard power coefficient by BEMT, which is more significant than the slight mid-span overestimation, leads to a reduced integral power coefficient (see Figures 6.5b and

6.8a). While CFD analyses could provide valuable insights into the flow behavior across various radial sections of the blade and help quantify the uncertainties in BEMT predictions, this is beyond the scope of this study.

At $J = 2.3$, viscous effects become increasingly significant due to the lower Reynolds numbers associated with high advance ratios. The BEMT does not inherently account for these viscous effects. However, even with slight overpredictions in the mid-span region, the thrust and power coefficients are reasonably well-modeled.

As discussed in Section 4.3 the engineering method to predict the propeller aerodynamic performance in non-uniform flow requires the blade loading distributions in uninstalled condition, i.e. the so-called performance maps. These were obtained using the BEMT for this work and a comparison with the performance maps obtained by Van Arnhem et al. [21] by means of CFD simulations is provided in Figures 6.9, 6.10 and 6.11. Figure 6.9 presents the normalized thrust coefficient radial distribution with varying advance ratio at $V = 40\,\text{m/s}$. The CFD-obtained distribution is displayed on the left, while the one computed with the BEM code on the right. For the nominal operating range of the propeller ($J = 1.4$ to $J = 2$) both the BEMT and the CFD performance maps indicate that the shape of such loading distribution is approximately constant. Furthermore, both the maps feature a maximum loading region around $r/R_p = 0.8$ to 0.9. Notably, the loading distribution computed by means of the BEM code shows an excellent agreement with the CFD one. It is highlighted that especially the gradients in the performance map with respect to the advance ratio are important, as they are used to predict the installation effects on the baseline loading, as previously discussed. Figure 6.10 portrays the sectional disk loading distribution with varying advance ratio at $V = 40\,\text{m/s}$. A good agreement is found in this case as well, with a slight offset in the contours of the BEMT map with respect to the CFD one at the lowest advance ratios due to the non-linear effects which characterize that operating range. Finally, Figure 6.11 displays the the sectional disk loading distribution with varying advance ratio at $n = 109.4\,\text{Hz}$. The two performance maps display a satisfactory concordance in this case as well, with just a slight offset in the contours of the BEMT map with respect to the CFD one at the lowest advance ratio caused by, once again, the non-linear effects arising in that operating range.

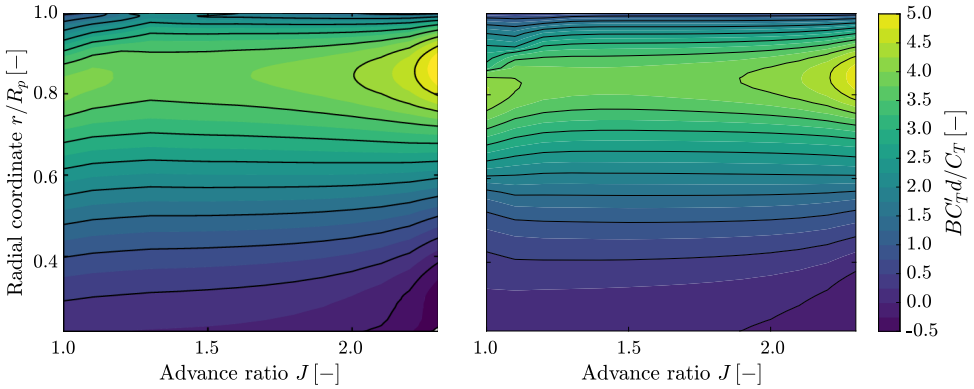

Figure 6.9: Normalized thrust coefficient distribution obtained with CFD simulations by Van Arnhem et al. [21] (left) and with the BEM code (right); $V = 40\,\text{m/s}$.

6.2. AERODYNAMIC MODEL FOR NON-UNIFORM FLOW

The engineering method to predict the aerodynamic performance of a propeller in an arbitrary non-uniform flow is hereby validated. While Van Arnhem et al. [21] obtained the performance maps needed as inputs to the method by means of CFD simulations, this work makes use of a BEM model to obtain the performance maps. It is therefore necessary to validate the results obtained with a fully

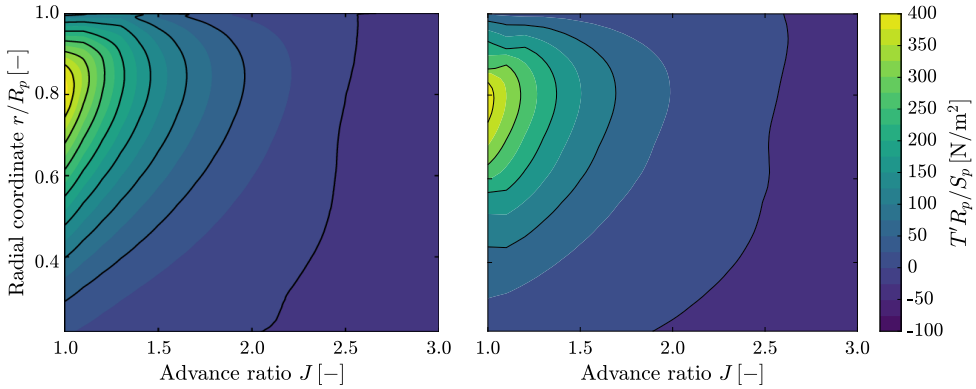

Figure 6.10: Sectional disk loading distribution obtained with CFD simulations by Van Arnhem et al. [21] (left) and with the BEM code (right); $V = 40\,\mathrm{m/s}$.

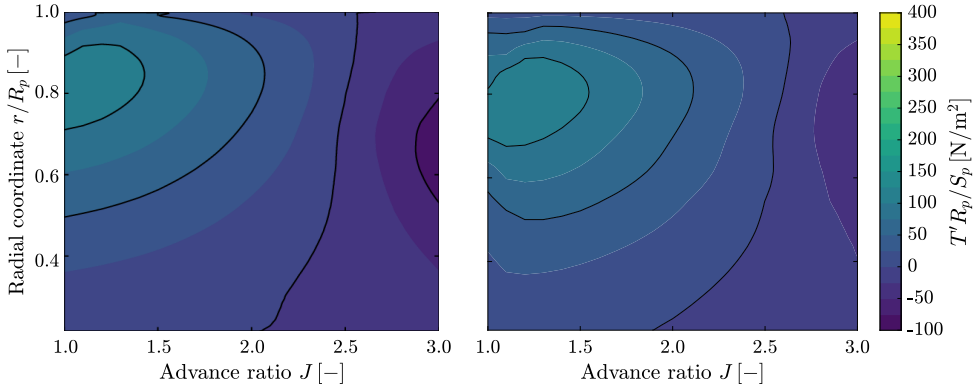

Figure 6.11: Sectional disk loading distribution obtained with CFD simulations by Van Arnhem et al. [21] (left) and with the BEM code (right); $n = 109.4\,\mathrm{Hz}$.

low-fidelity approach.

Figure 6.12 shows the change in the advance ratio for the XPROP-S due to a non-zero angle of attack (case 1) and a wake encounter (case 2) with respect to uniform inflow. As said, these two typical non-uniform flow conditions are the ones selected for the analyses performed in this work. The time step of the analysis used here and for the rest of the aerodynamic performance predictions in this work is 2° of propeller rotation.

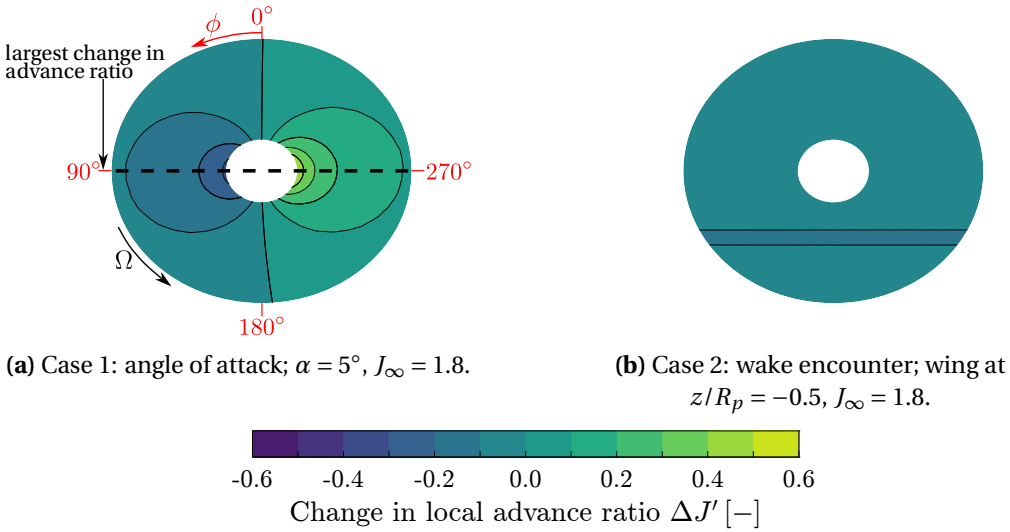

(a) Case 1: angle of attack; $\alpha = 5°$, $J_\infty = 1.8$.

(b) Case 2: wake encounter; wing at $z/R_p = -0.5$, $J_\infty = 1.8$.

Figure 6.12: Change in local advance ratio with respect to uniform inflow condition.

Figure 6.12a pertains to the angle of attack scenario, specifically $\alpha = 5°$ at $J_\infty = 1.8$. The advance ratio variation trend features a reduction on the advancing side due to an increased in-plane velocity and an increase on the retreating side due to a diminished in-plane velocity. The largest negative and positive changes in advance ratio occur at $\phi = 90°$ and $\phi = 270°$, respectively. The change in the advance ratio is the largest near the hub region due to the low Ωr, which causes the originally low local tangential velocity to vary greatly. The largest positive and negative changes in the local advance ratio are 28% and 18% of the free-stream value, respectively.

Figure 6.12b pertains to the wake encounter case. The inflow profile was generated by placing a straight, untapered, and untwisted wing wing whose trailing edge was placed at an axial location $3.2R_p$ upstream of the propeller and at the vertical location $z/R_p = -0.5$ (according to the reference frame defined in Figure 4.1a). The propeller operates at $J_\infty = 1.8$. The viscous wake of the wing causes an axial velocity deficit at the propeller disk, which results in a reduction in the advance ratio confined to a specific part of the disk up to 10% of the free-stream value.

Figure 6.13 validates the change in local thrust coefficient resulting from the change in local advance ratio shown in Figure 6.12 retrieved by employing a full-blade CFD approach (left) and by the CFD-based method (center) with the one estimated by feeding the BEMT-computed performance maps as inputs to the method (right). Figure 6.13a pertains to the $\alpha = 5°$ case. The wholly low-fidelity approach features the expected thrust coefficient trend, with an increase on the advancing side (where the advance ratio reduces) and a decrease on the retreating side. The BEMT-based analysis predicts the largest change in loading due to the flow unsteadiness to occur with a phase delay of approximately $\Delta\phi = 12°$, compared to $\Delta\phi = 15°$ of the full-blade CFD simulation. The change in loading shows a good agreement with the full-blade simulation data near the hub. Overall, although the trend is well estimated, the change in loading over the disk is underpredicted in the outboard part of the blade. Being this region the most loaded in uniform inflow condition, as expected, the change in loading is the highest. The underestimated variation magnitude is due to the changes in induction

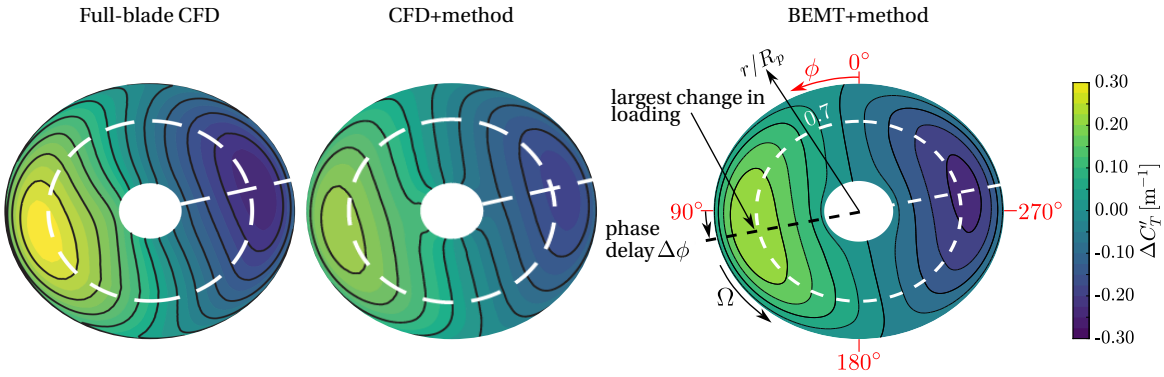

(a) Case 1: angle of attack; $\alpha = 5°$, $J = 1.8$.

(b) Case 2: wake encounter; wing at $z/R_p = -0.5$, $J = 1.8$.

Figure 6.13: Change in local thrust coefficient with respect to uniform inflow condition computed with a full-blade CFD simulation by Van Arnhem et al. [21] (left), CFD+method (center) and with BEMT+method (right).

not being accounted for properly. In fact, the method assumes that the whole propeller disk is subject to the same local change in the induced velocity field, while in reality that varies. On the other hand, the full-blade CFD simulation correctly accounts for the flow field induced by the non-uniform propeller slipstream. This slipstream causes an increase in the blade forces, thus explaining the larger loading variation in the outboard part of the blade computed by CFD. This underprediction is also evident in the CFD+method predictions, to which the BEMT-based computations are then closer. This underestimation of loading is likely to influence the amplitude of noise emissions. However, since the overall trend is well captured, the directivity is expected to be properly represented. Given that the focus of this work is on trends rather than precise amplitude predictions, this is considered acceptable.

Figure 6.13b illustrates the change in local thrust coefficient due to a wake caused by an upstream wing at $z/R_p = -0.5$. Despite a slight offset caused by imperfect slipstream modeling, the overall trend is fairly well captured. Two regions of heightened sensitivity can be identified due to the fact that the most heavily loaded part of the blade is the most responsive to changes in advance ratio [21].

Figure 6.14 illustrates the azimuthal (left) and radial (right) variation of the local thrust coefficient compared to the uniform inflow condition. Figure 6.14a pertains to the angle of attack case. The azimuthal variation is plotted at the radial location $r/R_p = 0.7$. The nearly sinusoidal behavior of the loading is effectively predicted by the method. However, due to the non-uniform slipstream modeling being not fully accurate as discussed above, the absolute magnitude of the variation is underpredicted by the BEMT-based approach. This is especially evident near the azimuthal angles of largest change in loading. A curve representing the results obtained by using the CFD-computed performance maps as input to the method is also shown, revealing a larger offset from the full-blade CFD data with respect to the BEMT-based approach. The radial variation of the local thrust coefficient compared to the uniform inflow condition is plotted at the azimuthal location $\phi = 270°$, marked with a white-dashed line in Figure 6.13a. An offset with respect to the validation data is present. This discrepancy is smaller for the CFD-based method in radial regions where r/R_p is less than 0.35 and greater than 0.85. Conversely, within the range $0.35 \leq r/R_p \leq 0.85$, the BEMT-based method shows a smaller offset in values. The different trend and offset between the BEMT+method and CFD+method predictions can be explained by looking at Figure 6.7. As the BEM overpredicts the sectional loading in the mid-to-outboard span region of the blade, the variation in local thrust coefficient is also larger locally. On the other hand, as BEMT predicts a worse performance close to the hub and the tip compared to CFD, the local thrust change is also smaller.

Figure 6.14b refers to the wake encounter case. The azimuthal variation is plotted at the radial location $r/R_p = 0.85$. Two distinct peaks are noticeable. They are due to, as said, to the increase sensitivity to a change in advance ratio of the most loaded blade region, particularly relevant at this wing location. Both the phase and the magnitude of the BEMT-based method peaks are reasonably close to the full-blade CFD simulations, albeit a more prominent deviation in magnitude for the first peak. The radial variation of the local thrust coefficient compared to the uniform inflow condition is plotted at the azimuthal location $\phi = 125°$, marked with a white-dashed line in Figure 6.13b. Although a slight peak magnitude overestimation and phase shift are present, good agreement is found.

Figure 6.15 shows the azimuthal variation of the blade thrust coefficient. Figure 6.15a pertains to the angle of attack case. A deviation with respect to the validation data exists due to the inaccuracies in non-uniform slipstream modeling. The BEMT-based approach underpredicts the root mean square of the blade thrust variation with respect to full-blade simulations by 5.1 and 18.6% respectively, while the method coupled with CFD underpredicts it by 24.6%. These figures highlight the impact of slipstream modeling inaccuracies on the reliability of the predictions.

Figure 6.15b refers to the wake encounter case. Overall, the low-fidelity predictions are in reasonable agreement with higher-fidelity simulations.

Table 6.3 presents a comparison of the change in integral propeller forces for the two non-uniform

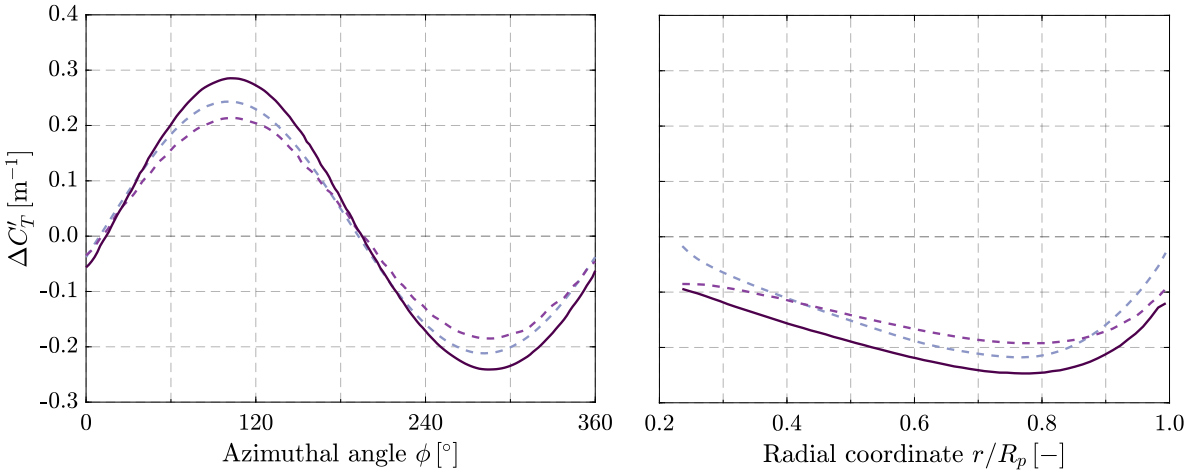

(a) Case 1: angle of attack; $\alpha = 5°$, $J = 1.8$. Azimuthal variation plotted at $r/R_p = 0.7$; radial variation plotted at $\phi = 270°$.

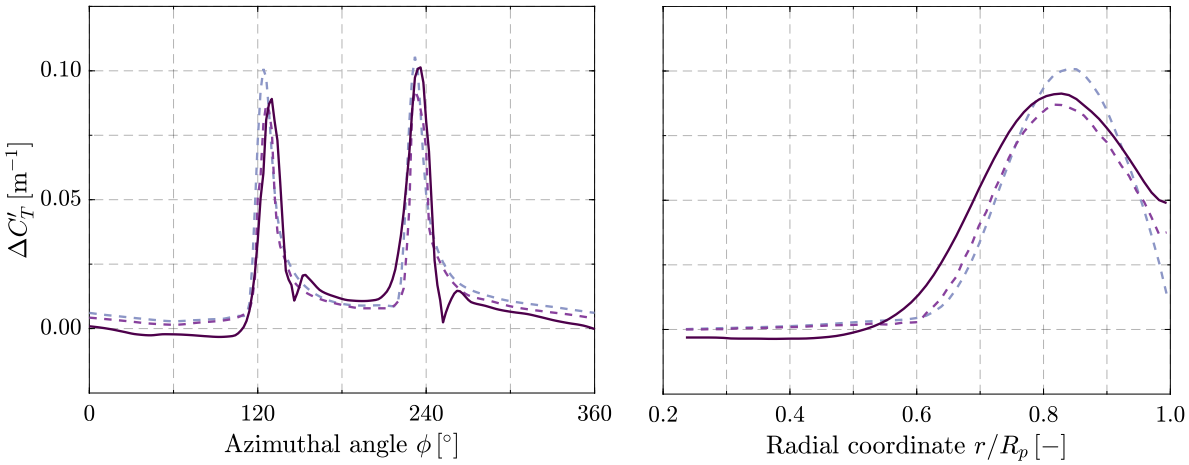

(b) Case 2: wake encounter; wing at $z/R_p = -0.5$, $J = 1.8$. Azimuthal variation plotted at $r/R_p = 0.85$; radial variation plotted at $\phi = 125°$.

Figure 6.14: Variation of local thrust coefficient over propeller azimuthal angle (a) and blade radial coordinate (b) with respect to uniform inflow condition.

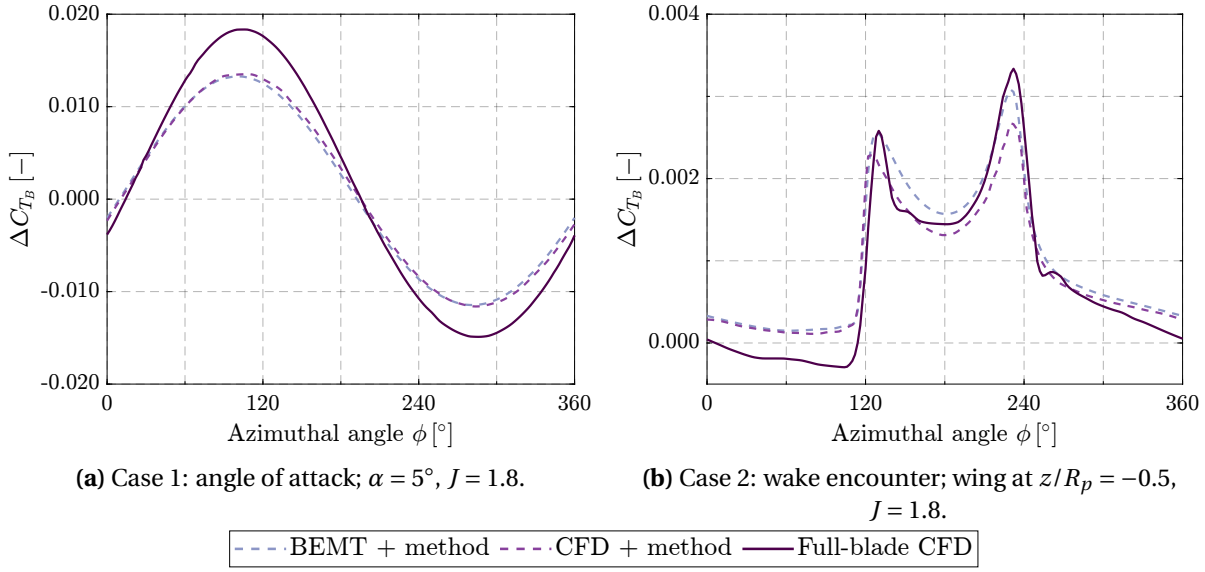

(a) Case 1: angle of attack; $\alpha = 5°$, $J = 1.8$.

(b) Case 2: wake encounter; wing at $z/R_p = -0.5$, $J = 1.8$.

Figure 6.15: Variation of blade thrust coefficient over propeller azimuthal angle with respect to uniform inflow condition.

inflow cases analyzed relative to the uniform inflow condition. The comparison is expressed as the percentage difference between the performance metrics obtained using the BEMT+method approach and those calculated using higher-fidelity approaches, namely CFD+method and full-blade CFD.

Angle of attack, $\alpha = 5°$					
Metric	BEMT+method, uns.	CFD+method, uns.	Full-blade CFD	$\Delta\%_{\text{CFD+method}}$	$\Delta\%_{\text{Full-blade CFD}}$
ΔC_T	3.703×10^{-3}	4.167×10^{-3}	5.167×10^{-3}	−11.14%	−28.33%
ΔC_Q	4.519×10^{-4}	5.000×10^{-4}	5.000×10^{-4}	−9.62%	−9.62%
Wake encounter, $z/R_p = -0.5$					
Metric	BEMT+method, uns.	CFD+method, uns.	Full-blade CFD	$\Delta\%_{\text{CFD+method}}$	$\Delta\%_{\text{Full-blade CFD}}$
ΔC_T	6.029×10^{-3}	5.262×10^{-3}	4.717×10^{-3}	14.58%	27.81%
ΔC_Q	1.240×10^{-3}	1.117×10^{-3}	1.262×10^{-3}	11.01%	−1.74%

Table 6.3: Comparison of the change in integral propeller forces between low and high(er)-fidelity approaches.

In the case of the angle of attack, both the changes in thrust and torque coefficients are under-predicted by BEMT+method compared to the CFD-based methods. The lower predicted values, as compared to the full-blade CFD approach, can be attributed to the previously discussed inaccuracies in modeling the non-uniform slipstream, as also suggested by the underpredicted change in thrust of the CFD+method approach compared to the full-blade CFD one. However, it is important to interpret the percentage differences with caution, as the values used in the computation are on the order of 10^{-3} to 10^{-4}, being the change in integral propeller performance minor.

In the wake encounter case, the thrust coefficient predicted by BEMT+method is higher than that of the CFD-based methods, which aligns with the overpredictions shown in Figure 6.15b. How-

ever, the variation in the torque coefficient is closer to the full-blade CFD value, exhibiting only a slight underprediction, compared to the CFD+method. This behavior is attributed to the inherent uncertainties in the low-fidelity approach, rather than indicating a sudden improvement in its performance.

6.3. HANSON'S TIME-DOMAIN THEORY

The numerical data required for validating the low-fidelity aeroacoustic code, which is grounded in Hanson's near-field theory, were obtained from the results of Zarri et al. [44] for the isolated XPROP-S propeller in uniform inflow. Such numerical data were retrieved by means of simulations that employed a Lattice-Boltzmann Method (LBM) combined with a Very Large Eddy Simulation (VLES) approach for modeling turbulence. For this purpose, SIMULIA PowerFLOW®was utilised. This hybrid method was integrated with SIMULIA PowerACOUSTICS®, an acoustic solver that utilises Farassat's 1A formulation of the FWH equation, allowing for the prediction of both broadband noise and tonal components due to thickness and loading effects. The essential geometrical and operational parameters for validating the aeroacoustic model are provided in Table 6.16a. Figure 6.16b shows the reference frame employed in the aeroacoustic code. The rotation direction of the propeller is anti-clockwise if seen from the front. For the purposes of this validation and throughout this work, the observers are positioned in the far field, at a distance of 10 diameters from the center of the reference frame.

It should be noted that the high-fidelity data feature a chordwise loading distribution characterised by a peak near the leading edge due to a zig-zag trip located at 10% of the chord length. The low-fidelity method features a similar distribution. The implications of potential differences in the chordwise loading distribution on the noise signature will be discussed later. Meanwhile, the thickness distribution used accurately reflects the real one, as the blade STL files were available for this study.

Prior to performing the validation, it is essential to assess the sensitivity of the model to the number of time steps per period. As discussed in Chapter 5, the implemented theory relies on a time-domain approach, making the number of time steps per period a crucial parameter. This sensitivity analysis is presented in Figure 6.17 for observers located in the xz-plane. Figure 6.17a present the directivity of the SPL at the first BPF. As in the uniform inflow case the polar noise directivity is symmetric around the propeller axis, only the observers located at the axial angles $0° \leq \theta \leq 180°$ have been considered, with $\theta = 0°$ located along the propeller axis in front of the propeller. The results show some deviation near the propeller axis when using fewer than 200 time steps. However, at 200 time steps, the noise levels are nearly indistinguishable from those obtained with higher resolutions. It is important to note that near the propeller axis, the values of p'_{RMS} are lower, resulting in reduced noise levels. This indicates that numerical fluctuations, while minor compared to acoustic pressure fluctuations, could have a more significant local impact, complicating convergence. To gain further insight on the p'_{RMS}, Figure 6.17b shows the sensitivity of the maximum (computed across observers in the range $0° \leq \theta \leq 180°$) root mean square of the acoustic pressure fluctuations related to the far-field first BPF SPL to the number of time steps per period and the corresponding code execution time per observer. This sensitivity study focuses on the SPL rather than the OSPL, as the validation data available from Zarri et al. [44] pertains specifically to the SPL at the first BPF. The maximum number of time steps is constrained by the 24-hour computational time limit set by the Delft High Performance Computing Centre (DHPC) for student accounts [45]. As N_t increases, the maximum p'_{RMS} also rises and approaches convergence. Meanwhile, Figure 6.17c illustrates the relative difference between the maximum p'_{RMS} values obtained with various amounts of time steps and that computed with the finest time resolution defined as:

$$\epsilon_{p'_{RMS}} = \frac{p'_{RMS} - p'_{RMS,max\,N_t}}{p'_{RMS,max\,N_t}} \tag{6.2}$$

Parameter	Value	Unit
Propeller diameter - D	0.2032	m
Hub-to-tip ratio - R_{hub}/R_p	0.23	–
Blade pitch at $r/R_p = 0.7$	30	°
Number of blades - N_B	6	–
Free-stream static pressure - p_∞	101330	Pa
Free-stream static temperature - T_∞	288.15	K
Free-stream Mach number - M_∞	0.088	–
Helical tip Mach number - M_{ht}	0.357	–
Advance ratio - J	0.8	–
Maximum chord-based Reynolds number - max Re_c	1.07×10^5	–

(a) Geometrical parameters and operating conditions.

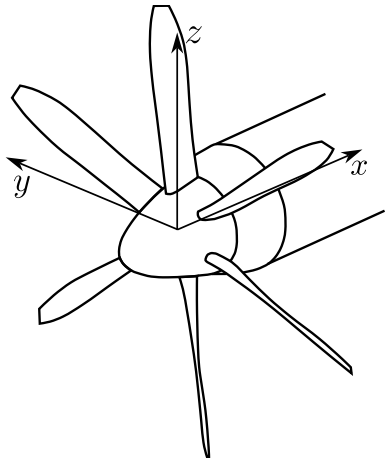

(b) Aeroacoustic code reference frame.

Figure 6.16: Key parameters for validating the aeroacoustic model with [44] (a) and acoustic code reference frame (b).

A threshold of 0.1% relative difference was set to determine an appropriate number of time steps per period. According to Figure 6.17c, 500 time steps fulfill the accuracy requirement on the p'_{RMS}. Figure 6.17d presents the relative difference in p'_{RMS} computed at all the axial directivity angles. The plot only considers the observer locations where p'_{RMS} is greater than the reference acoustic pressure for all the time steps. Since the p'_{RMS} values and the corresponding noise levels are lower for the observer angles close to the propeller axis, the relative difference threshold of 0.1% appears to be too strict. Therefore, for angles in that region, here and for the rest of this work a relative difference in the order of 10^{-3} (not necessarily lower than that) is deemed acceptable. According to the computations, using 500 time steps satisfies the strict threshold requirement even at $\theta = 30°$ and $\theta = 150°$, thus making it the chosen time resolution.

To ensure accurate sampling and prevent aliasing in the acoustic analysis, the Nyquist criterion is applied. Aliasing is the misrepresentation of high-frequency content as lower frequencies due to insufficient sampling. This criterion requires that the sampling frequency, F_s, be at least twice the maximum frequency of interest [46]. In this case, the propeller BPF is 1107.28 Hz, which represents the highest frequency of interest for the analysis conducted in this specific validation case, as it only focuses on the first BPF. With a sampling frequency of $F_s = 92263.37$ Hz, the Nyquist limit is $F_s/2 = 46131.69$ Hz, which is more than sufficient to accurately capture the BPF signal. Therefore, with the chosen time resolution, the Nyquist criterion is respected, ensuring that the sampled data represent the acoustic signal faithfully with no risk of aliasing at the BPF.

Figure 6.18 compares the first BPF SPL directivity between the low-fidelity approach (BEMT coupled with Hanson's near-field theory) and the high-fidelity data (LBM/VLES coupled with Farassat's 1A formulation). In agreement with expectations, the obtained noise directivity is symmetric around the propeller axis. As for the xz-plane directivity, depicted on the left plot, satisfactory agreement is found for $30° \leq \theta \leq 150°$, with underpredictions of less than 3.3 dB for all observer angles except for $\theta = 30°$, where the deviation is 9.5 dB. The greater mismatch at this location can be attributed to the absence of broadband noise in the low-fidelity model, leading to zero predicted noise near the propeller axis. As a result, the noise levels and directivity close to the propeller axis differs significantly from the high-fidelity data that instead account for broadband noise, which is known to dominate in those regions.

As for the xy-plane directivity, represented on the right, the low-fidelity code shows reasonable agreement with the validation data for $30° \leq \psi \leq 150°$, with underpredictions below 3.9 dB for all observer angles, except for $\psi = 30°$, where the deviation is just below 7 dB. Deviations near the propeller axis are due, as said, to the broadband noise not being captured by the low-fidelity code. Overall, for an observer in the propeller plane (i.e., where tonal noise dominates) at $\psi = 90°$, a promising difference of below 2 dB is observed.

What needs further discussion is the fact that the predicted noise levels are lower than those of the validation case, despite the latter having a lower propeller thrust - 18.05 N compared to 20.16 N, a difference of about 12% - than the BEM model. The lower thrust predicted by the high-fidelity method is due to the implementation of a leading-edge transition trip, which forces the turbulent boundary layer to develop and enables the VLES to shift from a modeled-scale to a resolved-scale approach. The primary purpose of the trip is therefore not to mitigate flow separation but to enhance the accuracy of flow physics representation in the simulation. Consequently, the lift does not benefit from the transition, while the increased skin friction drag leads to a reduction in thrust. A possible explanation for lower noise levels despite a higher integral loading is that the BEM model may not accurately predict the location of the most highly loaded radial section and underestimate the outboard loading. While this cannot be confirmed due to the absence of CFD data on sectional loading, Figure 6.7 suggests that BEM may predict the highest loaded section slightly more inboard than CFD. The highly-loaded fast-rotating outboard sections are more efficient in radiating noise. Even slight deviations in loading at the outboard sections can impact the noise levels considerably.

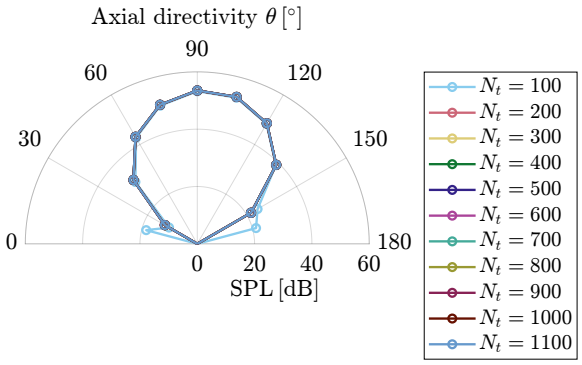

(a) First BPF SPL directivity with varying amount of time steps.

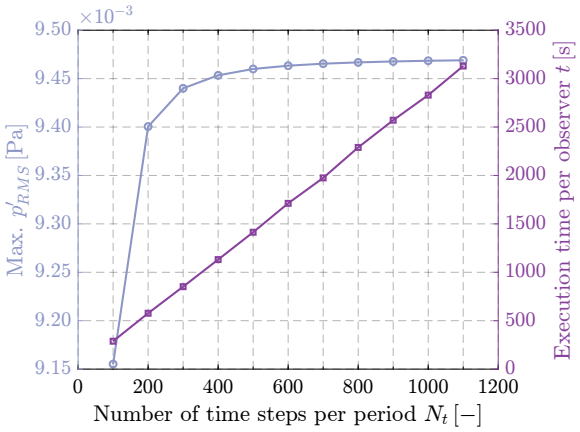

(b) Maximum p'_{RMS} and execution time per observer versus number of time steps.

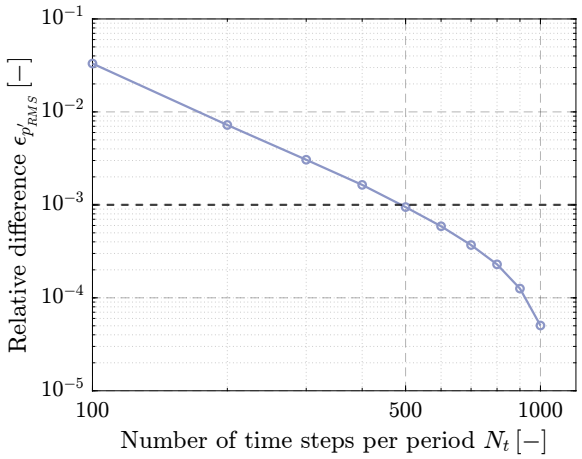

(c) p'_{RMS} relative difference versus number of time steps.

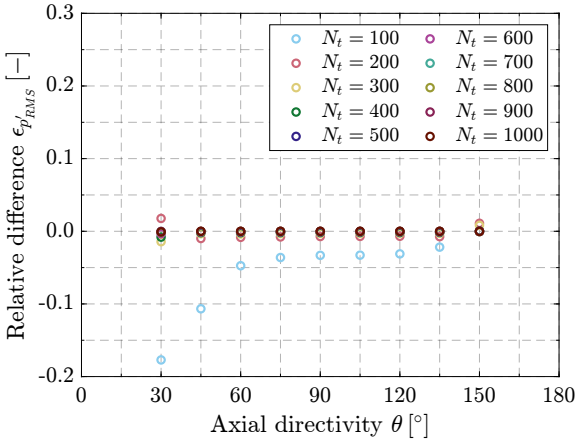

(d) p'_{RMS} relative difference with respect to the finest time resolution.

Figure 6.17: p'_{RMS} and first BPF SPL sensitivity to number of time steps per period; uniform inflow.

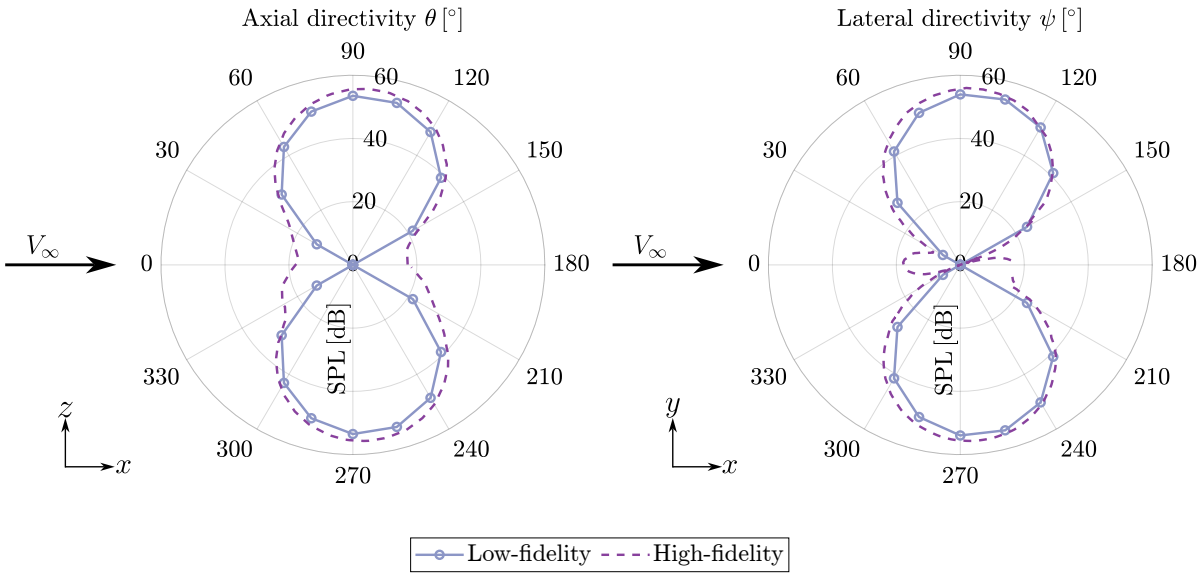

Figure 6.18: Comparison of first BPF SPL between low-fidelity acoustic code and high-fidelity simulations in the xz-plane (left) and xy-plane (right); uniform inflow.

Lower noise levels may result even if the inboard radial sections are more loaded than the validation data, as this does not offset the effect of higher loading at the rapidly rotating outboard sections. This highlights the importance of accurately predicting the radial loading distribution, as integral propeller thrust alone is not fully indicative of aeroacoustic emissions.

Another potential reason for the discrepancies is the difference in chordwise loading distribution between the low-fidelity and high-fidelity models. As previously mentioned, the validation data exhibit a peaky loading distribution, with the peak occurring near the leading edge due to a zig-zag trip located at 10% from the blade leading edge. Hanson [47] highlighted that the manner in which the load is distributed along the blade chord can influence noise emissions. In particular, uniform loading across the chord tends to produce lower noise levels, as illustrated in Figure 6.19.

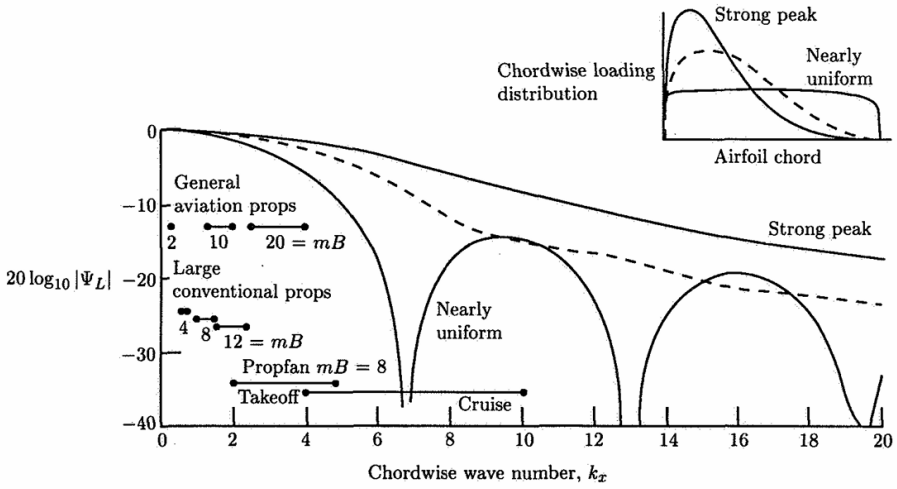

Figure 6.19: Impact of chordwise loading distribution on blade element loading noise [47].

The extent to which uniform chordwise distributions are quieter depends on the acoustic

wavenumber:

$$k_x = \frac{2mN_B B_D M_{rot}}{M_{hr}(1 - M_f \cos\theta)} \tag{6.3}$$

where m is the harmonic of the blade passage frequency, N_B is the number of blades, $B_D = c/D$ is the chord to diameter ratio, $M_{rot} = \Omega R_p / c_0$ is the tip rotational Mach number, M_{hr} is the sectional helical Mach number, M_f is the flight Mach number and θ is the radiation angle from the propeller axis to the observer. k_x dictates the spatial frequency of pressure fluctuations.

For the analyzed propeller geometry and operating conditions, the acoustic wavenumber k_x at $r/R_p = 0.7$ does not exceed 1.4 for the first harmonic m, where the majority of the propeller noise is concentrated. This value remains relatively insensitive to both the radiation angle and the section rotational Mach number, as observed by Hanson [47]. When considering the second harmonic, k_x does not surpass 2.8. Given the relatively low wavenumbers at the most relevant harmonics for propeller noise, as seen in Figure 6.19, the influence of a uniform chordwise loading distribution is expected to be minimal, at least in the uniform inflow case analyzed. However, when blade loading becomes unsteady, noise emissions at higher harmonics may become more significant. The chosen aerodynamic methods are not designed to model the chordwise loading. Assuming a uniform loading over the chord stations can potentially lead to reduced noise levels in case of non-uniform inflow, being the contribution of higher harmonics potentially more relevant than the uniform inflow case. For this reason, in an effort to represent a realistic chordwise loading profile, the loading distribution was suitably weighted. The applied weighting results in a distribution featuring a moderate peak near the blade's leading edge. The pressure difference between the upper and lower surfaces of a given blade is shown at a fixed time in Figure 6.20. The peak near the leading edge is visible and becomes more evident at the outboard radial stations, where the loading is greater.

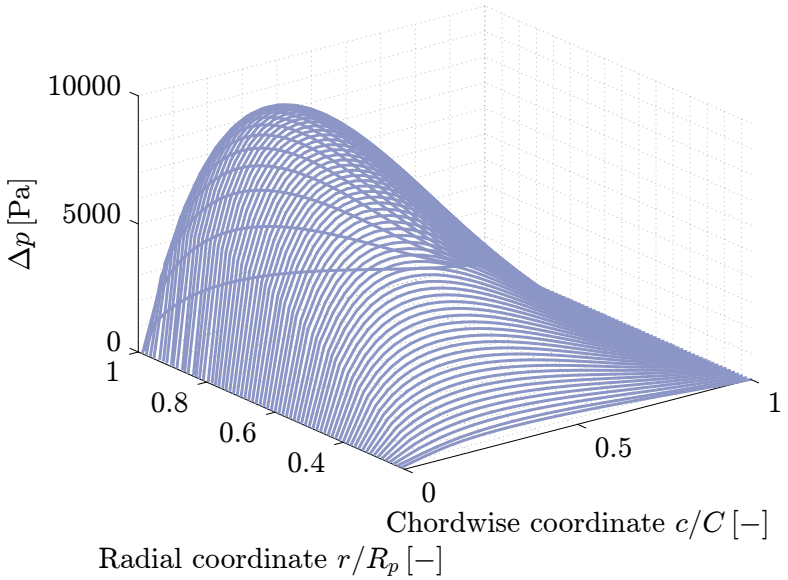

Figure 6.20: Low-fidelity blade pressure distribution; uniform inflow.

Since the validation case is characterized by low wavenumbers, the shape of the chordwise loading distribution has a reduced influence. Consequently, this factor has less significance in explaining the lower noise levels found in the low-fidelity predictions despite the higher propeller thrust. An alternative explanation is the potential destructive interference between thrust and torque noise, leading to an overall reduction in noise levels. However, since torque noise data for the validation case were not available, this remains a plausible but unverified hypothesis.

A qualitative assessment of the polar directivity was then conducted. Directivity patterns are crucial in propeller aeroacoustics, as they describe how noise is distributed in different directions around the propeller, helping to identify loud regions and guide noise reduction. Figure 6.21 illustrates the theoretical noise directivity patterns for propeller noise, focusing on thickness (left), torque (center), and thrust (right) noise along the propeller axis of rotation. The polar directivity

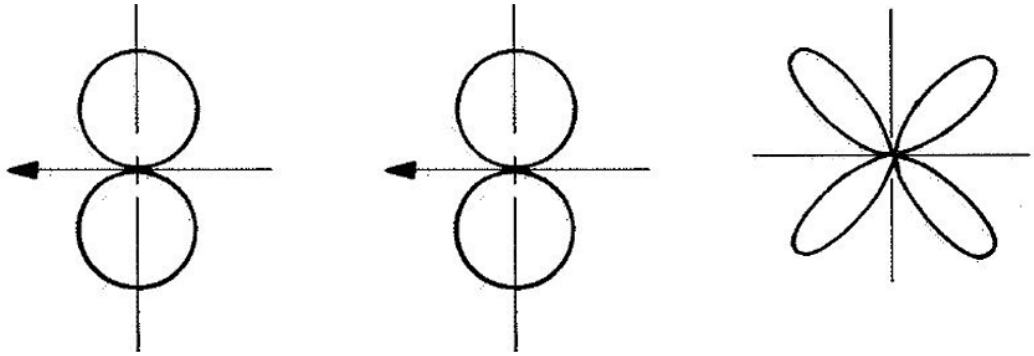

Figure 6.21: Theoretical noise patterns for propeller noise [48]. From left to right: thickness, torque, and thrust noise directivity.

predicted by Hanson's near-field theory in the xz-plane is shown in Figure 6.22. A comparison reveals that the patterns qualitatively correspond with theoretical expectations. Torque and thickness noise are characterized by two-lobed, figure-eight patterns, while thrust noise exhibits a four-lobed pattern, consistent with theoretical predictions. For completeness, loading noise, which includes both thrust and torque noise contributions, is also plotted, revealing a two-lobed emission pattern. Discrepancies between the computed and theoretical patterns arise because, while the theoretical directivities are based on an idealized model, the computed patterns reflect a specific blade geometry and operating conditions.

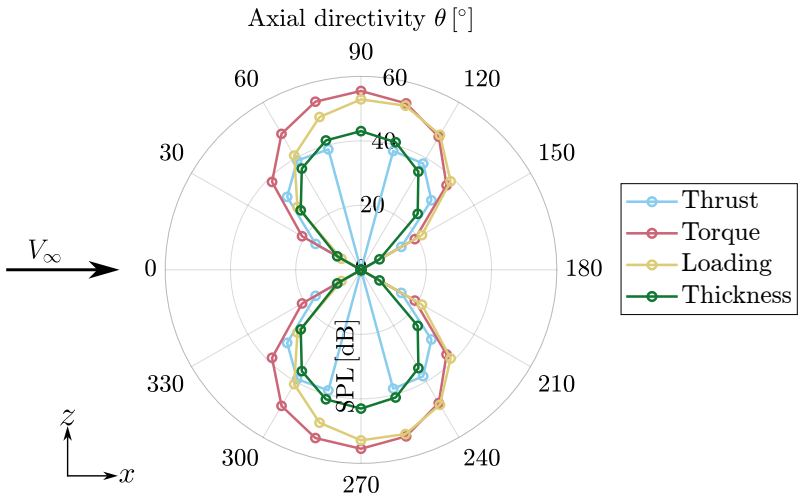

Figure 6.22: Thrust, torque, loading (thrust + torque) and thickness noise directivity; uniform inflow.

In an effort to validate the acoustic solver in a non-uniform inflow case too, comparison were performed against the high-fidelity results obtained by Goyal et al. [8] employing LBM/VLES simulations implemented in SIMULIA PowerFLOW® coupled with the FWH analogy solved based on Farassat's 1A formulation using SIMULIA PowerACOUSTICS®. The key propeller geometrical and operational parameters are listed in Table 6.4. The rotation direction of the propeller is anti-clockwise.

Parameter	Value	Unit
Propeller diameter - D	0.4064	m
Hub-to-tip ratio - R_{hub}/R_p	0.23	–
Blade pitch at $r/R_p = 0.7$	15	°
Number of blades - N_B	3	–
Free-stream static pressure - p_∞	101325	Pa
Free-stream static temperature - T_∞	288.15	K
Free-stream Mach number - M_∞	0.088	–
Helical tip Mach number - M_{ht}	0.470	–
Advance ratio - J	0.60	–
Maximum chord-based Reynolds number at $\alpha = 0°$ - max $Re_{c_{\alpha=0°}}$	2.73×10^5	–
Maximum chord-based Reynolds number at $\alpha = 10°$ - max $Re_{c_{\alpha=10°}}$	2.83×10^5	–

Table 6.4: Key parameters for validating the aeroacoustic model with [8].

The maximum Reynolds number, calculated based on the sectional chord, increases from 2.73×10^5 at $\alpha = 0°$ to 2.83×10^5 at $\alpha = 10°$. This increase is attributed to the higher effective velocity experienced by the downgoing blades at non-zero angles of attack.

Table 6.5 presents a comparison of the integral propeller performance obtained using the low-fidelity aerodynamic models employed in this thesis and the high-fidelity simulations.

	$\alpha = 0°$			$\alpha = 10°$		
	Low-fidelity	High-fidelity	Δ%	Low-fidelity	High-fidelity	Δ%
T_C	0.1169	0.1135	3.00%	0.1244	0.1243	0.08%
P_C	0.1559	0.1645	−5.23%	0.1620	0.1736	−6.68%
η	0.7496	0.6898	8.67%	0.7675	0.7163	7.15%
Y_C	0	0	–	0.0019	0.0043	−55.81%
N_C	0	0	–	0.0055	0.0152	−63.82%

Table 6.5: Comparison of propeller performance metrics between low-fidelity model and CFD simulation at $\alpha = 0°$ and $\alpha = 10°$.

At $\alpha = 0°$, the low-fidelity thrust coefficient is overestimated compared to the high-fidelity result, with a deviation of 3%. The power coefficient, however, shows a larger discrepancy, being underestimated by 5.23%. Consequently, the propeller efficiency is overpredicted by 8.67%. At $\alpha = 10°$, the low-fidelity thrust coefficient closely matches the high-fidelity value, with a deviation of only 0.08%. However, the power coefficient is underestimated by 6.68%, leading to an overestimated efficiency of 7.15%. At non-zero angles of attack, in addition to thrust and torque, two in-plane shaft forces - the side force (Y_C) and the normal force (N_C) - arise due to the different variation in torque between the advancing and retreating sides. The low-fidelity model underpredicts the side-force coefficient by 55.81% and the normal-force coefficient by 63.82%. This significant underprediction is attributed to two factors. First, the CFD inflow data required by Van Arnhem's engineering method is available only for the XPROP-S, while the current analysis focuses on the XPROP. Differences in nacelle design

between the two propellers influence the results. Second, the predicted coefficients are on the order of 10^{-3}, making small deviations appear amplified when expressed as percentages.

Figure 6.23 compares the sectional thrust coefficient variation at at $\alpha = 10°$ with respect to at $\alpha = 0°$ predicted by the high-fidelity simulation (left) with the low-fidelity estimated one (right). Although the distributions are similar, the low-fidelity predictions underestimate the thrust coefficient variation on the retreating side. As for the advancing side, the region of highest loading is more extended compared to the CFD simulation. Additionally, discrepancies are noticeable near the hub, particularly on the retreating side, primarily due to the use of inflow data corresponding to a different nacelle.

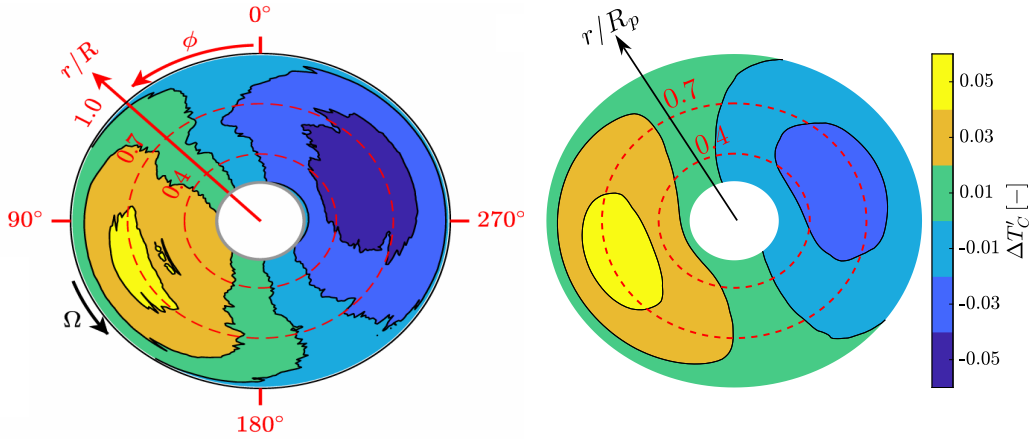

Figure 6.23: Comparison of change in sectional thrust coefficient between CFD simulation (left) and low-fidelity model (right); $\alpha = 10°$.

Figure 6.24 presents the findings from a sensitivity analysis on the OSPL in the xz-plane calculated within the BPF range $0.9 \leq \text{BPF} \leq 10$ with respect to the number of time steps per period. Figure 6.24a shows the OSPL polar directivity for varying amounts of time steps, revealing that the noise levels produced with different time resolutions are nearly indistinguishable. Figure 6.24b illustrates the maximum p'_{RMS} as a function of the number of time steps per period. It is observed that, as N_t increases, the maximum p'_{RMS} also increases and tends towards convergence. Figure 6.24c indicates that using 400 time steps per period allows to stay within the 0.1% threshold for the maximum p'_{RMS}. Lastly, Figure 6.24d demonstrates that 400 time steps per period also guarantee a relative difference in p'_{RMS} on the order of 10^{-3} close to the propeller axis, making it the preferred time resolution.

Finally, some considerations about data sampling are due. In this case, the BPF is 369.09 Hz, and the maximum frequency of interest is 10 BPF = 3690.94 Hz. With a sampling frequency of $F_s = 49205.76$ Hz, the Nyquist limit is $F_s/2 = 24602.88$ Hz, which is well above the maximum frequency of interest. Thus, the Nyquist criterion is respected, ensuring that, with the chosen time resolution, the sampled data accurately captures the relevant acoustic frequencies without aliasing.

Figure 6.27 displays the validation results in the xz-plane at $\alpha = 0°$. The upper section of the figure pertains to the first BPF SPL calculated within the BPF range $0.9 \leq \text{BPF} \leq 1.1$, while the lower section relates to the OSPL computed over the BPF range $0.9 \leq \text{BPF} \leq 10$. Figure 6.25a depicts the first BPF SPL associated with loading noise. Excellent agreement is observed for observer angles within the range $195° \leq \theta \leq 330°$, with underpredictions remaining below 2 dB. At the rotor plane, deviations are even smaller, staying under 1 dB. However, at the propeller axis, the low-fidelity solver predicts null noise emissions, in contrast to the high-fidelity method. This discrepancy arises because the high-fidelity solver accounts for broadband noise, while the low-fidelity aeroacoustic code considers only tonal noise. Since tonal sources predominantly radiate in the propeller plane and do not contribute along the propeller axis, the low-fidelity solver performs as expected. The

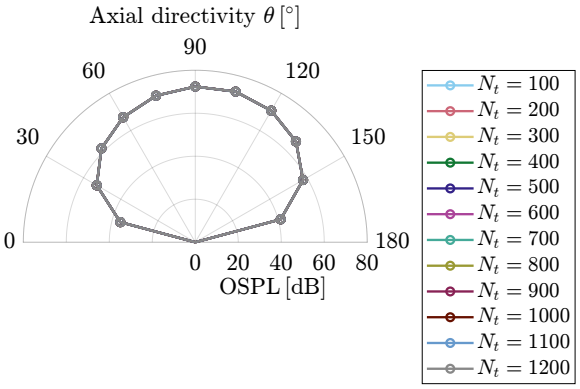

(a) OSPL directivity with varying amount of time steps.

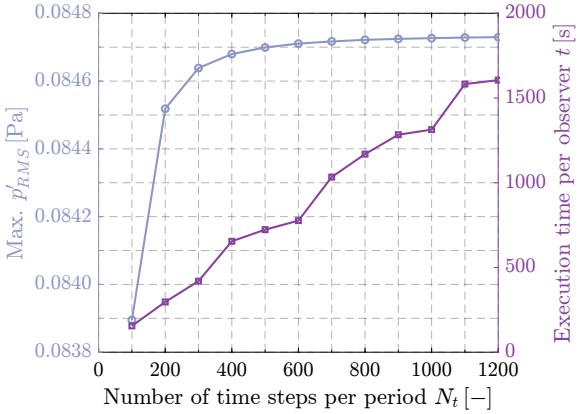

(b) Maximum p'_{RMS} and execution time per observer versus number of time steps.

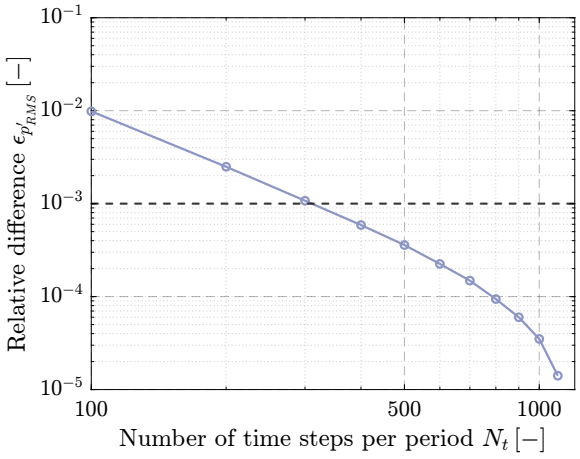

(c) p'_{RMS} relative difference versus number of time steps.

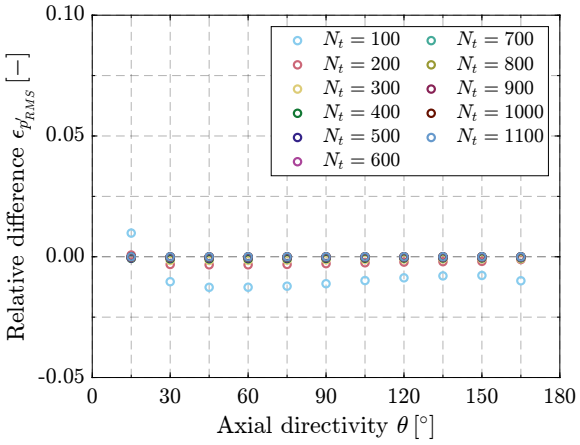

(d) p'_{RMS} relative difference with respect to the finest time resolution.

Figure 6.24: p'_{RMS} and OSPL sensitivity to number of time steps per period; $\alpha = 0°$.

larger discrepancy observed for observers along the propeller axis in front of the propeller, compared to those behind it, is due to the broadband noise in the frequency range $0.9 \leq \text{BPF} \leq 1.1$ primarily propagating forward. In contrast, thickness noise is entirely tonal, resulting in a close match between the low- and high-fidelity results across all observer angles. This is evident in Figure 6.25b, where the maximum deviation does not exceed 1 dB. Regarding total noise, Figure 6.25c shows a similar pattern to loading noise, with a close correlation throughout, except for the observer angles aligned with the propeller axis. Similar trends are observed for the OSPL. The loading noise OSPL presented in Figure 6.25d still demonstrates strong agreement near the propeller plane, but a greater mismatch is noted for the observer angles close to the propeller axis compared to the first BPF SPL. This is attributed to the increased dominance of broadband noise at higher frequencies. The thickness noise OSPL shown in Figure 6.25e continues to exhibit very close alignment, while the total noise OSPL depicted in Figure 6.25f, similarly to loading noise, reveals the anticipated mismatch near the propeller axis.

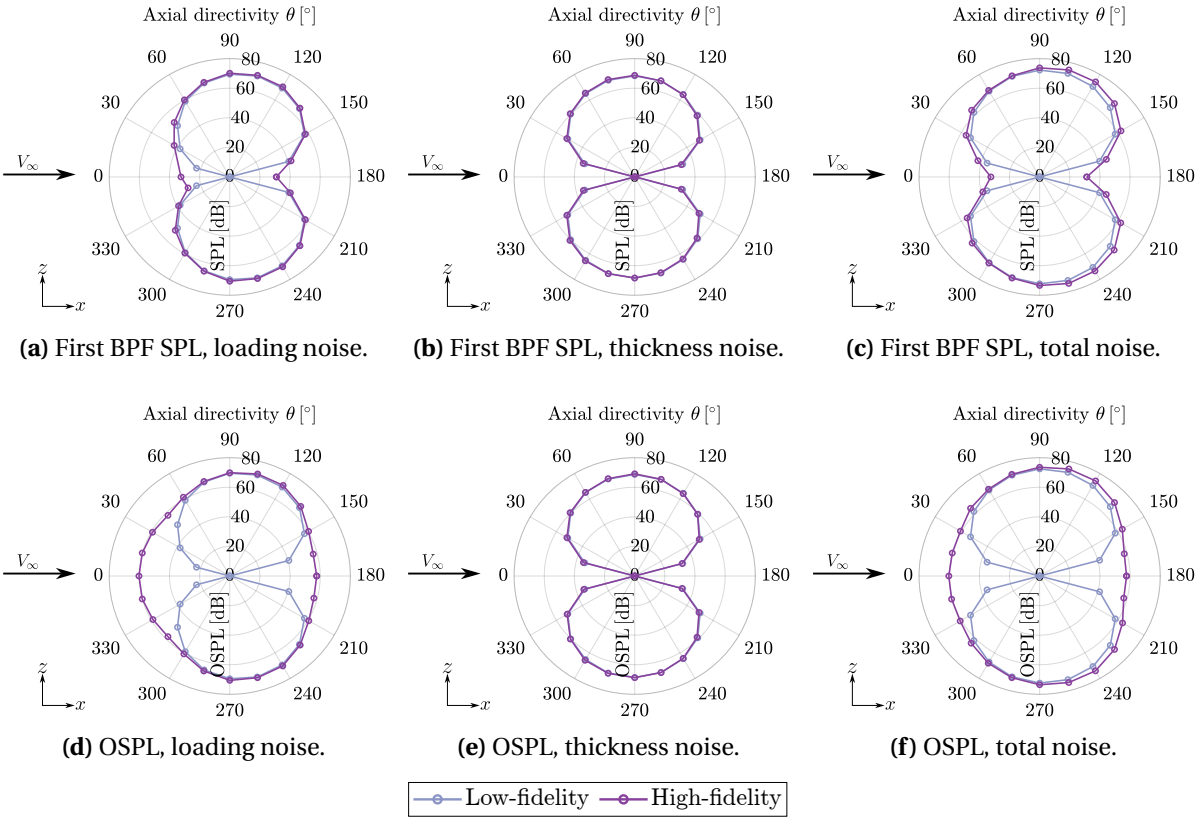

(a) First BPF SPL, loading noise. **(b)** First BPF SPL, thickness noise. **(c)** First BPF SPL, total noise.

(d) OSPL, loading noise. **(e)** OSPL, thickness noise. **(f)** OSPL, total noise.

Figure 6.25: xz-plane, first BPF SPL (top row) and OSPL (bottom row) validation; $\alpha = 0°$.

A sensitivity study was conducted to demonstrate that the first BPF is the primary frequency responsible for propeller noise emissions. Table 6.6 presents the total OSPL (accounting for both loading and thickness noise) computed for the $\theta = 90°$ observer angle across different frequency ranges, along with the corresponding differences relative to the SPL at the first BPF. The results show that these differences remain on the order of 10^{-1} when harmonic contributions up to the 10th BPF are included, indicating that the first BPF SPL is indeed the dominant component.

Frequency range	$\text{OSPL}_{\theta=90^\circ}$ [dB]	$\text{OSPL}_{\theta=90^\circ} - \text{SPL}_{\theta=90^\circ,\text{1st BPF}}$ [dB]
$0.9 \leq \text{BPF} \leq 2$	72.3955	1.5934×10^{-1}
$0.9 \leq \text{BPF} \leq 3$	72.4023	1.6609×10^{-1}
$0.9 \leq \text{BPF} \leq 4$	72.4026	1.6641×10^{-1}
$0.9 \leq \text{BPF} \leq 5$	72.4026	1.6643×10^{-1}
$0.9 \leq \text{BPF} \leq 6$	72.4026	1.6644×10^{-1}
$0.9 \leq \text{BPF} \leq 7$	72.4026	1.6645×10^{-1}
$0.9 \leq \text{BPF} \leq 8$	72.4026	1.6646×10^{-1}
$0.9 \leq \text{BPF} \leq 9$	72.4027	1.6647×10^{-1}
$0.9 \leq \text{BPF} \leq 10$	72.4027	1.6648×10^{-1}

Table 6.6: Total (loading + thickness) OSPL values at $\theta = 90^\circ$ and corresponding difference relative to the first BPF SPL for various BPF ranges.

With the $\alpha = 0^\circ$ case validated, attention is now shifted to the $\alpha = 10^\circ$ case. Figure 6.26 presents the results of a sensitivity study on the OSPL in the xz-plane, computed within the BPF range $0.9 \leq \text{BPF} \leq 10$, with varying numbers of time steps per period. The OSPL polar directivity for different time step resolutions is depicted in Figure 6.26a, showing that for more than 100 time steps per period, the computed noise levels are nearly identical. Figure 6.26b displays the maximum p'_{RMS} as a function of the number of time steps per period, highlighting the convergence of p'_{RMS} with increasing time resolution and the approximately linear rise in computational time. Furthermore, Figure 6.26c shows that a resolution of 300 time steps per period allows to maintain the maximum p'_{RMS} within the 0.1% relative difference threshold. Meanwhile, Figure 6.26d suggests that achieving a relative difference on the order of 10^{-3} for p'_{RMS} near the propeller axis necessitates 500 time steps per period, which is therefore selected as the time resolution.

Finally, considerations regarding data sampling are necessary. As previously discussed, the BPF is 369.09 Hz, and the maximum frequency of interest is 10 BPF = 3690.94 Hz. With a sampling frequency of $F_s = 61508.91$ Hz, the Nyquist limit is $F_s/2 = 30754.46$ Hz, which comfortably exceeds the maximum frequency of interest. Thus, the Nyquist criterion is satisfied.

Figure 6.27 presents the validation results in the xz-plane for $\alpha = 10^\circ$. The top row of the figure corresponds to the first BPF SPL computed within the range $0.9 \leq \text{BPF} \leq 1.1$, while the bottom row represents the OSPL evaluated over the broader range $0.9 \leq \text{BPF} \leq 10$. Figure 6.27a illustrates the first BPF SPL associated with loading noise. Compared to the axisymmetric distribution around the propeller axis observed at $\alpha = 0^\circ$ (see Figure 6.25a), noise levels increase in the region away from which the propeller is tilted and decrease on the opposite side. In the rotor plane at $\theta = 90^\circ$, the low-fidelity method slightly overpredicts the noise reduction compared to the $\alpha = 0^\circ$ case by less than 2 dB. Overall, despite some deviations for observer angles near the propeller axis—primarily due to broadband noise not captured by the low-fidelity approach—the general trends are reasonably well predicted. However, the high-fidelity data exhibit a valley at $\theta = 135^\circ$, indicating destructive interference not captured by the low-fidelity method.

The thickness noise predictions shown in Figure 6.27b align well with high-fidelity data, except at observer angles within the propeller plane. This discrepancy arises because changes in source speed due to the non-zero angle of attack are considered in the high-fidelity loading noise calculations but not in the thickness noise predictions. However, the low-fidelity method does account for the effect of the circumferential variation in source speed, the fluctuations of which amount to ±3% of the $\alpha = 0^\circ$ value at the blade tip, on thickness noise. While these variations are small, they still result in

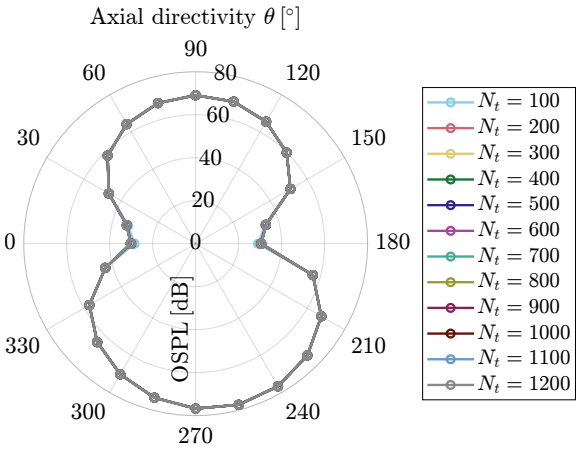

(a) OSPL directivity with varying amount of time steps.

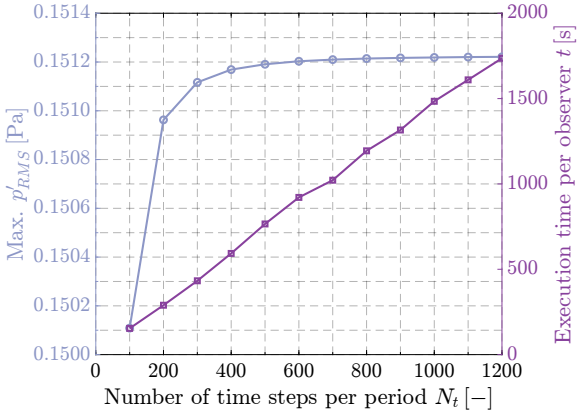

(b) Maximum p'_{RMS} and execution time per observer versus number of time steps.

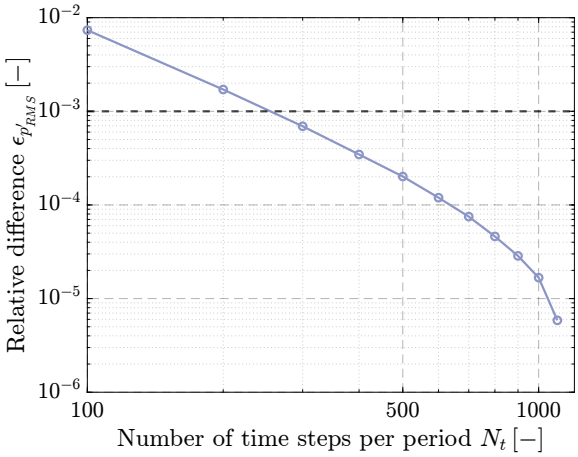

(c) p'_{RMS} relative difference versus number of time steps.

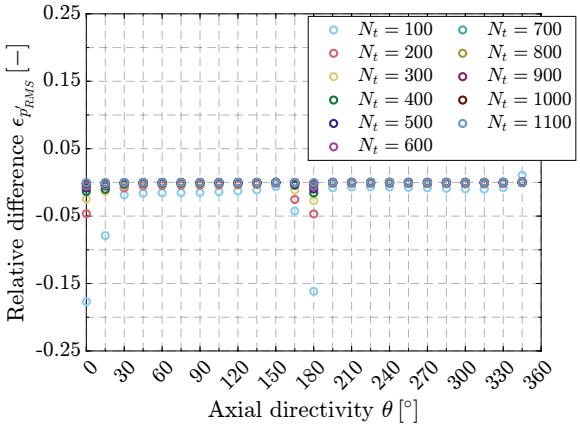

(d) p'_{RMS} relative difference with respect to the finest time resolution.

Figure 6.26: OSPL sensitivity to number of time steps per period; $\alpha = 10°$.

non-zero thickness noise levels near the propeller axis.

The total noise shown in Figure 6.27c demonstrates reasonably good agreement between analytical predictions and CAA results. Apart from the significant discrepancies near the propeller axis, underpredictions in the axial angle range $45° \leq \theta \leq 135°$ remain below 6 dB, while those in the range $225° \leq \theta \leq 315°$ stay within 4.5 dB. The destructive interference observed in loading noise at $\theta = 135°$ is not evident in the total noise directivity, as it is mitigated by higher local thickness noise levels.

For the OSPL directivities of loading noise (Figure 6.27d) and total noise (Figure 6.27f), larger discrepancies occur near the propeller axis due to the increase in higher-frequency broadband noise. Meanwhile, the thickness noise follows a trend similar to the first BPF SPL, as illustrated in Figure 6.27e. Overall, Hanson's time-domain theory effectively predicts tonal noise levels and directivity trends with reasonable accuracy, affirming its suitability for this study.

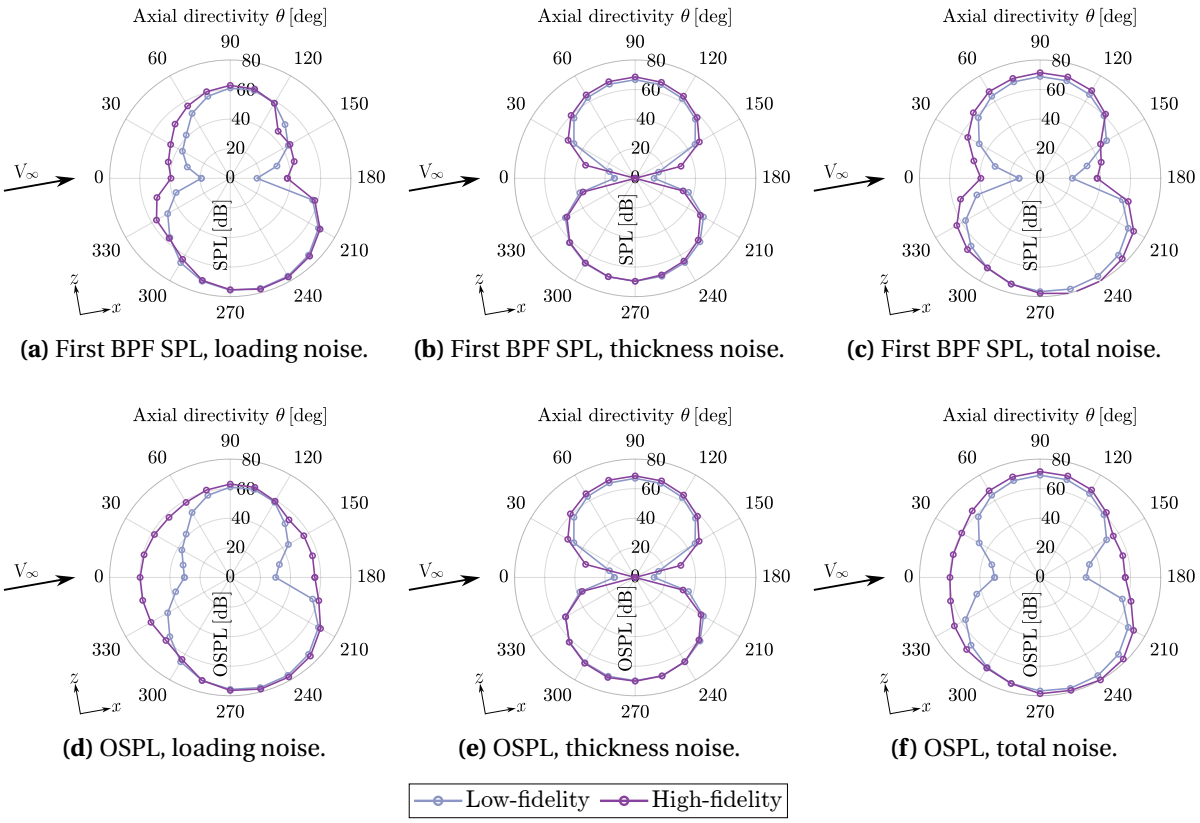

(a) First BPF SPL, loading noise. **(b)** First BPF SPL, thickness noise. **(c)** First BPF SPL, total noise.

(d) OSPL, loading noise. **(e)** OSPL, thickness noise. **(f)** OSPL, total noise.

Figure 6.27: xz-plane, first BPF SPL (top row) and OSPL (bottom row) validation; $\alpha = 10°$.

7

ANALYSIS SETUP

This chapter outlines the analysis setup utilized for this work. Section 7.1 details the baseline propeller employed in this study, along with its main geometrical parameters and operating conditions. Section 7.2 elucidates how the velocity perturbation to the propeller was incorporated in the analysis. Finally, Section 7.3 discusses the reasoning behind the variation of the helical tip Mach number.

7.1. BASELINE PROPELLER

The propeller employed for this study is the XPROP-S propeller, details of which have previously been given in Section 6.1. The main geometrical parameters and operating conditions are given in Table 7.1.The pitch setting $\beta_{0.7R_p} = 30°$, also used in the aeroacoustic validation study, was chosen. The advance ratio $J = 0.8$, previously used in the validation study and representative of a positive thrust condition with a moderate thrust setting, is maintained across the analyses performed in this thesis. The rotation direction is anti-clockwise if seen from the front. The aeroacoustic analyses are perfomed in the far field, with the observers positioned at a distance of 10 diameters from the center of the propeller.

Parameter	Value	Unit
Propeller diameter - D	0.2032	m
Hub-to-tip ratio - R_{hub}/R_p	0.23	–
Blade pitch at $r/R_p = 0.7$	30	°
Number of blades - N_B	6	–
Free-stream static pressure - p_∞	101325	Pa
Free-stream static temperature - T_∞	288.15	K
Free-stream Mach number - M_∞	**0.088**	–
Helical tip Mach number - M_{ht}	**0.357**	–
Advance ratio - J	0.8	–
Maximum chord-based Reynolds number - max Re_c	$\mathbf{1.07 \times 10^5}$	–

Table 7.1: Geometrical parameters and operating conditions. Parameters shown in bold represent those varied in this work.

7.2. INFLOW VELOCITY PERTURBATIONS

The inflow field necessary for the non-uniform flow method applied in this study was taken from the work of Van Arnhem et al. [21], who employed CFD simulations. The velocity perturbations were calculated at the propeller plane in the absence of the propeller itself, disregarding its interaction with the incoming flow. The suction effect of the propeller on the incoming flow is considered to have an insignificant influence on the velocity perturbation at moderate thrust settings. Furthermore, this effect can be relevant in pusher propeller configurations [10], while their significance diminishes further in non-pusher configurations.

Figure 7.1 illustrates the inflow velocities at the propeller disk normalized by V_∞ for an angle of attack $\alpha = 10°$. The inflow velocities are defined according to the reference frame displayed in Figure 4.1a. Figure 7.1a presents the axial velocity perturbation. It is evident that the nacelle contributes only a minor inflow asymmetry, with the most significant azimuthal variation occurring near the propeller hub. Here, the maximum percentage difference relative to the free-stream reaches an absolute value of 8% V_∞. Figure 7.1b and Figure 7.1c illustrate the in-plane side and vertical velocity perturbations, respectively. Notably, the largest disturbances are close to the propeller hub due to the vicinity to the nacelle.

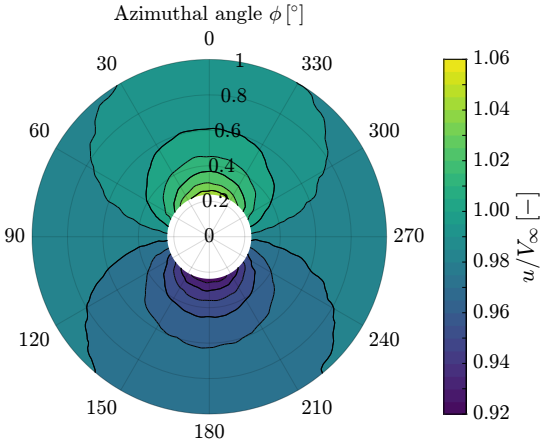

(a) Axial velocity.

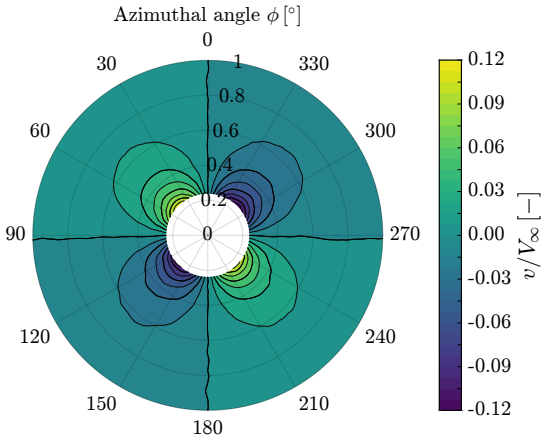

(b) In-plane side velocity.

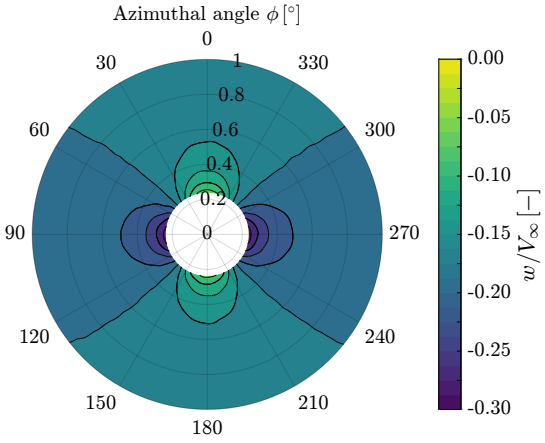

(c) In-plane vertical velocity.

Figure 7.1: Velocity perturbations at $\alpha = 10°$ in absence of the propeller computed using CFD for the work of Van Arnhem et al. [21].

As discussed in Section 5.2, the current implementation of the aeroacoustic solver cannot account

for the deformation of the helical surface caused by an inflow velocity asymmetry which impacts the blade elements differently over the azimuth. The velocity disturbances presented in Figure 7.1 exhibit circumferential asymmetry resulting from the nacelle's upwash. The current version of the acoustic code, while able to account for the resulting periodic variation of the source speed, is unable to model the periodic stretching/contraction that the helical path of a blade element would undergo as a result of those inflow perturbations if such deformation differs over the azimuth. Therefore, while these velocity disturbances are used as inputs for the aerodynamic performance prediction method in non-uniform inflow conditions, they cannot be directly utilized in the acoustic solver.

However, at an angle of attack, the axial velocity component $V_\infty \cos(\alpha)$ and the in-plane vertical velocity component, $V_\infty \sin(\alpha)$, resulting from the application of simple trigonometry to project V_∞ onto the relevant coordinate axes, can still be included in the acoustic solver. The in-plane component leads to an increase in the source speed on the advancing side and a reduction on the retreating side. Since its magnitude does not vary across the blade elements over the azimuth, it is feasible to incorporate it. On the other hand, if the nacelle influence were considered, the code could account for its effect on the source speed but would be unable to model the periodic stretching and contraction of the helical surface caused by it.

As discussed in Subsection 2.3.2, Mani [24] pointed out that for highly loaded, high-tip-speed propellers, especially with a large number of blades, the modulation of steady loading and thickness noise caused by the in-plane velocity component may be significant. This effect is considered in this thesis.

It is important to assess the extent to which disregarding the nacelle's influence may affect the results. As seen in Figure 7.1a, the nacelle-induced upwash in the axial direction is relatively minor and primarily localized near the propeller hub. The axial velocity component, $V_\infty \cos(\alpha)$, is already accounted for in the acoustic code. When neglecting the nacelle's influence, the maximum difference in the axial velocity at $\alpha = 10°$ is approximately 7%. To evaluate the variation in the in-plane velocity component when the nacelle's influence is disregarded, Figure 7.2 presents a comparison of the tangential velocity fluctuation, normalized by ΩR_p, both with (Figure 7.2a) and without (Figure 7.2b) the nacelle's upwash effect. The tangential velocity, V_{tan}, includes contributions from the local tangential velocity, Ωr, as well as the in-plane inflow velocity. The sinusoidal variation of the tangential velocity is evident, with a maximum occurring at $\phi = 90°$ and a minimum at $\phi = 180°$. As expected, the largest differences are observed near the hub, where neglecting the nacelle's influence results in a percentage difference of up to 42% compared to including its effect. However, since the source speed is relatively low at the hub, this difference is not expected to significantly impact the noise modulation mechanism. Further along the blade span, the relative difference remains below 8%. Given the low-fidelity approach employed in this thesis, this deviation is considered acceptable.

Unlike what happens for an angle of attack, in case of wake encounter the velocity perturbation is purely axial, as shown in Figure 7.3. The wake induces a velocity deficit that reduces the axial inflow speed to as low as $0.9V_\infty$. This type of inflow profile would cause a periodic deformation of the helical trajectory of a blade element and is, therefore, excluded from the acoustic solver. Due to the specific characteristics of this inflow profile and the aforementioned limitations, the velocity deficit in the source speed at certain azimuthal positions is entirely disregarded in the acoustic analysis. However, since the axial velocity perturbations during wake encounter are confined to a localized section of the propeller disk, their omission is unlikely to have a significant impact on the loading noise signature. While the source speed reduction caused by the axial velocity deficit modulates the noise radiative efficiency, this modulation is limited to a restricted area of the disk. Consequently, the primary mechanisms of noise generation can still be analyzed with reasonable fidelity. Nevertheless, it should be noted that the thickness noise will remain unaffected with respect to uniform inflow conditions.

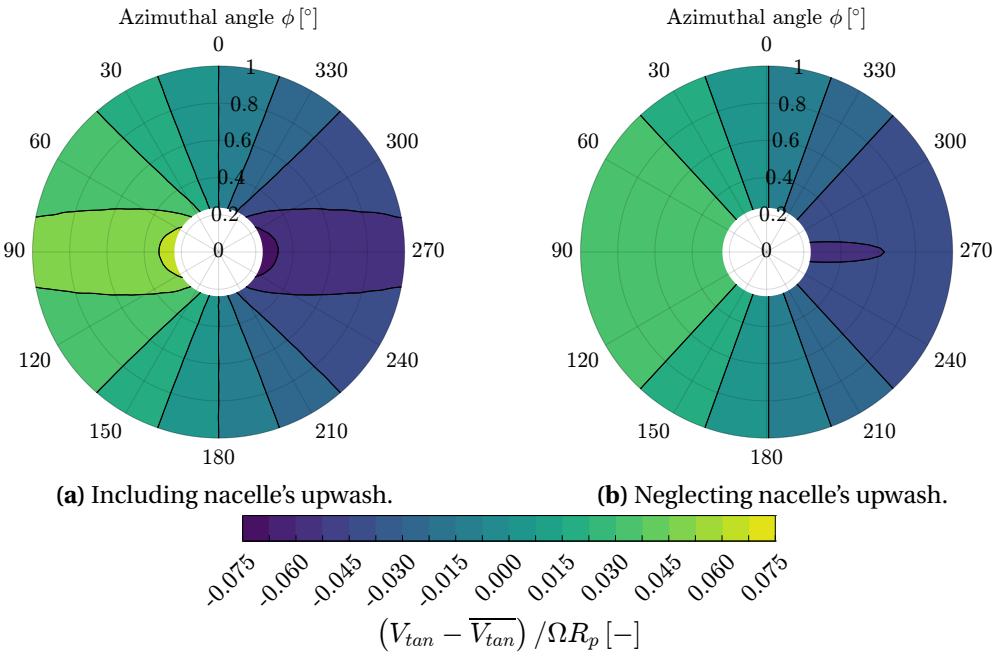

(a) Including nacelle's upwash. **(b)** Neglecting nacelle's upwash.

Figure 7.2: Normalized tangential velocity fluctuation at $\alpha = 10°$ including (left) and neglecting (right) the nacelle's upwash effect.

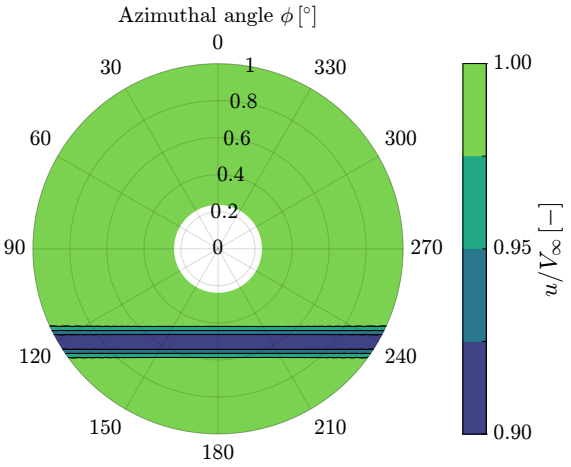

Figure 7.3: Axial velocity perturbation in case of wake encounter (wing at $z/R_p = -0.5$) in absence of the propeller computed using CFD by Van Arnhem et al. [21].

7.3. HELICAL TIP MACH NUMBER VARIATION

This thesis investigates the impact of varying the propeller helical tip Mach number on the resulting noise signature.

In experimental setups conducted at ambient conditions, a reduction in the free-stream Mach number typically results in a lower tip Mach number, provided the advance ratio remains constant to replicate that of the full-scale model. This reduction leads to diminished performance predictions due to the lack of compressibility effects, as illustrated in Figure 6.6.

To compensate for the lower Mach number experienced in wind tunnel experiments while maintaining the same J and thrust coefficient T_C, hence the same disk loading, the blade pitch angle can be adjusted accordingly. This is shown in Figure 7.4. As J was maintained, M_{ht} was increased by increasing the free-stream velocity and the propeller rotational speed. It can be observed that, for a given T_C requirement, the blade pitch decreases in a nearly linear trend.

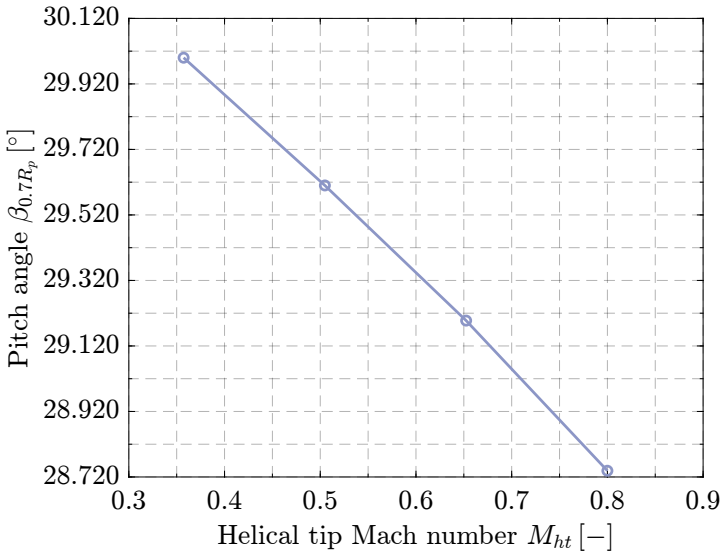

Figure 7.4: Blade pitch angle at $r/R_p = 0.7$ versus helical tip Mach number keeping the thrust coefficient T_C constant; $J = 0.8$.

While it may appear advantageous to adopt this approach to measure the noise signature of a propeller at higher Mach numbers, caution must be exercised in evaluating how potential associated variations in propeller performance could influence the noise emissions.

Figure 7.5 illustrates the variation of the thrust-to-torque coefficient ratio as a function of helical tip Mach number for the baseline propeller geometry and operating conditions. The analysis is conducted under two scenarios: when T_C is not kept constant and when it is held constant by changing the blade pitch distribution. In the scenario where the thrust coefficient is not kept constant, the ratio of thrust to torque exhibits a slight increase from a helical tip Mach number of 0.357 to 0.505. This increase can be attributed to the increasing lift associated with the rising tip speed, which is more significant than the increase in drag at this condition, leading to a higher thrust. As the tip Mach number continues to increase, the ratio decreases more significantly up to 0.8. This more pronounced decline indicates the increasing influence of compressibility effects at higher tip speeds, which becomes evident as the drag forces rise and negatively impact the efficiency of thrust generation.

Conversely, when the thrust coefficient is maintained constant, the behavior of the thrust-to-torque ratio changes significantly. An initial increase in the ratio is observed as the tip Mach number rises to 0.652. This is because the propeller's design and pitch setting might be closer to optimal for this tip speed. However, as the tip Mach number continues to increase beyond this point, a decrease

in the thrust-to-torque coefficient ratio becomes evident. This decline indicates the growing impact of compressibility effects, which are more pronounced at higher tip speeds, leading to increased drag and a less efficient conversion of thrust. Consequently, the overall performance of the propeller deteriorates.

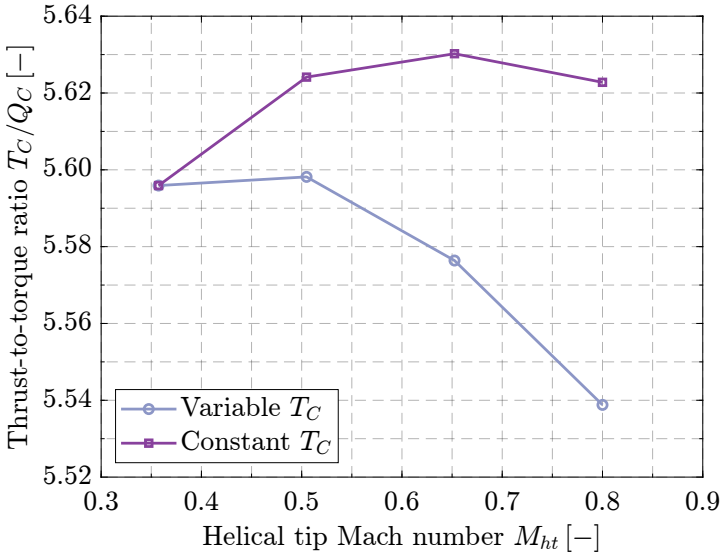

Figure 7.5: Thrust-to-torque coefficients ratios versus helical tip Mach number at variable and constant T_C; $J = 0.8$.

Given that the thrust-to-torque ratio influences propeller noise directivity due to constructive/destructive interference between thrust and torque noise [43], the previously discussed method of adjusting the blade pitch to maintain a constant T_C across varying tip Mach numbers is unsuitable for this analysis, as the thrust-to-torque ratio would change. If this method was applied, the resulting noise data at different Mach numbers would be misleading due to a combination of the Mach number and thrust-to-torque ratio effects. Since the goal is to examine the acoustic effects of varying the helical tip Mach number, an alternative approach is necessary. In this work, isolating the acoustic effects is paramount, even if it results in a less precise assessment of the aerodynamic loads.

Hence, for the present research, a consistent pressure coefficient was assumed across different Mach numbers at $J = 0.8$ and the dimensional sectional pressure was scaled appropriately using the effective velocity at a blade section to reflect variations in the Mach number. Such pressure coefficient, based on the pressure difference between the blades' upper and lower surfaces needed for Hanson's theory, is defined as:

$$C_{\Delta p} = \frac{\Delta p}{0.5 \rho_\infty V_E^2} \tag{7.1}$$

where V_E is the effective velocity, defined, at $\alpha = 0°$ and uniform flow conditions, in Equation 4.3. The baseline operating conditions from which the pressure coefficient value was derived are shown in Table 7.1. The propeller design remains unchanged with varying Mach number. This method guarantees a constant thrust-to-torque ratio, providing unambiguous results for noise directivity. The scaled propeller performance is unaffected. On the other hand, this approach does not fully correctly account for the scaling of forces due to compressibility effects.

8

AEROACOUSTIC CHARACTERIZATION OF THE UNINSTALLED PROPELLER IN UNIFORM FLOW

Rather than simply presenting the noise signature of the isolated propeller in uniform inflow, this chapter aims to provide a physical understanding of its acoustic emissions. The focus here is on the fundamental physics behind Hanson's time-domain method. Section 8.1 elaborates on the aerodynamic performance of the propeller, whereas Section 8.2 delves into its noise characteristics.

8.1. AERODYNAMIC PERFORMANCE

The propeller geometry and operating conditions were previously detailed in Section 7.1. As outlined in Section 7.3, the effects of the helical tip Mach number M_{ht} are analyzed by scaling the sectional pressure according to the square of the effective velocity, while maintaining the sectional pressure coefficient. The advance ratio is held constant at $J = 0.8$. Table 8.1 presents the operating conditions considered in this study. Specifically, an evenly spaced array of four different M_{ht} values is considered, ranging from $M_{ht} = 0.357$ to $M_{ht} = 0.8$. Since the variation in M_{ht} is performed at a constant J, the parameters adjusted are the free-stream velocity and the propeller's rotational speed. Although the scaled aerodynamic loads are maintained across different Mach numbers, this variation affects the effective chord-based Reynolds number at each blade section, the maximum value of which ranges from a maximum $Re_c = 1.07 \times 10^5$ at $M_{ht} = 0.357$ to a maximum $Re_c = 2.40 \times 10^5$ at $M_{ht} = 0.8$, as well as the free-stream Mach number due to changes in free-stream velocity, ranging from $M_\infty = 0.088$ at $M_{ht} = 0.357$ to $M_\infty = 0.197$ at $M_{ht} = 0.8$.

Helical tip Mach number - M_{ht}	0.357	0.505	0.652	0.8
Free-stream Mach number - M_∞	0.088	0.125	0.161	0.197
Maximum chord-based Reynolds number - max Re_c	1.07×10^5	1.52×10^5	1.96×10^5	2.40×10^5

Table 8.1: Variation of operating conditions.

Table 8.2 provides key propeller performance parameters. At an advance ratio of $J = 0.8$, the values of $C_T = 0.2834$ and $C_P = 0.3183$ result in a propeller efficiency of $\eta = 0.7125$.

Parameter	Value
Thrust coefficient - C_T	0.2834
Power coefficient - C_P	0.3183
Propeller efficiency - η	0.7125

Table 8.2: Characteristic propeller performance parameters.

8.2. AEROACOUSTIC PERFORMANCE

Prior to the aeroacoustic analysis, a sensitivity study is performed to determine the appropriate number of time steps per period for the computations. The results of this study and a detailed discussion are illustrated in Section A.1.

Unlike what previously shown in Figure 6.17, for which the focus was on the SPL at the 1st BPF (and related p'_{RMS}), this sensitivity analysis focuses on the OSPL (and related p'_{RMS}) in the xz-plane, with the observers positioned in the far field at a distance of 10 diameters from the center of the propeller. The analysis is conducted at $M_{ht} = 0.8$, the highest Mach number evaluated in this study. This operating condition was chosen because it results in higher levels of high-frequency noise, requiring sufficient time resolution to capture the data accurately. The selected number of time steps per period is 600, which allows to maintain a deviation below 0.1% in maximum p'_{RMS} (according to Equation 6.2) and ensures that the sampled data accurately captures the relevant acoustic frequencies without aliasing.

Figure 8.1 presents the axial directivity of the thrust-specific sound pressure level for different helical tip Mach numbers. It is observed that as the Mach number increases, the thrust-normalized noise levels also rise at all the observer angles. At the rotor plane ($\theta = 90°$), the noise level increases by 39 dB as the helical tip Mach number increases from $M_{ht} = 0.357$ to $M_{ht} = 0.8$.

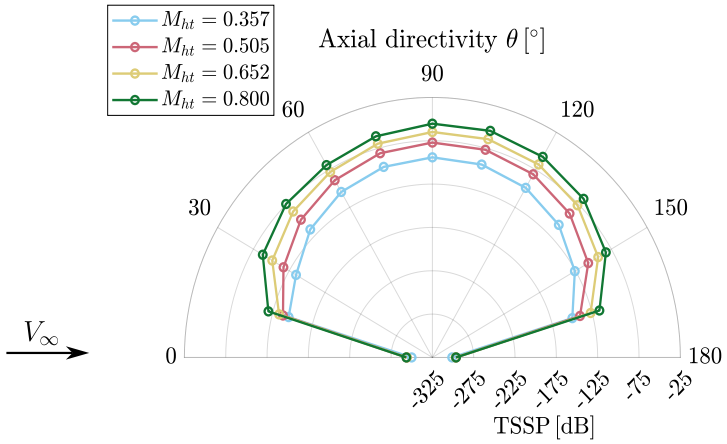

Figure 8.1: Thrust-specific sound pressure level at different helical tip Mach numbers.

To assess the acoustic reason behind the noise increase, the acoustic pressure fluctuation waveforms at an observer angle $\theta = 90°$ are presented in Figure 8.2 for $M_{ht} = 0.357$ and in Figure 8.3 for $M_{ht} = 0.8$. By analyzing the interference between the blades' acoustic pressure waveforms, it is possible to spot any acoustic reason for the noise increase.

The pressure waveforms are plotted over one complete revolution against the observer reception time, normalized by the propeller period T. t_0 represents the first element of the vector defining the time at which the acoustic planform data are received by the observer. In both figures, the left plot illustrates the loading pressure of each of the six blades, obtained by superimposing the near- and

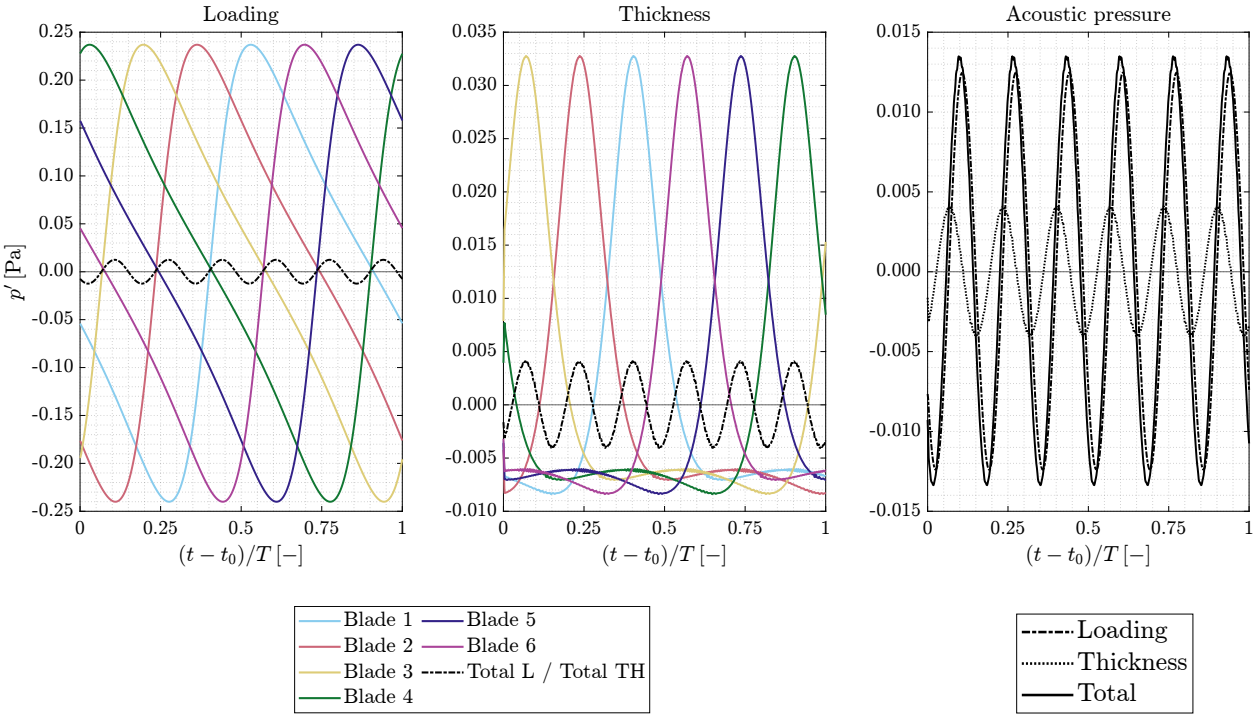

Figure 8.2: Acoustic pressure waveforms of the individual blades and the propeller; $M_{ht} = 0.357$, $\theta = 90°$.

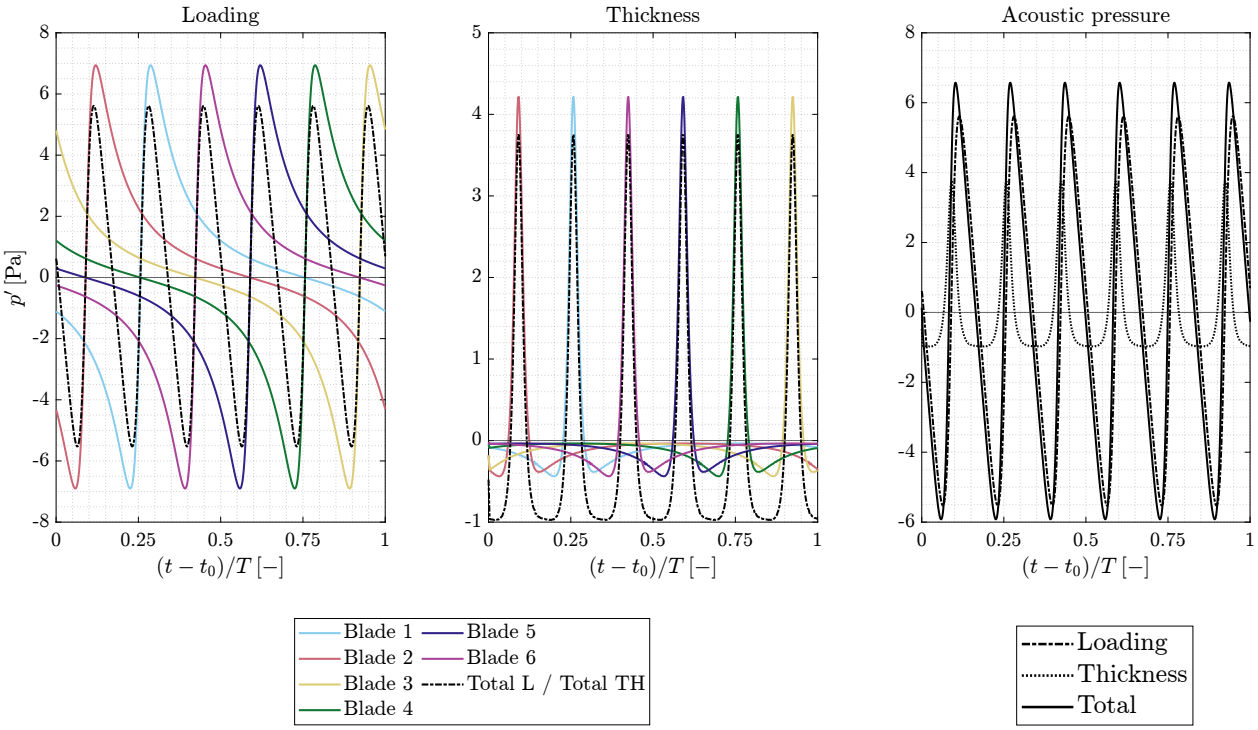

Figure 8.3: Acoustic pressure waveforms of the individual blades and the propeller; $M_{ht} = 0.8$, $\theta = 90°$.

far-field loading pressures as defined in Equation 5.14 and Equation 5.16. The center plot displays the thickness pressure of the blades, as described in Equation 5.19. Additionally, the total loading and thickness pressures, derived by summing the waveforms of all six blades, are shown. The right plot, in contrast, presents the propeller's loading and thickness acoustic pressures along with the total pressure waveform retrieved by superimposing the two.

The pressure waveform generated by each blade is periodic, repeating at every blade-passing frequency, which explains the presence of six peaks in the plots. As observed, the waveforms of the individual blades exhibit the same amplitude but are phase-shifted relative to each other. At both $M_{ht} = 0.357$ and $M_{ht} = 0.8$, the interaction between the blades' loading and thickness waveforms is destructive, as evidenced by the reduced amplitude of the propeller's loading and thickness pressure. Conversely, the total loading and thickness pressures combine constructively, leading to an increased total acoustic pressure amplitude. Additionally, it is observed that the loading pressure amplitude dominates over the thickness pressure at both Mach numbers.

However, from an acoustic standpoint, it is not the peak amplitude alone that determines noise levels but rather the root mean square of the pressure signal. The RMS provides a measure of the signal's average energy content and is also influenced by the waveform shape. Table 8.3 presents a comparison of the peak-to-peak amplitude (defined as $A_{pp} = \max(p') - \min(p')$) and the RMS values of the loading pressure fluctuations for both the propeller and an individual blade at $M_{ht} = 0.357$ and $M_{ht} = 0.8$ at the axial directivity angle $\theta = 90°$. At $M_{ht} = 0.357$, the destructive interference among the blades' loading waveforms leads to a 94.80% drop in the peak-to peak amplitude and a 94.22% reduction in the RMS of the propeller's pressure signal compared to that of a single blade. Conversely, at $M_{ht} = 0.8$, the destructive interference observed in Figure 8.3 leads to a less pronounced reduction in the peak-to-peak amplitude of the propeller's pressure, which decreases by 19.49%. Meanwhile, the RMS value increases by 35.63%, suggesting a higher overall energy content in the pressure fluctuations.

M_{ht}	$A_{\text{L pp, prop}}$	$A_{\text{L pp, blade}}$	$p'_{\text{L RMS, prop}}$	$p'_{\text{L RMS, blade}}$	$\Delta\%_{A_{\text{L pp}}}$	$\Delta\%_{p'_{\text{L RMS}}}$
0.357	0.0248	0.4770	0.0088	0.1522	−94.80%	−94.22%
0.8	11.1454	13.8442	3.7770	2.7848	−19.49%	35.63%

Table 8.3: Comparison between the peak-to-peak amplitude and the root mean square of the loading pressure fluctuations of the propeller and of a single blade at two helical tip Mach numbers; $\theta = 90°$.

The higher RMS of the propeller's loading pressure with respect to a single blade at $M_{ht} = 0.8$ can be attributed to the fact that, as shown in Figure 8.3, although the loading waveforms of the individual blades exhibit higher peak amplitudes, they remain near the equilibrium position for longer periods, thereby reducing their average energy content and presenting a more imperfect de-phasing compared to $M_{ht} = 0.357$.

To provide an explanation for this behavior, attention is drawn to the underlying physics of Hanson's pressure equations presented in Section 5.2. In particular, the focus is on the loading noise, which is the primary noise component at the directivity angle and operating conditions analyzed. Specifically, the far-field loading pressure is examined. The far-field component p_{LF}, defined in Equation 5.16, dominates over the near-field component p_{LN} defined in Equation 5.14, as it includes a R^{-2} term (where R is the source-to-observer distance) that accounts for wave propagation through space, while the near-field component scales with R^{-3}. Therefore, a detailed understanding of the far-field loading pressure is crucial for gaining deeper insights into the noise behavior. The integrand of p_{LF}, provided in Equation 5.16, includes a Δp term, i.e. the pressure difference between the upper and lower surfaces of the blade, indicative of the source strength, along with a directivity

factor. A similar directivity factor is also present in the time-domain formulation of Najafi-Yazdi et al. [49] and its interpretation is straightforward [50]. While Δp remains constant over the azimuth in uniform flow, the directivity factor exhibits notable variability. Figure 8.4 illustrates the chordwise distribution (from leading to trailing edge) of this directivity factor for blade 1 as a function of the normalized reception time for the radial station $r/R = 0.7$ at both $M_{ht} = 0.357$ and $M_{ht} = 0.8$. While the amplitude of the directivity factor is not affected by a change in the Mach number, a phase shift between the two operating conditions is evident.

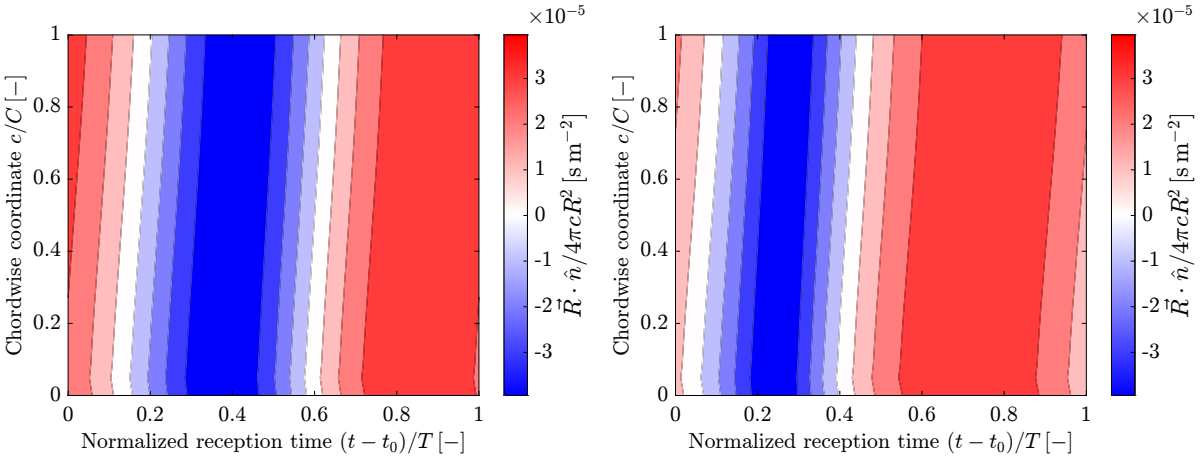

(a) $M_{ht} = 0.357$ **(b)** $M_{ht} = 0.8$

Figure 8.4: Chordwise distribution of the directivity factor of the far-field loading pressure at $r/R_p = 0.7$; blade 1, $\theta = 90°$.

The characteristic variability of the directivity factor can be understood by examining a schematic of the main forces involved, as shown in Figure 8.5a. The sectional forces are depicted in Figure 8.5a. The pressure force used in Hanson's loading equations is labeled as dF_p. Given the thrust dT, the torque force dF_Q, and the pitch angle β, dF_p can be calculated as the force normal to the airfoil's chord.

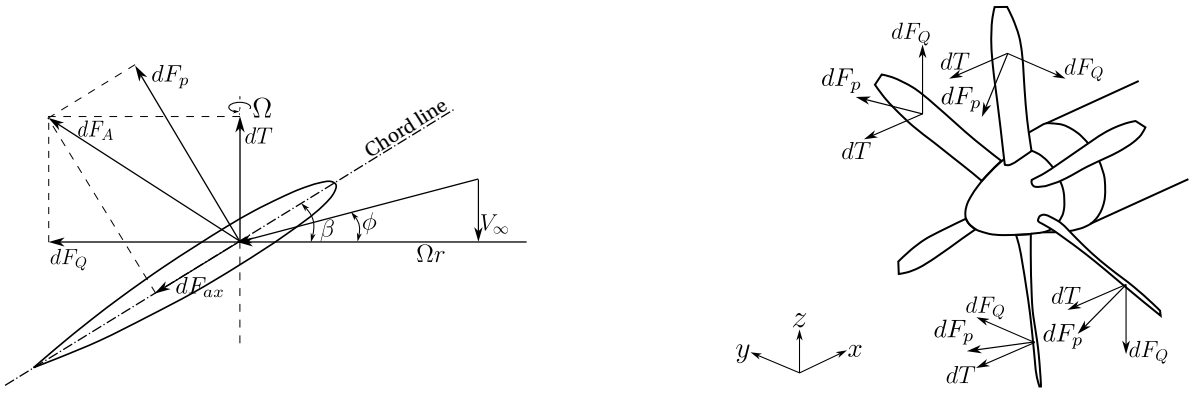

(a) 2D view. **(b)** Isometric view.

Figure 8.5: 2D (a) and isometric (b) view of propeller forces.

Figure 8.5b shows an isometric view of the forces acting on a given blade section at various azimuthal positions. The $\hat{n}$ unit vector, as used in Hanson's loading equations, defines the direction of the pressure force. The dot product $\vec{R} \cdot \hat{n}$ represents the projection of the vector $\vec{R}$ (from the source to the observer) along the direction of $\hat{n}$. Its value depends on the relative orientation of the two

vectors. This explanation clarifies why the directivity factor in Figure 8.4 exhibits time-dependent behavior. The fact that its amplitude remains unchanged with Mach number is due to its dependence only on the relative orientation between $\vec{R}$ and $\hat{n}$ over time, as well as the distance magnitude between the source and the observer.

The directivity factor modulates Δp in the integrand, periodically amplifying and reducing its value. However, it does not clarify by itself the loading waveform shape displayed in Figure 8.3. To further explore this, Figures 8.6 and 8.7 illustrate the acoustic planform of the propeller for an observer positioned in the rotor plane at $\theta = 90°$ (equivalently, $\phi = 0°$) at different reception times for both $M_{ht} = 0.357$ and 0.8. A red marker is placed on blade 1. Note that the rotation is anti-clockwise.

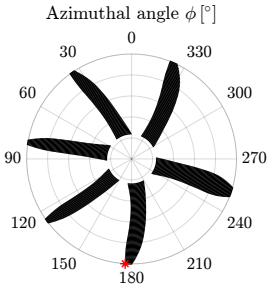

(a) $(t - t_0)/T = 0.19$

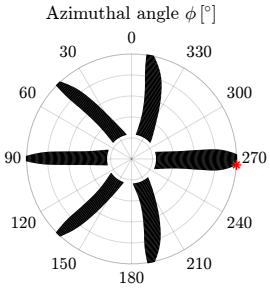

(b) $(t - t_0)/T = 0.39$

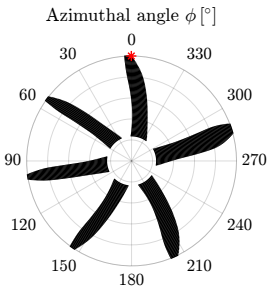

(c) $(t - t_0)/T = 0.59$

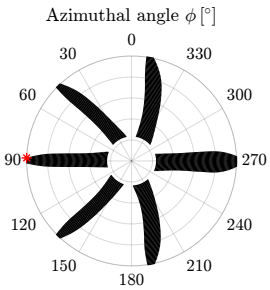

(d) $(t - t_0)/T = 0.89$

Figure 8.6: Acoustic planform; $M_{ht} = 0.357$, $\theta = 90°$ ($\phi = 0°$). Red marker on blade 1. Anti-clockwise rotation.

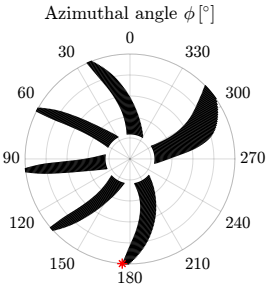

(a) $(t - t_0)/T = 0.12$

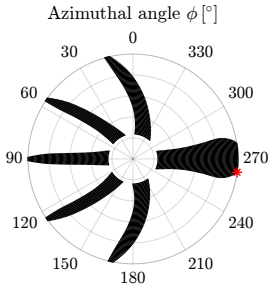

(b) $(t - t_0)/T = 0.26$

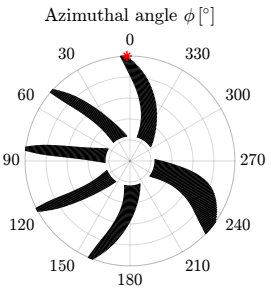

(c) $(t - t_0)/T = 0.39$

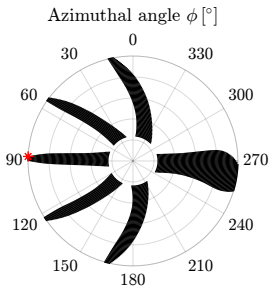

(d) $(t - t_0)/T = 0.75$

Figure 8.7: Acoustic planform; $M_{ht} = 0.8$, $\theta = 90°$ ($\phi = 0°$). Red marker on blade 1. Anti-clockwise rotation.

As previously stated, the acoustic planform represents the surface defined by the positions of the blade elements at the retarded time. It is evident that the acoustic planforms of the blades undergo periodic deformation. Due to the non-linearity of the retarded time, the acoustic planform can exhibit both stretching and contraction within a revolution, depending on whether the source is moving towards or away from the observer. In particular, the variation occurs in the acoustic chord γ, which Hanson employs as the integration variable in his pressure equations. It should be observed that the presence of the acoustic chord is a distinguishing feature of Hanson's near-field theory, marking a difference with other time-domain formulations. Unlike the physical chord, γ expands and contracts throughout the revolution.

Examining Figure 8.6, it can be observed that at $M_{ht} = 0.357$, the maximum stretching of γ for blade 1 occurs around $(t - t_0)/T = 0.39$, which corresponds to when the helical source velocity U is in the observer's line of sight direction. Conversely, when the source velocity is directed opposite to the source-to-observer vector, around $(t - t_0)/T = 0.59$, γ experiences maximum contraction. Compared to the lower Mach number scenario, at $M_{ht} = 0.8$ significantly greater stretching and contraction can be observed due to the increased source speed, as shown Figure 8.7. In this case, the non-compact nature of the source becomes particularly apparent. Furthermore, the observer reception times at

which the blade is at a particular azimuthal angle differ from the $M_{ht} = 0.357$ case, explaining the phase shift observed in Figure 8.4.

As observed, Hanson's pressure equations involve an integration over γ, with the integration limits spanning from the leading edge to the trailing edge of the blade. Variations in this integration range, due to the stretching or contraction of γ, lead to an increase or decrease in the integral's value. For example, at $M_{ht} = 0.8$ and $(t - t_0)/T = 0.26$, the directivity factor at $r/R_p = 0.7$ for blade 1 negatively modulates Δp (see Figure 8.4b). The extended γ integration range at this instant amplifies the negative value of the integral, making it more negative. Additionally, it can be noted that at $M_{ht} = 0.8$, the acoustic planform of a given blade remains on the advancing side (where the blade moves away from the observer) for a longer duration compared to $M_{ht} = 0.357$. This behavior is attributed to the larger source speed at higher Mach numbers, which causes greater variability in the parameters computed at the retarded time as the blade approaches the observer, and a more gradual variation as it moves away. On the advancing side, where γ contracts, the integral values tend to be lower. This explains why the loading pressure waveforms of individual blades at $M_{ht} = 0.8$, shown in Figure 8.3, remain at lower instantaneous values for an extended period. Moreover, at higher Mach numbers, an increased asymmetry in the acoustic planforms of opposite blades leads to a more imperfect phase shift between their waveforms. Consequently, the positive value of the pressure signal from one blade at a given instant is less effectively canceled by the negative value of the opposite blade's signal at the same instant. This results in weaker destructive interference and a higher RMS value of the propeller's loading pressure compared to that of a single blade.

For the purpose of analyzing the directivity of different noise sources, Figure 8.8 presents the OSPL directivity in the xz-plane at various helical tip Mach numbers. The characteristic two-lobed pattern associated with thrust is clearly visible. This pattern emerges because, at $\theta = 90°$, the source-to-observer vector $\vec{R}$ is orthogonal to the thrust unit vector $\hat{t}$. As illustrated in Figure 8.8a, at $M_{ht} = 0.357$, torque noise dominates over thrust noise for the polar angles $15° \leq \theta \leq 165°$, thereby suppressing the two-lobed thrust pattern when the two take part in loading noise. However, Figure 8.8b shows that at $M_{ht} = 0.505$, thrust noise levels exceed torque noise at $\theta = 15°$. As the Mach number increases further, thrust noise becomes comparable to or even greater than torque noise in both the frontal lobe ($15° \leq \theta \leq 45°$) and the backward lobe ($135° \leq \theta \leq 165°$) of the thrust. Since the thrust-to-torque ratio is maintained across the different operating conditions, this behavior will be further investigated. As the dominant noise source transitions from thrust to torque near the rotor plane, a valley in loading noise is observed at $\theta = 60°$, though this phenomenon does not occur at $\theta = 120°$, which also requires further analysis. Across all Mach numbers, thrust and torque noise interfere destructively in the frontal lobe of the thrust, reducing loading noise levels, while their interference is constructive in the backward lobe, amplifying noise levels. Loading noise dominates over thickness noise in the rearward lobe of the thrust across all operating conditions, while their relative significance in the frontal lobe varies with Mach number. Nonetheless, at the propeller plane, acoustic emissions due to the blade's loading on the fluid always exceed those caused by fluid displacement. Furthermore, constructive interference between loading and thickness noise is observed at all observer angles, leading to a higher total OSPL. Even at $M_{ht} = 0.652$ and $M_{ht} = 0.8$, where a valley in loading noise directivity appears at $\theta = 60°$, the increased thickness noise partially offsets the reduction in loading noise, resulting in higher total noise levels.

An explanation of why thrust noise becomes comparable to or even higher than torque noise at some axial positions in the frontal and backward lobes of the thrust as the Mach number increases is hereby provided. Figure 8.9 presents the chordwise distribution of the directivity factor associated with the far-field loading pressure due to both thrust and torque for $r/R_p = 0.7$ of blade 1 at $M_{ht} = 0.357$, at an observer angle $\theta = 30°$. The distinction between the two directivity factors arises from the unit vector definition, with $\hat{t}$ representing the thrust unit vector and $\hat{q}$ representing the torque's one. The thrust directivity factor, depicted in Figure 8.9a, remains positive throughout all reception times

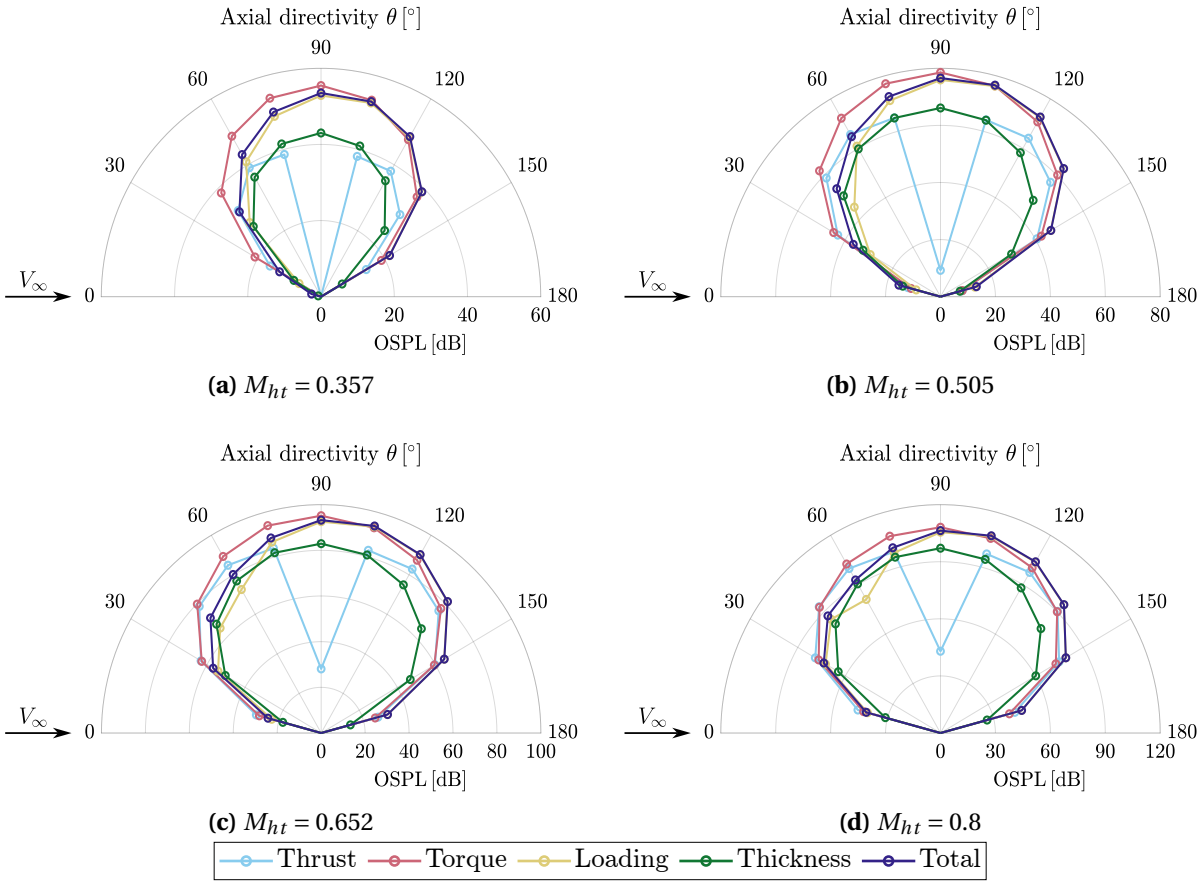

(a) $M_{ht} = 0.357$ **(b)** $M_{ht} = 0.505$

(c) $M_{ht} = 0.652$ **(d)** $M_{ht} = 0.8$

Figure 8.8: Axial directivity of OSPL at different helical tip Mach numbers.

due to the relatively small angle between $\vec{R}$ and $\hat{t}$ at $\theta = 30°$. Conversely, since $\hat{q}$ lies tangentially to the propeller plane, the relative orientation of $\vec{R}$ and $\hat{q}$ during a full revolution leads to an alternating pattern of positive and negative values in the torque directivity factor, as illustrated in Figure 8.9b. The directivity factor modulates the Δp contribution from both thrust and torque. Since both thrust and torque forces scale with the square of the effective velocity at a given blade section, the thrust-to-torque ratio remains constant across the investigated Mach numbers. Nevertheless, it should be noted that the magnitude of the thrust force exceeds that of the torque force, resulting in a greater absolute variation in Δp. Consequently, for the conditions studied here, thrust noise exhibits greater sensitivity to Mach number variations compared to torque noise. As the Mach number increases, the amplitude of the directivity factors remains unchanged, as previosuly shown. The term $\vec{R} \cdot \hat{q}$ undergoes significant alternations between positive and negative values, potentially leading to greater overall fluctuation energy in torque-related noise contributions with respect to thrust. However, since the pressure difference between the blade's upper and lower surfaces due to thrust exhibits a larger absolute variation as the Mach number is increased compared to torque, the resulting greater modulation of source strength leads to a comparable or even higher OSPL due to thrust than torque in the frontal and backward lobes of the thrust.

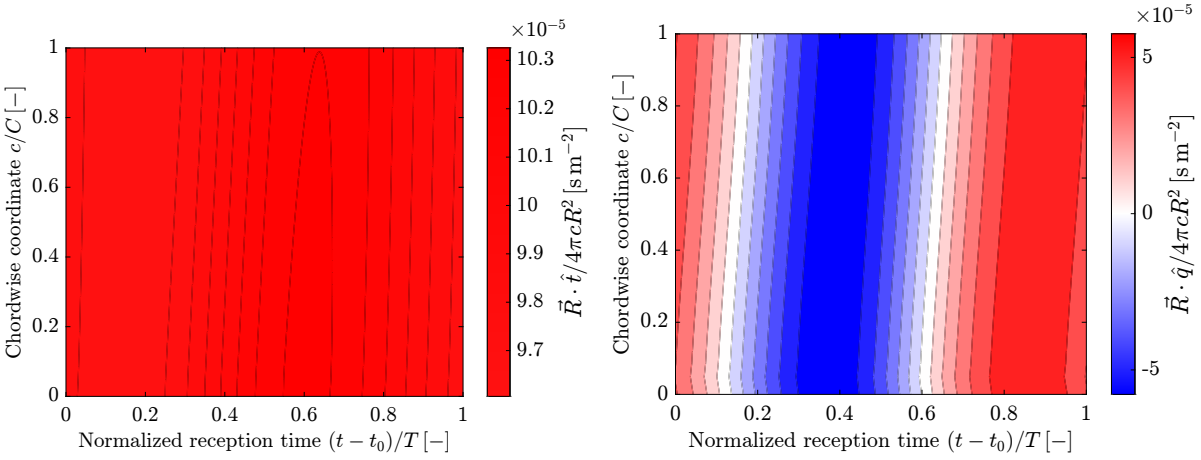

(a) Thrust directivity factor.

(b) Torque directivity factor.

Figure 8.9: Chordwise distribution of the directivity factor of the far-field loading pressure due to thrust (a) and torque (b) at $r/R_p = 0.7$; $M_{ht} = 0.357$, blade 1, $\theta = 30°$.

It is now of interest to understand why the interference between thrust and torque is destructive in the frontal lobe of the thrust, leading to reduced loading noise levels, and constructive in the backward lobe. As evidenced by Kingan and Parry [50], the blades' radial pressure waveforms provide a wealth of information on the mechanism of noise emissions. Hence, Figure 8.10 displays the thrust and torque far-field loading radial pressure contours for blade 1 at $M_{ht} = 0.357$ at the directivity angle $\theta = 30°$. P^*_{LF} and P_{LF} are defined from Equation 5.16 as, respectively:

$$P^*_{LF}(r_o, \vec{r}, t) = \int_{-\infty}^{\infty} \Delta p(\gamma_o + Ut - M_r R, r_o) \frac{\vec{R} \cdot \hat{n}}{4\pi cR^2} \, d\gamma \tag{8.1}$$

and:

$$P_{LF}(r_o, \vec{r}, t) = \frac{\partial}{\partial t} \int_{-\infty}^{\infty} \Delta p(\gamma_o + Ut - M_r R, r_o) \frac{\vec{R} \cdot \hat{n}}{4\pi cR^2} \, d\gamma \tag{8.2}$$

Figure 8.10a and Figure 8.10c present the radial distributions of the far-field loading pressure for thrust and torque, respectively, prior to the application of the time derivative. Thus, the plots reflect the modulation effects of Δp induced by the directivity factors shown in Figure 8.9, along

with the integration over γ, which either amplifies or attenuates the integral value. Notably, the maximum stretching in γ occurs at $(t-t_0)/T \approx 0.4$. Upon applying the time derivative and computing the radial contours for thrust and torque, the resulting distributions are illustrated in Figure 8.10b and Figure 8.10d, respectively. It is observed that, while the radial pressure fluctuations for thrust remain positive up to $(t-t_0)/T \approx 0.4$, those for torque exhibit negative values over the same time interval. Beyond this point, the signs reverse, with thrust fluctuations becoming negative and torque fluctuations becoming positive. This phase difference between thrust and torque sources leads to partial cancellation, thereby reducing the overall loading noise levels when both contributions are considered.

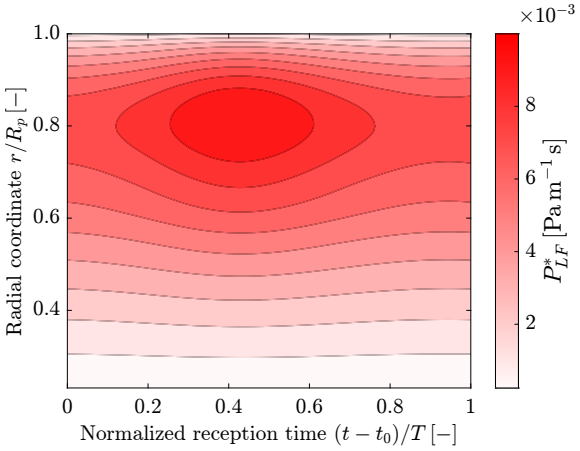

(a) Thrust, without $\partial/\partial t$.

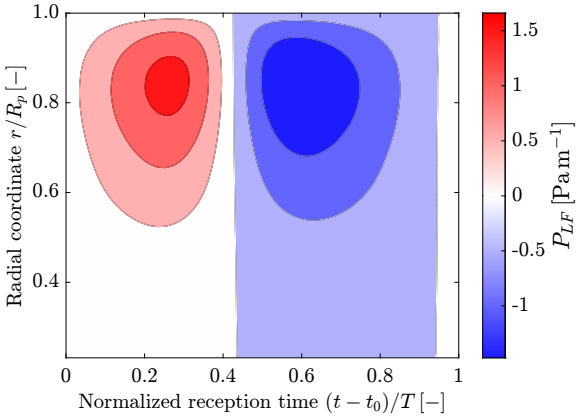

(b) Thrust, with $\partial/\partial t$.

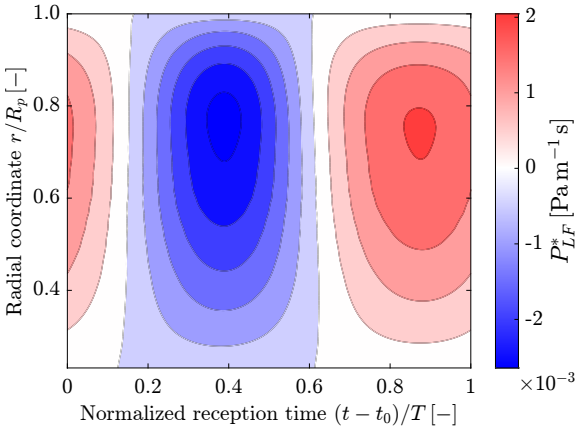

(c) Torque, without $\partial/\partial t$.

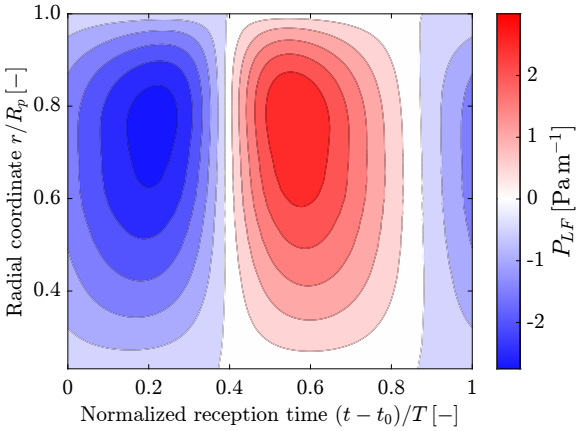

(d) Torque, with $\partial/\partial t$.

Figure 8.10: Thrust (top row) and torque (bottom row) far-field loading pressure radial distributions without (left) and with (right) the time derivative; $M_{ht} = 0.357$, blade 1, $\theta = 30°$.

On the other hand, at the axial directivity angle $\theta = 150°$, the interference between thrust and torque becomes constructive, as demonstrated in Figure 8.11. The radial distributions of thrust and torque before the time derivative is applied, shown in Figure 8.11a and Figure 8.11c, reveal that the torque P^*_{LF} distribution remains largely unchanged compared to that at $\theta = 30°$, maintaining similar amplitude and shape. However, the thrust P^*_{LF} distribution exhibits a similar amplitude to the one at $\theta = 30°$, but with an opposite sign. The similarity in the torque signs arises from the symmetry of $\vec{R} \cdot \hat{q}$ around the vertical axis, since the torque vector is tangential to the propeller plane. In contrast, the sign of $\vec{R} \cdot \hat{t}$ varies depending on whether the observer is positioned in front of or behind the

propeller. After applying the time derivative, the thrust and torque P_{LF} distributions are shown in Figure 8.11b and Figure 8.11d, respectively. It is evident that the torque distribution retains a similar shape and values to that at $\theta = 30°$, while the thrust distribution exhibits a similar shape but with opposite values. Consequently, the thrust and torque radial distributions are in phase, leading to constructive interference and higher loading noise levels. It is therefore clear that the reason for the switch in the interference mechanism between the frontal and backward lobes of the thrust lies in the change of sign of the thrust directivity factor.

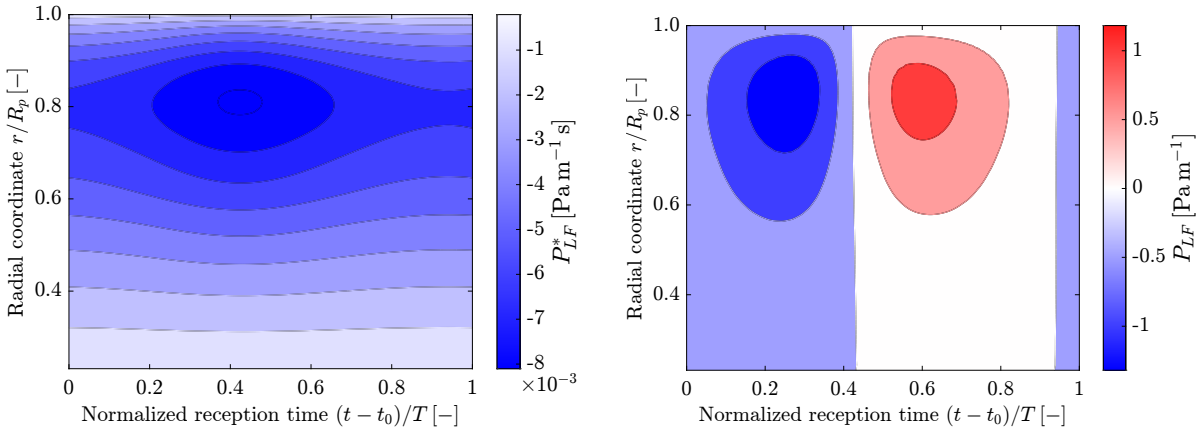

(a) Thrust, without $\partial/\partial t$.

(b) Thrust, with $\partial/\partial t$.

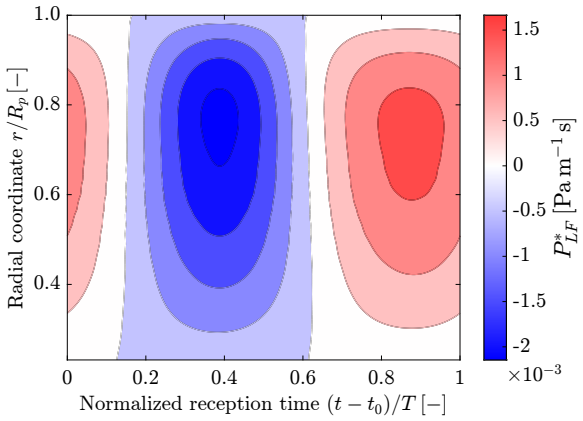

(c) Torque, without $\partial/\partial t$.

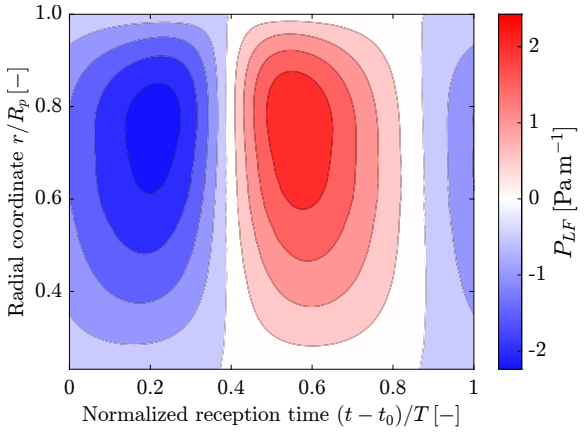

(d) Torque, with $\partial/\partial t$.

Figure 8.11: Thrust (top row) and torque (bottom row) far-field loading pressure radial distributions without (left) and with (right) the time derivative; $M_{ht} = 0.357$, blade 1, $\theta = 150°$.

Finally, the sudden drop in loading noise observed at $\theta = 60°$ for $M_{ht} = 0.652$ and $M_{ht} = 0.8$ requires further clarification. To this end, Figure 8.13 presents relevant parameters for blade 1 at $M_{ht} = 0.8$ and $\theta = 60°$. The chordwise distributions of the far-field loading directivity factor at the radial positions $r/R_p = 0.3$ and $r/R_p = 0.9$ are depicted in Figure 8.12a and Figure 8.12b, respectively. It is evident that, within a certain time interval during the revolution, the directivity factor exhibits opposite signs between these two radial positions. This behavior arises from the realistic blade geometry, which causes the relative orientation of $\vec{R}$ and $\hat{n}$ to yield a negative dot product at certain blade sections while remaining positive at others. The plot of P^*_{LF} provided in Figure 8.12c, representing the far-field loading pressure before the time derivative is applied, indicates that around $(t-t_0)/T = 0.25$, the inboard blade sections exhibit negative instantaneous pressure values, whereas the mid-span and outboard sections display positive values. This phenomenon

results from the sign variation of the directivity factor across the blade, which modulates the Δp term differently at each radial location—negatively for inboard stations and positively for the others. Notably, near $(t-t_0)/T = 0.25$, γ undergoes maximum stretching. As previously discussed, an increased integration range enhances (in absolute terms) the integral value, significantly amplifying the phase shift in P^*_{LF} between different radial locations on the blade. Consequently, applying the time derivative to compute P_{LF}, as illustrated in Figure 8.12d, results in negative instantaneous acoustic pressure values at inboard stations and positive values at outboard stations during certain time intervals. This phase discrepancy induces destructive interference, leading to a local reduction in the OSPL of loading noise.

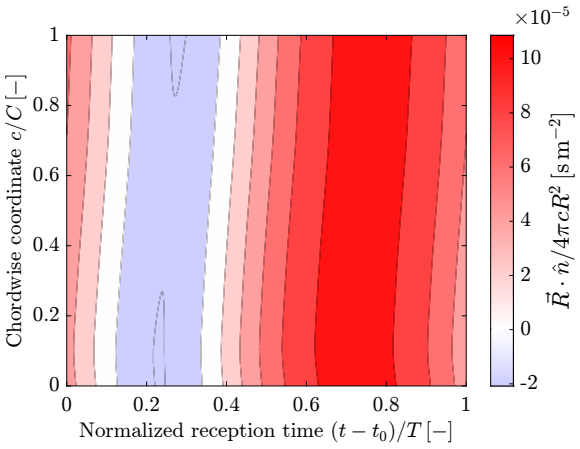

(a) Directivity factor, $r/R = 0.3$.

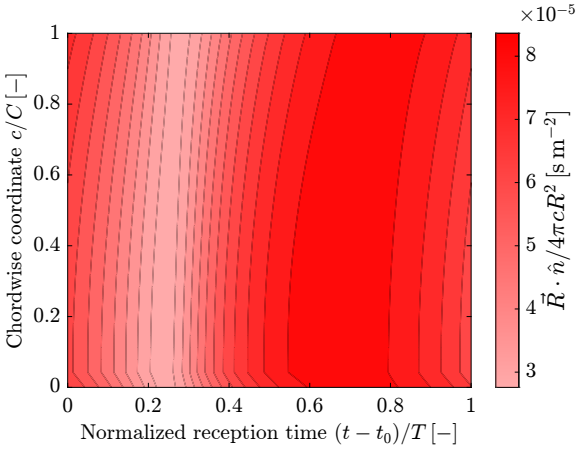

(b) Directivity factor, $r/R = 0.9$.

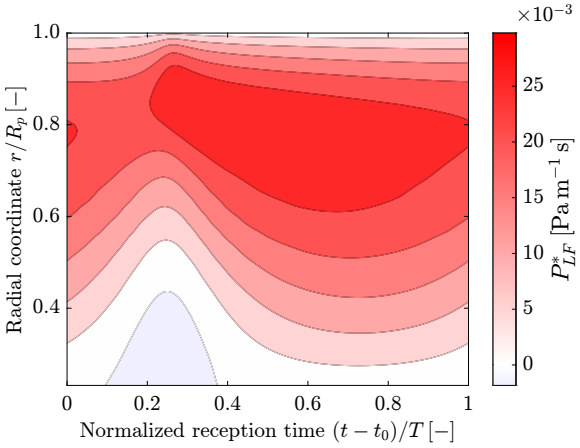

(c) Far-field loading pressure, without $\partial/\partial t$.

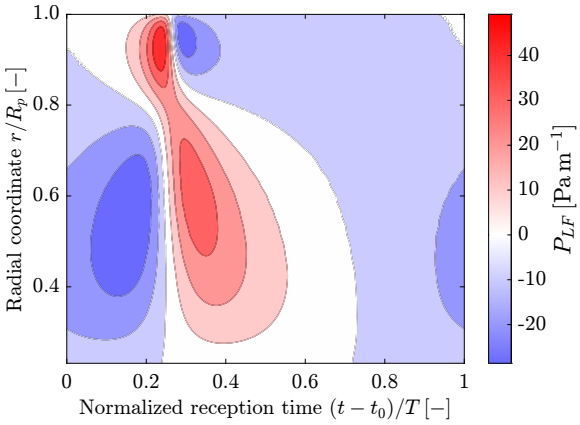

(d) Far-field loading pressure, with $\partial/\partial t$.

Figure 8.12: Chordwise far-field loading directivity factor at two radial stations (top row) and far-field loading pressure radial distributions without (c) and with (d) the time derivative; $M_{ht} = 0.8$, blade 1, $\theta = 60°$.

However, it is necessary to clarify why this destructive interference does not occur at the axial directivity angle $\theta = 120°$. This analysis is presented in Figure 8.13. The directivity factors at $r/R_p = 0.3$ and $r/R_p = 0.9$ are shown in Figure 8.13a and Figure 8.13b, respectively. Although a sign change between these two radial positions is evident around $(t-t_0)/T = 0.75$, this reversal occurs during the period of maximum γ contraction rather than at maximum stretching. Consequently, when the integration over γ is performed to obtain P^*_{LF}, as shown in Figure 8.13c, the contraction of the acoustic chord at $(t-t_0)/T = 0.75$ results in a lower integral value (in absolute terms), thereby

reducing the phase difference between pressure signals across different radial positions. As a result, no significant phase shift is observed between the inboard and outboard stations in P_{LF}, as displayed in Figure 8.13d. Instead, the radial pressure signals at a given time reinforce each other, leading to constructive interference and an increase in the OSPL of loading noise.

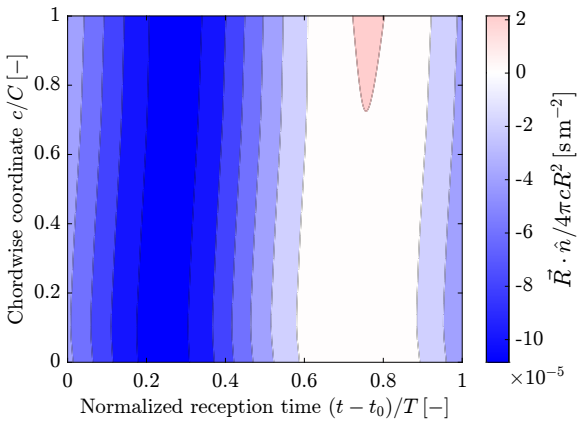

(a) Directivity factor, $r/R = 0.3$.

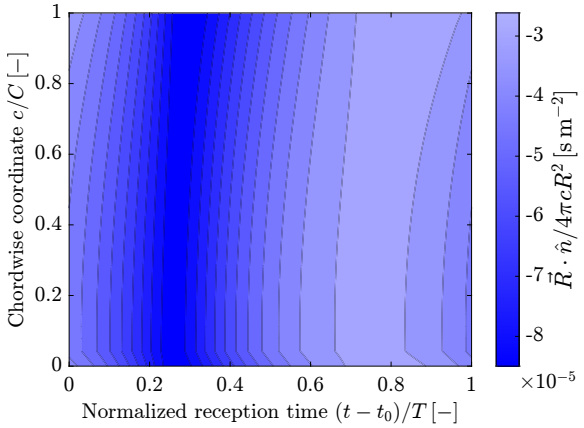

(b) Directivity factor, $r/R = 0.9$.

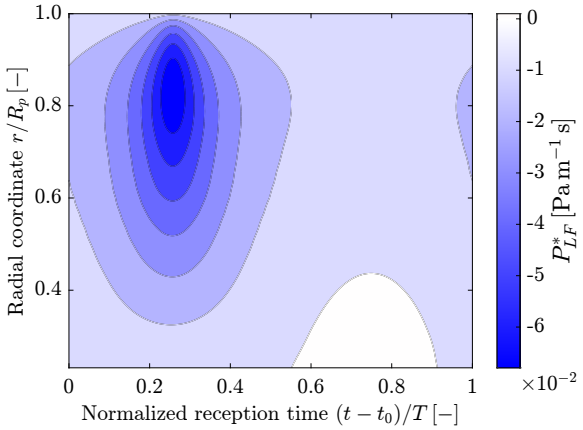

(c) Far-field loading pressure, without $\partial/\partial t$.

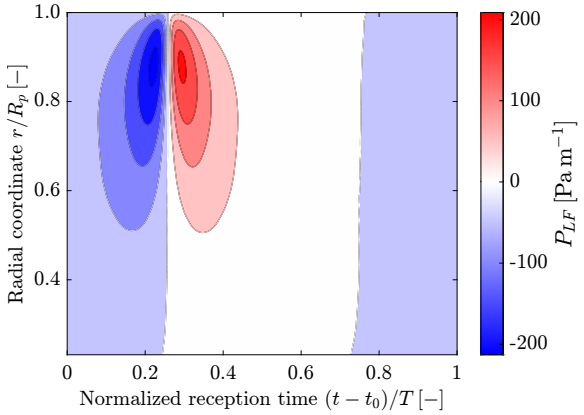

(d) Far-field loading pressure, with $\partial/\partial t$.

Figure 8.13: Chordwise, far-field loading directivity factor at two radial stations (top row) and far-field loading pressure radial distributions without (c) and with (d) the time derivative; $M_{ht} = 0.8$, blade 1, $\theta = 120°$.

Figure 8.14 explains why no reduction in loading noise occurs at $\theta = 60°$ for $M_{ht} = 0.357$.

The radial distribution of the far-field loading pressure before applying the time derivative is shown in Figure 8.14a. As previously discussed, the directivity factor for different Mach numbers exhibits the same amplitude but with a phase shift. However, the stretching of γ—which, in this case, reaches its maximum around $(t-t_0)/T = 0.38$—is significantly more pronounced at higher Mach numbers. At $M_{ht} = 0.357$, this stretching remains relatively small. Consequently, while a phase shift in P^*_{LF} between inboard and outboard stations is present, it is not as strongly amplified as in Figure 8.12c. As a result, even though applying the time derivative to compute the far-field loading pressure P_{LF} reveals some phase shift across different radii at specific time intervals, as shown in Figure 8.14b, this phase shift remains relatively minor, leading to no significant reduction in loading noise.

Among the four Mach numbers analyzed, a significant phase shift between the pressure signals at different radii at the observer angle $\theta = 60°$ was observed only for $M_{ht} = 0.652$ and 0.8. No notable

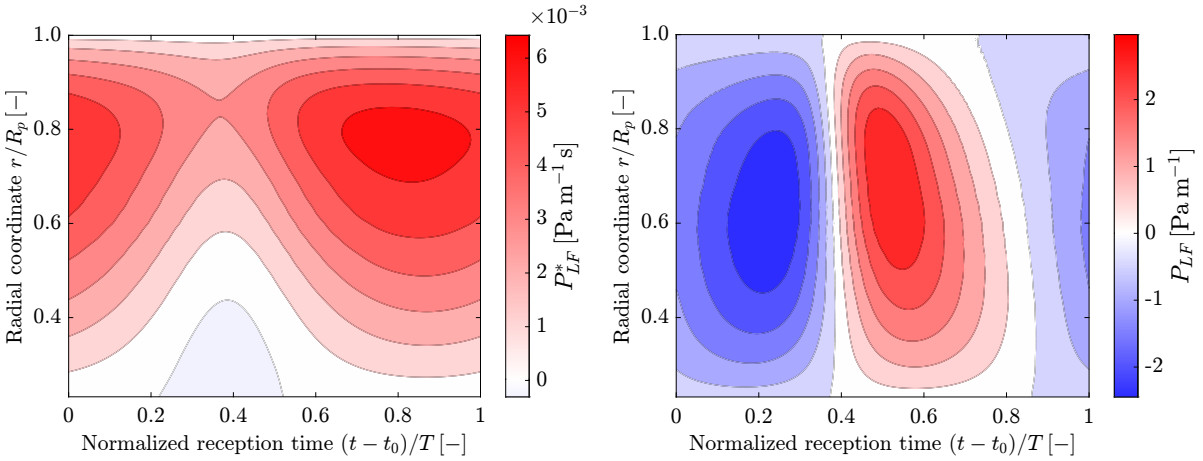

(a) Far-field loading pressure, without $\partial/\partial t$.

(b) Far-field loading pressure, with $\partial/\partial t$.

Figure 8.14: Radial distribution of the far-field loading pressure without (c) and with (d) the time derivative; $M_{ht} = 0.357$, blade 1, $\theta = 60°$.

reduction in loading noise was observed for $M_{ht} = 0.357$ and 0.505. This behavior is attributed to the increased γ integration range over a given time interval, which amplifies the integral values, thereby enhancing the phase shift between radii induced by the directivity factor.

These findings underscore two key points. First, compact-source models are inadequate for predicting noise levels at high-subsonic Mach numbers. It is instead appropriate to account for chordwise distributions of noise sources as well. The acoustic planform illustrates the non-compactness of the source at high tip speeds, highlighting that the acoustic planform must be considered over the blade's physical planform. Second, in principle, experimental results obtained at lower Mach numbers cannot be directly scaled to the high Mach numbers characteristic of full-scale propellers in forward flight.

9

WAKE ENCOUNTER EFFECTS

This chapter investigates the influence of wake encounter on the propeller aeroacoustic performance. The aerodynamic loading of the propeller is discussed in Section 9.1, while a physical interpretation of its noise signature is provided in Section 9.2.

9.1. AERODYNAMIC PERFORMANCE

The inflow profile required as input for the engineering method in non-uniform flow was generated by Van Arnhem et al. [21] by positioning a straight, untapered and untwisted wing upstream of the propeller at a vertical location of $z/R_p = -0.5$. The axial distance between the wing's trailing edge and the propeller is $\Delta x = 3.2R_p$. This configuration is illustrated schematically in Figure 9.1a and Figure 9.1b. As discussed in Section 6.2, inflow perturbations induce a variation in the local advance ratio. This variation can be attributed to changes in the axial inflow (Figure 9.1c), tangential inflow (Figure 9.1d), and their combined effects (Figure 9.1e). It is evident that the axial velocity field change is the most significant, resulting in a reduction of $\Delta J_a = 0.08$ due to a velocity deficit of $0.9V_\infty$, as shown in Figure 7.3. Conversely, the change in the in-plane velocity field is minimal. Therefore, $\Delta J_t \approx 0$. As a result, the maximum reduction in advance ratio is 10% of the free-stream value.

The reduced effective advance ratio at the location of wake encounter leads to a decrease in the sectional inflow angle, resulting in an increase in the angle of attack for a given pitch setting. Consequently, the propeller's self-induced velocity increases. However, the inflow velocity deficit reduces the axial velocity perceived by the blade sections, and this reduction is just slightly larger than the increase in induced velocity. As a result, the maximum chord-based Reynolds number for each M_{ht} remains nearly unchanged compared to the values presented in Table 8.1 for uniform flow. Specifically, the percentage decrease with respect to the uniform flow figures is on the order of 10^{-3}.

Figure 9.2 depicts the differences in the local thrust and torque coefficients in case of wake encounter compared to the uniform flow condition. As noted in Section 6.2, the loading increase following the reduction in advance ratio (and the consequent increase in local angle of attack) is particularly pronounced in two regions of the disk, corresponding to where the wake interacts with the highest-loaded blade sections, which are most sensitive to changes in the local advance ratio. Thus, the largest loading variation occurs near $r/R_p = 0.8$. The extent of deviation from uniform flow in the sectional loading is influenced by the propeller advance ratio, with higher advance ratios leading to greater variations [23]. Nevertheless, the overall azimuthal distribution remains consistent.

While the absolute magnitude of the change in loading provides valuable insights, Figure 9.3 focuses on the relative deviation represented as a ratio with respect to the uniform flow loading. Figure 9.3a depicts the azimuthal variation of this ratio for the thrust coefficient at three radial stations of the propeller operating in the disturbed flow field. At $r/R_p = 0.3$, the effect of the wake

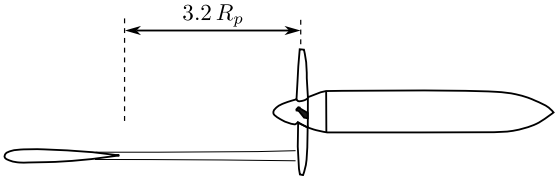

(a) Schematic of wake encounter, side view (adapted from [22]).

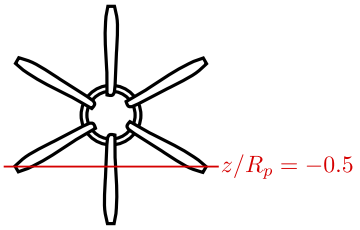

(b) Schematic of wake encounter, front view (adapted from [22]).

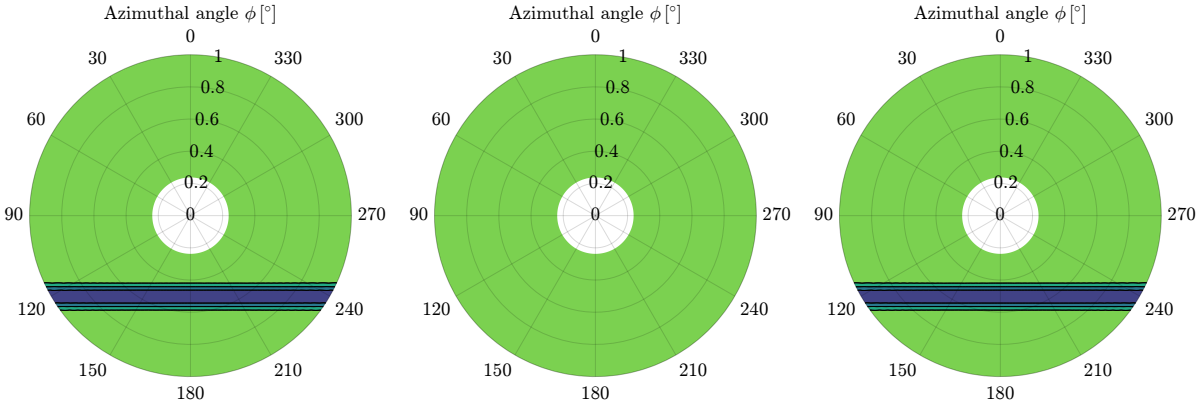

(c) Change in advance ratio due to axial inflow.

(d) Change in advance ratio due to tangential inflow.

(e) Overall change in advance ratio.

Figure 9.1: Wake encounter schematic (a,b) and change in local advance ratio (c,d,e) resulting from wake encounter.

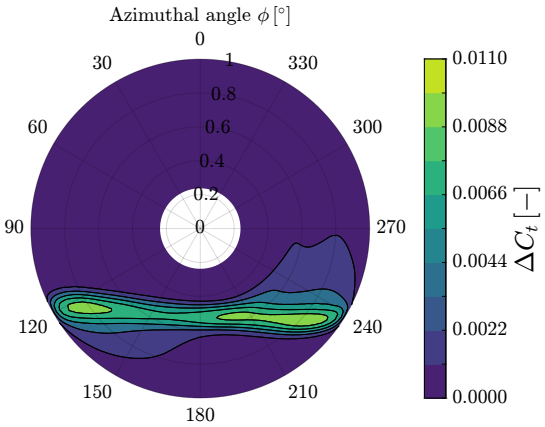

(a) Change in local thrust coefficient.

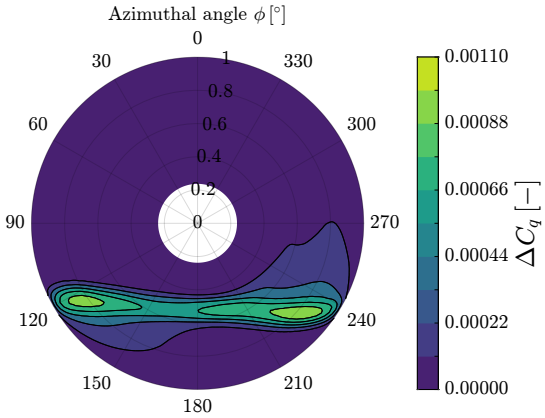

(b) Change in local torque coefficient.

Figure 9.2: Azimuthal change in local thrust (a) and torque (b) coefficient due to wake encounter with respect to uniform inflow.

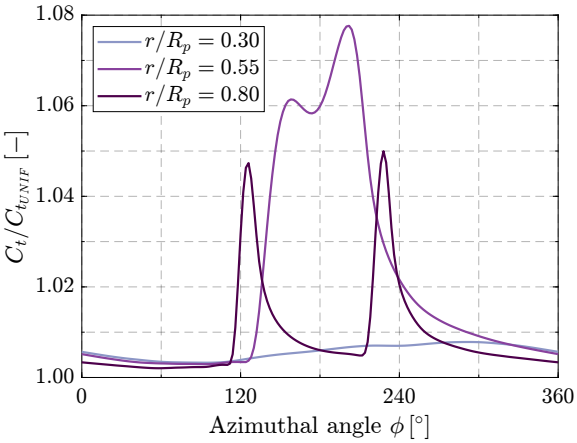

(a) Ratio of thrust coefficients for three radial stations.

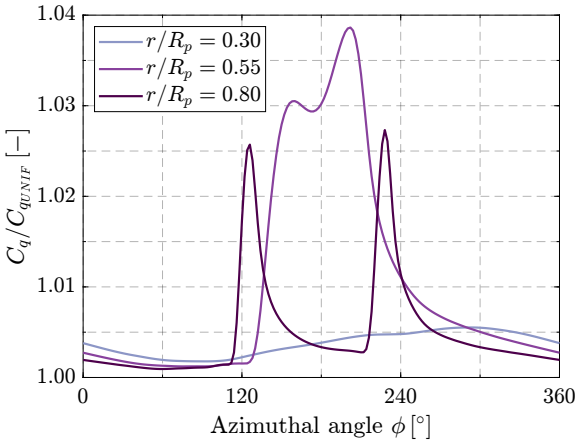

(b) Ratio of torque coefficients for three radial stations.

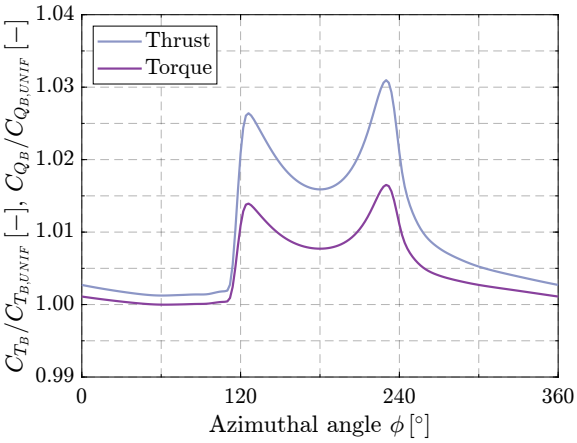

(c) Ratio of blade thrust and torque coefficients.

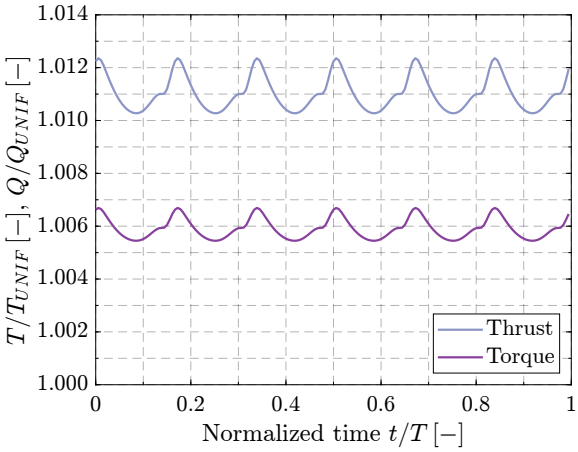

(d) Ratio of propeller thrust and torque.

Figure 9.3: Ratio of sectional thrust (a) and torque (b) coefficients, blade thrust and torque coefficients (c) and propeller thrust and torque (d) between wake encounter and uniform flow cases.

encounter is negligible, as wake impingement occurs further down on the disk. At $r/R_p = 0.55$, two peaks are observed. Specifically, a thrust increase occurs at $\phi = 160°$, where this radial station first intersects the wake region. A peak is reached, and as the section moves towards an azimuthal region with a lower ΔJ, the loading deviation diminishes. At $\phi = 200°$, a second thrust enhancement occurs. The second peak is higher than the first, as the sectional loading has already adapted to the new flow conditions after the first peak. The maximum positive deviation from the uniform flow condition reaches just below 8%. Since the azimuthal locations where the non-uniform flow has the highest effect are close for mid-span sections, the two peaks appear closely spaced. At $r/R_p = 0.8$, the two peaks are more distinct, with the thrust enhancement reaching up to 5% of the undisturbed value, which is lower than at $r/R_p = 0.55$ due to the higher sectional thrust under uniform flow conditions locally.

The same analysis is performed for the torque coefficient in Figure 9.3b, revealing similar trends to those observed for thrust. The maximum torque coefficient enhancements for $r/R_p = 0.55$ and $r/R_p = 0.8$ are just below 4% and approximately 2.5%, respectively, relative to their undisturbed values.

Figure 9.3c shows the ratio of the blade thrust and torque coefficients to their respective uniform flow values, plotted against the azimuth. The maximum deviations in thrust and torque from their uniform flow values are 3% and 1.5%, respectively. Clearly, at the analyzed wake encounter location, the integral blade loads vary twice per period. As noted by Van Arnhem [22], if the wake location is at $z/R_p = -1$, the loading fluctuation occurs once per revolution instead. From an aeroacoustic standpoint, this influences the dominant frequencies of propeller noise.

Figure 9.3d depicts the ratio of the integral propeller thrust and torque to their values in uniform flow over one revolution. Six distinct peaks are identifiable, corresponding to the number of blades of the XPROP-S. The plot emphasizes the periodic nature of the fluctuations, with the frequency corresponding to the blade-passing frequency. At the blade-passing frequency, fluctuations of 1.2% of the propeller thrust and 0.7% of the torque can be observed.

Since this thesis seeks to evaluate the relative significance of steady and unsteady components of the forces on noise emissions under a wake encounter condition, Figure 9.4 presents the time-averaged and fluctuating components (Figure 9.4a and Figure 9.4b) of the pressure force coefficient (Figure 9.4c). The corresponding steady, unsteady, and overall (steady+unsteady) pressures are subsequently incorporated into Hanson's equations, introduced in Section 5.2. Notably, the steady component of the pressure coefficient at the most loaded blade sections reaches values two orders of magnitude greater than its unsteady counterpart, indicating its aerodynamic dominance. This raises the question of how each component influences the propeller's aeroacoustic signature, which will be explored in Section 9.2.

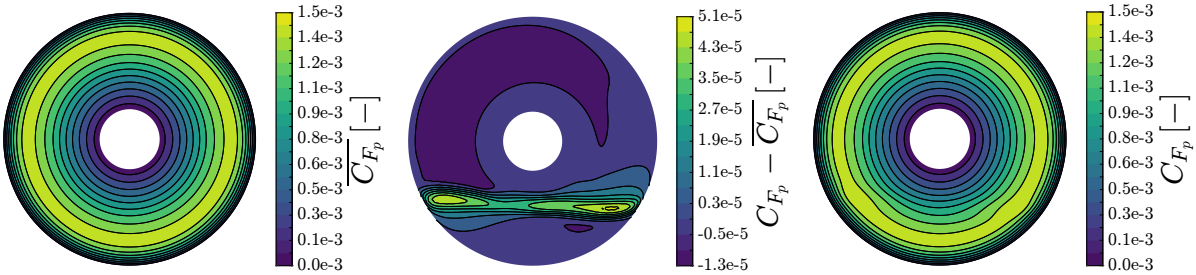

(a) Time-averaged component of the pressure force coefficient.

(b) Fluctuating component of the pressure force coefficient.

(c) Pressure force coefficient (time-averaged + fluctuating).

Figure 9.4: Time-averaged (a) and fluctuating (b) components of the pressure force coefficient (c) resulting from wake encounter.

Table 9.1 presents the percentage variation of the main propeller performance metrics in the

wake encounter scenario compared to the uniform flow values. The observed increases in sectional thrust and torque lead to a 1% and 0.49% rise in propeller thrust and power, respectively. Since the thrust increase exceeds the power increase, propeller efficiency improves by 0.5%. The change in torque differs between the advancing and the retreating sides, resulting in the generation of in-plane forces. The side force (C_Y) and normal force (C_N) coefficients are 4.212×10^{-4} and -1.450×10^{-4}, respectively. Therefore, the magnitudes of the side force and normal force are, respectively, 0.15% and 0.05% of the propeller thrust in uniform flow. Although the change in integral propeller performance is minor due to the relatively small disk region affected by the wake, the abrupt variations in blade loading over the azimuth are expected to notably influence the noise emissions [10, 28].

Flow condition	C_T	C_P	η	C_Y	C_N
Uniform flow	0.2834	0.3183	0.7125	0	0
Wake encounter, $z/R_p = -0.5$	0.2863	0.3198	0.7161	4.212×10^{-4}	-1.450×10^{-4}
Δ%	1.00%	0.47%	0.50%	–	–

Table 9.1: Propeller performance metrics under uniform flow conditions and wake encounter.

9.2. AEROACOUSTIC PERFORMANCE

Prior to the aeroacoustic analysis, a sensitivity study is conducted to determine the appropriate number of time steps per period for the computations. The findings of this study are discussed in detail in Section A.2. The chosen number of time steps per period is 600, which ensures a deviation in the maximum p'_{RMS} of less than 0.1% (as per Equation 6.2) and guarantees that the sampled data accurately represents the relevant acoustic frequencies without any aliasing.

9.2.1. NOISE DIRECTIVITY IN THE PROPELLER PLANE

Figure 9.5 illustrates the impact of the wake encounter on the azimuthal directivity of the thrust-specific sound pressure level for different helical tip Mach numbers. The axial directivity angle remains constant at $\theta = 90°$, aligning with the propeller plane. Figure 9.5a presents the noise emissions in the yz-plane under uniform flow conditions, whereas Figure 9.5b corresponds to the wake encounter scenario. In the uniform flow case, the directivity pattern is axisymmetric, as expected. However, in the wake encounter case, variations in the azimuthal pattern are evident. At $M_{ht} = 0.357$, the maximum reduction, approximately 7 dB compared to the undisturbed flow case, occurs at $\phi = 270°$. Noticeable reductions are also observed at $\phi = 0°$, $\phi = 90°$, and $\phi = 180°$, while the non-uniform flow case exhibits a peak increase of 6.5 dB in noise levels at $\phi = 225°$. As the Mach number increases, the difference in noise emissions between the two flow conditions diminishes. At $M_{ht} = 0.8$, the TSSP decreases by only 0.25 dB at $\phi = 180°$, where the largest decrease occurs, and increases by approximately the same amount at $\phi = 225°$, marking the location of maximum rise in noise levels. Notably, the azimuthal position of largest reduction in noise differs with respect to $M_{ht} = 0.357$ (although the difference with $\phi = 270°$ is marginal), indicating a different interference between loading and thickness noise sources. Moreover, it is noted that while the isolated propeller exhibits a TSSP variation of 39 dB between the lowest and highest Mach numbers considered, a variation in the range 33-46 dB is found when exposed to wake impingement. In general, wake encounter amplifies the sensitivity of noise to the operating condition at observer positions where noise levels decrease compared to uniform flow; conversely, the sensitivity is mitigated. This behavior arises from the fact that, as the Mach number increases, the variation in noise emissions relative to uniform flow diminishes.

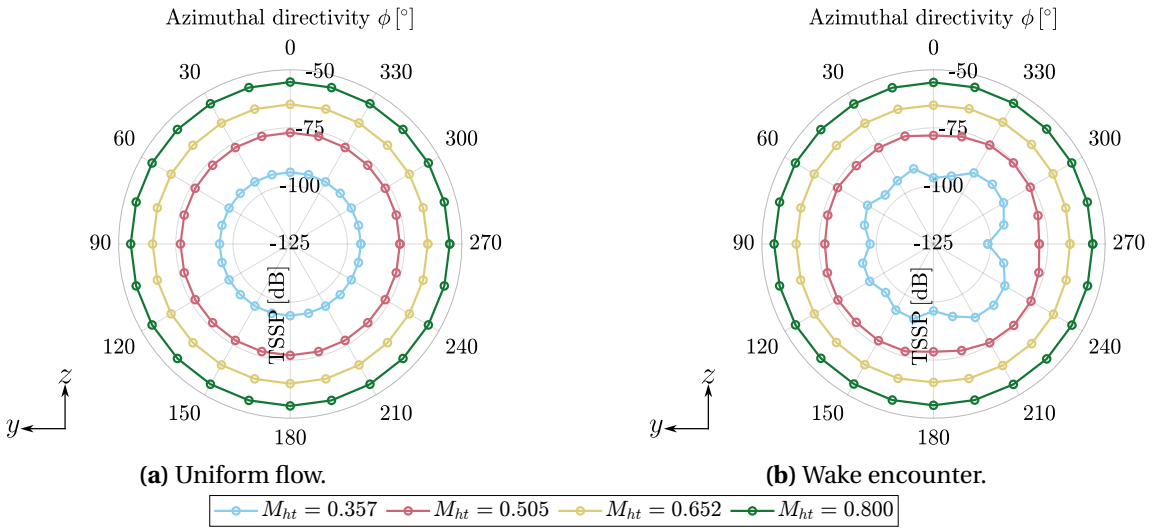

(a) Uniform flow. **(b)** Wake encounter.

Figure 9.5: Effect of the wake encounter on the azimuthal directivity of the thrust-specific sound pressure level at different helical tip Mach numbers; $\theta = 90°$.

Figure 9.6 depicts the influence of the wake encounter on the azimuthal directivity of the overall sound pressure level of various noise sources computed in the BPF range $0.9 \leq \text{BPF} \leq 10$ at $M_{ht} = 0.357$ and $M_{ht} = 0.8$. At $M_{ht} = 0.357$, the noise emissions resulting from the flow non-uniformity, shown in Figure 9.6b, exhibit significant deviations compared to the uniform flow case presented in Figure 9.6a. Since variations in source speed were not considered in the wake encounter case, as outlined in Section 7.2, the thickness noise remains unchanged between the two cases. For both Mach numbers, loading noise shows a peak increase at $\phi = 225°$, amounting to 7 dB for $M_{ht} = 0.357$ and 0.4 dB for $M_{ht} = 0.8$. However, unlike in the uniform flow scenario, the interaction between loading and thickness noise is not consistently constructive. Instead, their interference becomes destructive at several observer angles, leading to a reduction in total noise locally. This phenomenon is attributed to a phase shift in the loading pressure waveform, warranting further investigation. Consistent with the observations in Figure 9.5, at $M_{ht} = 0.8$, the noise levels remain largely unaffected. Notably, in both the inflow conditions, the interference between loading and thickness noise remains constructive.

To further investigate the impact of wake encounter on loading noise, Figure 9.7 presents the loading noise results obtained by inputting the time-averaged, fluctuating, and total aerodynamic loading of the propeller into the aeroacoustic solver, as illustrated in Figure 9.4. At $M_{ht} = 0.357$, the SPL at the first BPF and the OSPL evaluated in the BPF range $0.9 \leq \text{BPF} \leq 10$ are depicted in Figure 9.7a and Figure 9.7b, respectively. It is observed that while the steady loading noise exhibits only a minor increase when considering the extended frequency range, the unsteady component experiences a more pronounced rise, with a maximum increase of 3 dB at $\phi = 225°$. This suggests that the noise due to load unsteadiness is radiated at frequencies higher than the BPF more efficiently than the time-averaged one, consistent with literature [10]. Additionally, unsteady loading noise is found to be more prominent on the retreating side of the blade. The interaction between the steady and fluctuating components alternates, resulting in constructive interference at some observer angles and destructive interference at others. The underlying physical explanation for this behavior will be provided. Similar plots are presented for $M_{ht} = 0.8$. Specifically, Figure 9.7c illustrates the SPL at the first BPF, while Figure 9.7d shows the OSPL of the total loading noise along with its mean and fluctuating components. Once again, the steady component remains largely unaffected by the broader frequency range. However, more significant variations are observed in the unsteady loading

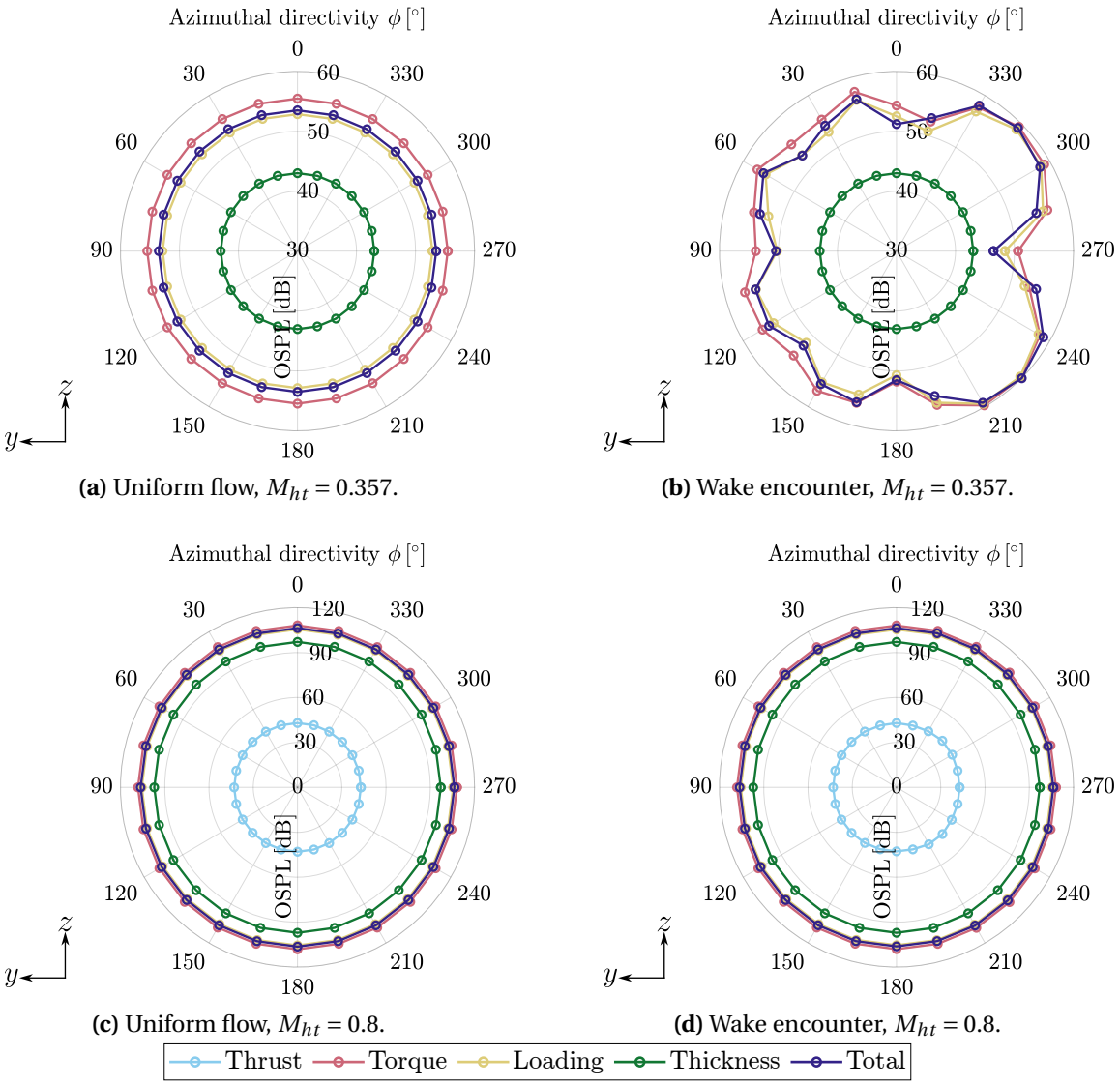

(a) Uniform flow, $M_{ht} = 0.357$.

(b) Wake encounter, $M_{ht} = 0.357$.

(c) Uniform flow, $M_{ht} = 0.8$.

(d) Wake encounter, $M_{ht} = 0.8$.

Figure 9.6: Effect of the wake encounter on the azimuthal directivity of the overall sound pressure level at $M_{ht} = 0.357$ and $M_{ht} = 0.8$; $\theta = 90°$.

noise levels. A distinct pattern emerges, with unsteady loading noise being more pronounced on the retreating side of the blade. Conversely, on the advancing side, not only are the noise levels lower, but also greater variations between adjacent observers are apparent. The maximum increase in unsteady loading OSPL occurs at $\phi = 225°$, consistent with the trend observed at the lower Mach number, showing an increase of approximately 10 dB compared to the first BPF. It should also be noted that while at $M_{ht} = 0.357$ the steady and unsteady loading noise levels are comparable at multiple azimuthal positions, at $M_{ht} = 0.8$ the steady component becomes dominant. Consequently, while interference effects play a more significant role at the lower Mach number, the directivity pattern at the higher Mach number is primarily governed by the steady component and interference effects are minor.

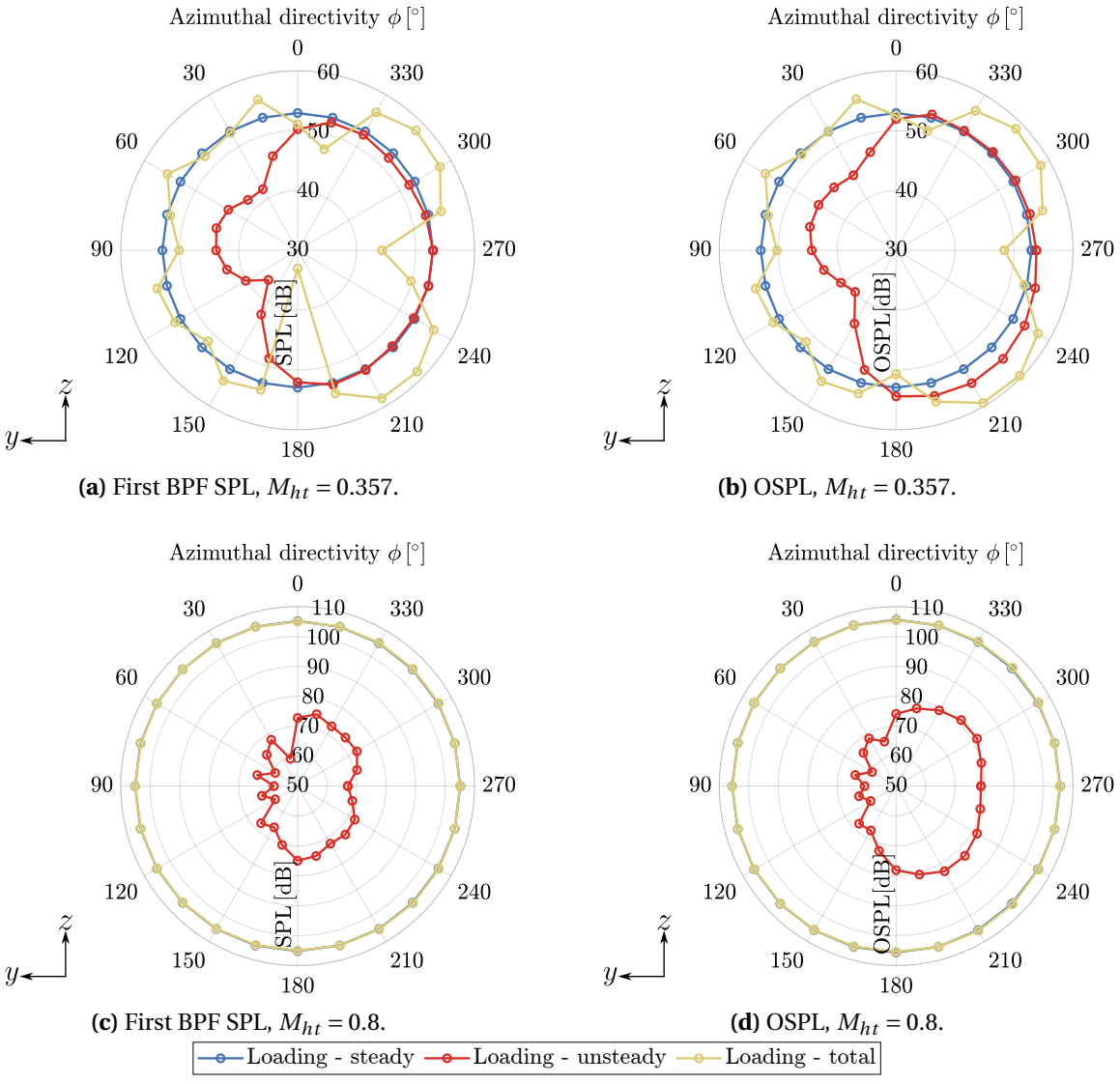

(a) First BPF SPL, $M_{ht} = 0.357$.

(b) OSPL, $M_{ht} = 0.357$.

(c) First BPF SPL, $M_{ht} = 0.8$.

(d) OSPL, $M_{ht} = 0.8$.

Figure 9.7: First BPF SPL and OSPL azimuthal directivity of steady, unsteady and total loading noise under wake encounter conditions at $M_{ht} = 0.357$ and $M_{ht} = 0.8$; $\theta = 90°$.

The underlying reason for this behavior lies in the fact that, although both the mean and fluctuating components of the aerodynamic loading in this study scale similarly with increasing Mach number, the amplitude of the waveforms does not scale the same way, as will be shown later.

A physical interpretation of the aeroacoustic signature can be gained by examining the pres-

sure waveforms. Figure 9.8 presents the steady, unsteady, and total loading pressure waveforms for individual blades and the entire propeller at $M_{ht} = 0.357$ and $\phi = 225°$. It is noteworthy that the smooth, continuous oscillations in the steady loading waveforms of the blades result in effective destructive interference. Conversely, the unsteady loading waveforms exhibit a pronounced impulsive nature due to the wake encounter, leading to an increased fluctuation range in the propeller's waveform. At this location, the steady and unsteady loading noise components of the propeller interfere constructively, thereby amplifying the loading noise levels, as observed in Figure 9.7b.

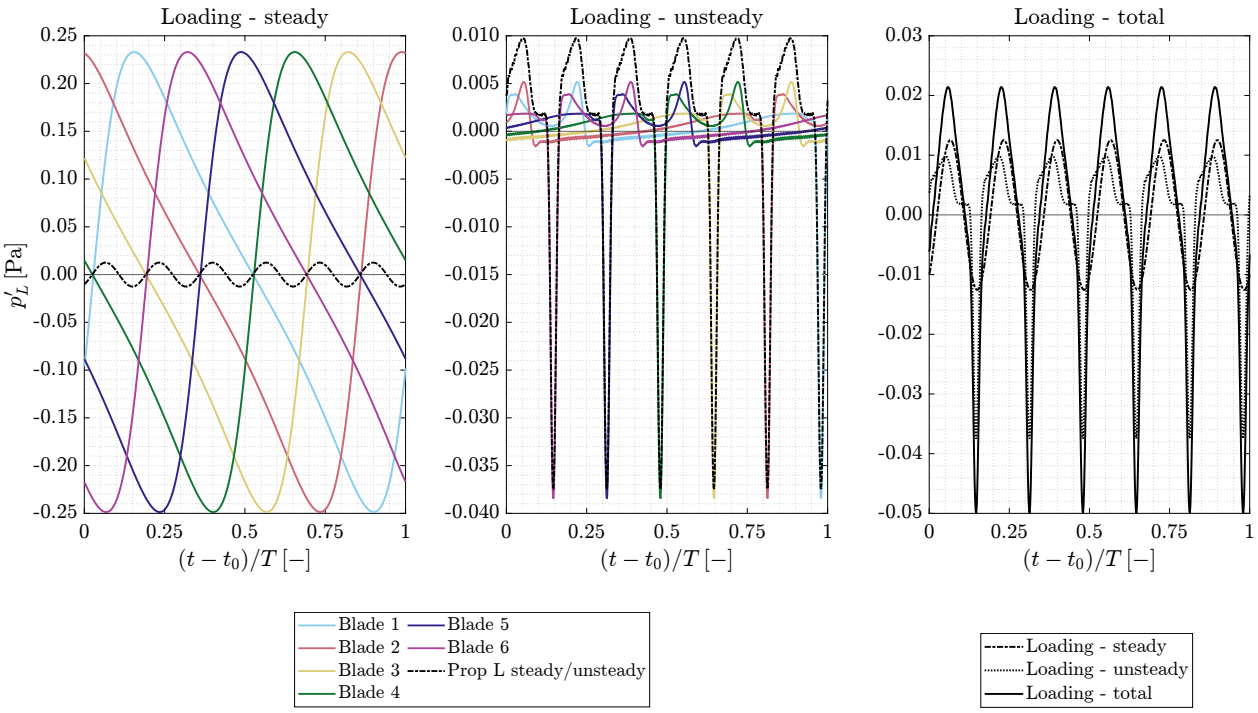

Figure 9.8: Steady, unsteady and total loading pressure waveforms of the individual blades and the propeller; $M_{ht} = 0.357$, $\phi = 225°$, $\theta = 90°$.

To further investigate the unsteady loading pressure at $\phi = 225°$, Figure 9.12 illustrates the radial distribution of unsteady loading pressure fluctuations for blade 1 at $M_{ht} = 0.357$ and the blades' acoustic planform, with a red marker on blade 1. Notably, the wake encounter region exhibits strong fluctuations, displayed in Figure 9.9a, whose sign depends on the directivity factor and the time gradient used in Hanson's equations. The reception time of the most significant fluctuations aligns with the timing of the impulse observed in Figure 9.8. The wake is initially encountered by the outboard radial stations, whereas mid-span radial stations traverse the wake region later but remain within it for a longer duration, as depicted in Figure 9.3a. A second contour region of relatively lower fluctuation magnitudes is observed. This behavior can be attributed to variations in the acoustic chord. The maximum stretching in γ—which occurs with a phase lead of approximately 90° relative to the observer location, as shown in Figure 9.9b— at this azimuthal position coincides with the moment the blade traverses the disk region where a significant portion of the blade (particularly the highly-loaded outboard stations) experiences a load increase (see Figure 9.2). The subsequent contraction in γ partially mitigates the pressure fluctuations on the retreating side of the blade.

The waveforms corresponding to the individual blades and the propeller for steady, unsteady, and total loading noise at $M_{ht} = 0.8$ and $\phi = 225°$ are presented in Figure 9.10. As discussed in Section 8.2, the distinct waveform shape compared to the lower Mach number results from the temporal variation of γ throughout a revolution.

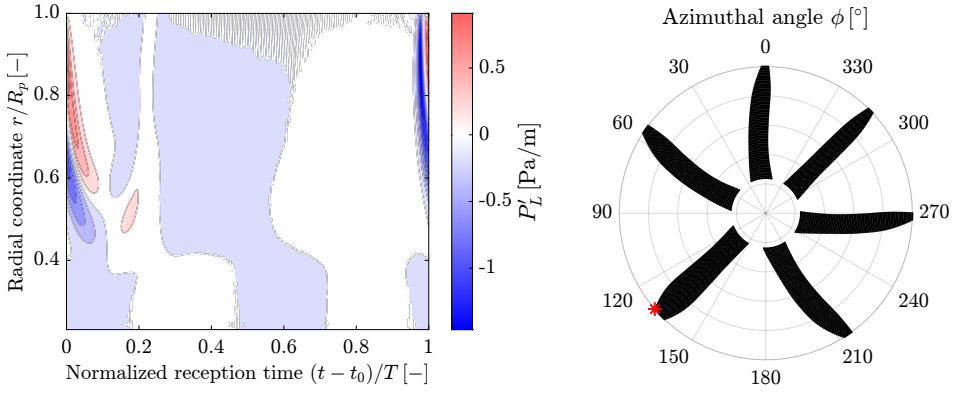

(a) Unsteady loading pressure fluctuations.

(b) $(t-t_0)/T = 0.01$. Red marker on blade 1.

Figure 9.9: Radial distribution of unsteady loading pressure fluctuations for blade 1 (a) and acoustic planform (b); $M_{ht} = 0.357$, $\phi = 225°$, $\theta = 90°$.

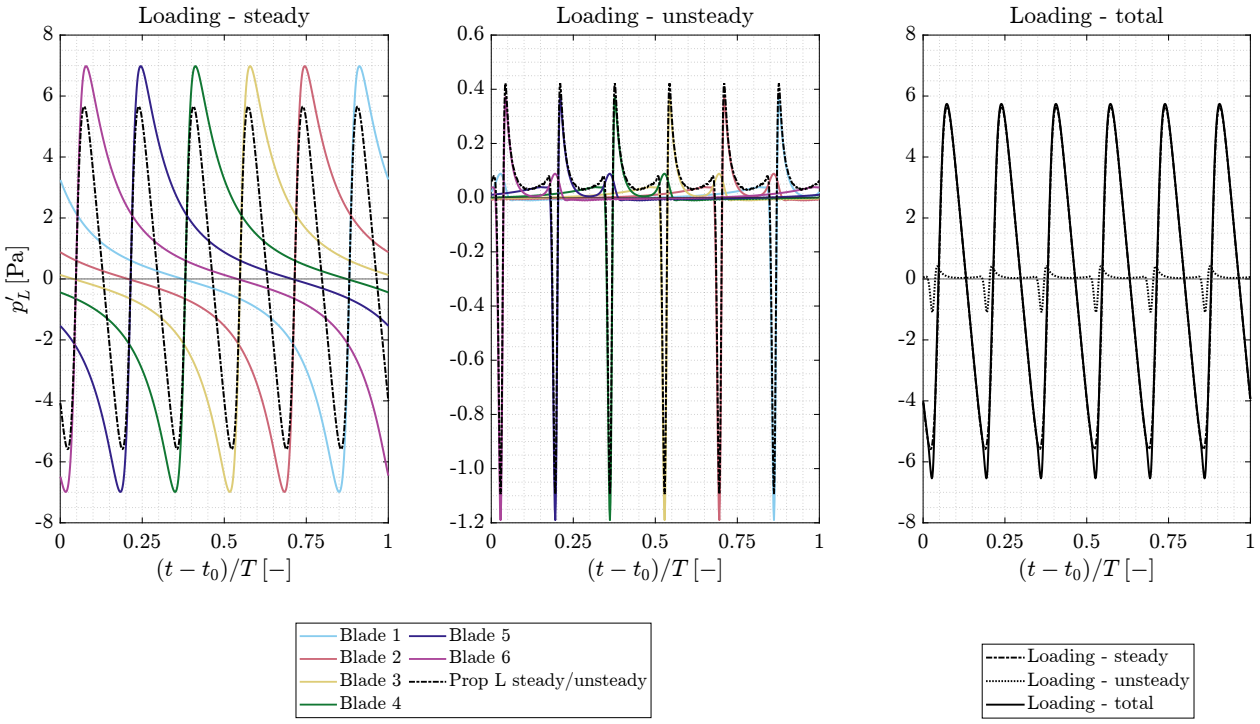

Figure 9.10: Steady, unsteady and total loading pressure waveforms of the individual blades and the propeller; $M_{ht} = 0.8$, $\phi = 225°$, $\theta = 90°$.

As presented in Table 9.2, at the Mach number $M_{ht} = 0.8$, the peak-to-peak amplitude of the steady loading waveform exceeds that of the unsteady component by a factor of more than 7, whereas at $M_{ht} = 0.357$, it is only half as large. Consequently, at the higher Mach number, the total loading waveform is predominantly shaped by the mean component of the loading. As previously discussed, the different waveform shape as the Mach number is increased is attributed to the temporal variation of γ over a revolution, leading to less effective destructive interference between the steady loading waveforms of individual blades at $M_{ht} = 0.8$. Regarding unsteady loading, its peak-to-peak amplitude does not experience the same level of increase as the steady loading component. Since the waveform shape of individual blades is strongly influenced by the aerodynamic loading distribution over the

disk, the effect of a different temporal variation in the acoustic chord at a higher Mach number, which changes the degree of interference between the waveforms of individual blades, is less pronounced for unsteady loading than for steady loading. Consequently, while the ratio between the mean and fluctuating aerodynamic loading remains consistent across different operating conditions, the acoustic significance of the steady component increases with Mach number.

M_{ht}	$A_{\text{L pp, prop}}$ (Steady)	$A_{\text{L pp, prop}}$ (Unsteady)	Ratio (Steady/Unsteady)
0.357	0.0251	0.0473	0.5307
0.8	11.2439	1.5165	7.4114

Table 9.2: Peak-to-peak amplitude of loading pressure fluctuations for the propeller under steady and unsteady loading, along with the steady-to-unsteady ratio at two helical tip Mach numbers; $\phi = 225°$, $\theta = 90°$.

Figure 9.11 presents the loading pressure waveforms at the observer location $\phi = 345°$, where, as shown in Figure 9.7b, noticeable destructive interference between the steady and unsteady noise components occurs. As observed, at this azimuthal position, the propeller's unsteady loading waveform exhibits a higher amplitude than the steady loading one. Moreover, a pronounced de-phasing between the two components is evident, leading to destructive interference and a reduction in total loading noise levels.

The radial loading pressure contours shown in Figure 9.12a indicate that, at this azimuthal position, the radial stations encountering the wake on the retreating side experience larger pressure fluctuation magnitudes than those on the advancing side due to the larger γ. However, owing to the variation in the acoustic chord at this azimuthal location, both contour regions indicating wake encounter are clearly identifiable. This occurs because the maximum stretching of the acoustic chord (see acoustic planform in Figure 9.12b), which is phase-shifted by approximately 15° relative to the disk region where a prominent part of the blade span is subject to a loading increase, enhances the pressure fluctuations on the retreating side, while the acoustic chord is not significantly lower than the physical chord as the blade traverses the inflow velocity deficit region on the advancing side. This results in an efficiently radiating unsteady loading noise. However, the phase shift between the steady and unsteady noise components leads to effective destructive interference between the two sources.

Based on the directivity pattern for $M_{ht} = 0.357$ shown in Figure 9.7b and the waveform analyses at two observer azimuthal positions, a general rule of thumb can be established. At azimuthal locations where a significant stretching of the acoustic chord is mostly in phase with the region of loading increase due to wake encounter affecting a substantial portion of the blade span (particularly the highly-loaded outboard stations), unsteady loading noise exhibits a significant amplitude and, most importantly, remains largely in phase with steady loading noise. As a result, constructive interference occurs. Since the maximum acoustic chord stretching occurs with a phase lead of approximately 90° relative to the observer's position, this effect becomes most significant when such region of increase in loading due to wake interaction also exhibits a phase lead of about 90° with respect to the observer's location. Therefore, it can also be understood why, at such locations, the interference between total loading noise (which accounts for forces' unsteadiness) and thickness noise (inherently steady, having the source speed variation being neglected) is constructive, as their respective waveforms are mostly in phase. Conversely, at azimuthal positions where significant stretching of the acoustic chord happens partially within the region where the loading increase affects a substantial portion of the blade and partially outside of it (e.g., at an observer location $\phi = 345°$), or when it occurs in a region where the wake does not strongly couple mid-span and outboard loading fluctuations (e.g., at an observer location $\phi = 270°$), steady and unsteady components are not in phase and destructive

interference between the two may arise. The phase of the total loading waveform is therefore affected and the nature of the interference with thickness noise (constructive/destructive) is challenging to anticipate, being they two different noise sources. In summary, the close phase alignment between the steady and unsteady loading waveforms arises because significant γ stretching remaps the effective acoustic source such that both the mean (steady) and the fluctuating (unsteady) components—when generated by a wake that influences both mid-span and outboard regions—share similar phase. This "phase locking" means that the fluctuations, which are inherently unsteady, arrive in phase with the steady load, resulting in constructive interference. On the contrary, when the γ stretching maps steady and unsteady loading in a mismatched way, they appear out of phase, leading to destructive interference. Beyond these specific conditions, the interference mechanism becomes more complex to predict. At $M_{ht} = 0.8$, since steady loading noise is dominant, any constructive/destructive interference with the unsteady component has a reduced effect and loading noise is mainly driven by its time-averaged component. This also explains why, at higher Mach numbers, the interaction between loading and thickness noise sources may differ from that observed at lower Mach numbers. As a result, the azimuthal positions of maximum total noise increase or reduction, relative to the uniform flow case, may shift accordingly, as observed in Figure 9.5.

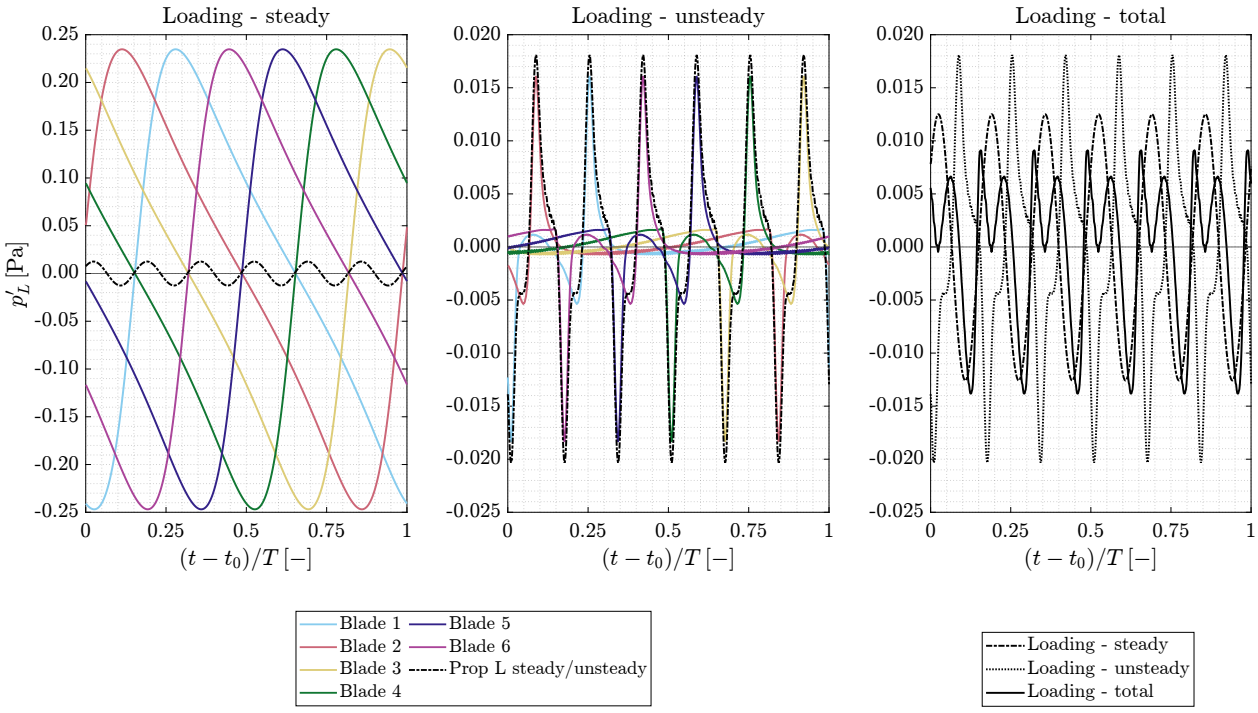

Figure 9.11: Steady, unsteady and total loading pressure waveforms of the individual blades and the propeller; $M_{ht} = 0.357$, $\phi = 345°$, $\theta = 90°$.

As previously discussed, the steady component of loading noise becomes increasingly dominant over the unsteady component as the Mach number increases. To further examine this behavior, Figure 9.13 presents the ratio of the root mean square of the steady and unsteady to total loading pressure fluctuations for different helical tip Mach numbers. The analysis is conducted at $\phi = 225°$ and $\phi = 345°$. This investigation aims to assess the contribution of each component relative to the total loading noise at each Mach number, thereby providing insights into the effectiveness of radiation. It is noted that values of the plotted ratio above 1 are because of interference effects. A clear trend emerges: while at $M_{ht} = 0.357$ the unsteady loading is dominant, increasing the Mach number results in a gradual decrease of the unsteady-to-total loading ratio towards zero, while the steady-to-total ratio asymptotically approaches unity. This confirms that, as the Mach is increased,

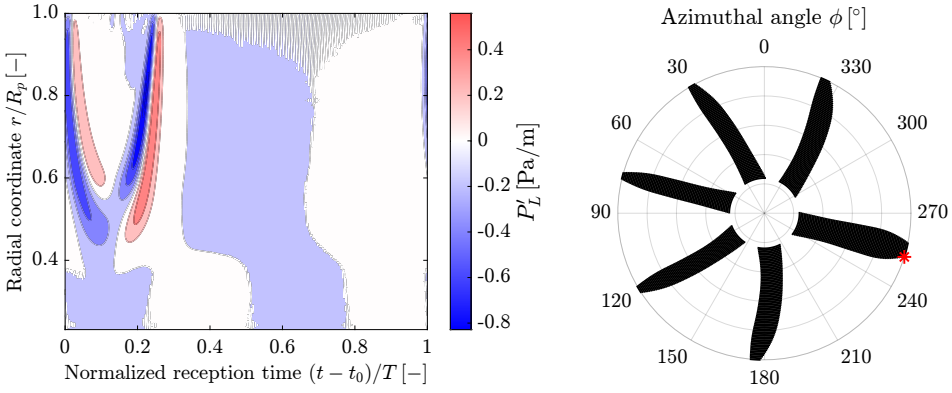

(a) Unsteady loading pressure fluctuations.

(b) $(t-t_0)/T = 0.35$. Red marker on blade 1.

Figure 9.12: Radial distribution of unsteady loading pressure fluctuations for blade 1 (a) and acoustic planform (b); $M_{ht} = 0.357$, $\phi = 345°$, $\theta = 90°$.

loading noise in the propeller plane is predominantly governed by steady forces.

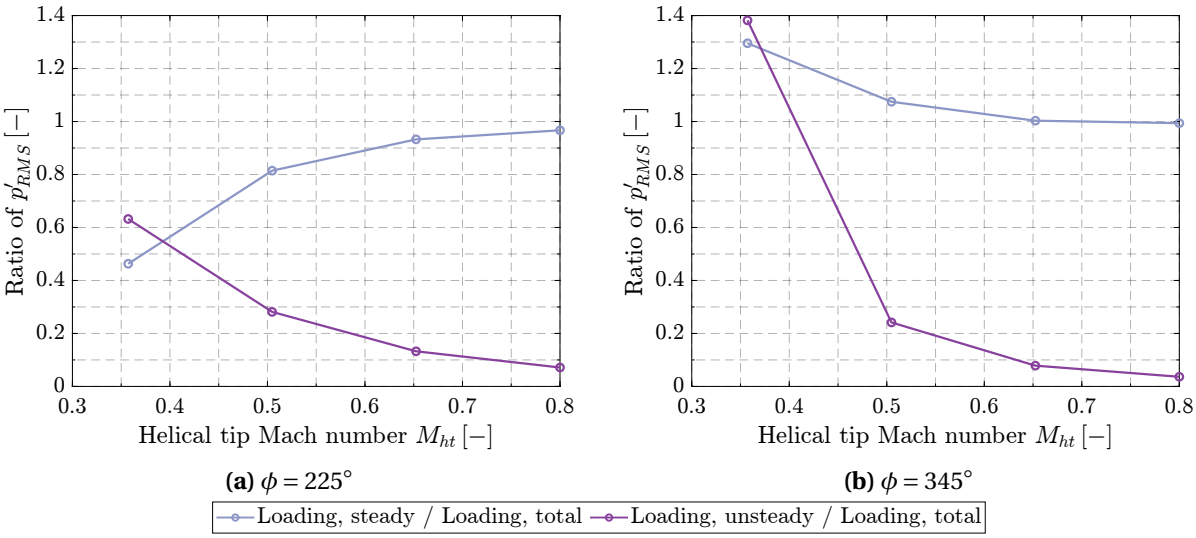

(a) $\phi = 225°$

(b) $\phi = 345°$

Figure 9.13: Ratio of root mean square of steady and unsteady to total loading pressure fluctuations with varying helical tip Mach number; $\theta = 90°$.

To examine the spectral characteristics of the propeller's noise emissions, Figure 9.14 presents the power spectral density under uniform flow and wake encounter conditions at different helical tip Mach numbers, evaluated at $\phi = 225°$ and $\phi = 345°$. At $M_{ht} = 0.357$, in uniform flow, the first BPF is the most dominant. Although it remains dominant under non-uniform flow conditions, higher noise levels are observed at higher BPFs. At $M_{ht} = 0.8$, the first BPF continues to dominate the noise spectrum. However, the difference in noise levels between uniform and non-uniform flow conditions across the spectrum is significantly reduced due to the predominance of steady loading noise. Only at higher frequencies, does the wake encounter case exhibit greater noise emissions at $\phi = 225°$. This is especially evident around 8–10 BPFs. At $\phi = 345°$, the noise levels in uniform flow are dominant within the 5–8 BPF range but become lower than those in the wake encounter case at 9–10 BPFs.

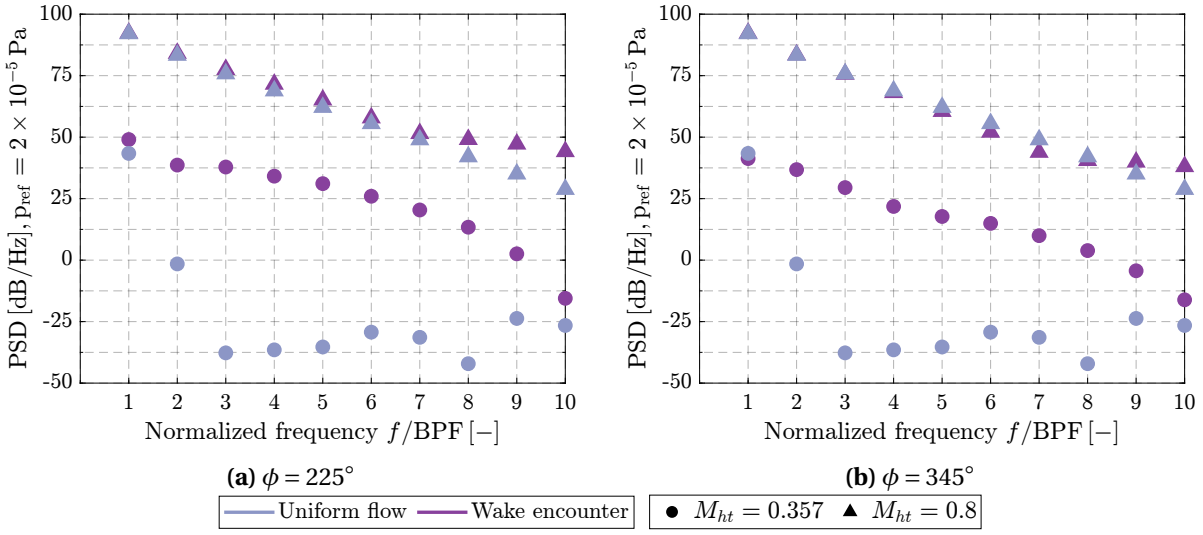

Figure 9.14: Power spectral density under uniform flow and wake encounter conditions with varying helical tip Mach number.

9.2.2. NOISE DIRECTIVITY IN THE PLANE ALONG THE PROPELLER AXIS

Figure 9.15 illustrates the influence of wake encounter on the axial directivity of the thrust-specific sound pressure level for different helical tip Mach numbers. The noise emissions in the xz-plane under uniform flow conditions are depicted in Figure 9.15a, while Figure 9.15b refers to the wake encounter scenario. Unlike the symmetric noise distribution observed in uniform flow, the wake encounter case exhibits an asymmetric pattern around the propeller axis. Additionally, significant noise levels are present along the propeller axis in non-uniform flow conditions. Although increasing the Mach number leads to higher noise levels, the rise is more pronounced in the propeller plane. Specifically, in the wake encounter case, as the Mach number increases from $M_{ht} = 0.357$ to $M_{ht} = 0.8$, the TSSP increases by 41 dB at $\theta = 90°$, whereas along the propeller axis at $\theta = 0°$, the increase is limited to 8 dB. At $M_{ht} = 0.357$, the maximum noise amplification due to wake encounter occurs at $\theta = 0°$, reaching +210 dB. Across all axial positions, the noise levels in the wake encounter case generally exceed those in uniform flow, except in certain regions near the propeller plane. Notably, the greatest reduction in TSSP relative to uniform flow is observed at $\theta = 105°$, with a decrease of approximately 4 dB. At $M_{ht} = 0.8$, the peak noise increase compared to uniform flow is again observed at $\theta = 0°$, reaching +212 dB, while in the propeller plane, the difference between the two flow conditions is negligible. Furthermore, it should be observed that the highest noise levels in the wake encounter condition are found at the propeller axis at $M_{ht} = 0.357$ and at the propeller plane at $M_{ht} = 0.8$.

Figure 9.16 illustrates the impact of wake encounter on the axial directivity of the overall sound pressure level of different noise sources computed in the BPF range $0.9 \leq \text{BPF} \leq 10$ at $M_{ht} = 0.357$ and $M_{ht} = 0.8$. At $M_{ht} = 0.357$, the radiation pattern due to flow non-uniformity, shown in Figure 9.16b, differs substantially from the uniform flow case presented in Figure 9.16a. A key distinction is the presence of non-zero noise levels along the propeller axis in the wake encounter case. Thrust noise dominates within the angular ranges $60° \leq \theta \leq 300°$ and $120° \leq \theta \leq 240°$, whereas torque noise exhibits higher levels near the propeller plane, particularly in the regions $75° \leq \theta \leq 105°$ and $255° \leq \theta \leq 285°$. While thrust noise vanishes at the propeller plane, torque noise is absent along the propeller axis. As previously discussed, thickness noise remains unchanged between the two inflow conditions, as the source speed is not modified in this analysis. However, due to the phase shift in the loading noise waveform, destructive interference between thickness and loading noise

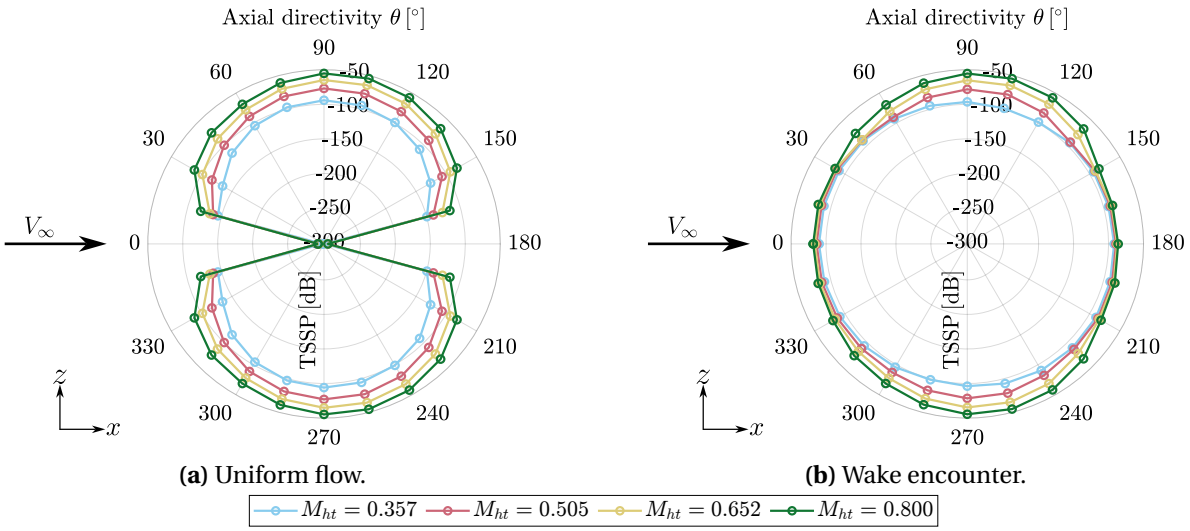

(a) Uniform flow. **(b)** Wake encounter.

Figure 9.15: Effect of the wake encounter on the axial directivity of the thrust-specific sound pressure level at different helical tip Mach numbers.

occurs near the propeller plane, leading to a reduction in total OSPL at $60° \leq \theta \leq 120°$. At $M_{ht} = 0.8$, the noise levels close to the propeller plane are largely unaffected by wake encounter compared to uniform flow, whereas a significant increase in OSPL is observed along the propeller axis. In both inflow conditions, the interference between loading and thickness noise remains mostly constructive, expect for $\theta = 30°$ at which a slight reduction in OSPL is observed. This directivity pattern can be attributed to the predominance of steady loading noise at higher Mach numbers, as confirmed by the yz-plane analysis. Furthermore, the fact that noise levels along the propeller axis show significantly larger variations under flow non-uniformity compared to those close to the propeller plane, suggests that unsteady loading noise radiates more efficiently along the propeller axis. The dominance of steady loading noise at higher Mach numbers, coupled with its primary radiation direction being within the rotor plane, explains why the highest total noise levels are observed at the propeller plane for $M_{ht} = 0.8$ and along the propeller axis for $M_{ht} = 0.357$.

Figure 9.17 presents the loading noise results obtained by providing the aeroacoustic solver with the time-averaged, fluctuating, and total aerodynamic loading of the propeller. At $M_{ht} = 0.357$, the SPL at the first BPF and the OSPL evaluated in the BPF range $0.9 \leq \text{BPF} \leq 10$ are shown in Figure 9.17a and Figure 9.17b, respectively. Similar to the observations in the yz-plane, the OSPL of the steady loading noise exhibits only a slight increase compared to the first BPF. However, the noise levels associated with unsteady loading show more significant variations, with a peak increase of approximately 5 dB at $\theta = 225°$. Consistent with the findings from the azimuthal directivity analysis, this suggests that noise generated by load fluctuations is radiated more efficiently at frequencies above the first BPF compared to the time-averaged contribution. In regions where the noise due to fluctuating forces is dominant, particularly near the propeller axis, any effect of the interference between steady and unsteady loading components is minimal, making the unsteady contribution the primary driver of the loading noise emissions. Conversely, near the rotor disk, destructive interference leads to a reduction in total loading noise at several observer angles. Equivalent plots are provided for $M_{ht} = 0.8$. Specifically, Figure 9.17c displays the SPL at the first BPF, while Figure 9.17d illustrates the OSPL of the total loading noise along with its mean and fluctuating components. While the steady component remains largely unaffected by the expanded frequency range, the unsteady one exhibits a more substantial increase, with the OSPL deviating from the first BPF SPL by up to 10 dB at $\theta = 300°$. Notably, the steady component predominantly shapes the loading noise emission pattern in the

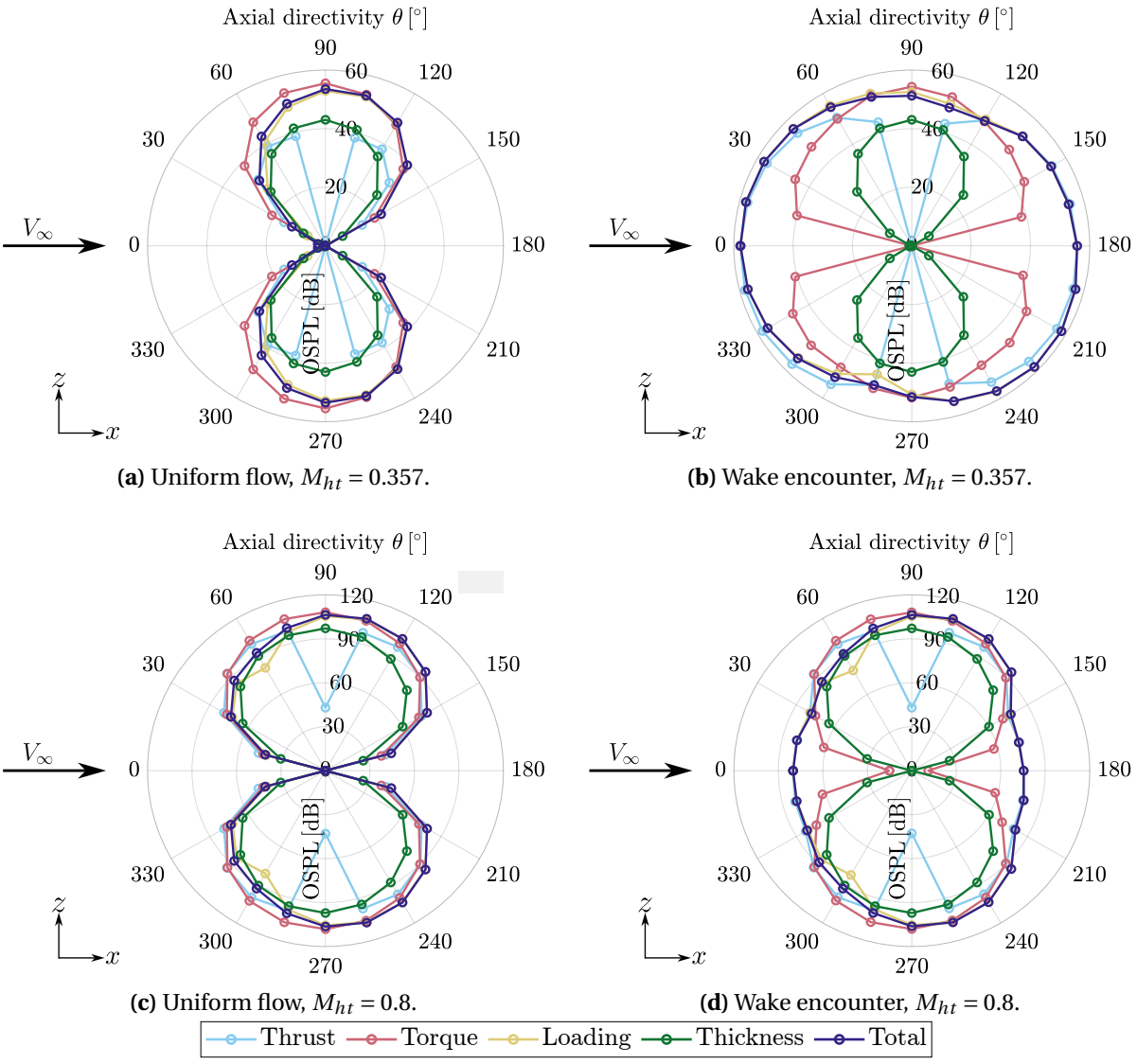

(a) Uniform flow, $M_{ht} = 0.357$.

(b) Wake encounter, $M_{ht} = 0.357$.

(c) Uniform flow, $M_{ht} = 0.8$.

(d) Wake encounter, $M_{ht} = 0.8$.

Figure 9.16: Effect of the wake encounter on the axial directivity of the overall sound pressure level at $M_{ht} = 0.357$ and $M_{ht} = 0.8$.

propeller plane, whereas the unsteady component governs loading noise along the propeller axis. At $\theta = 60°$ and $\theta = 300°$, the reduction in loading noise results from destructive interference between the blades' radial sections, as discussed in Section 8.2. Meanwhile, at other locations where the relative dominance of the mean and fluctuating noise components shifts (e.g., at $\theta = 150°$ and $\theta = 210°$), the observed valleys in loading noise can be attributed to this change in dominance.

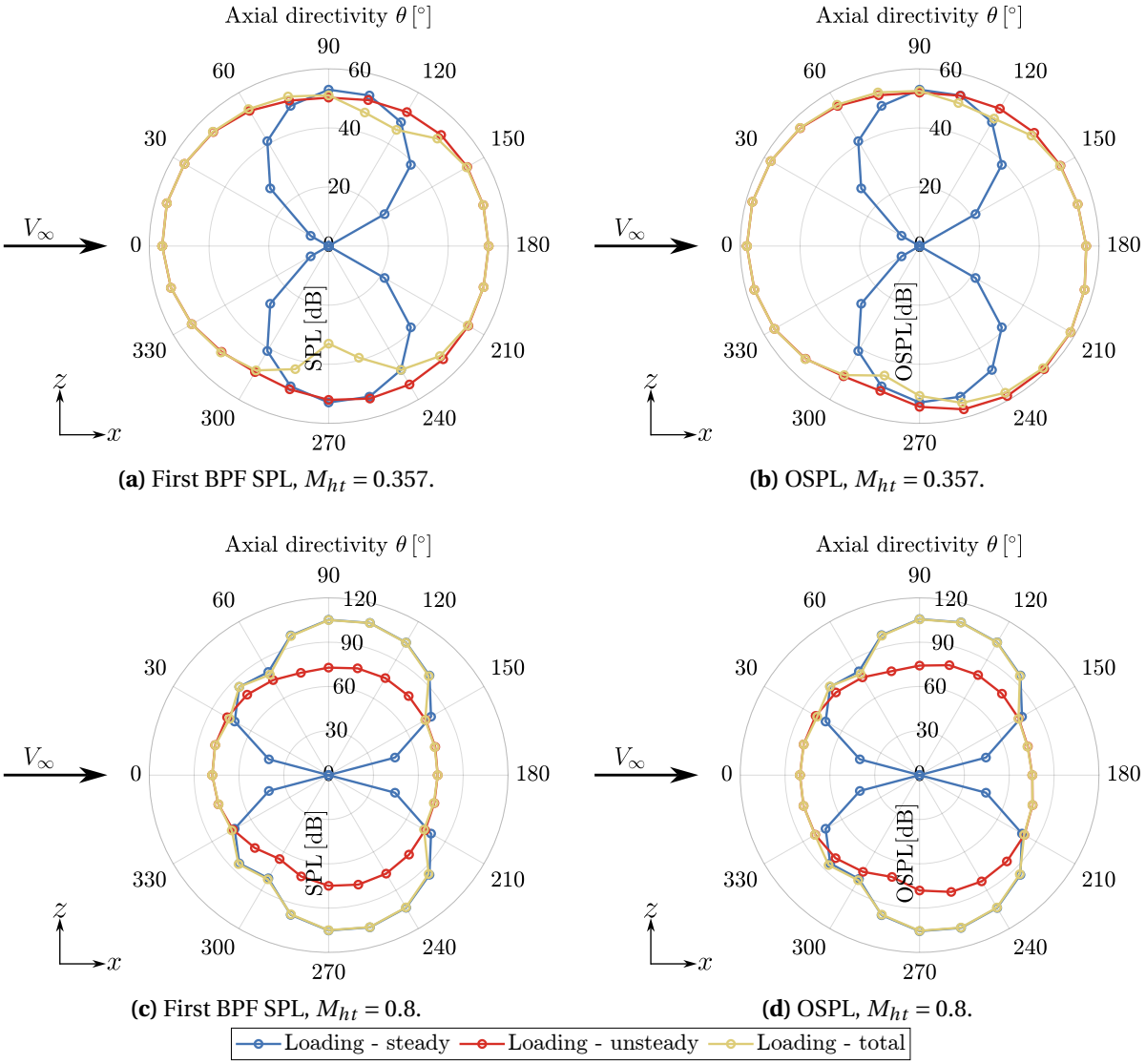

(a) First BPF SPL, $M_{ht} = 0.357$.

(b) OSPL, $M_{ht} = 0.357$.

(c) First BPF SPL, $M_{ht} = 0.8$.

(d) OSPL, $M_{ht} = 0.8$.

Figure 9.17: First BPF SPL and OSPL axial directivity of steady, unsteady and total loading noise under wake encounter conditions at $M_{ht} = 0.357$ and $M_{ht} = 0.8$.

To analyze the differences in the directivity pattern between the steady and unsteady loading noise components at different observer positions, Figure 9.18 presents the radial distribution of steady, unsteady, and total loading pressure fluctuations (bottom row) for blade 1 at $M_{ht} = 0.357$, considering observer locations at $\theta = 0°$ (top row) and $\theta = 120°$ (bottom row). At $\theta = 0°$, corresponding to the propeller axis, the steady loading pressure is negligible due to the minimal temporal variation of the directivity factor, as depicted in Figure 9.18a. However, since Δp includes a fluctuating component, unsteady loading noise is generated, as illustrated in Figure 9.18b. Consequently, the total blade loading noise shown in Figure 9.18c is primarily governed by the fluctuating component. It is worth noting that variations in the directivity factor also explain the differences observed in

the directivity pattern of torque and thrust noise resulting from wake encounter (see Figure 9.16b and Figure 9.16d). Specifically, torque noise levels remain minimal near the propeller axis due to torque's directivity factor being close to zero for an observer in this region, as $\vec{R}$ and $\hat{q}$ are about orthogonal. In contrast, thrust noise exhibits non-zero levels, as the small temporal variation of its directivity factor at the propeller axis is outweighed by the time-varying Δp. Conversely, at $\theta = 120°$, the directivity factor significantly modulates both the time-averaged and fluctuating components of Δp, resulting in significant noise fluctuations, as depicted in Figure 9.18d and Figure 9.18e. As a result, when these two components are superimposed, both the mean and fluctuating contributions to the loading noise become evident in the contours, as seen in Figure 9.18f.

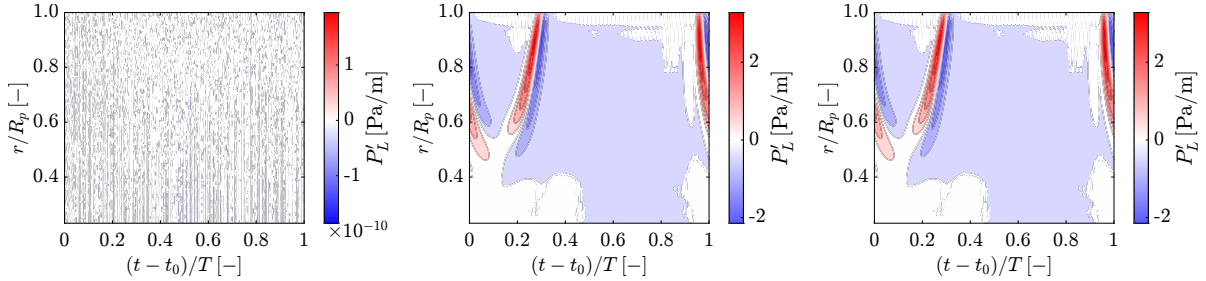

(a) Loading, steady; $\theta = 0°$. **(b)** Loading, unsteady; $\theta = 0°$. **(c)** Loading, total; $\theta = 0°$.

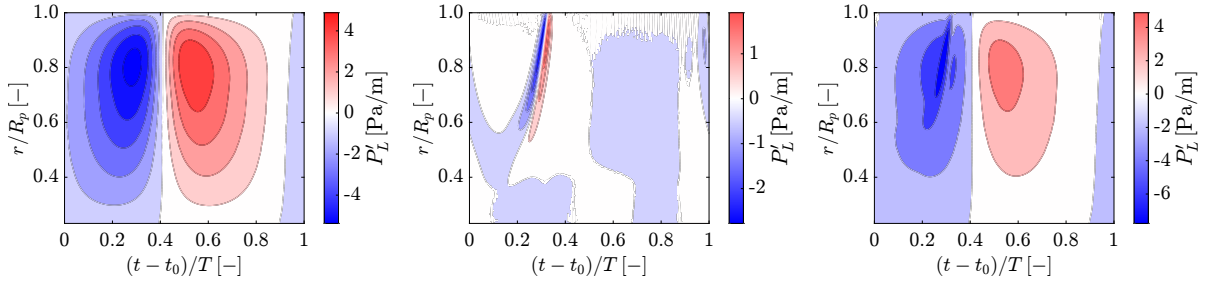

(d) Loading, steady; $\theta = 120°$. **(e)** Loading, unsteady; $\theta = 120°$. **(f)** Loading, total; $\theta = 120°$.

Figure 9.18: Radial distribution of steady, unsteady and total loading pressure fluctuations at $\theta = 0°$ (top row) and $\theta = 120°$ (bottom row); $M_{ht} = 0.357$, blade 1.

An analysis at the propeller level, obtained by superimposing the pressure waveforms of all six blades, is presented in Figure 9.19. Notably, at $\theta = 0°$, the steady loading pressure remains negligible, and the total loading noise is primarily driven by the unsteady component, as illustrated in Figure 9.19a. In contrast, at $\theta = 120°$, as depicted in Figure 9.19b, the unsteady loading pressure exhibits a significantly greater amplitude than its steady counterpart. However, due to the phase difference between the two waveforms, the fluctuation range of the total loading noise is reduced, leading to lower overall noise levels.

Figure 9.20 illustrates the ratio of the root mean square of steady and unsteady loading pressure fluctuations to the total loading pressure fluctuations for various helical tip Mach numbers. The analysis is carried out at $\theta = 0°$ and $\theta = 120°$. At $\theta = 0°$, no significant variations are observed as the Mach number increases, since the steady component remains negligible and the total loading noise is primarily governed by the unsteady component. Conversely, at $\theta = 120°$, while the fluctuating component dominates at $M_{ht} = 0.357$, its relative contribution to the total loading noise decreases rapidly to zero as the Mach number increases, whereas the steady component's contribution asymptotically approaches unity. This confirms that, while in the propeller plane loading noise is primarily governed by steady forces, at the propeller axis the fluctuating loading's contribution is dominant.

Figure 9.21 presents the spectral content of the propeller's noise emissions under both uniform

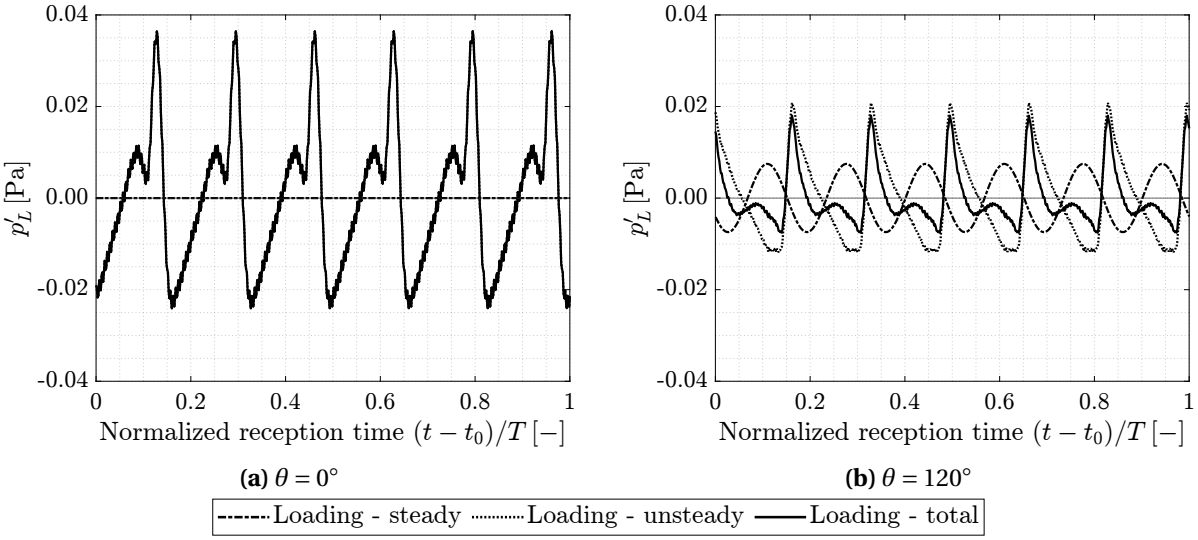

Figure 9.19: Propeller steady, unsteady and total loading pressure fluctuations at $\theta = 0°$ (a) and $\theta = 120°$ (b); $M_{ht} = 0.357$.

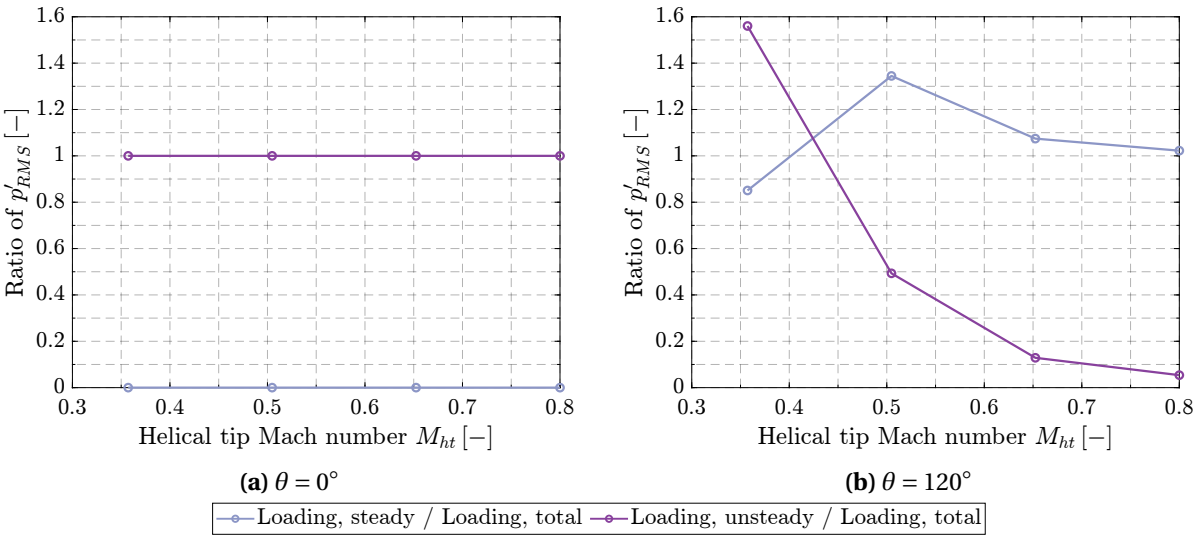

Figure 9.20: Ratio of root mean square of steady and unsteady to total loading pressure fluctuations with varying helical tip Mach number.

and wake encounter conditions at $M_{ht} = 0.357$ and $M_{ht} = 0.8$. At $\theta = 0°$, in uniform flow, the first BPF is not the dominant harmonic at either Mach numbers. However, in wake encounter conditions, where noise is more effectively radiated along the propeller axis, the first BPF becomes the dominant frequency. Notably, the distribution of spectral contributions is largely different for the two inflow conditions, owing to the significantly different radiation efficiency along the propeller axis. At $\theta = 120°$ and $M_{ht} = 0.357$, while the first BPF is the primary frequency component in uniform inflow, load unsteadiness enhances the second BPF contribution by approximately +2.5 dB compared to the the first BPF. At $M_{ht} = 0.8$, the first BPF remains the dominant frequency for noise emissions, with comparable noise levels between the two inflow conditions within the 1-3 BPF range. However, for frequencies spanning 4-10 BPFs, the non-uniform flow condition result in a greater contribution to the noise levels.

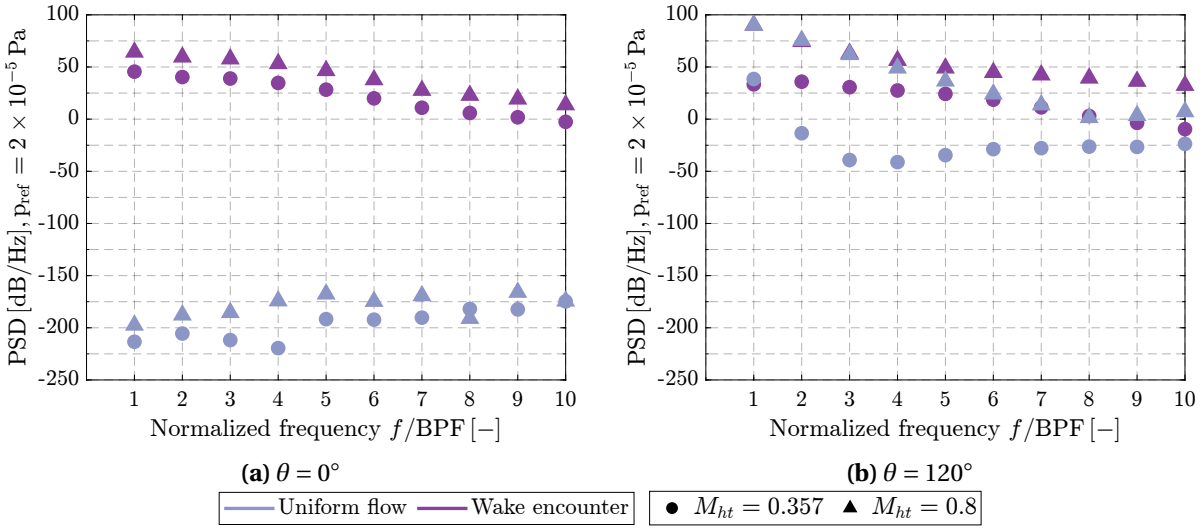

Figure 9.21: Power spectral density under uniform flow and wake encounter conditions with varying helical tip Mach number.

10

Non-Zero Angle of Attack Effects

This chapter investigates the influence of a non-zero angle of attack on the propeller aeroacoustic performance. The aerodynamic loading of the propeller is discussed in Section 10.1, while a physical interpretation of its noise signature is provided in Section 10.2.

10.1. Aerodynamic Performance

A side view of the propeller at a non-zero angle of attack is illustrated in Figure 10.1a. Due to the shaft tilt, both thrust and normal force (which is absent at $\alpha = 0°$) have components aligned with and perpendicular to the free-stream direction. As noted by Van Arnhem et al. [21], although the nacelle's upwash modifies the axial advance ratio, the dominant effect is on the tangential advance ratio. This can be observed in Figures 10.1b and 10.1c. As discussed in Section 6.2, the advance ratio decreases on the advancing side because of an increase in the in-plane velocity component experienced by the blade sections, whereas it increases on the retreating side. The maximum variation in the effective advance ratio, depicted in Figure 10.1d, reaches 44% of the free-stream value, occurring near the hub where the rotational velocity is relatively low. The presence of an in-plane velocity component results in a variation of ±4% in the effective velocity at the blade tip. This change in effective velocity also affects the maximum chordwise Reynolds number, which increases by 5% relative to $\alpha = 0°$ values for each M_{ht} presented in Table 8.1.

Figure 10.2 presents the variation in local thrust and torque coefficients at $\alpha = 10°$ compared to $\alpha = 0°$. The reduced effective advance ratio on the advancing side leads to an increase in the sectional angle of attack, causing a rise in aerodynamic loading, which peaks at $\phi = 104°$. Conversely, a loading reduction occurs on the retreating side due to the increased advance ratio.

Similarly to the wake encounter case, in addition to analyzing the absolute magnitude of the loading variations, emphasis is placed on the relative deviation expressed as a ratio to the loading at $\alpha = 0°$. This is illustrated in Figure 10.3. The azimuthal distribution of this ratio for the thrust coefficient and torque coefficient at three radial stations is shown in Figure 10.3a and Figure 10.3b, respectively. Notably, the relative change is less pronounced at the highest-loaded radial position, i.e., $r/R_p = 0.8$, due to the inherently higher loading at $\alpha = 0°$ locally. The sinusoidal nature of the loading variation along the azimuthal direction is evident, with an increase on the advancing side nearly 1.3 times as large than the reduction on the retreating side for outboard sections, in agreement with literature [9]. Figure 10.3c illustrates the variation in source speed for $\alpha = 10°$, expressed as a ratio relative to the value at $\alpha = 0°$. As discussed in Section 7.2, contrary to the wake encounter case, for the angle of attack case the source speed variation is taken into account. However, unlike the loading distribution, the depicted source speed does not incorporate the nacelle's upwash effect. It is observed that at $r/R = 0.8$, the source speed exhibits fluctuations of approximately ±5%. Moreover,

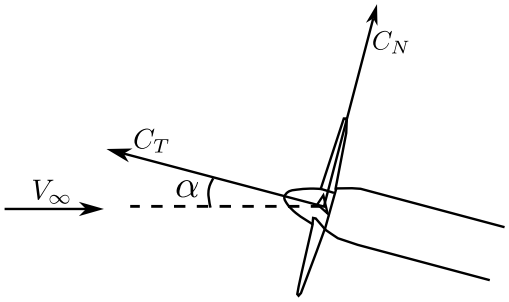

(a) Schematic of propeller at a non-zero angle of attack, side view (adapted from [22]).

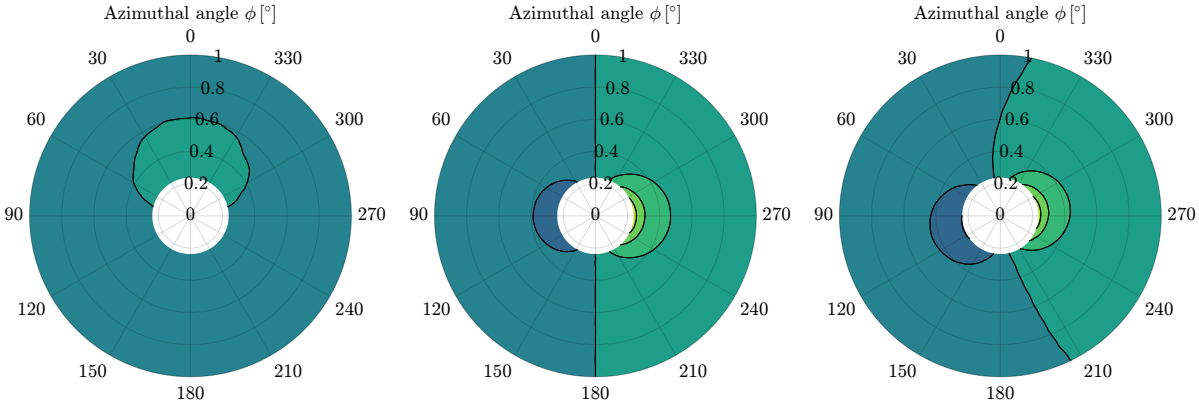

(b) Change in advance ratio due to axial inflow.

(c) Change in advance ratio due to tangential inflow.

(d) Overall change in advance ratio.

Figure 10.1: Schematic of propeller at a non-zero angle of attack (a) and change in local advance ratio (b,c,d) at $\alpha = 10°$.

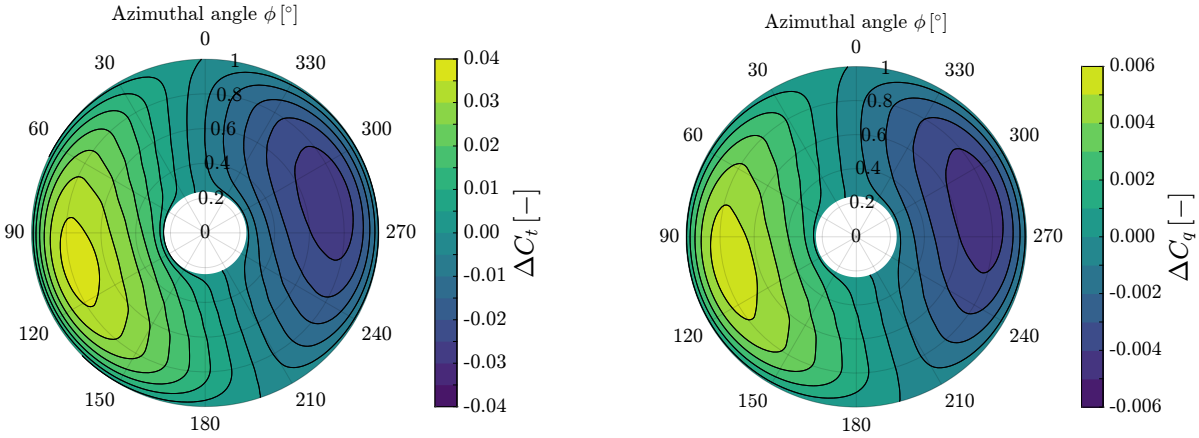

(a) Change in local thrust coefficient.

(b) Change in local torque coefficient.

Figure 10.2: Azimuthal change in local thrust (a) and torque (b) coefficient at $\alpha = 10°$ with respect to $\alpha = 0°$.

the sinusoidal variation reaches its maximum at $\phi = 90°$ and its minimum at $\phi = 270°$, being it only dependent on the non-uniform inflow, while loading variation also depends on unsteady aerodynamic effects, and thus features a 14° phase delay relative to the source speed variation. Figure 10.3d illustrates the azimuthal variation of the ratio of blade thrust and torque coefficients to their counterparts at $\alpha = 0°$. The most positive and most negative deviations in thrust relative to $\alpha = 0°$ values are +22% and −17%, respectively, while for torque, these deviations are +17.5% and −15%. Figure 10.3e presents the ratio of the total propeller thrust and torque to their $\alpha = 0°$ values over a full revolution. Given the sinusoidal nature of the blade loading variation and the 60° phase shift between blades, the overall propeller loading exhibits only minor oscillations. Over time, the total propeller thrust and torque are found to be 2.2% and 1.2% higher than their respective values at $\alpha = 0°$.

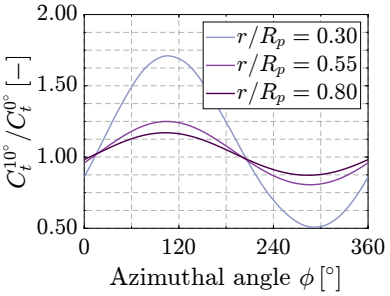

(a) Ratio of thrust coefficients for three radial stations.

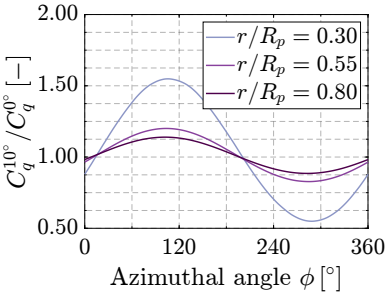

(b) Ratio of torque coefficients for three radial stations.

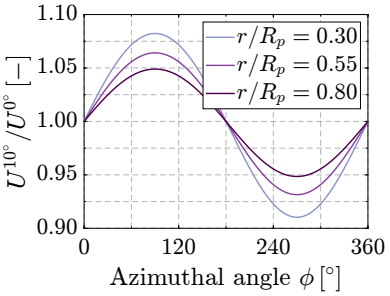

(c) Ratio of source speed for three radial stations.

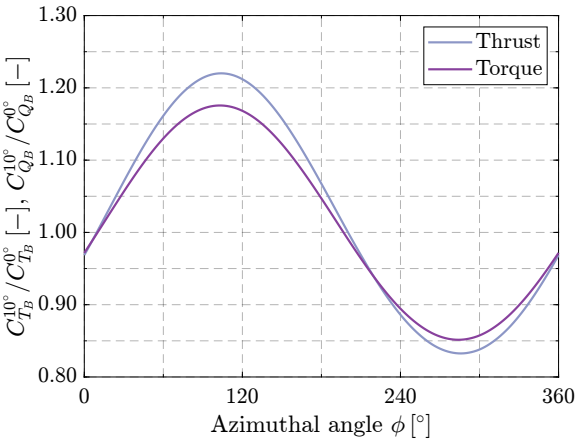

(d) Ratio of blade thrust and torque coefficients.

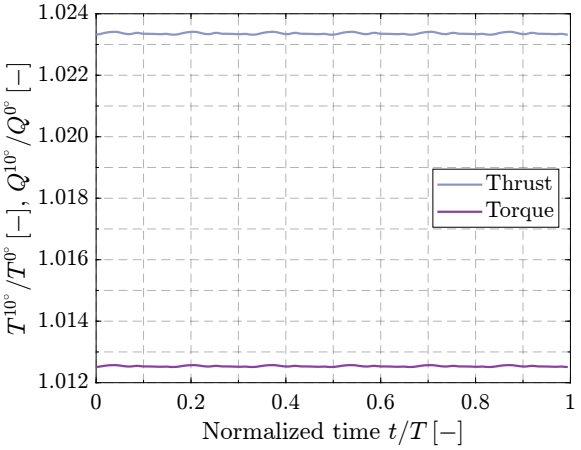

(e) Ratio of propeller thrust and torque.

Figure 10.3: Ratio of sectional thrust (a) and torque (b) coefficients, source speed (c), blade thrust and torque coefficients (d) and propeller thrust and torque (e) between $\alpha = 10°$ and $\alpha = 0°$.

To assess the relative significance of steady and unsteady loading components, Figure 10.4 illustrates the time-averaged and fluctuating contributions of the pressure force coefficient. Specifically, Figure 10.4a and Figure 10.4b depict the steady and unsteady components, while their combined effect is shown in Figure 10.4c. The corresponding steady, unsteady, and total (steady + unsteady) pressure distributions are subsequently incorporated into Hanson's formulation, introduced in Section 5.2, to examine their respective contributions to noise emissions. Notably, at the most loaded blade sections, the steady component of the pressure coefficient exhibits values that are an order of magnitude greater than its unsteady counterpart, highlighting its aerodynamic dominance.

Table 10.1 reports the percentage variation of the key propeller performance metrics for the

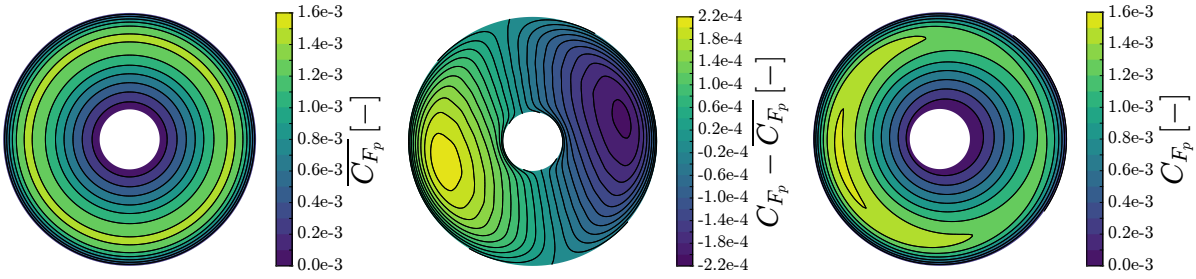

(a) Time-averaged component of the pressure force coefficient.

(b) Fluctuating component of the pressure force coefficient.

(c) Pressure force coefficient (time-averaged + fluctuating).

Figure 10.4: Time-averaged (a) and fluctuating (b) components of the pressure force coefficient (c) at $\alpha = 10°$.

$\alpha = 10°$ case relative to $\alpha = 0°$. As previously observed, the increase in loading on the advancing side exceeds the reduction on the retreating side, leading to an increase in the thrust and power coefficients by 2.23% and 1.15%, respectively. Since the thrust augmentation surpasses that of power, the propeller efficiency improves by 1.07%. The different change in torque between the advancing and the retreating sides generates in-plane forces. Specifically, the side force coefficient is $C_Y = 3.399 \times 10^{-3}$, while the normal force coefficient is $C_N = 1.362 \times 10^{-2}$. The magnitudes of the side force and normal force are, respectively, 1.2% and 4.8% of the propeller thrust at $a = 0°$, indicating a significantly higher load unsteadiness than the wake encounter case. To ensure a fair evaluation of propeller performance, forces along the freestream direction are also examined. The thrust coefficient along the flight direction (C_{T_∞}) decreases by 0.16%, while the efficiency η_∞ reduces by 1.30%. This degradation in performance along the freestream direction is attributed to the normal force having a component acting against the flight direction. Such a decline in propeller performance at high angles of attack is consistent with expectations [22].

Flow condition	C_T	C_P	η	C_Y	C_N	C_{T_∞}	C_{N_∞}	η_∞
$\alpha = 0°$	0.2834	0.3183	0.7125	0	0	0.2834	0	0.7125
$\alpha = 10°$	0.2898	0.3219	0.7201	3.399×10^{-3}	1.362×10^{-2}	0.2830	0.0637	0.7033
$\Delta\%$	2.23%	1.15%	1.07%	–	–	−0.16%	–	−1.30%

Table 10.1: Propeller performance metrics at $\alpha = 0°$ and at $\alpha = 10°$.

10.2. AEROACOUSTIC PERFORMANCE

Prior to the aeroacoustic analysis, a sensitivity study is performed to determine a suitable number of time steps per period for the computations. The findings of this study are discussed in detail in Section A.3. The chosen number of time steps per period is 600, which ensures a deviation in the maximum p'_{RMS} of less than 0.1% (as per Equation 6.2) and guarantees that the sampled data accurately represents the relevant acoustic frequencies without any aliasing. It is highlighted that, since the chosen time resolution remains the same for the uniform and the two non-uniform flow cases analyzed in this work, the non-uniformity of the flow does not affect the selected time resolution at the analyzed conditions.

10.2.1. NOISE DIRECTIVITY IN THE PROPELLER PLANE

Figure 10.5 illustrates how a non-zero angle of attack influences the azimuthal directivity of the thrust-specific sound pressure level across various helical tip Mach numbers. The axial directivity angle is fixed at $\theta = 90°$, corresponding to the propeller plane. While Figure 10.5a displays the noise radiation in the yz-plane for $\alpha = 0°$, Figure 10.5b represents the corresponding distribution for $\alpha = 10°$. To ensure a fair comparison between these cases, the TSSP for $\alpha = 10°$ was retrieved using the thrust computed along the free-stream direction. The axisymmetric directivity observed at $\alpha = 0°$ is no longer present at $\alpha = 10°$. In agreement with previous studies [8, 9, 30], the total noise increases in the region where the propeller tilts away from ($90° < \phi < 270°$) and decreases in the opposite one ($270° < \phi < 90°$). At $M_{ht} = 0.357$, the maximum reduction in noise, approximately 7 dB relative to the undisturbed flow case, occurs at $\phi = 15°$, whereas the most significant increase, around 6 dB, is found at $\phi = 180°$. Similar to the wake encounter scenario, the disparity in noise emissions between the two flow conditions decreases as the Mach number increases due to the relatively higher importance of steady noise sources. At $M_{ht} = 0.8$, the TSSP exhibits a reduction of approximately 3 dB at $\phi = 15°$, where the largest decrease occurs, while an increase of about the same amount is observed at $\phi = 195°$, marking the location of maximum amplification. As previously explained, any mismatch in terms of the locations of maximum rise or reduction in total noise with respect to lower Mach numbers are due to the increased importance of steady sources at higher Mach numbers, which leads to a different interference between loading and thickness noise. Additionally, it is observed that while the propeller at $\alpha = 0°$ exhibits a TSSP variation of 39 dB between the lowest and highest Mach numbers analyzed, a variation in the range 36-43 dB is found at $\alpha = 10°$. Similar to the wake encounter scenario, a non-zero angle of attack enhances the sensitivity of noise to the operating condition at observer locations where noise levels are lower than those in uniform flow; conversely, the sensitivity is attenuated. Once more, this behavior stems from the fact that, as the Mach number increases, the change in noise emissions relative to uniform flow decreases.

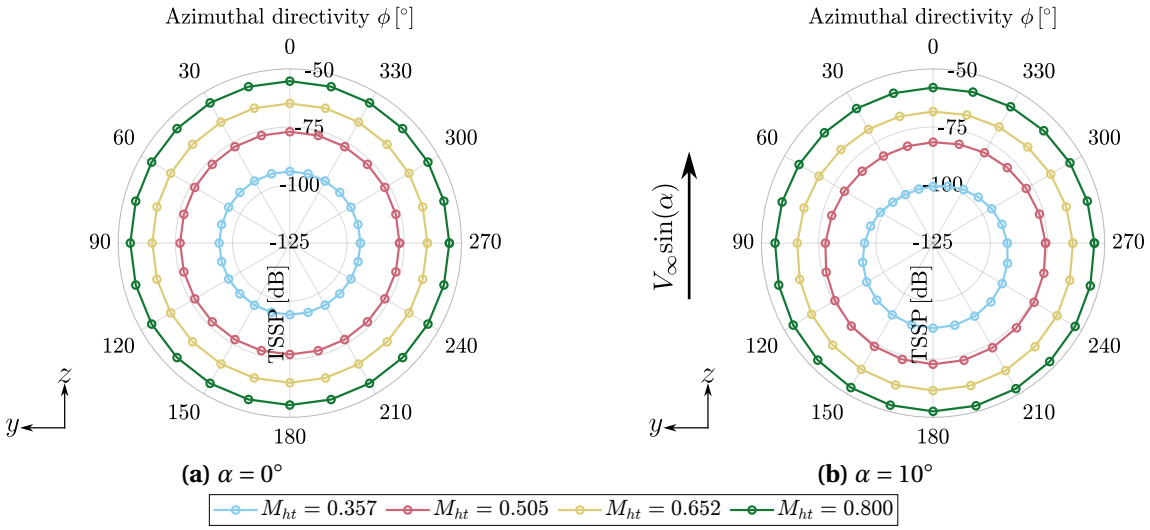

Figure 10.5: Effect of the angle of attack on the azimuthal directivity of the thrust-specific sound pressure level at different helical tip Mach numbers; $\theta = 90°$.

Figure 10.6 illustrates the effect of a non-zero angle of attack on the azimuthal directivity of the overall sound pressure level for different noise sources, computed within the BPF range $0.9 \leq \text{BPF} \leq 10$, at $M_{ht} = 0.357$ and $M_{ht} = 0.8$. At $\alpha = 10°$, the directivity patterns shown in Figure 10.6b and Figure 10.6d differ from those at $\alpha = 0°$, depicted in Figure 10.6a and Figure 10.6c. This discrepancy arises from both the periodic variations in blade loading and the asymmetric modulation of noise

sources caused by the cross-flow velocity component [24]. As previously mentioned, the sinusoidal variation in source speed, illustrated in Figure 10.3c, reaches its maximum at $\phi = 90°$ and minimum at $\phi = 270°$, exhibiting a 14° phase lead relative to the blade loading variation. This has an effect on the acoustic chord γ, which is therefore subject to a stretching on the advancing side and a contraction on the retreating side. Due to the periodic variation in source speed, thickness noise follows a similar trend to loading noise, decreasing in the region where the propeller tilts away and increasing in the opposite region. At $M_{ht} = 0.357$, the maximum reduction in OSPL is 2 dB at $\phi = 0°$, while the peak increase is 1.5 dB at $\phi = 180°$. These azimuthal locations remain unchanged at $M_{ht} = 0.8$, where the maximum reduction and increase are 0.8 dB and 0.7 dB, respectively. Thus, it can be observed that the azimuthal variation in thickness noise is lower at $M_{ht} = 0.8$ compared to $M_{ht} = 0.357$. This may appear to contradict Mani's findings [24], where it is stated that the asymmetric modulation effect of steady noise sources due to the cross-flow component should scale with the tip rotational Mach number, in addition to the number of blades and the harmonic number. However, as shown in Subsection 2.3.2, Mani observed a significantly smaller impact of the cross-flow effect for the 9-bladed rear rotor of the counter-rotation propeller compared to the 11-bladed front rotor. Since 6 blades are used in this work, it is likely that the cross-flow effect is smaller than the discussed higher contribution of steady sources at higher Mach numbers.

Notably, for both Mach numbers, the locations of maximum reduction and increase in loading noise remain at $\phi = 0°$ and $\phi = 180°$, respectively. The reason why they are not located 90° after the location of most positive and negative aerodynamic loading variation, as literature suggests [8, 9], will be given later. Specifically, at $M_{ht} = 0.357$, the OSPL decreases by 8 dB at $\phi = 0°$ and increases by 6 dB at $\phi = 180°$, while at $M_{ht} = 0.8$, similar reductions and increases of approximately 3 dB are observed. At $\alpha = 0°$, the interference between loading and thickness noise is constructive for both Mach numbers, resulting in higher overall noise levels. In contrast, at $\alpha = 10°$ and $M_{ht} = 0.357$, destructive interference occurs in the range $45° \leq \phi \leq 150°$, whereas at $M_{ht} = 0.8$, constructive interference persists due to the predominance of steady noise components.

For further insights on loading noise, Figure 10.7 presents the loading noise results obtained by inputting the time-averaged, fluctuating, and total aerodynamic loading of the propeller into the aeroacoustic solver, as illustrated in Figure 10.4. It should be noted that the steady, unsteady and total loading noise components plotted here (and, in general, in all the analyses at a non-zero angle of attack in this work) all account for the source speed modulation effect, since the source speed azimuthal variation has been considered. At $M_{ht} = 0.357$, the SPL at the first BPF and the OSPL evaluated in the BPF range $0.9 \leq \text{BPF} \leq 10$ are depicted in Figure 9.7a and Figure 9.7b, respectively. It is observed that both the steady and the unsteady loading noise components only exhibit a negligible increase (in the order of 10^{-3} dB) when considering the extended frequency range. The interference between the time-averaged and the fluctuating noise components is constructive at $90° \leq \phi \leq 270°$ and destructive at $285° \leq \phi \leq 75°$. At $M_{ht} = 0.8$, both the steady and the unsteady loading noise components exhibit an increase of about 0.4 dB compared to the first BPF. Again, constructive interference is observed in the region where the propeller tilts away from and destructive in the opposite one. However, compared to $M_{ht} = 0.357$, the reduction/increase in total loading noise levels resulting from such acoustic interference is smaller due to the increased dominance of steady noise.

An analysis of the pressure waveforms is essential to gain insight into the physics of acoustic interference. To this end, Figure 10.8 displays the steady, unsteady, and total loading pressure waveforms for individual blades and the propeller at $M_{ht} = 0.357$ and $\phi = 0°$, which corresponds to the azimuthal location where the greatest reduction in loading noise is observed relative to $\alpha = 0°$. Again, it is important to note that the source speed modulation effect is incorporated in the computation of the steady, unsteady and total loading noise hereby plotted. The distinguishing factor between the steady and unsteady components is the aerodynamic loading. The increased number of oscillations in the waveforms of individual blades over a period arises from the combined effects of

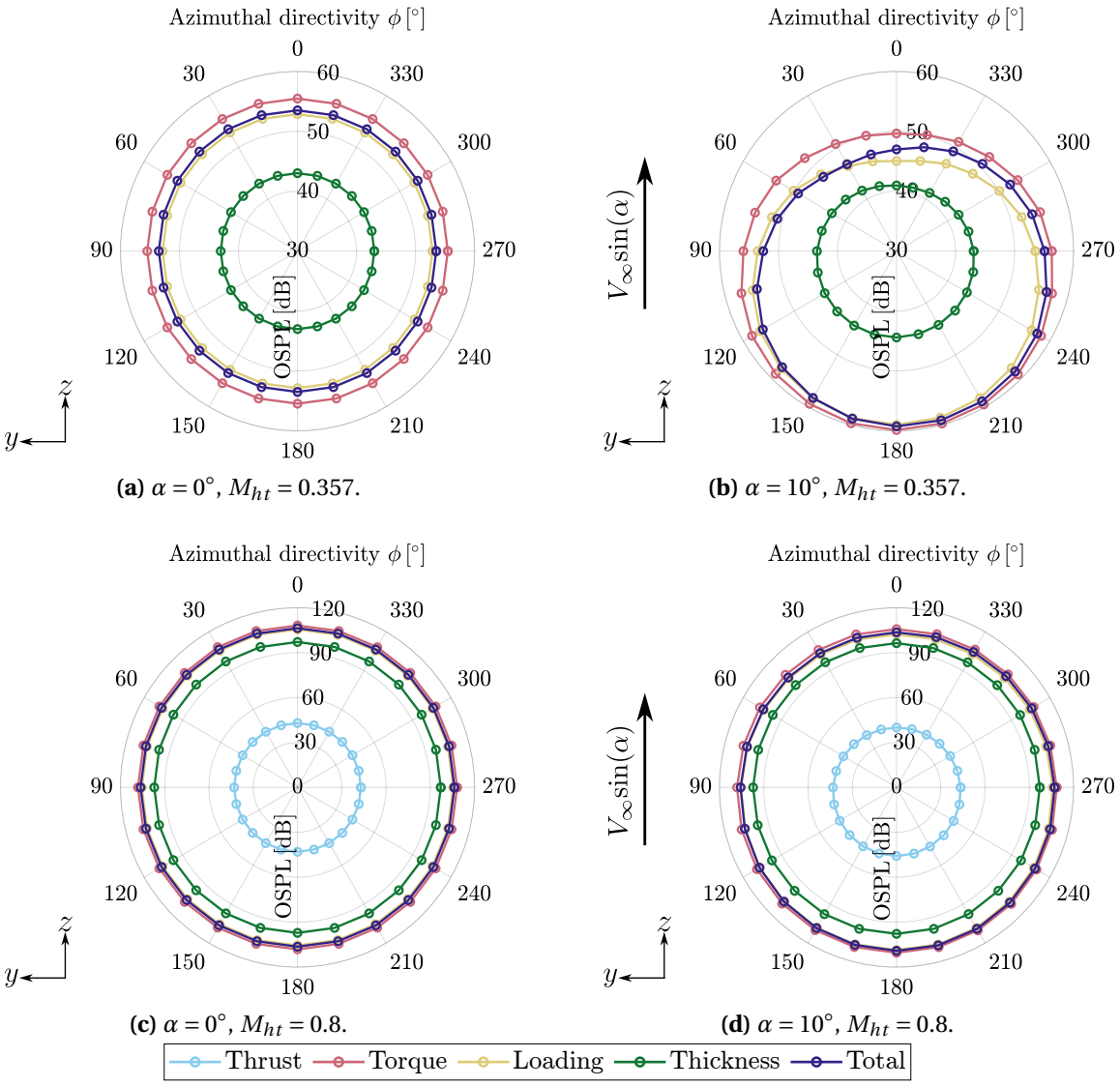

(a) $\alpha = 0°$, $M_{ht} = 0.357$.

(b) $\alpha = 10°$, $M_{ht} = 0.357$.

(c) $\alpha = 0°$, $M_{ht} = 0.8$.

(d) $\alpha = 10°$, $M_{ht} = 0.8$.

Figure 10.6: Effect of the angle of attack on the azimuthal directivity of the overall sound pressure level at $M_{ht} = 0.357$ and $M_{ht} = 0.8$; $\theta = 90°$.

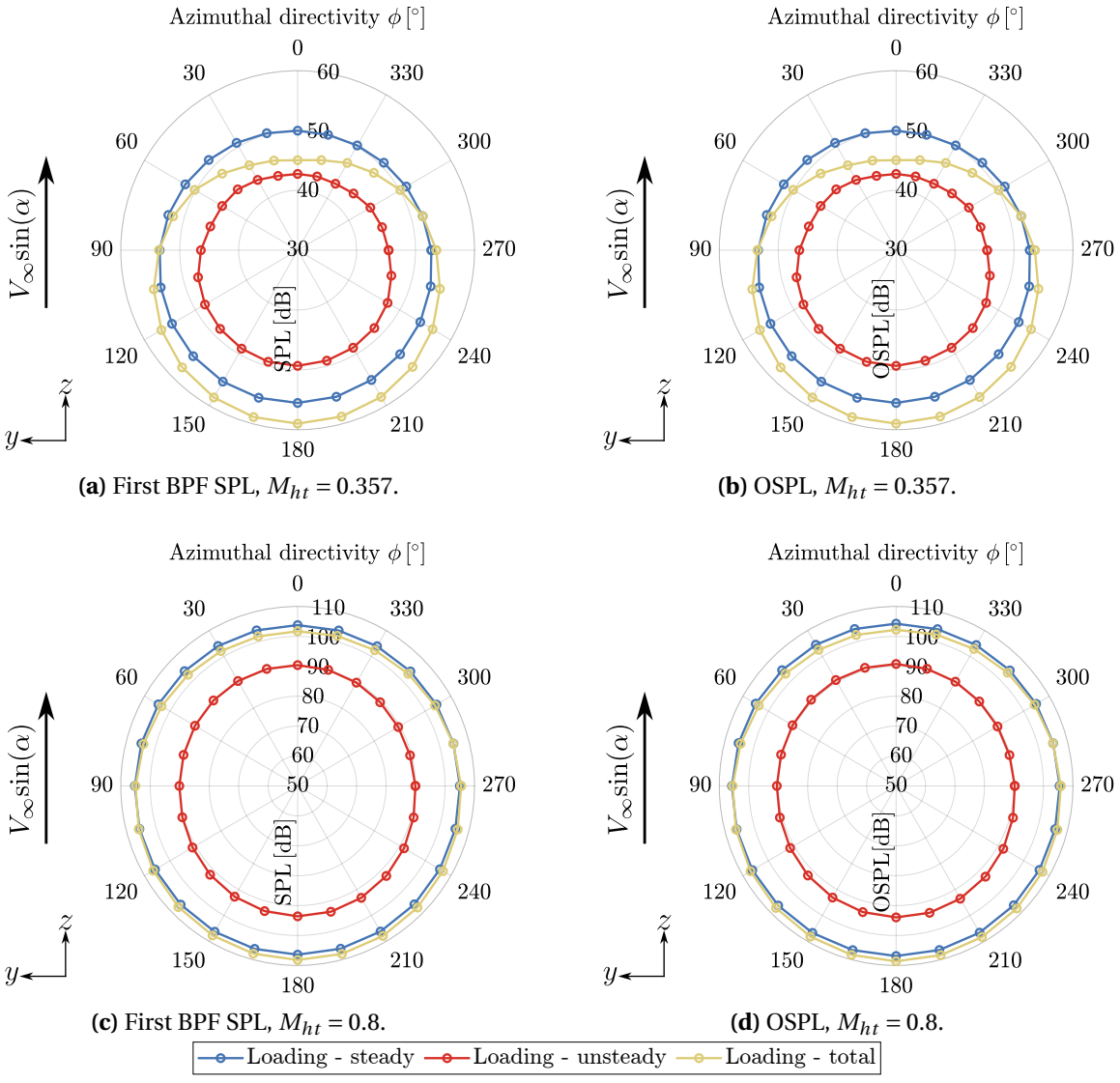

(a) First BPF SPL, $M_{ht} = 0.357$.

(b) OSPL, $M_{ht} = 0.357$.

(c) First BPF SPL, $M_{ht} = 0.8$.

(d) OSPL, $M_{ht} = 0.8$.

Figure 10.7: First BPF SPL and OSPL azimuthal directivity of steady, unsteady and total loading noise at $\alpha = 10°$; $M_{ht} = 0.357$ and $M_{ht} = 0.8$, $\theta = 90°$.

the directivity factor, as well as the periodic variations in aerodynamic loading (as for the fluctuating component) and source speed. Interestingly, the pressure waveforms of the blades exhibit close phase alignment. Consequently, they interfere constructively. However, at this specific azimuthal location, the propeller's steady and unsteady noise components exhibit a phase shift. As a result, their interaction leads to destructive interference, thereby reducing the amplitude of the waveform of total loading noise. This phenomenon is associated with the sign change in the fluctuating blade aerodynamic pressure between the advancing and retreating sides. From an aeroacoustic perspective, a negative unsteady aerodynamic blade pressure generates an acoustic pressure that is phase-shifted with respect to the one generated by the positive steady blade aerodynamic pressure. For an observer at $\phi = 0°$, the maximum stretching of the acoustic chord γ occurs near $\phi = 270°$, where the fluctuating aerodynamic loading is negative. Consequently, the steady and unsteady loading noise waveforms are de-phased, leading to destructive interference.

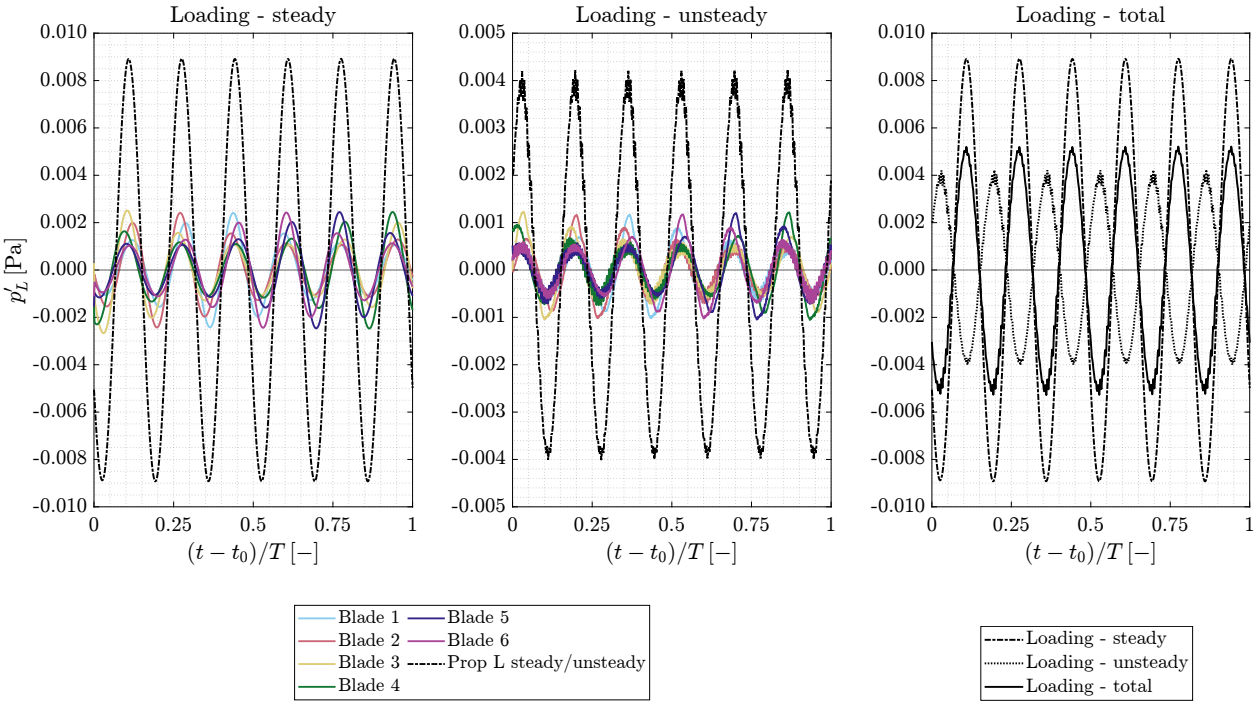

Figure 10.8: Steady, unsteady and total loading pressure waveforms of the individual blades and the propeller; $M_{ht} = 0.357$, $\phi = 0°$, $\theta = 90°$.

The waveforms corresponding to the individual blades and the propeller for steady, unsteady, and total loading noise at $M_{ht} = 0.8$ and $\phi = 0°$ are presented in Figure 10.9. As shown in Table 10.2, at the Mach number $M_{ht} = 0.357$, the peak-to-peak amplitude of the steady loading waveform is approximately 2.2 times larger than that of the unsteady component, whereas at $M_{ht} = 0.8$, it is nearly 4.8 times as large. Consequently, at the higher Mach number, the total loading waveform is primarily governed by the mean component of the loading, in agreement with the observations from the wake encounter case. Although the ratio between the mean and fluctuating aerodynamic loading remains unchanged across different operating conditions, the unsteady loading peak-to-peak amplitude does not scale with Mach number to the same extent as the steady loading component. At higher Mach numbers, the impact of temporal variation in the acoustic chord, which, as previously discussed, alters the degree of interference between the waveforms of individual blades, is less effective for unsteady loading than for steady loading. This occurs because the shape of the unsteady loading waveforms depend on both unsteady mechanisms—namely, circumferential variation in aerodynamic loading and source speed—while the only unsteady mechanism influencing steady

loading waveforms is the circumferential variation in source speed. As a result, the periodic change in the acoustic chord has a more significant effect on the shape of the steady loading waveforms and their interference. Consequently, the steady loading component becomes increasingly more relevant acoustically as Mach number increases.

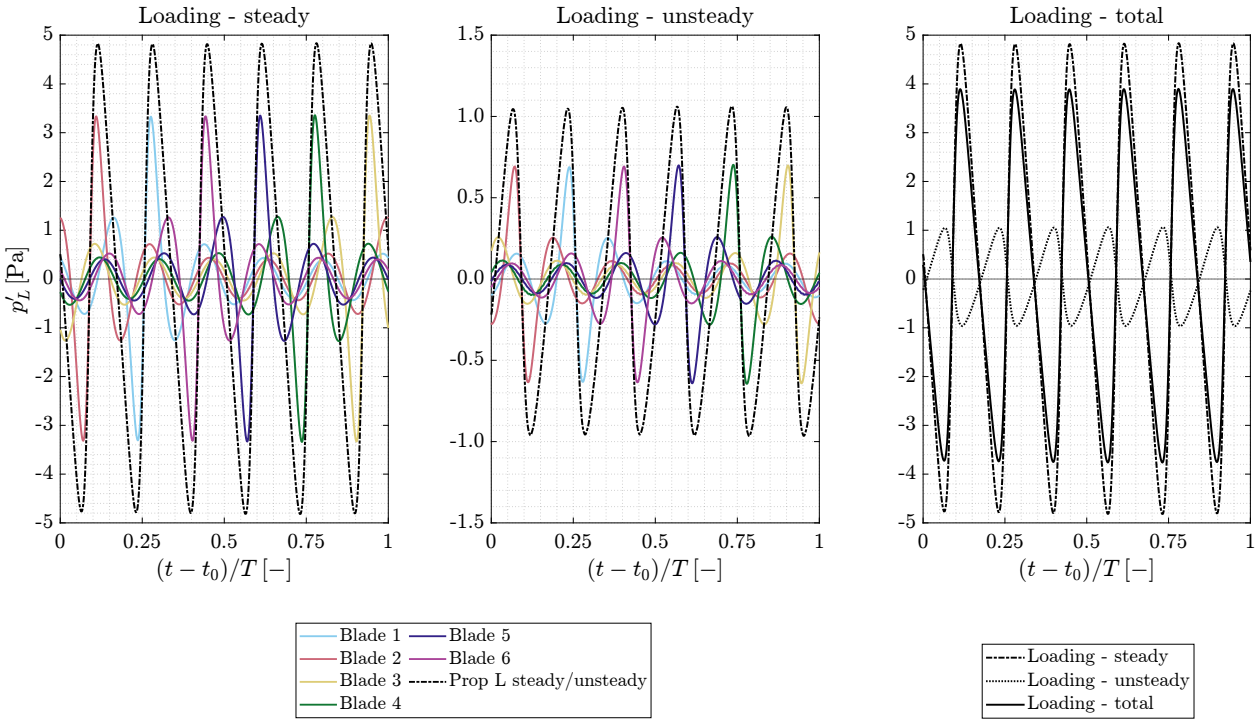

Figure 10.9: Steady, unsteady and total loading pressure waveforms of the individual blades and the propeller; $M_{ht} = 0.8$, $\phi = 0°$, $\theta = 90°$.

M_{ht}	$A_{\text{L pp, prop}}$ (Steady)	$A_{\text{L pp, prop}}$ (Unsteady)	Ratio (Steady/Unsteady)
0.357	0.0179	0.0082	2.1829
0.8	9.6635	2.0294	4.7621

Table 10.2: Peak-to-peak amplitude of loading pressure fluctuations for the propeller under steady and unsteady loading, along with the steady-to-unsteady ratio at two helical tip Mach numbers; $\phi = 0°$, $\theta = 90°$.

For an observer at $\phi = 180°$, which corresponds to the azimuthal location of maximum increase in total loading noise relative to $\alpha = 0°$, Figure 10.10 shows that the interference between the waveforms of individual blades remains constructive. Compared to $\phi = 0°$, the amplitude of the unsteady loading pressure waveforms of individual blades is higher, leading to an increased amplitude in the propeller's unsteady loading waveform due to constructive interference. This occurs because, as previously mentioned, the loading enhancement on the advancing side is more pronounced than the reduction on the retreating side, with the maximum and minimum being at diametrically opposite locations over the disk. Considering the use of a time gradient in Hanson's far-field loading pressure equation (Equation 5.16), the greater time rate of change in the blade's pressure on the advancing side is responsible for the increased amplitude observed at $\phi = 180°$. Moreover, the interaction between the steady and unsteady loading noise components also results in constructive interference. This occurs

because, at this observer location, the acoustic chord γ experiences its maximum stretching near $\phi = 90°$, where the fluctuating aerodynamic loading is positive. Consequently, the time-averaged and fluctuating noise sources are mostly in phase, leading to an increased amplitude of the total loading pressure waveform.

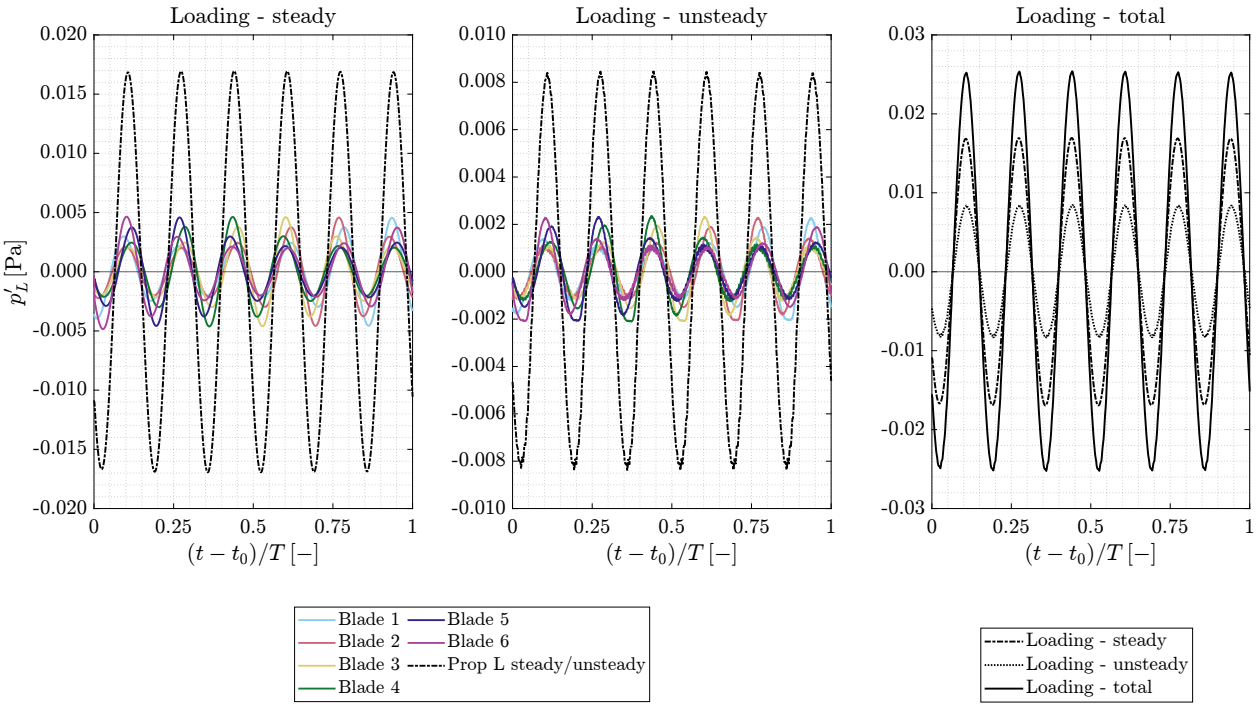

Figure 10.10: Steady, unsteady and total loading pressure waveforms of the individual blades and the propeller; $M_{ht} = 0.357$, $\phi = 180°$, $\theta = 90°$.

The reason why the observer locations corresponding to the maximum increase and decrease in loading noise at $\alpha = 10°$ relative to $\alpha = 0°$ do not exhibit a $\phi = 90°$ phase lag with respect to the locations of maximum positive and negative aerodynamic loading variations—situated at $\phi = 104°$ and $\phi = 284°$, respectively—can now be explained. Firstly, considering the effects of γ stretching, the theoretical azimuthal observer angles for the highest increase and decrease in loading noise should be $\phi = 194°$ and $\phi = 14°$. However, these positions are not included in the analysis due to the discrete observer spacing of $\phi = 15°$. More importantly, the computed loading noise incorporates the effects of source speed variation, which reaches its peak at $\phi = 90°$ and its minimum at $\phi = 270°$, introducing a phase advance of $\phi = 14°$ relative to the aerodynamic loading variation (see Figure 10.3c). As a result, the combined influence of source speed and aerodynamic loading variations leads to $\phi = 0°$ being the location of maximum loading noise reduction and $\phi = 180°$ the location of maximum loading noise increase.

It is also insightful to compare the results obtained at $\alpha = 10°$ with those from the wake encounter case. Specifically, the loading pressure waveforms at $\alpha = 10°$ and $M_{ht} = 0.357$, shown in Figure 10.10, can be compared with those for the wake encounter case, illustrated in Figure 9.8, at the two azimuthal locations corresponding to the maximum increase in loading noise relative to the uniform inflow case. It can be observed that, despite the wake encounter case exhibiting a lower magnitude of aerodynamic blade loading unsteadiness—previously evidenced by the reduced in-plane force coefficients as a percentage of the isolated thrust—the amplitude of the unsteady loading waveform is significantly higher than at $\alpha = 10°$ and a significant time gradient is observable. Consequently, the unsteady loading noise at the respective observer angles is also higher, as seen in Figure 9.7b and Figure 10.7b. This arises from the time gradient present in Hanson's far-field loading pressure equation. In essence,

an impulsive blade loading unsteadiness, characterized by a rapid and abrupt variation—such as that induced by wake impingement—has a more pronounced effect on noise emissions than the more gradually varying blade loading associated with an angle of attack. However, at $M_{ht} = 0.8$, the unsteady loading noise levels are greater at $\alpha = 10°$ compared to the wake encounter case, as shown in Figure 9.7d and Figure 10.7d. This is attributed to the fact that the strong periodic variation in the acoustic chord at the higher Mach number has a larger effect on the pressure waveforms in the angle of attack case, while the shape of the waveforms in the wake encounter case is primarily driven by the time gradient. Hence, despite the lower time gradient of aerodynamic loading, the root mean square of the unsteady loading pressure is still higher for the angle of attack case.

To further assess the relative contribution of steady and unsteady loading noise to the total loading noise, Figure 10.11 presents the ratio of the root mean square of the steady and unsteady loading pressure fluctuations to the total loading pressure fluctuations for various helical tip Mach numbers. The analysis is performed at $\phi = 0°$ and $\phi = 180°$. The results indicate that, in agreement with observations from the wake encounter case, as the Mach number increases, the steady-to-total loading noise ratio approaches unity, while the unsteady-to-total loading noise ratio tends towards zero. However, in contrast to the wake encounter scenario, unsteady noise plays a non-negligible role even at higher Mach numbers. This is attributed to the larger fluctuating blade pressure Δp, which is effectively modulated by the directivity factor, thereby sustaining a notable contribution to the overall noise radiation, despite the lower time gradient of aerodynamic loading compared to the wake impingement case.

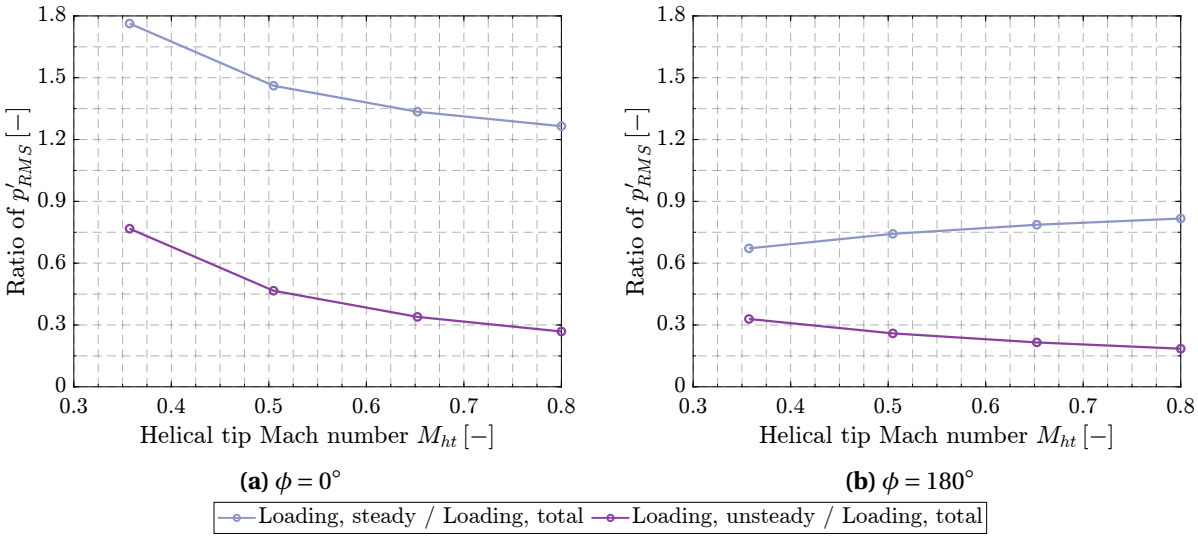

Figure 10.11: Ratio of root mean square of steady and unsteady to total loading pressure fluctuations with varying helical tip Mach number; $\theta = 90°$.

To analyze the spectral characteristics of the propeller's noise emissions, Figure 10.12 presents the power spectral density at $\alpha = 0°$ and $\alpha = 10°$ for different helical tip Mach numbers, evaluated at $\phi = 0°$ and $\phi = 180°$. At $M_{ht} = 0.357$, the first BPF, which is the dominant harmonic, exhibits a higher amplitude for $\alpha = 0°$ at $\phi = 0°$ and for $\alpha = 10°$ at $\phi = 180°$, consistent with the trends observed in Figure 10.6. Similar to the wake encounter scenario (Figure 9.14), at $\alpha = 10°$ higher noise levels are observed at elevated frequencies, particularly in the range of 3-8 BPFs. However, the difference between the two cases is less pronounced than in the wake encounter scenario, indicating that the first BPF has a relatively greater contribution at an angle of attack, in agreement with the findings of Figure 10.7. At $M_{ht} = 0.8$, although the first BPF remains dominant, appearing stronger at $\phi = 0°$ for $\alpha = 0°$ and at $\phi = 180°$ for $\alpha = 10°$, the discrepancy between the two flow conditions diminishes at

higher BPFs due to the increasing influence of steady noise sources.

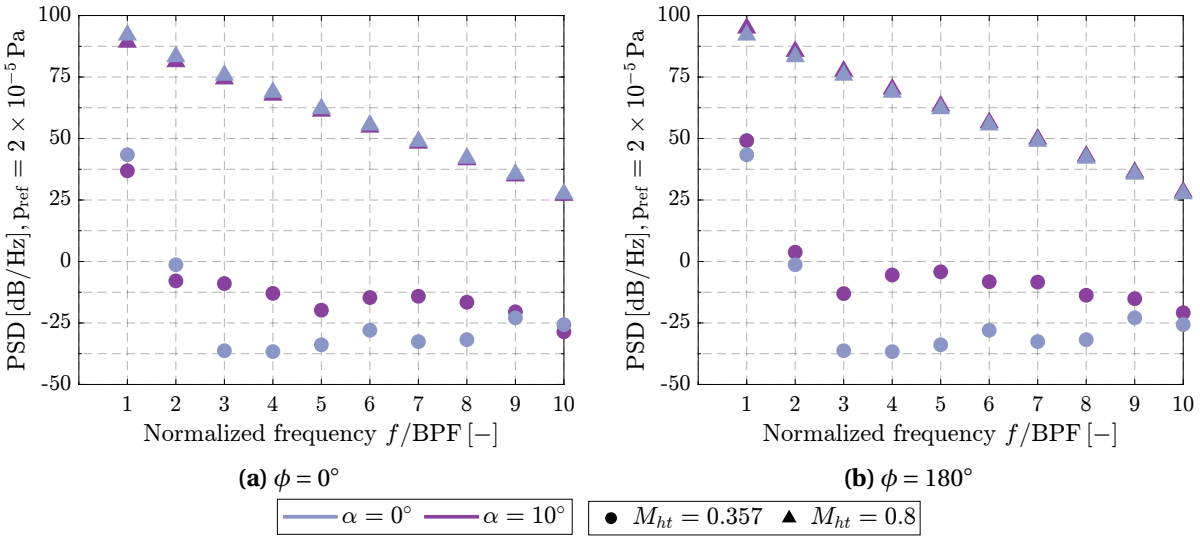

Figure 10.12: Power spectral density at $\alpha = 0°$ and $\alpha = 10°$ with varying helical tip Mach number; $\theta = 90°$.

10.2.2. NOISE DIRECTIVITY IN THE PLANE ALONG THE PROPELLER AXIS

Figure 10.13 illustrates the effect of a non-zero angle of attack on the axial directivity of the thrust-specific sound pressure level for various helical tip Mach numbers. The noise emissions in the xz-plane at $\alpha = 0°$ are shown in Figure 10.13a, while Figure 10.13b refers to the $\alpha = 10°$ case. In contrast to the symmetric noise distribution observed at $\alpha = 0°$, the $\alpha = 10°$ case exhibits an asymmetric pattern around the propeller axis. As noted in Subsection 10.2.2, the noise levels at the non-zero angle of attack increase in the region where the propeller is tilted away and decrease in the opposite region. Notably, significant noise levels are present at the propeller axis, which, as discussed in the wake encounter case, result from load unsteadiness. Increasing the Mach number results in higher noise levels. However, at $\alpha = 10°$, this increase is more pronounced in the propeller plane. Specifically, as the Mach number rises from $M_{ht} = 0.357$ to $M_{ht} = 0.8$, the TSSP increases by 43 dB at $\theta = 90°$, whereas at the propeller axis, $\theta = 0°$, the increase is limited to 7 dB. At $M_{ht} = 0.357$, the maximum noise amplification due to the non-zero angle of attack occurs at $\theta = 180°$, reaching +183 dB. The maximum noise reduction occurs at $\theta = 135°$, reaching −183 dB. At $M_{ht} = 0.8$, the maximum TSSP amplification due to the non-zero angle of attack occurs at $\theta = 0°$, reaching +185 dB, while the maximum noise reduction is observed at $\theta = 150°$, reaching −6 dB. As mentioned, differences in the axial locations of the maximum increase or decrease of total noise across different Mach numbers arise from different interference mechanisms between loading and thickness noise. In contrast to what observed for the wake encounter case (Figure 9.15), the highest noise levels are observed at the propeller plane for all Mach numbers analyzed.

Figure 10.14 illustrates the effect of a non-zero angle of attack on the axial directivity of the overall sound pressure level for different noise sources, computed in the BPF range $0.9 \leq \text{BPF} \leq 10$ at $M_{ht} = 0.357$ and $M_{ht} = 0.8$. For $M_{ht} = 0.357$, the radiation pattern at $\alpha = 10°$, depicted in Figure 10.14b, exhibits increased total noise levels in the direction where the propeller tilts away, while the opposite region experiences a decrease, relative to the $\alpha = 0°$ pattern shown in Figure 10.14a. Besides loading noise, this trend also holds for thickness noise, which is influenced by the periodic variation in source speed. As previously discussed for the wake encounter case, thrust noise dominates along

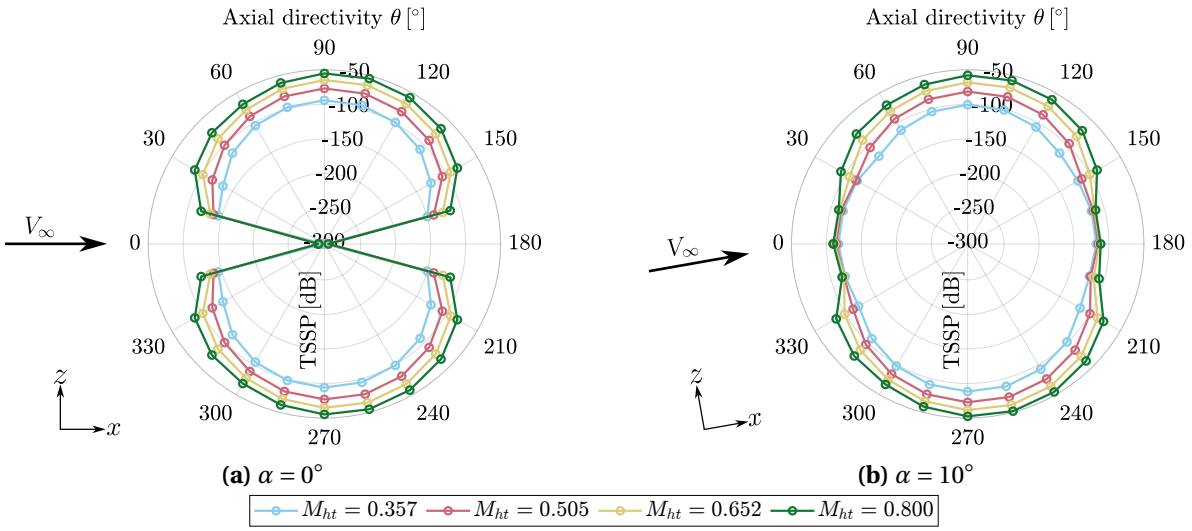

(a) $\alpha = 0°$ **(b)** $\alpha = 10°$

Figure 10.13: Effect of the angle of attack on the axial directivity of the thrust-specific sound pressure level at different helical tip Mach numbers.

the propeller axis, whereas torque noise is more prominent near the rotor disk. This is due to the unsteadiness of the blade loading and their respective directivity factors. Regarding thickness noise, null noise levels are observed at the propeller axis, independent of the modulation effect of source speed. This is attributed to the small variation in source speed (±4% at the blade tip) and the effective destructive interference between the waveforms of the six blades. However, as seen in Figure 6.27, this cancellation may not occur for a lower number of blades (three, in that case). Despite the similarly small source speed variation (±3% at the blade tip in the validation case), the out-of-phase relationship between the pressure waveforms is less effective than with a higher number of blades, reducing the strength of destructive interference. Consequently, complete cancellation does not take place, and some residual thickness noise remains at the propeller axis. The interference between loading and thickness noise remains constructive at all observer angles, as in the $\alpha = 0°$ case, except at $\theta = 45°$, indicating a phase shift between the two waveforms occurs locally. The predominance of constructive interference can be attributed to the similar phasing of the underlying unsteady mechanisms affecting both noise sources. Specifically, loading noise is influenced by periodic aerodynamic loading and source speed variations, while thickness noise is modulated by the periodic variation in source speed, resulting in predominantly in-phase waveforms. At $M_{ht} = 0.8$, the total noise levels near the propeller plane follow the expected increase and decrease compared to the $\alpha = 0°$ case in the lower and upper directivity regions, respectively. However, the absolute magnitude of this variation is smaller than that observed for $M_{ht} = 0.357$. As previously explained, this is due to the dominance of steady noise sources at higher tip Mach numbers. For the same reason, the interference between loading and thickness noise remains constructive at all observer angles. Higher overall noise levels are found along the propeller axis due to unsteady noise sources.

Figure 10.15 presents the loading noise results obtained by providing the aeroacoustic solver with the time-averaged, fluctuating, and total aerodynamic loading of the propeller. For $M_{ht} = 0.357$, the SPL at the first BPF and the OSPL in the BPF range $0.9 \leq \text{BPF} \leq 10$ are depicted in Figure 10.15a and Figure 10.15b, respectively. In the vicinity of the propeller plane, the increase in steady and unsteady loading noise when extending the frequency range remains marginal. However, at observer angles close to the propeller axis, contributions from frequencies beyond the first BPF become more pronounced. Specifically, the maximum increase in unsteady loading noise relative to the first BPF

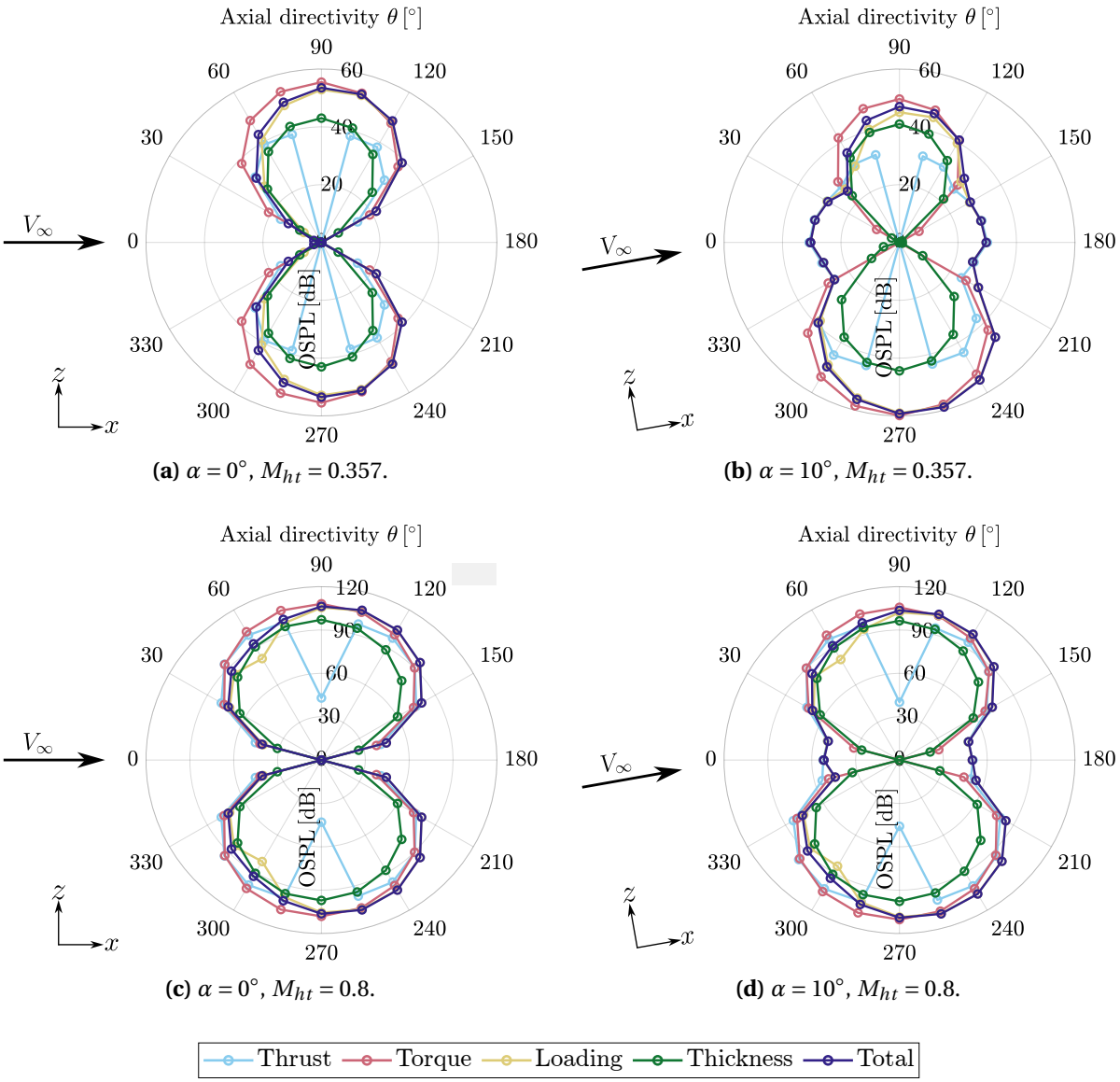

(a) $\alpha = 0°$, $M_{ht} = 0.357$.

(b) $\alpha = 10°$, $M_{ht} = 0.357$.

(c) $\alpha = 0°$, $M_{ht} = 0.8$.

(d) $\alpha = 10°$, $M_{ht} = 0.8$.

Figure 10.14: Effect of the angle of attack on the axial directivity of the overall sound pressure level at $M_{ht} = 0.357$ and $M_{ht} = 0.8$.

reaches 8 dB at $\theta = 180°$. Near the rotor disk, interference between steady and unsteady loading noise components is constructive in the region from which the propeller tilts away and destructive in the opposite region, consistent with the previously discussed noise emission characteristics in the yz-plane. Along the propeller axis, steady noise contributions—similar to thickness noise, as they are only influenced by source speed variations—vanish, making the directivity pattern primarily governed by the unsteady loading noise component. Equivalent plots are provided for $M_{ht} = 0.8$. Figure 10.15c presents the SPL at the first BPF, while Figure 10.15d illustrates the OSPL of the total loading noise, along with its mean and fluctuating components. The largest increase in unsteady loading noise within the extended frequency range remains 8 dB at $\theta = 180°$. A similar interference pattern between steady and unsteady loading noise components is observed as in the lower Mach number case. However, due to the increased dominance of the steady component at higher Mach numbers, the resulting interference leads to a smaller absolute reduction/increase in total loading noise.

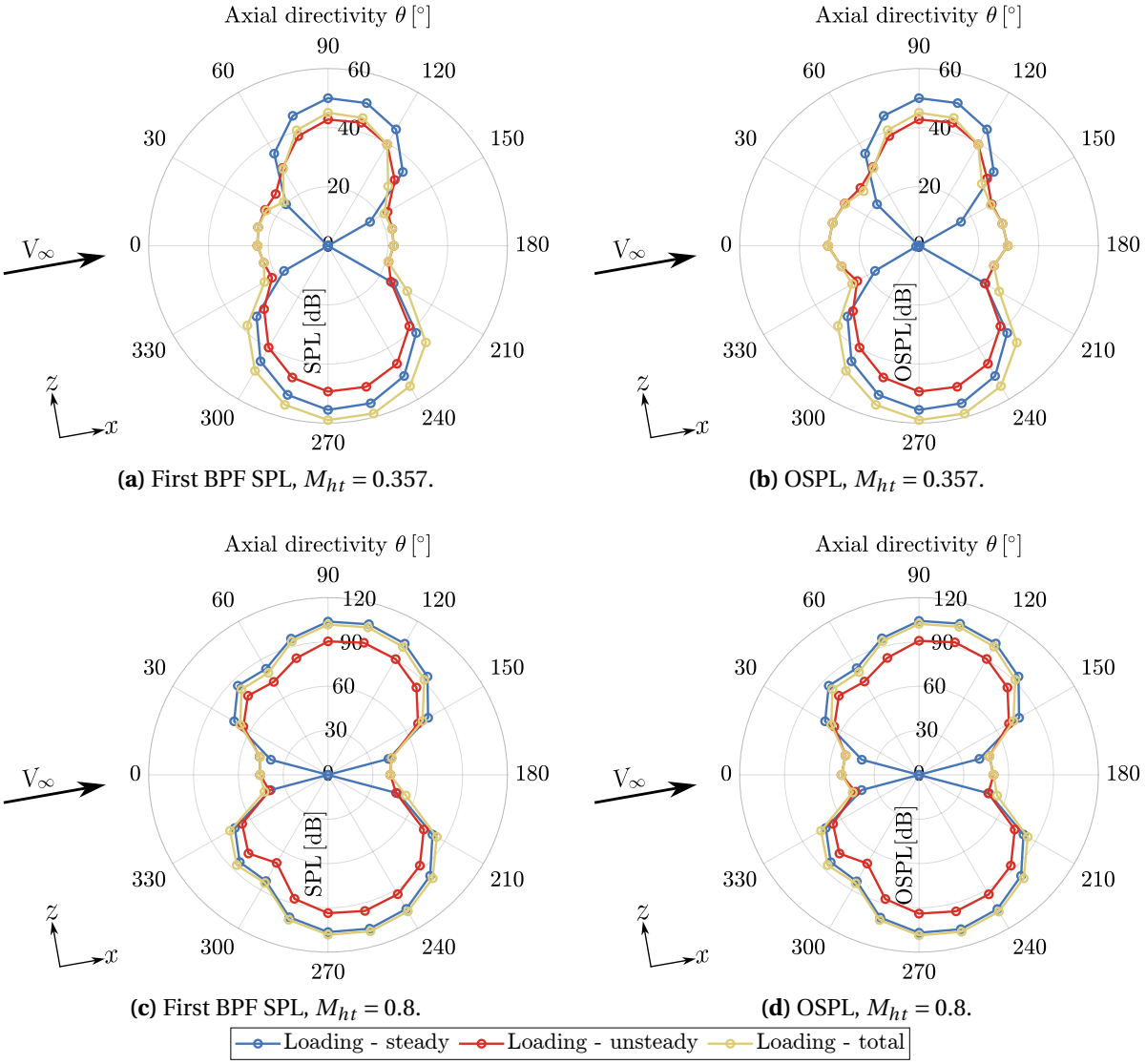

(a) First BPF SPL, $M_{ht} = 0.357$.

(b) OSPL, $M_{ht} = 0.357$.

(c) First BPF SPL, $M_{ht} = 0.8$.

(d) OSPL, $M_{ht} = 0.8$.

Figure 10.15: First BPF SPL and OSPL axial directivity of steady, unsteady and total loading noise at $\alpha = 10°$; $M_{ht} = 0.357$ and $M_{ht} = 0.8$.

Notably, at the propeller axis, where loading noise is primarily governed by its unsteady compo-

nent, the unsteady loading noise levels are lower than those observed in the wake encounter case (Figure 9.17) at both Mach numbers. Conversely, in the propeller plane, as previously discussed, the fluctuating loading noise component at $\alpha = 10°$ exhibits lower levels at $M_{ht} = 0.357$ and higher at $M_{ht} = 0.8$. The absence of this trend at the propeller axis is attributed to the directivity factor. Specifically, while within the rotor disk the directivity factor effectively modulates Δp, its influence at the rotor axis is weaker due to its small temporal variation locally. Thus, at the propeller axis, the impulsive nature of wake encounter pressure waveforms has a significant effect, leading to a higher root mean square of the unsteady loading pressure compared to the non-zero angle of attack case, and elevated noise levels.

It is important to highlight that while the steady (influenced by the modulation effect of source speed variation) and unsteady (influenced by periodic aerodynamic loading and source speed variations) loading noise components can interfere either constructively or destructively, the interaction between loading and thickness noise remains predominantly constructive. Although total loading noise is affected by the same unsteady mechanisms as the unsteady loading component, whereas thickness noise is influenced by the same unsteady mechanism as the steady loading component, while destructive interference between steady and unsteady loading noise arises due to the opposite sign of Δp on the retreating side of the blade, the interaction between total loading noise and thickness noise, leading to predominantly constructive interference, is governed by unsteady mechanisms that are closely phased.

For a deeper understanding of the radiation efficiency of steady and unsteady noise sources at the propeller axis, Figure 10.16a illustrates the ratio of the root mean square of steady and unsteady loading pressure fluctuations to the total loading pressure fluctuations for different helical tip Mach numbers at the observer angle $\theta = 0°$. The results confirm that, across all analyzed Mach numbers, loading noise emissions at the propeller axis are dictated by the unsteady component.

Furthermore, Figure 10.16b presents the spectral content of the propeller's noise emissions for both $\alpha = 0°$ and $\alpha = 10°$ at $M_{ht} = 0.357$ and $M_{ht} = 0.8$, evaluated at the observer location $\theta = 0°$. At $\alpha = 0°$, the first BPF does not represent the dominant spectral component at either Mach number. However, at $\alpha = 10°$, where noise radiation along the propeller axis is more efficient, the results reveal a significant contribution from higher harmonics beyond the first BPF, in agreement with the observations in Figure 10.15. Notably, the spectral distribution varies significantly between the two angles of attack, reflecting the substantial differences in radiation efficiency along the propeller axis.

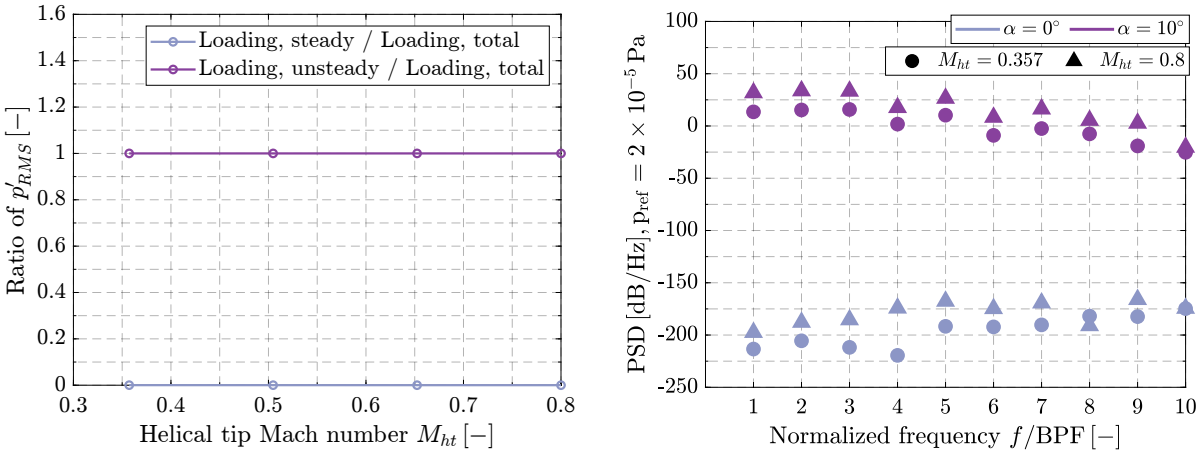

(a) p'_{RMS} ratio. **(b)** PSD comparison.

Figure 10.16: Ratio of root mean square of steady and unsteady to total loading pressure fluctuations (a) and power spectral density at $\alpha = 0°$ and $\alpha = 10°$ (b) with varying helical tip Mach number; $\theta = 0°$.

IV

Conclusions & Recommendations

11

CONCLUSIONS

The objective of this thesis was to investigate the sensitivity of a propeller's far-field tonal noise emissions to changes in the helical tip Mach number when operating at an angle of attack and encountering a wake. Furthermore, the study sought to provide a physical interpretation of the propeller's aeroacoustic signature.

To achieve this objective, low-fidelity numerical tools were utilized. Specifically, the propeller's aerodynamic performance in uniform flow conditions was estimated using Blade Element Momentum Theory (BEMT). The obtained performance maps, i.e., the blade loading radial distributions across a range of advance ratios, were provided as input to the non-uniform flow aerodynamic performance solver, which is based on the engineering method developed by Van Arnhem et al. [21]. The inflow profiles previously computed with CFD to validate the method were made available for this thesis. Specifically, for the wake encounter case, the inflow profile generated by placing a wing $3.2R_p$ upstream of the propeller location at a vertical position $z/R_p = -0.5$ was provided. On the other hand, for the angle of attack case, the employed inflow profile is representative of a propeller at $\alpha = 10°$. The computed unsteady blade pressure distribution was then used as input for an in-house time-domain aeroacoustic solver, which is based on Hanson's near-field theory, as implemented by Monteiro et al. [39]. Notably, the solver extends Hanson's original theory—designed for steady blade loading—to account for periodic unsteady loading in propeller noise predictions.

A comprehensive validation of the aerodynamic and aeroacoustic solvers was performed under both uniform and non-uniform flow conditions, demonstrating a reasonable agreement with high-fidelity data.

Due to inherent limitations of the current implementation of the aeroacoustic code, variations in source speed have not been considered in the wake encounter case, while they have been accounted for in the angle of attack case (although not fully correctly, as the nacelle upwash effect could not be considered, as said). Overall, it is expected that the modulation effect of a varying source speed on noise sources is more relevant for the angle of attack case, while this effect is reduced for the wake encounter case being the velocity deficit confined to a relatively small disk region.

In the analyses performed for this thesis , the advance ratio was maintained at $J = 0.8$ as the helical tip Mach number was varied from a low baseline value, i.e. $M_{ht} = 0.357$, to a value representative of full-scale propellers in cruise conditions, i.e. $M_{ht} = 0.8$. The blade pressure was suitably scaled from its value at the baseline Mach number while ensuring the propeller's non-dimensional performance remained unchanged. This approach allowed for the isolation of acoustic effects caused by Mach number variations while not fully accounting for the correct scaling of forces due to compressibility effects. The thesis objective was achieved, and the research questions are hereby answered:

RQ1. How can the physics of noise emissions be analyzed by employing Hanson's time-domain

aeroacoustic theory for propeller noise?

To answer this research question, an aeroacoustic characterization of the isolated propeller in uniform flow was conducted. This analysis allowed for a focus on the key features of Hanson's formulation. An investigation of the Thrust-Specific Sound Pressure Level (TSSP) at different helical tip Mach numbers showed that, at the rotor plane, the noise level increases by 39 dB as the helical tip Mach number rises from $M_{ht} = 0.357$ to $M_{ht} = 0.8$. An acoustic explanation for this was given. Specifically, waveform analyses of loading noise (the dominant noise component in the examined conditions) revealed that as the Mach number increases, the acoustic interference between the blade pressure waveforms is reduced, leading to a higher root mean square for the propeller's loading waveform. This is attributed to changes in the shape of the waveforms of individual blades, which occur due to the distinct behavior of the acoustic chord γ of each blade, a variable used by Hanson in his equations which represents a distinctive characteristic of his formulation. The maximum stretching and contraction of γ occur approximately 90° ahead and after a given observer's azimuthal position during a revolution. As the Mach number increases, the higher source speed results in more stretching and contraction, and acoustic planform (determined by blade element positions at their retarded time) visualizations show that the blade approaches the observer faster and retreats slower. This alters the shape of the acoustic pressure waveforms of individual blades, causing them to display a more peaky behavior and leading to less efficient de-phasing. Similar to other time-domain formulations [49], Hanson's loading pressure equations include a directivity factor that accounts for the relative orientation between the source-to-observer vector and the force vector (whether pressure force or another blade force), and modulates the source strength.

Blade radial pressure contours help explain the destructive interference between thrust and torque noise in the forward lobe and constructive interference in the backward lobe. This is due to the change in the sign of the thrust directivity factor between an observer location upstream and downstream of the propeller, while the torque directivity factor is symmetric around the vertical axis.

It was also observed that, at specific observer axial positions, destructive interference between the loading pressure waveforms of radial sections can occur, leading to a local reduction in loading noise. This effect becomes more pronounced at higher Mach numbers, where the significant stretching of γ results in a higher pressure signal, amplifying the de-phasing between the radial section waveforms induced by different directivity factors over the blade at a given time. This effect is a result of using a realistic blade geometry. Noise emissions from different propeller designs may exhibit similar or distinct behaviors depending especially on the sweep angle (the propeller analyzed in this thesis is unswept). However, since this effect is not observed at the low baseline Mach number, the main take-away is that experimental results obtained at lower Mach numbers, in principle cannot be directly scaled to the high Mach numbers typical of full-scale propellers in forward flight. Additionally, in line with literature [12], it is emphasized that compact-source models are inadequate for predicting noise levels at high-subsonic Mach numbers, at which it is also appropriate to consider the chordwise distributions of noise sources. The acoustic planform illustrates the non-compactness of the source at high tip speeds, underscoring the need to consider the acoustic planform of the blade rather than its physical planform.

RQ2. How does the aeroacoustic performance of a propeller scale with the helical tip Mach number under the influence of a wake impingment relative to a propeller operating in uniform flow?

The applied inflow profile causes a 10% reduction in advance ratio at a confined location on the propeller disk. For the wake encounter location under consideration, the blade loading displays two distinct peaks during the revolution, occurring at azimuthal positions where the wake interacts with the highly-loaded outboard sections. Since the wake only influences a small portion of the

disk, the overall propeller performance shows minimal change, with only a 1% and 0.5% increase in steady-state thrust and power, respectively. To provide context for the aeroacoustic analysis in comparison to the angle of attack case, it is noted that the magnitudes of the side force and normal force are 0.15% and 0.05% of the propeller thrust in uniform flow.

An investigation of the TSSP of total noise at the propeller plane showed that, while the isolated propeller demonstrates a TSSP variation of 39 dB between the lowest and highest helical tip Mach numbers considered, the variation increases to a range of 33-46 dB when subjected to wake impingement. In general, wake encounter amplifies the noise sensitivity to operating conditions at observer positions where noise levels are lower compared to uniform flow, while at other positions, the sensitivity is reduced. This behavior occurs because, as the Mach number increases, the variation in noise emissions relative to uniform flow diminishes. At $M_{ht} = 0.357$, the maximum reduction and increase in TSSP in the propeller plane relative to the uniform flow case amount to, respectively, 7 dB and 6.5 dB, while at $M_{ht} = 0.8$ they both amount to just 0.25 dB. It was shown that this results from the greater relative importance of steady loading noise sources as the Mach number increases.

The maximum increase in unsteady loading noise for both $M_{ht} = 0.357$ and $M_{ht} = 0.8$ shows a 90° phase delay with respect to the azimuthal position where the integral blade loading first peaks during the revolution, as the significant γ stretching increases the acoustic pressure fluctuations. Another significant increase occurs with a 90° phase delay relative to the second peak of integral blade loading, but with slightly lower noise levels due to a relatively smaller time gradient in the aerodynamic loading increase for some blade sections compared to the first peak. For both Mach numbers, the peak increase in loading noise occurs at the azimuthal directivity angle $\phi = 225°$, with an OSPL rise of 7 dB for $M_{ht} = 0.357$ and 0.4 dB for $M_{ht} = 0.8$. However, the loading noise directivity pattern changes significantly between the two Mach numbers, being steady forces dominant at $M_{ht} = 0.8$. The significant contribution of unsteady loading noise at lower Mach numbers leads to a shift in the interference between thickness and loading noise, which is no longer consistently constructive, as observed in uniform flow conditions. The acoustic reason behind the increased importance of the steady loading noise component at higher Mach numbers was identified. Since the waveform shape of individual blades is heavily influenced by the aerodynamic loading distribution over the disk, the effect of different temporal variations in the acoustic chord at higher Mach numbers—which alters the degree of interference between the waveforms of individual blades—is less significant for unsteady loading than for steady loading. Therefore, while the ratio of mean to fluctuating aerodynamic loading remains constant across different operating conditions, the acoustic significance of the steady component increases with Mach number.

Spectral analyses of the Power Spectral Density (PSD) indicated that, at $M_{ht} = 0.357$, there is a noticeable higher contribution from higher harmonics to the noise due to wake encounter. However, at $M_{ht} = 0.8$, the difference in noise levels between uniform and non-uniform flow conditions across the spectrum is significantly reduced due to the dominance of steady loading noise.

Similar conclusions can be drawn from noise analyses along the propeller axis. The dominance of steady loading noise at higher Mach numbers, combined with its primary radiation direction being within the rotor plane, explains why the highest total noise levels occur at the propeller plane for $M_{ht} = 0.8$ and along the propeller axis for $M_{ht} = 0.357$.

RQ3. How does the aeroacoustic performance of a propeller scale with the helical tip Mach number under the influence of a non-zero angle of attack relative to a propeller aligned with the free-stream?

The sinusoidal variation in blade loading at $\alpha = 10°$ results in a modest increase in integral propeller thrust and power, with a rise of 2.23% and 1.15%, respectively, compared to the $\alpha = 0°$ case. This is due to the slightly greater loading on the advancing side compared to the retreating side. The magnitudes of the side force and normal force are 1.2% and 4.8% of the propeller thrust at $\alpha = 0°$,

suggesting a considerably higher load unsteadiness than in the wake encounter case.

An analysis of the TSSP in the propeller plane shows, in line with previous studies [8, 9], that noise levels increase on the side away from the propeller's tilt and decrease on the opposite side. Additionally, while the propeller at $\alpha = 0°$ exhibits a variation of 39 dB between the lowest and highest Mach numbers analyzed, the variation for $\alpha = 10°$ is between 36 and 43 dB. As with the wake encounter scenario, a non-zero angle of attack enhances the sensitivity of noise to operating conditions at observer locations where noise levels are lower than those in uniform flow; conversely, the sensitivity is diminished in regions where the noise levels are higher. This behavior is again attributed to the fact that, as the Mach number increases, the change in noise relative to uniform flow decreases due to the dominance of steady noise components. At $M_{ht} = 0.357$, the maximum reduction and increase in TSSP relative to $\alpha = 0°$ amount to, respectively, 7 dB and 6 dB, while at $M_{ht} = 0.8$ they both amount to 3 dB.

By means of analyses on thickness noise, which at an angle of attack is only subject to the source speed variation as unsteady mechanism, it was possible to isolate the modulation effect of steady thickness (and loading) noise induced by the cross-flow component. At $M_{ht} = 0.357$, the maximum reduction in OSPL is 2 dB at $\phi = 0°$, with a peak increase of 1.5 dB at $\phi = 180°$. At $M_{ht} = 0.8$, the maximum reduction and increase are found at the same azimuthal locations and are 0.8 dB and 0.7 dB, respectively, showing a smaller azimuthal variation compared to $M_{ht} = 0.357$. This may appear to contrast with Mani's findings [24], which highlight the presence of a more prominent cross-flow effect at higher tip Mach numbers. However, such effect also depends on the number of blades. Specifically, Mani observed a smaller impact of the cross-flow effect for the 9-bladed rear rotor of a counter-rotation propeller compared to the 11-bladed front rotor. Given that this work uses 6 blades, the cross-flow effect is likely overshadowed by the greater contribution from steady sources at higher Mach numbers.

Notably, for both Mach numbers, the locations of maximum loading OSPL reduction (8 dB for $M_{ht} = 0.357$ and 3 dB for $M_{ht} = 0.8$) and increase (6 dB for $M_{ht} = 0.357$ and 3 dB for $M_{ht} = 0.8$) remain at $\phi = 0°$ and $\phi = 180°$, respectively. These are not located at a 90° phase shift relative to the location of maximum aerodynamic loading variation due to the fact that the computed loading noise also incorporates the effects of source speed variation, which reaches its peak at $\phi = 90°$ and minimum at $\phi = 270°$, causing a phase advance of $\phi = 14°$ relative to the aerodynamic loading variation. Waveform analyses indicate that the reduction in loading noise on the side of propeller tilt arises from destructive interference between steady and unsteady loading noise waveforms, caused by the opposite signs of blade aerodynamic pressure fluctuations on the retreating side compared to the steady aerodynamic pressure. Conversely, the interference in the opposite region is constructive.

When comparing the results for $\alpha = 10°$ and the wake encounter case for $M_{ht} = 0.357$ at the regions of maximum loading noise increase relative to uniform flow, it is observed that, although the wake encounter case exhibits lower aerodynamic blade loading unsteadiness, the amplitude of the unsteady loading waveform is significantly higher in the wake encounter case. Furthermore, a significant time gradient is observed. As a result, unsteady loading noise is higher at the respective observer angles in the wake encounter scenario. The impulsive nature of the unsteady loading caused by wake impingement leads to more pronounced noise emissions than the gradually varying loading associated with an angle of attack. However, at $M_{ht} = 0.8$, unsteady loading noise for $\alpha = 10°$ exceeds that of the wake encounter case, due to a larger effect of the strong periodic variation in acoustic chord, whereas the shape of the waveforms in the wake encounter case is primarily driven by the time gradient of aerodynamic loading. As a result, a higher root mean square of the unsteady loading waveform is produced in the angle of attack case despite a lower time gradient of the aerodynamic loading.

The PSD spectra for $\alpha = 10°$ show an increased contribution from higher harmonics at $M_{ht} = 0.357$, with the difference in spectral content relative to $\alpha = 0°$ diminishing at $M_{ht} = 0.8$ due to the

higher influence of steady noise sources.

At the propeller axis, where unsteady loading noise dominates, the noise levels are lower at $\alpha = 10°$ compared to the wake encounter condition at both $M_{ht} = 0.357$ and $M_{ht} = 0.8$. The discrepancy from the results in the propeller plane is due to the directivity factor, which efficiently modulates Δp in the rotor plane but has a weaker influence at the propeller axis. Thus, at the propeller axis, the impulsive characteristics of wake encounter pressure waveforms notably influence the unsteady loading pressure, resulting in a higher root mean square value compared to the non-zero angle of attack case and leading to increased noise levels.

In conclusion, the analyses conducted showed that variations in tonal noise amplitude, directivity, and spectral content due to a flow non-uniformity depend on the propeller helical tip Mach number. This is attributed to the increased influence of steady noise sources at higher Mach numbers. Waveform analyses indicated that the reason for the greater significance of steady noise sources at higher Mach numbers lies in the fact that the different temporal variations in the acoustic chord—affecting the interference between the waveforms of individual blades—have a lesser impact on unsteady loading than on steady loading noise. These results underscore the fact that, in principle, the aeroacoustic signature of a propeller obtained from experimental studies using low helical tip Mach numbers cannot be directly scaled to full-scale propellers operating at higher Mach numbers.

12

RECOMMENDATIONS

Based on the analysis performed and results obtained, a number of recommendations for future research can be made:

- **Properly accounting for source speed variation in the aeroacoustic solver**
  As outlined in Section 5.2, the current version of the aeroacoustic solver does not account for the deformation of the helical surface caused by an asymmetry in the inflow velocity, which affects the blade elements differently across the azimuth. Consequently, although the CFD-generated inflow disturbances were used as inputs for the aerodynamic performance prediction method under non-uniform inflow conditions, they could not be directly applied in the acoustic solver. The exclusion of the nacelle upwash is not expected to significantly impact the aeroacoustic results in the angle of attack case, provided that, as done in this work, the axial and in-plane velocity components computed through simple trigonometric application are accounted for, as discussed in Section 7.2, since its most significant effect is concentrated at the hub, where the relative velocity is naturally lower. However, the effect of the axial velocity deficit was entirely neglected when computing the source speed of the blade sections moving through the wake. Although the disk region of velocity is relatively small, it is recommended to verify these assumptions by including the adjustments to the source speed.

- **Verify dependency of number of blades on source speed modulation effect**
  While Mani [24] observed a more prominent cross-flow effect at higher tip Mach numbers, the comparison between different blade counts in his study indicates that this effect diminishes as the blade number decreases. The present analysis, conducted with a 6-bladed propeller, indicates that the modulation effect of the cross-flow component on steady thickness noise has a reduced influence at higher Mach numbers compared to lower Mach numbers. This behavior is attributed to the use of a moderate blade count, where the dominant contribution of steady noise sources masks the modulation effect of the cross-flow component. Overall, further investigation is required to assess the dependence of the source speed modulation effect on both blade count and Mach number. This can be achieved by utilizing Hanson's time-domain theory to gain deeper physical insights.

- **Incorporate broadband noise model**
  Although this thesis only considered tonal noise emissions, it would be interesting to account for random sources too by implementing a broadband noise model. This would add great value to the current version of the aeroacoustic solver, allowing to investigate broadband noise generation mechanisms at the propeller axis.

- **Accounting for propeller suction effect**
  As discussed in Section 2.3, the propeller suction on the incoming flow leads to a reduction in wake width and velocity deficit, especially at higher thrust settings [10]. This effect was neglected in this thesis, and is especially relevant for pusher propeller configurations. Future research should incorporate this effect in aerodynamic and aeroacoustic analyses.

- **Inclusion of aero-elastic models**
  This study assumed that the blade is perfectly rigid. However, it is known that the elasticity and interaction between structural mechanics and aerodynamics are heightened by propeller sweep and high aspect ratios, influencing both propeller performance and noise [51]. Therefore, especially if the propeller blades are swept (not the case for the current thesis, but potentially relevant for future studies) it is recommended to couple the aerodynamic and aeroacoustic solvers with aero-elastic models to account for the blade deformation.

- **Analyze the effects of design variables**
  With an understanding of how realistic operating conditions influence noise emissions, future studies can focus on the effects of propeller design variables—such as blade sweep, airfoil shape, and propeller diameter—on noise in arbitrary non-uniform flows. By utilizing waveform analysis for physics-based insights, these studies could explore ways to exploit destructive interference to mitigate noise due to steady sources, which dominates at the higher Mach numbers typical of full-scale designs, ultimately aiding in the design of quieter propellers.

These recommendations aim to advance research toward a deeper understanding of propeller aeroacoustics in non-uniform flow conditions while also guiding the development of quieter designs.

BIBLIOGRAPHY

[1] W. F. Durand. "Experimental Research on Air Propellers", naca technical report, naca-tr-141. 1917. URL https://ntrs.nasa.gov/citations/19930091041.

[2] C. Rohrbach and F. B. Metzger. "The Propfan: a New Look in Propulsors". *11th Propulsion Conference, Joint Propulsion Conferences*, Sep. 1975. doi: https://10.2514/6.1975-1208.

[3] L.L.M. Veldhuis. "Propeller Wing Aerodynamic Interference", Ph.D. thesis, Faculty of Aerospace Engineering, Delft University of Technology, Delft, The Netherlands. 2005. URL https://repository.tudelft.nl/islandora/object/uuid%3A8ffbde9c-b483-40de-90e0-97095202fbe3.

[4] A. E. Pyrzyk. "Flightpath 2050 - Europe's Vision for Aviation", Tech. rep. 2014. doi: https://doi.org/10.2777/50266.

[5] H.D. Kim. "Distributed Propulsion Vehicles". *27th Congress of the International Council of the Aeronautical Sciences 2010, ICAS 2010*, 1:55–65, Jan. 2010. URL https://api.semanticscholar.org/CorpusID:34280724.

[6] N. Herzog, A. Reeh, A. Kümmel, and C. Breitsamter. "Analysis of Distributed Electric Propulsion on Commuter Aircraft". *AIAA Scitech 2021 Forum*, Jan. 2021. doi: https://doi.org/10.2514/6.2021-1199.

[7] D. Acevedo Giraldo, M. Roger, M. Jacob, and H. Beriot. "Experimental and Analytical Study of the Aerodynamic Noise Emitted by Distributed Electric Propulsion Systems". *28th AIAA/CEAS Aeroacoustics 2022 Conference*, June 2022. doi: https://doi.org/10.2514/6.2022-2830.

[8] J. Goyal, T. Sinnige, C. Ferreira, and F. Avallone. "Aerodynamics and Far-field Noise Emissions of a Propeller in Positive and Negative Thrust Regimes at Non-zero Angles of Attack". *AIAA Aviation 2023 Forum*, June 2023. doi: https://doi.org/10.2514/6.2023-3217.

[9] G. Romani, E. Grande, F. Avallone, D. Ragni, and D. Casalino. "Computational Study of Flow Incidence Effects on the Aeroacoustics of Low Blade-Tip Mach Number Propellers". *Aerospace Science and Technology*, 120(1882):107275, Dec. 2021. doi: https://doi.org/10.1016/j.ast.2021.107275.

[10] T. Sinnige, D. Ragni, A. M. N. Malgoezar, G. Eitelberg, and L. L. M. Veldhuis. "APIAN-INF: an Aerodynamic and Aeroacoustic Investigation of Pylon-Interaction Effects for Pusher Propellers". *CEAS Aeronautical Journal*, 9:291–306, 2018. doi: https://doi.org/10.1007/s13272-017-0247-2.

[11] B. Magliozzi, D. B. Hanson, and R. K. Amiet. "Propeller and Propfan Noise". *Aeroacoustics of Flight Vehicles: Theory and Practice. Volume 1: Noise Sources*, edited by H. H. Hubbard, NASA Langley Research Center, Hampton, VA, U.S.A:1–64, 1991.

[12] D. Hanson. "Near Field Noise of High Tip Speed Propellers in Forward Flight". *3rd AIAA Aeroacoustics Conference*, pages 1–13, 1976. doi: https://doi.org/10.2514/6.1976-565.

[13] T. Sinnige. "Aerodynamic and Aeroacoustic Interaction Effects for Tip-Mounted Propellers",

Ph.D. thesis, Faculty of Aerospace Engineering, Delft University of Technology, Delft, The Netherlands. 2018. URL https://repository.tudelft.nl/islandora/object/uuid%3A214e1e9a-c53e-47c7-a12c-b1eb3ec8293b.

[14] R. Nederlof, D. Ragni, and T. Sinnige. "Experimental Investigation of the Aerodynamic Performance of a Propeller at Positive and Negative Thrust and Power". *AIAA Aviation 2022 Forum*, June 2022. doi: https://doi.org/10.2514/6.2022-3893.

[15] L. Miranda and J. Brennan. "Aerodynamic Effects of Wingtip-Mounted Propellers and Turbines". *4th Applied Aerodynamics Conference*, page 1802, 1986. doi: https://doi.org/10.2514/6.1986-1802.

[16] A. Koutsoukos. "Aerodynamic and Aeroacoustic Interaction Effects of a Distributed-Propeller Configuration in Forward Flight", M.Sc. thesis, Faculty of Aerospace Engineering, Delft University of Technology, Delft, The Netherlands. 2018. URL https://repository.tudelft.nl/islandora/object/uuid%3Ab746cbbe-2fc0-4506-a82a-b320e476521a.

[17] G. Bernardini, F. Centracchio, M. Gennaretti, U. Iemma, C. Pasquali, C. Poggi, M. Rossetti, and J. Serafini. "Numerical Characterisation of the Aeroacoustic Signature of Propeller Arrays for Distributed Electric Propulsion". *Applied Sciences*, 10(8), 2020. doi: https://doi.org/10.3390/app10082643.

[18] B. Marinus. "Multidisciplinary Optimization of Aircraft Propeller Blades", Ph.D. thesis, Faculty of Mechanical Engineering, Royal Military Academy. Nov. 2011. URL https://www.researchgate.net/publication/260622828_Multidisciplinary_Optimization_of_Aircraft_Propeller_Blades.

[19] S. Glegg and W. Devenport. *Aeroacoustics of Low Mach Number Flows: Fundamentals, Analysis, and Measurement*. Academic Press, Feb. 2017. ISBN 978-0-12-809651-2.

[20] F. Avallone and D. Casalino. "Fundaments of Aeroacoustics Course: Introduction to Aeroacoustics". *Lecture Notes, Delft University of Technology, Department of Aerospace Engineering*, 2022.

[21] N. van Arnhem, R. de Vries, T. Sinnige, R. Vos, G. Eitelberg, and L.L.M. Veldhuis. "Engineering Method to Estimate the Blade Loading of Propellers in Nonuniform Flow". *AIAA Journal*, 58: 5332–5346, Oct. 2020. doi: https://doi.org/10.2514/1.J059485.

[22] N. Van Arnhem. "Unconventional PropellerAirframe Integration for Transport Aircraft Configurations", Ph.D. thesis, Faculty of Aerospace Engineering, Delft University of Technology, Delft, The Netherlands. 2018. URL https://repository.tudelft.nl/islandora/object/uuid%3A4d47b0db-1e6a-4f38-af95-aafd33c29402.

[23] T. Sinnige, N. van Arnhem, T. Stokkermans, G. Eitelberg, and L.L.M. Veldhuis. "Wingtip-Mounted Propellers: Aerodynamic Analysis of Interaction Effects and Comparison with Conventional Layout". *Journal of Aircraft*, 56:1–18, Nov. 2018. doi: https://doi.org/10.2514/1.C034978.

[24] R. Mani. "The Radiation of Sound from a Propeller at Angle of Attack". *Proceedings: Mathematical and Physical Sciences*, 431(1882):203–218, 1990. doi: https://doi.org/10.1098/rspa.1990.0127.

[25] R. P. Woodward. "Noise of a Model High Speed Counterrotation Propeller at Simulated Takeoff/Approach Conditions (F7/A7)". *11th AIAA Aeroacoustics Conference*, 1987. doi: https://doi.org/10.2514/6.1987-2657.

[26] P. J. W. Block. "Experimental Study of the Effects of Installation on Single and Counter-Rotation Propeller Noise". *National Aeronautics and Space Administration, Scientific and Technical Information Branch*, 2541, 1986. URL https://ntrs.nasa.gov/citations/19860016690.

[27] G. L. Jr. Gentry and E. R. Jr. Booth. "Effect of Pylon Wake with and without Pylon Blowing on Propeller Thrust", NASA Langley Research Center, NASA-TM-4162. 1990. URL https://ntrs.nasa.gov/api/citations/19900004874/downloads/19900004874.pdf.

[28] P. J. W. Block and G. L. Jr. Gentry. "Directivity and Trends of Noise Generated by a Propeller in a Wake", NASA Langley Research Center, NASA-TP-2609. 1986. URL https://ntrs.nasa.gov/api/citations/19860021869/downloads/19860021869.pdf.

[29] NASA Glenn Research Center. Benson, T. (Ed.). "Mach Number Role in Compressible Flows", May 2021. URL https://www.grc.nasa.gov/www/BGH/machrole.html.

[30] B. Zhou, M. Morelli, P. Dehpanah, N. Gauger, and A. Guardone. "Aeroacoustic Analysis of a Wing-Tip Mounted Propeller Configuration". *AIAA Aviation 2021 Forum*, Aug. 2021. doi: https://doi.org/10.2514/6.2021-2224.

[31] C. Poggi, G. Bernardini, M. Gennaretti, and R. Camussi. "Scalability of Mach Number Effects on Noise Emitted by Side-by-Side Propellers". *Applied Sciences*, 12(19), 2022. doi: https://doi.org/10.3390/app12199507.

[32] E. Branlard, K. Dixon, and M. Gaunaa. "An Improved Tip-Loss Correction Based on Vortex Code Results". *Proceedings of EWEA 2012 - European Wind Energy Conference & Exhibition European Wind Energy Association (EWEA)*, 2012. URL https://backend.orbit.dtu.dk/ws/portalfiles/portal/7951124/An_improved_tip_loss.pdf.

[33] S. Gudmundsson. "The Anatomy of the Propeller". pages 581–659, Dec. 2014. doi: https://doi.org/10.1016/B978-0-12-397308-5.00014-3.

[34] R. Willemsen. "A Sensitivity Study on the Aerodynamic Performance of a Wingtip-Mounted Tractor Propeller-Wing System", M.Sc. thesis, Faculty of Aerospace Engineering, Delft University of Technology, Delft, The Netherlands. 2020. URL https://repository.tudelft.nl/islandora/object/uuid%3A24e1b2a5-1616-48f1-8628-8216c0cbce94.

[35] M. Drela. XFOIL: An Analysis and Design System for Low Reynolds Number Airfoils. In Thomas J. Mueller, editor, *Low Reynolds Number Aerodynamics*, pages 1–12, Berlin, Heidelberg, 1989. Springer Berlin Heidelberg. doi: https://doi.org/10.1007/978-3-642-84010-4$_1$.

[36] H. Snel. "Review of the Present Status of Rotor Aerodynamics: Review of Rotor Aerodynamics". *Wind Energy*, 1:46–69, 1998. doi: https://doi.org/10.1002/(SICI)1099-1824(199804)1:1+<46::AID-WE3>3.0.CO;2-9.

[37] W. R. Sears. "Some Aspects of Non-Stationary Airfoil Theory and Its Practical Application". *Journal of the Aeronautical Sciences*, 8(3):104–108, 1941. doi: https://doi.org/10.2514/8.10655.

[38] M. Kotwicz Herniczek, D. Feszty, S.-A. Meslioui, J. Park, and F. Nitzsche. "Evaluation of Acoustic Frequency Methods for the Prediction of Propeller Noise". *AIAA Journal*, 57:1–14, Mar. 2019. doi: https://doi.org/10.2514/1.J056658.

[39] F. do Nascimento Monteiro, D. Ragni, F. Avallone, and T. Sinnige. "Low-Order Acoustic Prediction Tool for Estimating Noise Emissions from Distributed Propeller Configurations". *AIAA Aviation 2023 Forum*, 2023. doi: https://doi.org/10.2514/6.2023-4180.

[40] D. L. Hawkings and M. V. Lowson. "Theory of Open Supersonic Rotor Noise". *J. Sound and Vibration*, 36(1), 1914. doi: https://doi.org/10.1016/S0022-460X(74)80340-8.

[41] N. van Arnhem, R. de Vries, R. Vos, and L. Veldhuis. "Aerodynamic Performance of an Aircraft Equipped with Horizontal Tail Mounted Propellers". *AIAA Aviation 2019 Forum*, Jun. 2019. doi: https://doi.org/10.2514/6.2019-3036.

[42] H Himmelskamp. "Profile Investigations on a Rotating Airscrew, Ph.D. thesis, Göttingen University, Göttingen, Germany". 1945.

[43] J. Goyal, T. Sinnige, F. Avallone, and C. Ferreira. "Aerodynamic and Aeroacoustic Characteristics of an Isolated Propeller at Positive and Negative Thrust". *AIAA Aviation 2021 Forum*, Aug. 2021. doi: https://doi.org/10.2514/6.2021-2187.

[44] A. Zarri, A. Koutsoukos, and F. Avallone. "Aerodynamic and Acoustic Interaction Effects of Adjacent Propellers in Forward Flight". *AIAA Aviation 2023 Forum*, June 2023. doi: https://doi.org/10.2514/6.2023-4489.

[45] Delft High Performance Computing Centre (DHPC). DelftBlue Supercomputer (Phase 2). `https://www.tudelft.nl/dhpc/ark:/44463/DelftBluePhase2`, 2024.

[46] E. Por, M. van Kooten, and V. Sarkovic. "Nyquist–Shannon Sampling Theorem". May 2019. URL `https://home.strw.leidenuniv.nl/~por/AOT2019/docs/AOT_2019_Ex13_NyquistTheorem.pdf`.

[47] D. Hanson. "The Influence of Propeller Design Parameters on Far Field Harmonic Noise in Forward Flight". *American Institute of Aeronautics and Astronautics Paper 79-0609*, 1979. doi: https://doi.org/10.2514/3.50887.

[48] J. E. Marte and D. W. Kurtz. "A Review of Aerodynamic Noise From Propellers, Rotors, and Lift Fans". *NASA Technical Report 32-1462*, Jan. 1970. URL `https://ntrs.nasa.gov/citations/19700005920`.

[49] A. Najafi-Yazdi, G. Brès, and L. Mongeau. "An Acoustic Analogy Formulation for Moving Sources in Uniformly Moving Media". *Proceedings of The Royal Society A: Mathematical, Physical and Engineering Sciences*, 467:144–165, June 2010. doi: https://10.1098/rspa.2010.0172.

[50] M.J. Kingan and A.B. Parry. "Acoustic Theory of the Many-Bladed Contra-Rotating Propeller: the Effects of Sweep on Noise Enhancement and Reduction". *Journal of Sound and Vibration*, 468(6–8):115089, Nov. 2019. doi: https://doi.org/10.1016/j.jsv.2019.115089.

[51] O. Bergmann, F. Möhren, C. Braun, and F. Janser. "On the Influence of Elasticity on Swept Propeller Noise". *AIAA SCITECH 2023 Forum*, Jan. 2023. doi: https://doi.org/10.2514/6.2023-0210.

A

AEROACOUSTIC SOLVER - SENSITIVITY STUDIES

This appendix presents sensitivity studies on the number of time steps per period, aiming to determine an appropriate number of time steps for the aeroacoustic analyses conducted in this thesis. All the studies focus on the OSPL (and related p'_{RMS}) in the xz-plane, with the observers positioned in the far field at a distance of 10 diameters from the center of the propeller. The analyses are carried out at $M_{ht} = 0.8$, which represents the highest Mach number considered in this study. This Mach number was selected due to the increased levels of high-frequency noise generated at this operating condition, necessitating adequate time resolution for accurate capture.

A.1. UNINSTALLED PROPELLER IN UNIFORM FLOW

Only the observer angles within the range $0° \leq \theta \leq 180°$ (where $\theta = 0°$ is located upstream with respect to the propeller) are considered since, under uniform flow conditions, the directivity pattern remains symmetric about the propeller axis. The OSPL was evaluated within the BPF range $0.9 \leq \text{BPF} \leq 10$. Figure A.1a presents the OSPL polar directivity for different numbers of time steps per period. For time steps exceeding 200, the noise levels computed at higher time resolutions are in close agreement. Figure A.1b displays the maximum (computed across the observer angles shown in Figure A.1a) root mean square of the pressure fluctuations as a function of the number of time steps per period, along with the corresponding computational time per observer. The results indicate that as N_t increases, the maximum p'_{RMS} also rises and approaches convergence, while the execution time exhibits a linear increase. Figure A.1c depicts the relative difference between the maximum p'_{RMS} values obtained for different time steps per period and that computed using the highest time resolution, as defined in Equation 6.2. The results show that using 600 time steps per period allows to maintain a deviation below 0.1% in maximum p'_{RMS}, while still ensuring a safety margin. Furthermore, Figure A.1d confirms that 600 time steps per period ensure a relative difference in p'_{RMS} on the order of 10^{-3} near the propeller axis, making it the chosen time resolution.

Lastly, considerations regarding data sampling are necessary. In this case, the highest frequency of interest is 10 BPF = 24795.84 Hz. With a sampling frequency of $F_s = 247935.41$ Hz, the Nyquist limit is $F_s/2 = 123967.71$ Hz, which far exceeds the maximum frequency of interest. Therefore, the selected time resolution ensures that the sampled data accurately captures the relevant acoustic frequencies without aliasing.

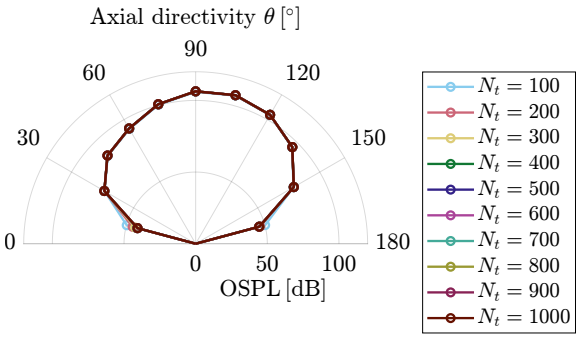

(a) OSPL directivity with varying amount of time steps.

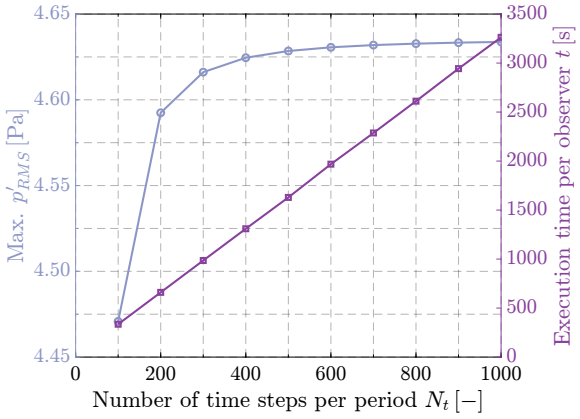

(b) Maximum p'_{RMS} and execution time per observer versus number of time steps.

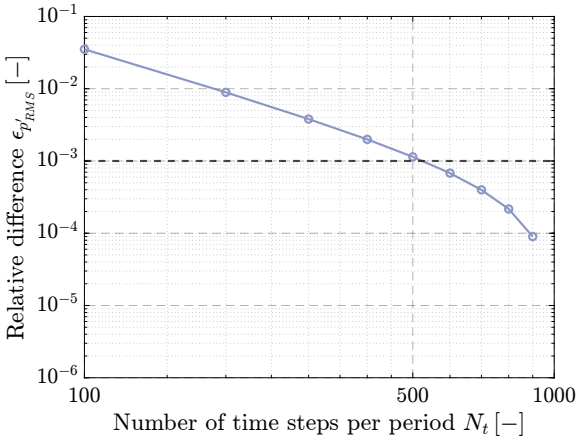

(c) p'_{RMS} relative difference versus number of time steps.

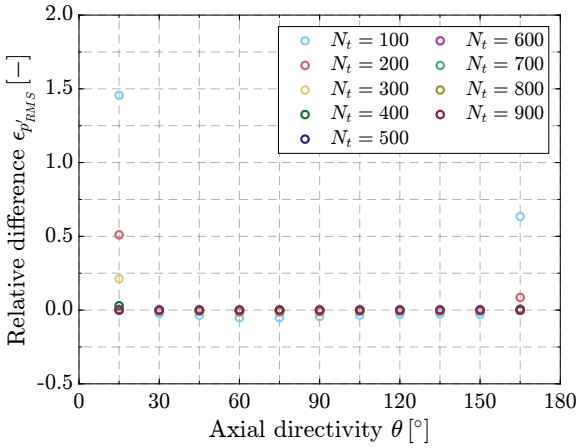

(d) p'_{RMS} relative difference with respect to the finest time resolution.

Figure A.1: p'_{RMS} and OSPL sensitivity to number of time steps per period; uniform inflow, $M_{ht} = 0.8$.

A.2. WAKE ENCOUNTER

Figure A.2a illustrates the OSPL polar directivity for various time step counts per period. The OSPL is evaluated within the BPF range $0.9 \leq \text{BPF} \leq 10$. For time steps exceeding 100, the noise levels obtained at higher resolutions exhibit close agreement. Figure A.2b presents the maximum root mean square of the pressure fluctuations, computed across the observer angles shown in Figure A.2a, as a function of the number of time steps per period, alongside the corresponding computational time. The results indicate that as p'_{RMS} converges, the computational time exhibits only a marginal difference compared to the uniform flow case shown in Figure A.1b. Figure A.2c illustrates the relative difference between the maximum p'_{RMS} values obtained for different time steps per period and that computed at the highest time resolution, as defined in Equation 6.2. The results demonstrate that 600 time steps ensure a deviation below 0.1% in maximum p'_{RMS}, while still ensuring a safety margin. Additionally, Figure A.2d confirms that 600 time steps per period guarantee a relative difference in p'_{RMS} never exceeding the order of 10^{-3} at all observer angles. As shown in Section A.1, this time resolution prevents aliasing at the maximum frequency of interest, i.e., 10 BPF. Therefore, the chosen number of time steps per period for the wake encounter case is 600.

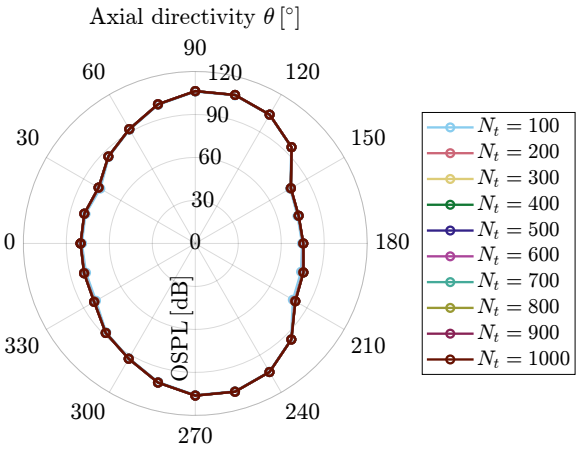

(a) OSPL directivity with varying amount of time steps.

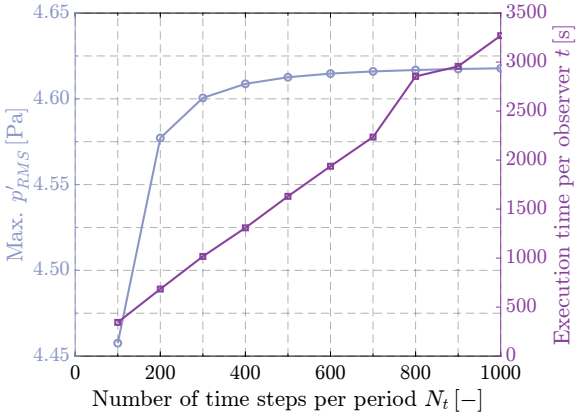

(b) Maximum p'_{RMS} and execution time per observer versus number of time steps.

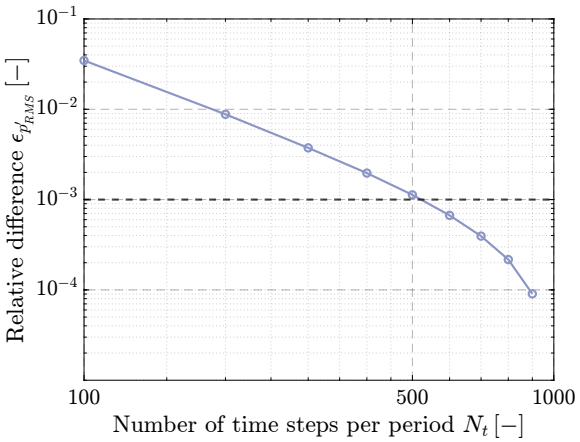

(c) p'_{RMS} relative difference versus number of time steps.

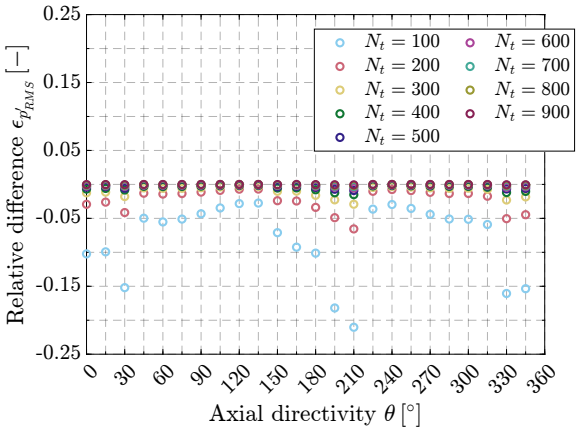

(d) p'_{RMS} relative difference with respect to the finest time resolution.

Figure A.2: p'_{RMS} and OSPL sensitivity to number of time steps per period; wake encounter, $M_{ht} = 0.8$.

A.3. NON-ZERO ANGLE OF ATTACK

Figure A.3a depicts the OSPL polar directivity for varying time step counts per period, where the OSPL is evaluated over the BPF range $0.9 \leq \text{BPF} \leq 10$. The results indicate that beyond 300 time steps, the noise levels obtained at higher resolutions exhibit minimal variation. Figure A.3b

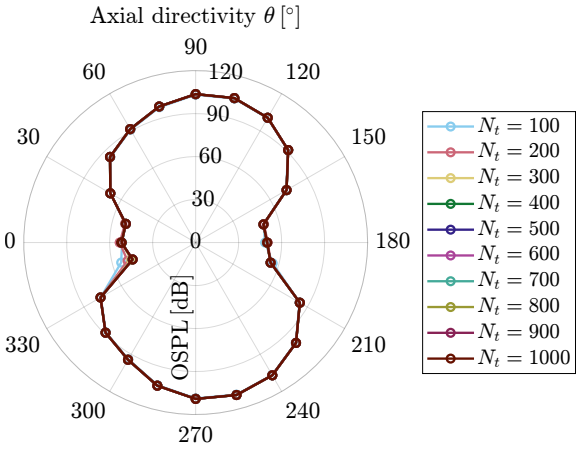

(a) OSPL directivity with varying amount of time steps.

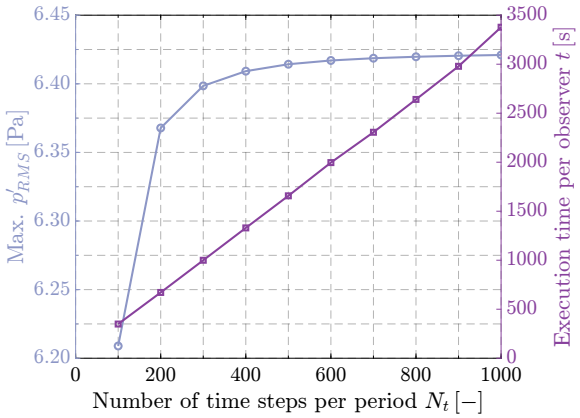

(b) Maximum p'_{RMS} and execution time per observer versus number of time steps.

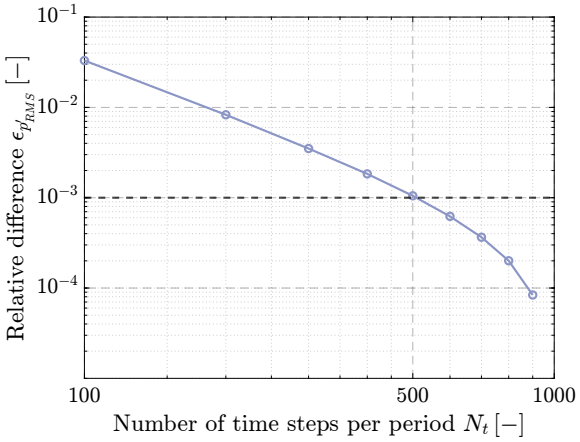

(c) p'_{RMS} relative difference versus number of time steps.

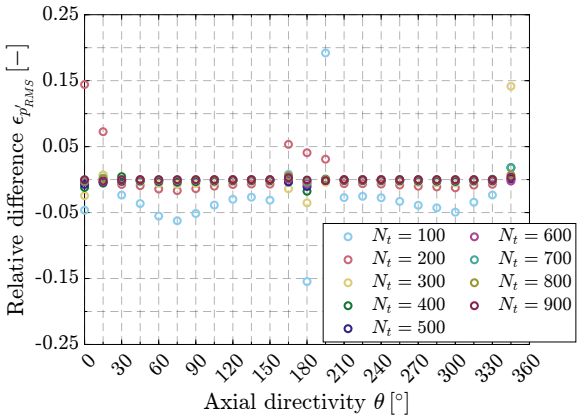

(d) p'_{RMS} relative difference with respect to the finest time resolution.

Figure A.3: p'_{RMS} and OSPL sensitivity to number of time steps per period; $\alpha = 10°$, $M_{ht} = 0.8$.

presents the maximum root mean square of the pressure fluctuations, computed across the observer angles depicted in Figure A.3a, as a function of the number of time steps per period. Additionally, the corresponding computational time is shown. The findings reveal that as p'_{RMS} converges, the computational time rises in a linear fashion. The relative difference between the maximum p'_{RMS} values obtained for different time step counts and that computed at the highest resolution is shown in Figure A.3c, following the definition in Equation 6.2.The results indicate that using 600 time steps per period ensures a deviation below 0.1% in maximum p'_{RMS} while maintaining a safety margin. Furthermore, Figure A.3d confirms that for all observer angles, the relative difference in p'_{RMS} remains on the order of 10^{-3} when 600 time steps per period are used. As demonstrated in Section A.1, this resolution effectively prevents aliasing at the highest frequency of interest, i.e., 10 BPF. Consequently, the selected time step resolution for the angle of attack case is 600 steps per period. As this is the same time resolution chosen for the uniform flow and the wake encounter cases, it can be concluded

that, for the analyzed inflow and operating conditions, the blade loading unsteadiness does not affect the chosen number of time steps per period.